



# **Optical diagnostics of soot formation in low pressure laminar premixed flames**

Safa Mohammed M Algoraini

A Thesis submitted in fulfilment for the degree of Doctor of Philosophy

PhD

School of Chemical Engineering

The University of Adelaide

November 2019

---

## Declaration of Originality

I certify that this work contains no material which has been accepted for the award of any other degree or diploma in my name, in any university or other tertiary institution and, to the best of my knowledge and belief, contains no material previously published or written by another person, except where due reference has been made in the text. In addition, I certify that no part of this work will, in the future, be used in a submission in my name, for any other degree or diploma in any university or other tertiary institution without the prior approval of the University of Adelaide and where applicable, any partner institution responsible for the joint award of this degree. I acknowledge that copyright of published works contained within this thesis resides with the copyright holder(s) of those works. I also give permission for the digital version of my thesis to be made available on the web, via the University's digital research repository, the Library Search and also through web search engines, unless permission has been granted by the University to restrict access for a period of time.

Signed: \_\_\_\_\_, \_\_\_\_\_ On: \_\_05\_\_ / \_\_11\_\_ / \_\_2019\_\_

## Abstract

Soot particles generated during combustion processes enhance heat transfer by thermal radiation. These particles are harmful to human health; therefore, control of soot emissions from combustion systems and mitigation of their negative effects is highly desirable. Soot particle formation is a complex process involving many processes. These are nucleation, surface growth, coagulation, aggregation, and finally oxidation. These processes are not completely understood. The aim of this research was to apply optical diagnostics as a tool to better understand the inception phase and surface growth of soot particles in low pressure premixed laminar flames. The work described in this thesis is based on quasi-one-dimensional, premixed C<sub>2</sub>H<sub>4</sub>-air (plus other additives) laminar flames, stabilised on a McKenna burner.

Three different flame settings were used to study the dependence of soot particle formation on pressure variation in the range of 48–27 kPa. Two flames were at stoichiometric ratios, at  $\Phi$  of 2.1 and 2.3. The third flame, at  $\Phi$  of 2.1 and pressure of 40 kPa, was chosen to evaluate the effect of gas additives on the soot formation process. Three gas additives to ethylene base flame (C<sub>2</sub>H<sub>4</sub>-air) were used. These gas additives are argon (Ar), nitrogen (N<sub>2</sub>) and carbon dioxide (CO<sub>2</sub>).

Laser-induced incandescence (LII) was used to carefully measure the spatial profile of the soot volume fraction ( $f_v$ ). Spatially resolved emission spectroscopy was then utilised to measure two key radicals (CH\* and C<sub>2</sub>\*) and to verify the location of the flame front ( $y^{ff}$ ) and soot particle temperature ( $T_s$ ). Probe thermocouple was employed to measure gas temperature ( $T_g$ ), while Laser Induced Fluorescence (LIF) was used to record the Polycyclic Aromatic Hydrocarbons (PAHs) with 2 – 3 rings (2-3R), 3 – 4 rings (3-4 R) and >5 rings (>5 R).

The gas velocity ( $v$ ) was modelling by using the Ansys-Fluent software package. The time ( $t$ ), at each axial location was calculated in a stepwise fashion, based on the modelled velocity profile. This helps to compute the soot surface growth rate and the phenomenological removing rates of PAH (2-3R) and PAH (3-4R).

From  $\Phi$  of 2.1 and 2.3 flames at different pressure settings, it was found that the thickness zone for CH\*, used as an indicator of the flame front, was larger than for C<sub>2</sub>\*. Furthermore, it was observed that the distance between the maximum recorded intensity of CH\* and C<sub>2</sub>\* decreased linearly with increasing pressure - with a slope of  $25 \times 10^{-9} \pm 0.062 \times 10^{-9}$  (mPa<sup>-1</sup>) and  $28 \times 10^{-9} \pm 0.048 \times 10^{-9}$  (mPa<sup>-1</sup>) for  $\Phi$  of 2.1 and 2.3, respectively. It was found that the lowest value of

$f_v$  was 0.0003 ppm, observed at a spatial location of 6 mm away from the burner surface. It was also observed that  $f_v$  scales with pressure following a simple power function of the form  $f_v = kPr^n$ , where  $k$  is a scaling factor and  $n$  was measured at a value of  $2.15 \pm 0.7$  and  $1.5 \pm 0.4$  for  $\Phi = 2.1$  and  $\Phi = 2.3$ , respectively.

The analysis of soot particle surface growth pointed to a soot growth rate constant,  $k_{SG}$ , of  $20 \text{ s}^{-1}$  for  $\Phi$  of 2.1, whereas at  $\Phi$  2.3 the values of  $k_{SG}$  was found to be  $32 \text{ s}^{-1}$ ,  $25.13 \text{ s}^{-1}$  and  $12.11 \text{ s}^{-1}$  for pressures of 27 kPa, 32 kPa and 35 kPa, respectively. This indicates that  $k_{SG}$  has a weak dependence on the pressure and equivalence ratio.

The measured values of  $T_g$  and  $T_s$  aligned well, with less than 70 degrees difference between the two. The values for  $T_g$  that were measured from the first recorded soot particles were  $\sim 1465 \pm 66 \text{ K}$ . This was termed the ‘soot inception temperature’.

The spatially phenomenological removing rate of PAHs with 2 – 3 rings ( $k_{phen}^{2-3R}$ ) and 3 – 4 rings ( $k_{phen}^{3-4R}$ ) were measured as  $24.61 \text{ s}^{-1}$  and  $21.64 \text{ s}^{-1}$ , respectively, at  $\Phi$  of 2.1 and pressure of 40 kPa. At a pressure of 27 kPa, the spatially phenomenological removing rate constants were measured as  $15.29 \text{ s}^{-1}$  and  $18.26 \text{ s}^{-1}$  for PAHs with 2 – 3 rings and 3 – 4 rings, respectively. This indicates that at a pressure of 40 kPa, ( $k_{phen}^{2-3R}$ ) is faster than ( $k_{phen}^{3-4R}$ ) by a factor of 1.14, whereas at a pressure of 27 kPa, ( $k_{phen}^{2-3R}$ ) is faster than ( $k_{phen}^{3-4R}$ ) by a factor of 1.19. At  $\Phi = 2.3$  and pressures of 40 kPa, ( $k_{phen}^{2-3R}$ ) and ( $k_{phen}^{3-4R}$ ) were found to be  $23.33 \text{ s}^{-1}$  and  $16.9 \text{ s}^{-1}$ , respectively. This indicates that ( $k_{phen}^{2-3R}$ ) is faster than ( $k_{phen}^{3-4R}$ ) by a factor of 1.13 under these flame conditions.

At  $\Phi$  of 2.1 and pressure of 40 kPa and with respect to  $\text{C}_2\text{H}_4$ -air, it was found that  $f_v$  decreased after addition of  $\text{N}_2$ ,  $\text{CO}_2$  and Ar. Ar was found to be the most effective additive for reducing  $f_v$ , and increasing the soot surface growth rate constant. The soot surface growth rate constant ( $k_{SG}$ ) was calculated to be  $8.3 \text{ s}^{-1}$ ,  $15.35 \text{ s}^{-1}$ ,  $35.65 \text{ s}^{-1}$  and  $60.35 \text{ s}^{-1}$  for  $\text{C}_2\text{H}_4$ -air,  $\text{C}_2\text{H}_4$ -air: $\text{N}_2$ ,  $\text{C}_2\text{H}_4$ -air: $\text{CO}_2$  and  $\text{C}_2\text{H}_4$ -air:Ar, respectively. However, it was found that  $f_v$  was reduced significantly in the presence of additives.

The values of ( $k_{phen}^{2-3R}$ ) were measured as  $14.1 \text{ s}^{-1}$ ,  $20.58 \text{ s}^{-1}$ ,  $7.8 \text{ s}^{-1}$  and  $11.2 \text{ s}^{-1}$  for  $\text{C}_2\text{H}_4$ -air,  $\text{C}_2\text{H}_4$ -air: $\text{N}_2$ ,  $\text{C}_2\text{H}_4$ -air: $\text{CO}_2$  and  $\text{C}_2\text{H}_4$ -air:Ar, respectively; whereas the values of ( $k_{phen}^{3-4R}$ ) were measured as  $10.3 \text{ s}^{-1}$ ,  $14.53 \text{ s}^{-1}$ ,  $4.7 \text{ s}^{-1}$  and  $3.9 \text{ s}^{-1}$  for  $\text{C}_2\text{H}_4$ -air,  $\text{C}_2\text{H}_4$ -air: $\text{N}_2$ ,  $\text{C}_2\text{H}_4$ -air: $\text{CO}_2$  and  $\text{C}_2\text{H}_4$ -air:Ar, respectively.

It was also observed that in these flames, the initial detection of the soot particles took place at a temperature of 1458.52 K, 1414.51 K, 1406.21 K, and 1377.16 K for C<sub>2</sub>H<sub>4</sub>-air, C<sub>2</sub>H<sub>4</sub>-air:N<sub>2</sub>, C<sub>2</sub>H<sub>4</sub>-air:CO<sub>2</sub> and C<sub>2</sub>H<sub>4</sub>-air:Ar, respectively.

## **Acknowledgements**

Firstly, I would like to express my sincerest gratitude to my advisor Prof. Zeyad Alwahabi for the continuous support of my Ph.D study and related research, along with his patience, motivation, and immense knowledge. His guidance helped me in all the time of research and writing of this thesis. I could not have imagined having a better advisor and mentor for my Ph.D study.

Special thanks should be given to Dr. Zhiwei Sun, for his professional guidance and valuable support and recommendations on this project.

I wish to thank various people for their contribution to this project Mr Jeffrey Hiorns and Mr Jason Peak, form the mechanical workshop at the School of Chemical Engineering, for building and testing the vacuum-chamber-system used in this study. Also, I would like to thank Ms Lydia Zhang for building the thermocouple. I also would like to thank the laser lab members, Kim Kueh, Adel Iqbal, Abdul Wakil, Wanxia Zhao and Matt Wall for their help and support throughout my project.

I must express my very profound gratitude to my partner Aymen Alqurain and to my lovely kids Ahmed, Bayan, Fatimah and Ayah for providing me with unfailing support and continuous encouragement throughout my years of study and through the process of researching and writing this thesis. This accomplishment would not have been possible without them.

Finally, I wish to thank my parents for their support and encouragement throughout my study.

# Table of Contents

<b>Declaration of Originality</b> .....	<b>I</b>
<b>Abstract</b> .....	<b>II</b>
<b>Acknowledgements</b> .....	<b>V</b>
<b>Table of Contents</b> .....	<b>VI</b>
<b>List of Figures</b> .....	<b>VIII</b>
<b>List of Tables</b> .....	<b>XIII</b>
<b>Nomenclature</b> .....	<b>XV</b>
Abbreviations .....	XV
Symbol.....	XV
Chemical Symbols.....	XVI
Units .....	XVI
<b>Chapter 1: Introduction</b> .....	<b>1</b>
<b>Chapter 2: Background</b> .....	<b>4</b>
2.1 Combustion.....	4
2.2 Combustion formed Particles .....	5
2.3 Mechanism of Soot Formation .....	6
2.4 Experimental Methods.....	10
2.4.1 Non-intrusive techniques .....	10
2.5 Literature Review .....	21
2.5.1 Soot formation under low-pressure conditions .....	21
2.5.2 Effect of pressure on soot formation.....	22
2.5.3 Soot surface growth .....	25
2.5.4 Effect of gas additives on soot formation .....	26
2.6 Motivation for the Study .....	30
<b>Chapter 3: Experimental</b> .....	<b>32</b>
3.1 Equipment Used Throughout the Experiments .....	32
3.1.1 Burner and gas handling .....	33
3.1.2 Vacuum chamber .....	36
3.1.3 Radiation source .....	40
3.1.4 Detection .....	41
3.2 Methodology.....	41
3.2.1 Laser-induced incandescence .....	41
3.2.2 Spatially resolved emission spectroscopy setup .....	47
3.2.3 Laser-induced fluorescence of PAHs .....	53
3.2.4 Flame temperature .....	54
<b>Chapter 4: Velocity field in a McKenna burner</b> .....	<b>59</b>
4.1 Velocity measurement in a McKenna burner .....	59
4.1.1 Cold flow velocity .....	59
4.1.2 Flame velocity.....	59
4.2 Computational fluid dynamics (CFD) model .....	60
4.2.1 Geometry and boundary conditions .....	60

4.2.2 Computational fluid dynamics (CFD) model .....	61
4.2.3 Cold flow velocity .....	63
4.2.4 Flame Velocity.....	66
<b>Chapter 5: Premixed Ethylene-Air at <math>\Phi</math> 2.1 .....</b>	<b>69</b>
5.1 Results and Discussion .....	69
5.1.1 Low pressure flames photography .....	69
5.1.2 Spatially resolved emission spectra of CH* and C <sub>2</sub> * radicals .....	71
5.1.3 Flame temperature .....	79
5.1.4 Laser-induced incandescence .....	85
5.1.5 Laser-induced fluorescence of PAHs .....	94
5.1.6 Spatial correlation among the measured parameters .....	98
5.2 Summary.....	104
<b>Chapter 6: Premixed Ethylene-Air at <math>\Phi</math> 2.3 .....</b>	<b>106</b>
6.1 Results and Discussion .....	106
6.1.1 Low pressure flames photography .....	106
6.1.2 Spatially resolved emission spectra of CH* and C <sub>2</sub> * radicals .....	108
6.1.3 Flame temperature .....	112
6.1.4 Laser-induced incandescence .....	115
6.1.5 Laser-induced fluorescence of PAHs .....	120
6.1.6 Spatial correlation among the measured parameters .....	123
6.2 Summary.....	128
<b>Chapter 7: Effect of gases additive .....</b>	<b>129</b>
7.1 Results and Discussion .....	130
7.1.1 Flame photographs.....	130
7.1.2 Spatially resolved emission spectra of CH* and C <sub>2</sub> * .....	132
7.1.3 Laser-induced incandescence .....	133
7.1.4 Flame temperature .....	136
7.1.5 Laser-induced fluorescence of PAHs .....	137
7.1.6 Spatial correlation among the measured parameters .....	140
7.2 Summary.....	143
<b>Chapter 8: Conclusion .....</b>	<b>145</b>
<b>References .....</b>	<b>148</b>
<b>Appendix A .....</b>	<b>157</b>
<b>Appendix B .....</b>	<b>160</b>
<b>Appendix C .....</b>	<b>166</b>
<b>Appendix D .....</b>	<b>184</b>
<b>Publications.....</b>	<b>204</b>



## List of Figures

Figure 2.1: Soot formation process in laminar premixed flame.....	9
Figure 2.2: Energy level diagram showing fluorescence emission: (1) excitation, (2) internal relaxation and (3) fluorescent emission, where $h =$ Planck's constant $\nu =$ frequency and $S_x =$ electronic energy level.....	15
Figure 3.1: The construction of the McKenna burner (L. Holthuis, Holthuis & Associates Flat Flame Burners. <a href="http://www.flatflame.com/home.html">http://www.flatflame.com/home.html</a> 2017).....	33
Figure 3.2: Schematic diagram of the mass flow controller for the reactants flowing into the McKenna burner.....	35
Figure 3.3: Schematic diagram of the burner with stabilizer.....	37
Figure 3.4: Schematic diagram of the vacuum chamber.....	38
Figure 3.5: Schematic diagram of the vacuum chamber connected to the burner: A, pressure controller and B, inside the chamber.....	39
Figure 3.6: LII signal sheet.....	42
Figure 3.7: LII experimental setup; HWP, half-wave plate; Pl, polariser; M, mirror; Ir, iris; W, window; Cly, cylindrical lens $f = 750$ mm; B, McKenna burner; SLR, single-lens reflex camera.....	43
Figure 3.8: Typical LII imaging set for different pressure and HAB $\Phi = 2.1$ .....	44
Figure 3.9: Calibration by the laser extinction method; 1, chopper; 2, mirror; 3, lens ( $f = 1000$ mm); 4, photodetector1.....	46
Figure 3.10: Experimental setup, where B is a McKenna burner and L1 and L2 represent lenses ( $f = 300$ mm and $f = 250$ mm, respectively); OF is an optical fibre.....	48
Figure 3.11: A typical spectrum for pressure of 27 kPa at $\Phi = 2.1$ .....	49
Figure 3.12: Flame emission without fibre optics set up.....	50
Figure 3.13: Flame emission image at $\Phi = 2.1$ .....	51
Figure 3.14: Flame emission image at $\Phi = 2.3$ .....	52
Figure 3.15: PAH experimental setup.....	53
Figure 3.16: PAH LIF spectra recorded at pressure of 40 kPa at different HAB at $\Phi = 2.1$ .....	54
Figure 3.17: Cross-section of the type R thermocouple.....	56
Figure 3.18: The thermocouple junction.....	56
Figure 3.19: Typical example of flame emission spectra at HAB of 13 mm and pressure 46 kPa. The fitting curve, red, of the emission spectra, black, are shown. Based	

on the Planck function the soot particle temperature was calculated at $1340 \pm 65$	
K.....	58
Figure 4.1: Computational domain .....	60
Figure 4.2: Cold flow velocity Contour profile at 10 l/min .....	63
Figure 4.3: Cold flow velocity vector profile at 10 l/min .....	64
Figure 4.4: Cold flow velocity Contour profile at 5 l/min .....	64
Figure 4.5: Cold flow velocity vector profile at 5 l/min .....	65
Figure 4.6: Cold flow velocity profile as measured, modelled and scaled at 10 l/min and 5	
l/min .....	66
Figure 4.7: Contour of velocity (top) and vector (bottom) profile at $\Phi$ 2.1 with total flow	
rate 5 l/min at a pressure of 46 kPa .....	67
Figure 4.8: Axial flame velocity profile as modelled and after converted at different	
pressures a; 46 kPa and b: 27kPa at $\Phi$ 2.1 .....	68
Figure 4.9: Normalise axial velocity profile with pressure 48 kPa at $\Phi$ 2.1 and compared to	
the published study [141] .....	68
Figure 5.1: Photographs of flat, rich premixed laminar flames at different pressures with $\Phi$	
=2.1.....	70
Figure 5.2: Flame photographs and spatially resolved emission spectra recorded at $\Phi$ =2.1	
for different pressures; A, 48 kPa; B, 46 kPa; C, 40 kPa; D, 38 kPa; E, 35 kPa; F,	
32 kPa; G, 27 kPa.....	72
Figure 5.3: The intensity of $\text{CH}^*$ at different pressures as a function of the HAB $\Phi$ =2.1 .....	75
Figure 5.4: The intensity of $\text{C}_2^*$ at different pressures as a function of the HAB at $\Phi$ = 2.1.....	76
Figure 5.5: Flame emission at pressure 32 kPa at HAB of 5 and 10 mm, at $\Phi$ = 2.1.....	76
Figure 5.6: (a) HAB of the locations with maximum $\text{CH}^*$ and $\text{C}_2^*$ emission in different	
pressure flames; and (b) the distance between the locations with maximum $\text{CH}^*$	
and $\text{C}_2^*$ emission at $\Phi$ = 2.1.....	78
Figure 5.7: Temperature measured by a thermocouple for flames with different pressures	
and HAB at $\Phi$ = 2.1. ....	81
Figure 5.8: Typical example of flame emission spectra at different HAB and pressure 32	
kPa. The fitting curve, black, of the emission spectra, blue, are shown. Based on	
the Planck function the soot particle temperature .....	82
Figure 5.9: Soot particle temperature at different HABs and pressures at $\Phi$ = 2.1. ....	83
Figure 5.10: Temperature of first soot inception, as measured by the thermocouple, at $\Phi$ =	
2.1, the data at 100 kPa [147].....	84

Figure 5.11: Laser induces Incandescence intensity as a function of incident laser fluence at HAB 16 mm under different pressures at $\Phi = 2.1$ .	86
Figure 5.12: LII imaging set for different pressures and HAB at $\Phi = 2.1$ .	87
Figure 5.13: Soot volume fraction and LII signal along HAB with different pressures at $\Phi = 2.1$ .	87
Figure 5.14: LII (circles) and an exponential fit curve (dashed line).	89
Figure 5.15: (a) LII (circles) measured at HAB = 7 mm in different flames and an exponential fit curve (dashed line) with a factor of $n$ ; (b) The exponential factors fitted at different HAB at $\Phi = 2.1$ .	90
Figure 5.16: Summary of previous studies' pressure exponent $n$ values in soot.	91
Figure 5.17: Derivative function $dfv/dt$ as a function of soot volume fraction and linear fit (dashed line) at $\Phi = 2.1$ .	94
Figure 5.18: PAH LIF spectra for different pressure a; 40 kPa and b; 27 kPa at different HAB	95
Figure 5.19: Three kinds of PAH LIF at different pressures; (a) 40 kPa and (b) 27 kPa.	96
Figure 5.20: Different types of PAH LIF as a function of reaction time at different pressures; (a) 40 kPa and (b) 27 kPa, exponential fit curve (dashed line)	98
Figure 5.21: Superimposition of the measured profiles for $f\nu$ , normalise $CH^*$ and $C_2^*$ emissions, $T_s$ and $T_g$ onto flame photographs.	101
Figure 5.22: Superimposition of measured profiles for $f\nu$ , PAH LIF, normalise of $CH^*$ and $C_2^*$ emissions, $T_s$ and $T_g$ onto the flame photographs at different pressure; (a) 40 kPa and (b) 27 kPa.	103
Figure 6.1: Photographs of flat rich premixed laminar flames at different pressures, at $\Phi = 2.3$ .	107
Figure 6.2: Flame photographs and spatially resolved emissions spectra recorded at $\Phi = 2.3$ for different pressures.	108
Figure 6.3: The intensity of $CH^*$ at different pressures as a function of the HAB at $\Phi=2.3$ .	110
Figure 6.4: The intensity of $C_2^*$ at different pressures as a function of the HAB at $\Phi = 2.3$ .	111
Figure 6.5: The distance between the locations with maximum $CH^*$ and $C_2^*$ emissions.	112
Figure 6.6: Temperature profiles measured by a thermocouple for flames with different pressures and HAB.	113
Figure 6.7: Typical example of flame emission spectra at different HAB and pressure 32 kPa. The fitting curve, black, of the emission spectra, blue, are shown. Based on the Planck function the soot particle temperature.	114

Figure 6.8: Soot particles temperature at different HAB for seven pressures as indicated. ....	115
Figure 6.9: LII imaging set for different pressure and HAB $\Phi = 2.3$ . .....	116
Figure 6.10: Axial profiles of soot volume fractions in the flames investigated under different pressures at $\Phi = 2.3$ . .....	117
Figure 6.11: (a) LII (circles) and an exponential fit curve (dashed line), (b) The exponential factors $n$ fitted at different HAB at $\Phi = 2.3$ . .....	118
Figure 6.12: Derivative function $df_v/dt$ as a function of soot volume fraction at $\Phi = 2.3$ . .....	119
Figure 6.13: Summary of previous studies' soot growth rate constant $k_{SG}$ ' .....	120
Figure 6.14: PAH LIF spectra for different pressure a; 40 kPa and b; 27 kPa at different HAB at $\Phi = 2.3$ . .....	121
Figure 6.15: PAH LIF as a function of HAB at different pressures; a, 40 kPa and b, 27 kPa... ..	122
Figure 6.16: PAH LIF as a function of reaction time at a pressure of 40 kPa. ....	123
Figure 6. 17: Superimposition of the measured profiles for flame and soot temperatures, normalise of $CH^*$ and $C_2^*$ emissions and soot volume fractions onto flame photographs. ....	125
Figure 6.18: Superimposition of the measured profiles for flame and soot temperatures, normalise of $CH^*$ and $C_2^*$ emissions, soot volume fractions and PAH LIF onto flame photographs. ....	127
Figure 7.1: Photographs of $C_2H_4$ -air with different additive of Ar, $CO_2$ and $N_2$ at pressure of 40 kPa .....	131
Figure 7.2: Flame emission for two radicals; a, $CH^*$ and b, $C_2^*$ as a function of HAB with different dilution gases at pressure of 40 kPa. ....	132
Figure 7.3: LII imaging at different gas addition at 40 kPa pressure.....	133
Figure 7.4: Soot volume fraction as a function of HAB with different gas additives at 40 kPa pressure .....	134
Figure 7.5: Derivative function $df_v/dt$ as a function of soot volume fraction, at pressure of 40 kPa; a = the whole flame condition, b = with gas additives.....	136
Figure 7.6: Temperature profile of different diluted flames at 40 kPa pressure .....	137
Figure 7.7: PAH LIF spectra for different flames at 40 kPa pressure a; $C_2H_4$ -air, b; $C_2H_4$ - air: $N_2$ c; $C_2H_4$ -air: $CO_2$ and d; $C_2H_4$ -air:Ar at different HAB .....	138
Figure 7.8: PAH LIF as a function of HAB; a, (2-3R) PAH LIF and b, (3-3R) PAH LIF with different gas additive at 40 kPa pressure .....	139
Figure 7.9: PAH LIF as a function of time and a fit curve (dashed line) with different PAH LIF a; (2-3R) PAH LIF and b; (3-4-R) PAH LIF at 40 kPa pressure.....	140

Figure 7.10: Superimposition of the measured profiles for flame and soot temperature, normalise of CH\* and C<sub>2</sub>\* emissions, soot volume fractions and PAH LIF onto flame photographs at 40 kPa pressure for different gas addition; a, C<sub>2</sub>H<sub>4</sub>-air; b, C<sub>2</sub>H<sub>4</sub>-air:N<sub>2</sub>; c, C<sub>2</sub>H<sub>4</sub>-air:CO<sub>2</sub>; d, C<sub>2</sub>H<sub>4</sub>-air:Ar..... 142

Figure A.1: Calibration sheets for C<sub>2</sub>H<sub>4</sub> mass flow controller..... 158

Figure A.2: Calibration sheets for Air mass flow controller..... 159

## List of Tables

Table 2.1: Thermocouple types.....	20
Table 2. 2: Summary of previous studies (pressure exponent $n$ in soot $\propto P^n$ ).....	23
Table 3.1: Flow composition of premixed $C_2H_4$ –air.....	32
Table 3.2: Camera setup.....	41
Table 3.3: Laser extinction method parameter.....	46
Table 4.1: Cold flow velocity as measured, scaled and modelled at 10 l/min and 5 l/min.....	65
Table 5. 1: Axial temperature after radiation correction at 46 kPa.....	80
Table 5. 2: Reaction time calculation at 46 kPa.....	92
Table 5. 3: The spatially phenomenological removing rate constant of PAHs.....	98
Table 5. 4: Superimposition of the measured profiles.....	103
Table 6. 1: The spatially phenomenological removing rate constant of PAHs.....	123
Table 6. 2: Superimposition of the measured profiles.....	126
Table 7.1: The spatially phenomenological removing rate constant of PAHs at 40 kPa pressure.....	140
Table 7.2: Superimposition of the measured profiles.....	141
Table 8. 1: Summarised of parameter measured.....	147
Table B.1: Temperature after radiation correction for 48 kPa, 46 kPa and 40 kPa at $\Phi$ 2.1.....	161
Table B.2: Temperature after radiation correction for 38 kPa, 35 kPa,32 kPa and 27 kPa at $\Phi$ 2.1.....	162
Table B.3: Temperature after radiation correction for 48 kPa, 46 kPa and 40 kPa at $\Phi$ 2.3.....	163
Table B.4: Temperature after radiation correction for 38 kPa, 35 kPa, 32 kPa and 27 kPa at $\Phi$ 2.3.....	164
Table B.5: Temperature after radiation correction with different gas additive to flame.....	165
Table C. 1: Reaction time calculation at 48 kPa.....	166
Table C. 2: Reaction time calculation at 46 kPa.....	167
Table C. 3: Reaction time calculation at 40 kPa.....	168
Table C. 4: Reaction time calculation at 38 kPa.....	169
Table C. 5: Reaction time calculation at 35 kPa.....	170
Table C. 6: Reaction time calculation at 32 kPa.....	171
Table C. 7: Reaction time calculation at 27 kPa.....	172
Table C. 8: Reaction time calculation at 48 kPa.....	173
Table C. 9: Reaction time calculation at 46 kPa.....	174
Table C. 10: Reaction time calculation at 40 kPa.....	175
Table C. 11: Reaction time calculation at 38 kPa.....	176
Table C. 12: Reaction time calculation at 35 kPa.....	177
Table C. 13: Reaction time calculation at 32 kPa.....	178
Table C. 14: Reaction time calculation at 27 kPa.....	179
Table C. 15: Reaction time calculation from flame $C_2H_4$ -air at pressure 40 kPa.....	180
Table C. 16: Reaction time calculation from flame $C_2H_4$ -air with addition of $N_2$ at pressure 40 kPa....	181
Table C. 17: Reaction time calculation from flame $C_2H_4$ -air with addition of $CO_2$ at pressure 40 kPa..	182

Table C. 18: Reaction time calculation from flame C <sub>2</sub> H <sub>4</sub> -air with addition of Ar at pressure 40 kPa ....	183
Table D. 1: Summarised result from flame at pressure 48 kPa .....	184
Table D. 2: Summarised result from flame at pressure 46 kPa .....	185
Table D. 3: Summarised result from flame at pressure 40 kPa .....	186
Table D. 4: Summarised result from flame at pressure 38 kPa .....	187
Table D. 5: Summarised result from flame at pressure 35 kPa .....	188
Table D. 6: Summarised result from flame at pressure 32 kPa .....	189
Table D. 7: Summarised result from flame at pressure 27 kPa .....	190
Table D. 8: Summarised result from flame at pressure 48 kPa .....	191
Table D. 9: Summarised result from flame at pressure 46 kPa .....	192
Table D. 10: Summarised result from flame at pressure 40 kPa .....	193
Table D. 11: Summarised result from flame at pressure 38 kPa .....	194
Table D. 12: Summarised result from flame at pressure 35 kPa .....	195
Table D. 13: Summarised result from flame at pressure 32 kPa .....	196
Table D. 14: Summarised result from flame at pressure 27 kPa .....	197
Table D. 15: Summarised result from flame C <sub>2</sub> H <sub>4</sub> -air at pressure 40 kPa.....	198
Table D. 16: Summarised result from flame C <sub>2</sub> H <sub>4</sub> -air with addition of N <sub>2</sub> at pressure 40 kPa .....	199
Table D. 17: Summarised result from flame C <sub>2</sub> H <sub>4</sub> -air with addition of CO <sub>2</sub> at pressure 40 kPa .....	200
Table D. 18: Summarised result from flame C <sub>2</sub> H <sub>4</sub> -air with addition of Ar at pressure 40 kPa .....	201
Table D. 19: Soot surface growth rate constant k <sub>SG</sub> .....	202
Table D. 20: The Spatially phenomenological removing rate constant of PAHs.....	203

# Nomenclature

## Abbreviations

HAB	Height Above Burner.
HACA	Hydrogen-Abstraction Carbon-Addition (Mechanism)
ICCD	Intensified Charged Couple Device
IR	Infrared.
LIF	Laser-Induced Fluorescence
LII	Laser-Induced Incandescence
MFC	The mass flow controller
Nd: YAG	Neodymium-doped Yttrium Aluminium Garnet (Laser)

## Symbol

$E(m)$	Refractive Index for Absorption
T	Temperature
t	Time
Y	Wavelength
$h$	Heat transfer coefficient (W/m <sup>2</sup> K)
$k$	Thermal conductivity (W/m K)
$Nu$	Nusselt number
$Pr$	Prandtl number
$Re$	Reynolds number
$k_{SG}$	Soot growth rate constant
$f_v$	Soot Volume Fraction
$T_g$	Gas temperature
$T_s$	Soot temperature
$v$	Gas velocity
$(k_{phen}^{2-3R})$ rings	The spatially phenomenological removing rate constant of PAHs with 2–3 rings
$(k_{phen}^{3-4R})$	The spatially phenomenological removing rate constant of 3–4 rings
$(\frac{df_v}{dt})$	Soot surface growth rate
$(\frac{d(2-3R)PAHs}{dt})$	The spatially phenomenological removing rates of (2-3R) PAH LIF
$(\frac{d(3-4R)PAHs}{dt})$	The spatially phenomenological removing rates of (3-4R) PAH LIF



## Chemical Symbols

CH <sub>4</sub>	Methane
C <sub>2</sub> H <sub>4</sub>	Ethylene
C <sub>2</sub> H <sub>2</sub>	Acetylene
CO <sub>2</sub>	Carbon dioxide
N <sub>2</sub>	Nitrogen
Ar	Argon
Pt	Platinum
Rh	Rhodium
C <sub>2</sub>	Diatomic carbon
CH	Methylidyne
PAHs	Polycyclic aromatic hydrocarbons
(2-3R) PAH LIF	(PAHs) with 2–3 rings
(3-4R) PAH LIF	(PAHs) with 3–4 rings
(>5R) PAH LIF	(PAHs) with 5 rings and more

## Units

°	Degree (Angle)
m	Metre
cm	Centimetre
mm	Millimetre
µm	Micrometre
nm	Nanometre
s	Second
ns	Nanosecond
kPa	Kilopascals
°C	Degrees Celsius
K	Degrees Kelvin
cm <sup>-1</sup>	Wavenumber
V	Volts

J	Joules
mJ	Millijoules

## Chapter 1: Introduction

Combustion is still a very versatile source of energy, although there are strong arguments in favour of shifting to more reliance on renewable energies. The availability of hydrocarbon fuels and the amount of energy produced from combustion fulfil the near-term demand of many industries which cannot be met with renewable energy. Combustion continues as a leading source of energy production and its role is expected to grow. Research in the field of combustion and related technologies has raised concerns toward its impact on human health and the environment. Research has been focused on improving combustion efficiency and reducing polluting emissions; however, combustion still remains a significant contributor to greenhouse gas emissions [1].

Soot, one product of the combustion process, is produced through incomplete combustion of hydrocarbons. The presence of aromatic hydrocarbons, e.g. polycyclic aromatic hydrocarbons (PAH), in combustion fuel is a key component of soot formation. PAH compounds are highly toxic to both humans and the natural environment. The introduction of soot to the body can lead to respiratory diseases. Some agents present in soot are considered genotoxic materials and being in close contact with these agents can result in major dermal complications [2-4]. Despite these hazardous effects, soot is still produced in very large amounts. Some industries use soot as an ingredient in their products; for example, as a reinforcement or filler in the production of tyres and rubber, pigmentation material for plastics, paints and printer ink, and as part of the electrode composition of batteries [5].

Given the known importance of soot formation and the negative effects it has on human life, researchers have long been faced with the significant challenge of determining the inception and growth process of soot. Industry and the scientific community has long been interested in the chemistry of fuel-rich combustion. The incomplete combustion of organic materials, including PAHs, releases contaminants into the atmosphere. Understanding the limitations of the soot formation process is vital if soot and PAH production is to be controlled. This requires an in-depth understanding of the gaseous phase (reaction zone) and the solid phase. However, aspects of the sooting phenomenon remain unclear. It occurs relatively rapidly, which hinders precise observation of the steps involved in fuel pyrolysis, nucleation, growth, coagulation, aggregation and oxidation. Thus, researchers are left with the significant challenge of determining the inception and growth process of soot formation under low pressure [6-16]. Reaction time resolution in low-pressure flames helps to examine the early steps of soot formation. However,

important steps in the formation of large PAHs that lead to the inception of the first soot particles remain unclear despite the huge number of experiments undertaken and modelling applied to date [17-22]. To investigate the relationship between the gaseous and solid phase, a range of optical and physical sampling procedures must be undertaken. Laser-based diagnostics that have been utilised to study soot formation in flames include Laser-Induced Incandescence (LII), Laser-Induced Fluorescence (LIF) and laser scattering. The first aim of the current study was to utilise LII to investigate the soot volume fraction and LIF to investigate PAHs in premixed flames. The second aim was to use optical laser diagnostics to understand the inception phase and surface growth of soot particles in premixed flames. The work described in this thesis is based on a study of low-pressure, quasi-one-dimensional, premixed C<sub>2</sub>H<sub>4</sub>-air (plus other additives) flames, stabilised on a McKenna burner.

This thesis consists of eight chapters including the Introduction; followed by Background; Methodology; Investigation of the dependence of pressure on soot particle formation; and Evaluation of the effect of gas additives on soot formation; and finally, Conclusions and Recommendations.

Chapter 2 discusses the current state of research in soot formation, including relevant techniques. Fundamental concepts and theory are introduced here facilitating further discussion in later chapters. Additionally, the chapter reviews the background literature regarding soot practically in the study of soot under low pressure and the effect of pressure and gas additives on soot formation.

Chapter 3 describes the experimental apparatus used throughout this work and includes the calibration of the system and the low-pressure vacuum system.

Chapter 4 presents the velocity field in a McKenna Burner, describes the velocity CFD simulation models, results generation and integration, and the procedure to validate the model.

Chapters 5 and 6 present the experimental findings confirming the dependence of soot particle formation on pressure in the range 48 – 27 kPa. Two flames at ( $\Phi$ ) of 2.1 and 2.3 were selected. Measurement of the soot volume fraction ( $f_v$ ), the location of the flame front, phenomenological removing rate constant of PAH LIF, and the gas and soot particle temperatures are presented and discussed.

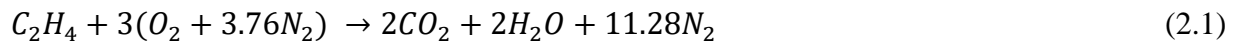
Chapter 7 presents the experimental findings using one flame at  $\Phi$  of 2.1 and pressure of 40 kPa to evaluate the effect of gas additives on the soot formation process. Three gas additives to C<sub>2</sub>H<sub>4</sub>-

air were studied: argon (Ar), nitrogen (N<sub>2</sub>) and carbon dioxide (CO<sub>2</sub>). The soot volume fraction, the location of the flame front, the gas temperature, and the spatially phenomenological removing rate constant of PAH LIF were measured.

## Chapter 2: Background

### 2.1 Combustion

A chemical reaction between a fuel a carbon based solid, liquid or gas and an oxidiser either oxygen or air oxygen is a combustion process and is exothermic. The following chemical formula represents the combustion of ethylene (C<sub>2</sub>H<sub>4</sub>) using Air:



This is an ideal form of combustion because only CO<sub>2</sub> and water are formed; however, there may be other species present. A large number of hidden intermediate species, that were formed eventually, continues to form product and some other species. In the combustion reaction (Equation 2.1), the fuel/oxygen (oxidizer) ratio is chosen to produce only CO<sub>2</sub> and water. If an ideal reaction were possible, it would be complete or stoichiometric with no excess distinct atoms or molecules. Given the circumstance that the reaction in Equation 2.1 is an ideal model, it represents what would happen if there was complete C<sub>2</sub>H<sub>4</sub> combustion in air. There are two commonly used definitions for describing the fuel–oxidiser ratio: the equivalence ratio,  $\Phi$ , and the carbon–oxygen (C – O) ratio. The definition of the former is:

$$\Phi = \frac{m_{fuel}/m_{air}}{(m_{fuel}/m_{air})_{st}} \quad (2.2)$$

Where  $m$  represents the mass and suffix  $st$  stands for stoichiometric condition.

Depending on the mixture, the relative amount of fuel and oxidiser which present in the flames could be either stoichiometric, lean or rich. This is typically defined using the fuel–air equivalence ratio ( $\Phi$ ); the distinction by definition is that a stoichiometric reaction has an equivalence ratio of  $\Phi = 1$ . If  $\Phi < 1$ , the combustion process is considered to be lean or it is rich if  $\Phi > 1$ . Equation 2.2 defines  $\Phi$  as the ratio between the relative mass ( $m$ ) of fuel and air present in the mixture and the relative amount of fuel and air found in a stoichiometric ( $st$ ) mixture.

As mentioned above, combustion is a process in which fuel oxidation occurs rapidly, producing heat and sometimes light. This process occurs in either a complete or an incomplete way, and this is directly related to the amount of oxidiser. The oxidiser is usually oxygen that is available in the area in which the process is occurring. The main objective of combustion is to ensure that the

maximum amount of heat is released from the fuel source. This is achievable by controlling some of the main important process variables throughout the combustion reaction; the temperature at which ignition is occurring, the mixing type of both fuel and oxidiser, and adequate time for the combustion process to take place [23].

Flames are usually observed where combustion reactions occur. Such flames are a result of the exothermic interaction between fuels and oxidants which usually happen in rapid stages to form this thin region; the flame. Flames are typically classified on the basis of the following characteristics: fuel; air mixing type (premixed, non-premixed or partially premixed); stream type (laminar or turbulent); and whether the flame is stable or unstable. It is important to point out that the way in which the reactants were mixed will determine flame type. When the fuel and oxidiser are mixed prior to the reaction taking place, a premixed flame is generated. On other hand, when these two reactants enter the reaction in a discrete way, a non-premixed or diffusion flame is generated. For stream-type classification, a turbulent regime is assigned a large Reynolds number about at least 4000 and is directly related to be steady or unsteady flows [23, 24].

## 2.2 Combustion formed Particles

Soot and nanoparticles are the two types of particles formed in combustion. Nanoparticles, exist in the transition state between gas phase and solid particles, are also known as; condensed phase, nano-organic carbon [21], nascent soot [19] or soot precursor particles [25-27]. Soot particles can be labelled as either young or mature [28], but they are still largely solid. Nanoparticles are usually found as PAH clusters that are compactly or loosely packed oligomers and have aromatic or aliphatic bonds [10]. They are not exclusively defined by size but are nominally less than 10 nm in diameter; generally in the range of 1 – 5 nm [21]. Since they are composed of oxygen-based organic species [29, 30] and have a high hydrogen-to-carbon (H – C) ratio [20, 31], these nanoparticles are more reactive. They retain the chemical reactivity and spectroscopic properties of their constituent gas phase products. However, their surface and transport related characteristics are similar to those of larger particles. On the other hand, soot particles with a diameter of 10 – 100 nm form chain-like structures in which primary particles can easily be distinguished from aggregates [21, 32]. The primary particles are covalently bonded to form aggregates with fractal dimension typically in the range of 1.7 to 1.9. Soot primary particles have a more graphite like structure, exhibiting low H – C [20]. Soot behaves like a black-body in terms of its absorption and emission spectra and does not display fluorescence or other molecular characteristics [20]. In

fact, the presence of soot can often be observed by eye as the yellow part of the flame in fuel-rich conditions caused by near black-body incandescence of hot solid particles.

In theory, there are two key progress pathways: particle inception and initial growth [21]. The first pathway is chemically driven, where polymerisation reactions cause the formation of particles. PAHs are joined by C – C  $\sigma$  bonds and aliphatic compounds, such that the constituent PAHs that make up these oligomers are distinguishable within branching chains [22]. In the presence of higher temperatures and oxygen, this pathway is more active. The growth mechanism is facilitated by a large number of radicals and the addition of aromatic radicals to other aromatics [21]. The second pathway relies more on Van der Waals attractive forces among peri-condensed PAHs and the ensuing physical interactions [33] that begin to stack in graphite-like structures, which is also known as dimerisation. The Van der Waals forces also encourage the further coagulation of these nanostructures into the first primary soot particles. This pathway is preferred in lower temperature pyrolytic and fuel-rich flame regions where radical concentrations are limited. The relative contribution of these two pathways to the inception of soot appears to be strongly dependent on the combustion conditions [34, 35]. Through dehydrogenation and oxidation reactions, the carbonisation of the soot particles is further increased.

In summary, the mechanism of soot formation can be presented as a two-stage mechanism. At the first stage, precursors entering the transition phase (the phase between gas and solid, as described previously) will react to form building blocks which then leads to formation of the initial soot particles. The next step occurs after leaving the transition phase, as the initial soot particles increase in size through nucleation, surface growth, particle coagulation, aggregation and, finally, oxidation [36]. The process of soot formation during combustion remains uncertain as a result of the highly complex nature of hydrocarbon flames [19, 37]. It is believed that the chemical reactions involved in the soot formation process are the same in both premixed and non-premixed flames, as the chemical characteristics of newly formed soot from both flame conditions are the same. The difference between these two flame conditions is considered to be at the precursor's reaction level. As the soot precursor is expected to be produced through oxidation in a premixed setting, it is produced as result of pyrolysis in non-premixed flames [19].

### **2.3 Mechanism of Soot Formation**

Soot formation is a complex process (Figure 2.1) that can be broken down into four different main processes. The first is nucleation, which is known to be a non-equilibrium process and the initial



process of soot inception. Surface growth is the second process that succeeds nucleation in which the soot particle will start to increase in size. Then, coagulation process occurs, in which spherical soot particles collide and produce a larger particle. Next is aggregation process, where large particles get together to form bigger cluster formation, which then follow by the final process; oxidation. These four processes of the reaction occur on a timescale of milliseconds and yield millions of carbon atoms [19]. Many issues remain unidentified or unclear throughout the whole combustion reactions, such as; heat transfer process and fluid flow, which further leaves the researchers perplexed [38].

The discussion now focusses more on nucleation processes, highlighting the main studies that have been done and their findings. Many proposals have been advanced to explain the origin of soot, including ionic species such as polyenes ( $C_{2n}H_2$ ), free radicals and PAHs [39]. Among these, PAHs have received the most attention, as they provide the clearest information about the inception of soot [19]. According to hypotheses relating to PAHs in the soot process, they will grow until the formation of the first solid soot particles, in a process known as inception. The next step involves granular aggregates of mature soot particles, which are the result of a series of processes that may include agglomeration and coagulation. The initial step involves the chemical decomposition of fuel. If the temperatures are well below adiabatic flame temperature, this step will limit the rate at which soot forms [40]. With regard to high temperatures, the diversity of pyrolysis products determines the rate at which soot is formed. There are two ways in which pyrolysis of an aliphatic fuel can occur: through H-atom abstraction or fission. High temperatures support fission reactions and high radical concentrations support H-atom abstraction. Decomposition of large hydrocarbons through fission is the easiest as they have weaker bonds [41]. Since different fuels burn in different ways, they produce different pyrolysis products. Thus, the choice of fuel should be considered in determining the rate and amount of soot formation [42].

The formation of the single aromatic ring molecule, benzene ( $C_6H_6$ ), is the most important in soot formation because this step is considered a rate-limiting process.  $C_6H_6$  can be formed via many possible chemical avenues, including acetylene ( $C_2H_2$ ) addition to n- $C_4H_3$  and n- $C_4H_5$  as the most important parts. When  $C_2H_2$  is added to n- $C_4H_3$ , it typically produces phenyl (n- $C_6H_5$ ) instead of  $C_6H_6$ . Both reactions, therefore, occur as a result of the presence of too much  $C_2H_2$  in a flame [5].

In summary, there are many ways in which the basic ring structure can be achieved. It is clear that the kind of precursors produced by a particular fuel structure has an important effect on the final soot produced. Growth of small PAHs occurs through the combination of many sub-mechanisms.

One is the recursive mechanism, which is based on the activation of radical sites by hydrogen. Abstraction and saturation of the resulting hydrogen abstraction–acetylene addition (HACA) is widely accepted by the research community in charge of combustion [19]. Pioneers of the HACA concept based their reasoning on the argument that the process is not reversible even though the recursive steps can be reversible and it proceeds in favour of high PAHs because each descendent PAH is thermodynamically more stable than its predecessor. Further, PAH isomerisation is believed to contribute to some extent to the growth [19].

The transition from the gaseous phase to the solid phase remains the least understood part of the soot formation process. Once in the solid phase, PAH species with a size ranging from 3,000 to 10, 000 atomic mass units accumulate to form the initial soot particle by a process known as soot inception [23]. After inception, the newly formed soot particles collide with each other to form larger particles as a result of Brownian motion. After inception, the newly formed particles display a spherical shape, whereas larger soot particles at later stage display a fractal shape. The explanation was that newly formed soot particles are governed by coalescent collision, while larger particles agglomerate into fractal aggregates.

The transformation process from a newly formed small particle into large fractal aggregate remains unclearly defined. Two factors were proposed as heavily influencing this transformation: the surface growth rate and the size of the colliding particles [43]. After inception, surface growth plays a dominant role in forming a spherical shape. However, at a later stage, larger particles become less affected by surface growth, and formation of a spherical shape is less common. An explanation for this is that surface growth declines with larger soot particles as result of the reduction in hydrogen atoms and active sites on the soot particle surface [44, 45]. Thus, fractal aggregates are common in larger soot particles with a fractal dimension range between 1.7 and 1.9.

Oxidation is an important part of the whole process. It is important to recall that the surface growth process is competing with oxidation. This assumption is based on the surface reaction process, which is more well-known as a coagulation process. However, small particles cannot undergo surface reaction processes, so they collide with each other, forming a fragile soot cluster. Being in contact with oxygen, these particles tend to experience a mass loss and reduction in their size, causing them to be less active in the surface growth process [39].

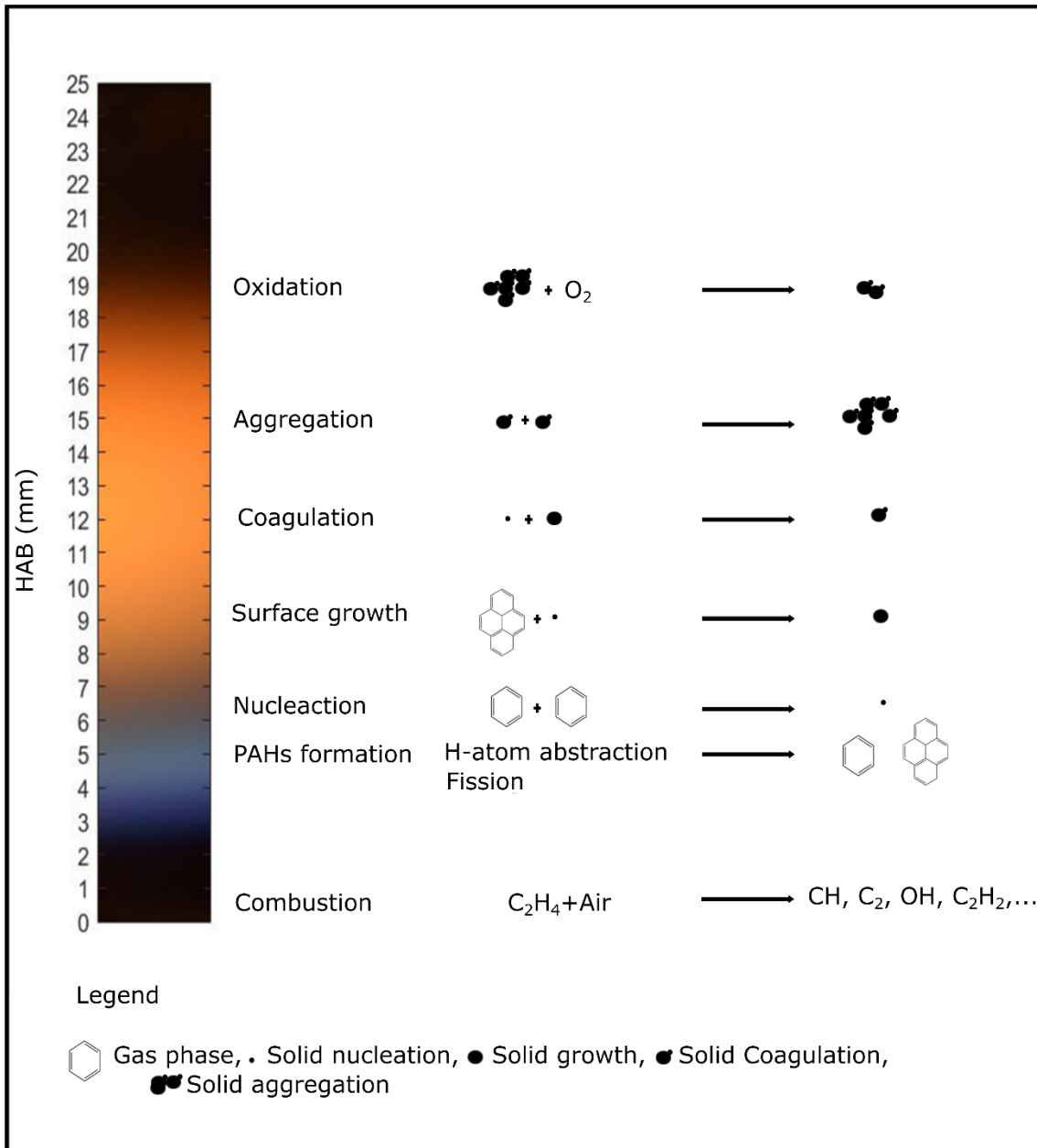


**Figure 2.1:** Soot formation process in laminar premixed flame.

## 2.4 Experimental Methods

Most research in this field has focused on the structural composition of soot particles and the underlying processes of their formation to gain a deeper understanding of their characteristics. An appropriate combination of this knowledge and the measurements applied in soot diagnostic procedures will be important for optimising combustion devices to minimise their levels of soot emission. The multiple techniques that have been applied in studying soot may be classified into two broad categories: non-intrusive and intrusive techniques [46]. Intrusive techniques are used to determine the kinetics of particle formation and concentration, while non-intrusive techniques provide better information about the structure and morphology of the examined particles. To examine the combustion and formation of soot particles, intrusive and non-intrusive techniques are required. Soot particles and their early precursors present in different sizes and possess different properties. Throughout combustion, soot particles display different physical and chemical characteristics compared either to their early precursors or to their mature soot particles. Therefore, different detection techniques are required to detect different particles.

One of the most suitable techniques for measuring soot particles under low pressure is LII. Desgroux et al. [10, 15] suggested that optical techniques are the most suitable for the study of soot under low pressure in combustion processes because of their ability to provide higher spatial and temporal resolution. Other methods, for example, the use of a scanning mobility particle sizer or electrical low-pressure impactor, could also be applied in the process of studying soot volume fraction at low pressure.

This study focused on the non-intrusive technique. Laser diagnostic techniques are widely used and may expand further in the future because of their capability for remote, non-intrusive, in situ and spatially and temporally precise measurement of important chemical parameters. Meanwhile, they provide a clear understanding of combustion phenomena that support sufficient and clean energy conversion [47].

### 2.4.1 Non-intrusive techniques

#### 2.4.1.1 Laser-induced incandescence

Laser-induced incandescence (LII) is one of the techniques used for soot diagnostic purposes. In the past two decades, LII has proved to be one of the most effective diagnostic instruments for resolving a wider range of soot volume fractions, in applications such as turbulent and laminar

flames, characterisation of engine exhaust gases and a wider array of in cylinder combustions. LII method is not a new method; it has gone through many adaptations to result in the approach currently followed. The first use of the LII technique was published in 1974 [48], when Weeks and Duley proposed the use of pulsed laser as a heating agent for aerosol particles for particle size estimation purposes. Eckbreth then discussed the process of interference of signals by Raman scattering [49]. This was followed in 1984 by a detailed study of the process of LII by Melton who used this method to estimate the volume fraction of soot and its particle sizes by employing equations of energy and mass balance and by noticing the related varying physical procedures [50]. All contemporary theoretical models are derived from Melton's work, providing important improvements to the original model.

The principle of LII is that after heating soot particles to 4000 K, they are sublimed using a nanosecond laser pulsed at high power; cooling processes are then initiated until thermal equilibrium in the combustion environment is reached. LII phenomena are described by the mass–energy balance between the diameter heated by an intense laser pulse and the signal from a spherical soot particle of mass  $m$  and its surroundings at temperature  $T_g$ . The energy balance of LII can be described by the following expression:

$$\dot{Q}_{int} = \dot{Q}_{abs} - \dot{Q}_{cond} - \dot{Q}_{rad} - \dot{Q}_{sub} \quad (2.3)$$

where  $\dot{Q}$  is the energy rate for each of the included mechanisms and the quasi-blackbody radiative emission ( $\dot{Q}_{rad}$ ) is the signal that is collected in LII measurements. This signal ( $M(\lambda)$ ) is temperature and wavelength dependent as dictated by Planck's law adapted for Equation 2.4, where  $h$  is the Planck constant;  $\lambda$  is the emission wavelength;  $\varepsilon_\lambda$  is the emissivity;  $c$  is the speed of light;  $k$  is the Stefan Boltzmann constant; and  $T$  is the temperature of the particle:

$$M(\lambda) = \varepsilon_\lambda \frac{2\pi^2 D^2 hc^2}{\lambda^5 e^{\frac{hc}{\lambda kt}} - 1} \quad (2.4)$$

The deviation of emissions from a perfect blackbody for particle dimensions is within the Rayleigh approximation ( $dp \ll \lambda$ ) emissivity ( $\varepsilon_\lambda(\lambda, m)$ ). If both temperature and wavelength influenced at least two distinct wavelengths or bands that are used for measurements, then only the LII temperature can be determined. Temperature changes rapidly in these measurements. Therefore, this is true only for temporarily resolved signals. Conduction is far more efficient at cooling soot than radiation, which can be denoted as, conductive cooling ( $\dot{Q}_{cond}$ ).

LII signal decays exponentially, predominantly because of  $\dot{Q}_{cond}$  at pressures equal to or greater than atmospheric pressure. This is true when laser fluences are too low to induce any significant sublimation mass loss.  $\dot{Q}_{cond}$ , described by Equation 2.5, is a function of the temperature difference of the particle from the surrounding bath gas;  $\alpha_t$  is the thermal accommodation coefficient;  $R$  is the universal gas constant;  $W_a$  is the molecular weight of air;  $T_0$  is the bath temperature;  $C_p$  is the heat capacity of air at constant pressure and  $p_0$  is the bath pressure:

$$\dot{Q}_{cond} = \frac{-\pi d_p^2 \alpha_t p_0}{RT_0} \sqrt{\frac{RT_0}{2\pi W_a} \left(C_p - \frac{R}{2}\right)(T - T_0)} \quad (2.5)$$

When particle mass and size were not taken to be constant, the complexity of these equations increases. Particle sublimation ( $\dot{Q}_{sub}$ ) began to influence the LII signal once laser fluences exceed around  $0.3 \text{ J cm}^{-2}$  for a 1064 nm laser pulses. Beyond these fluences, particle temperatures rise above 4000 K, which is the expected sublimation temperature of soot. Vaporised carbon clusters are in the form of radiated heat and mass. These clusters include  $C_2$  and  $C_3$  and are known to have excited emission bands in the visible spectrum. An initial decrease in signal is approximately contained within the laser pulse duration as expected because sublimation processes will drop significantly as the particle temperature falls below the sublimation temperature. After the laser pulse, the enduring signal remains dominated by conductive cooling. Choosing the correct laser fluence is a trade-off of signal magnitude versus its effect on particle size and morphology and the resultant signal interpretation.

LII detection and measurement spatially and temporally measures the soot volume fraction and primary soot particle size. This why the technique was chosen for this study. The basic laser used was an Nd:YAG with a wavelength of 1064 nm, which was preferred because it assists in avoiding obstructions between laser induced and molecular species, as confirmed by [51] and because of the availability, price and high production power of this wavelength.

It was considered important to examine soot formation in low-pressure flames. The level of soot volume fraction in these flames is very sensitive to the equivalence ratio,  $\Phi$ , and the pressure,  $p$  [15], which permits observation and management of the transformation from a non-sooting situation to a sooting one. The technique of LII was considered a suitable choice in low-pressure flames because of its brilliant sensitivity and spatial resolution. Further, low pressure was specified in experiments using the LII technique, as this permits further understanding of the four stages of soot formation and in clearer way than does high pressure.

The previous description of the LII measurement technique shows how imaging is used to determine soot volume fraction. A time-integrated LII signal was obtained using an intensified charge-coupled device (ICCD) camera. The soot volume fraction  $f_v$  is mathematically defined as:

$$f_v = NV_p = N \frac{\pi d_p^3}{6} \quad (2.6)$$

where  $N$  is the particle's number density,  $V_p$  is the volume of the particle and  $d_p$  is its diameter assuming the soot particle has a spherical shape. Thus, in many studies, a proportional relationship between LII signal ( $I^{LII}$ ) and soot volume fraction is obtained and represented as:

$$I^{LII} \propto f_v \quad (2.7)$$

This expression is frequently used in both laboratory and applied environments. This relationship only holds true if the laser fluence is high enough [52]; that is, above the point of particle sublimation. An extensive theoretical investigation of the dependence of soot volume fraction on the signal was presented by Bladh et al [52]. For this information to be quantitative there must be calibration that is generally via laser extinction measurements.

To study the soot volume fraction via LII measurement, the following processes were undertaken:

1. A laser emitted a light pulse which was partly absorbed by the soot particles to be investigated. The pulse encountered different kinds of optical elements before it arrived at the specified destination, the soot particle.
2. Upon absorbing the laser light, the soot particle temperature increased. The magnitude of this increase relied on the local fluence ( $\text{J cm}^{-2}$  per pulse) of the laser pulse which influenced the particles, and the physical characteristics of the soot and the surrounding gas. The soot particles radiated to the increasing temperature. This radiation increase was called the LII signal.
3. Depending on the physical procedure, the soot particles cooled after being heated. The cooling rate also depended on multiple factors in the surroundings such as pressure, temperature and the characteristics of the soot particles. The particles' thermal radiation decreased because the temperature itself decreased.
4. The detection of the thermal radiation increase of the particles heated by the laser was achieved using an ICCD camera or a photomultiplier. If determination of the time decay was completed, then information about the particle size (soot diameter) could be found.

### 2.4.1.2 Laser-induced fluorescence

Laser induced fluorescence (LIF) can interfere with laser light scattering causing major problem for the laser diagnostic techniques. Fluorescence is not easily avoidable because it occurs over a large wavelength extent of the Stoke side of the laser source. However, most of constituents common to air fed ( $N_2$ ,  $O_2$ ,  $H_2O$  and  $CO$  and hydrocarbon) display transition in the 200 – 250 nm region. This discrete transition can be avoided by proper laser selection and tuning because these compounds don't exhibit strong electronic absorptions unless under vacuum ultraviolet condition below 200 nm. Thus, most of these compounds pose no serious fluorescence interference threat in laser diagnostic techniques.

Species of interest ( $O_2$ ,  $H_2O$ ,  $CO$  and hydrocarbons) exhibit electronic resonance which is distinguishable from others. With appropriate laser wavelength selection and tuning, interference from these compounds can be avoided. Hydrocarbons fragments and the soot particles they form possess broad absorption and emission spectra throughout the violet and ultraviolet spectral region. Interference from hydrocarbons fluorescence is a serious interference because of their abundance. Fluorescence from polycyclic aromatic hydrocarbons (PAH) is a known strategy to detect hydrocarbons in various gaseous and spray flames throughout the visible and ultraviolet regions.

LIF was considered by [49, 53] as one of the most useful imaging techniques to be applied to combustion diagnostics. LIF has merit because of its ability to identify smaller molecules [54], especially radical species [55] within the flame. LIF is also used to determine the temperature of a flame [56] without requiring a probe to be inserted [57].

Fluorescence measurements are the optimal method for observing development from smaller molecules into larger PAHs because of their high absorption coefficients and quantum yields. As the size of the aromatic structure increases, the wavelength of the emitted light also increases as a result of the  $\pi - \pi^*$  transitions creating a spectrum. As PAHs increase in size, the energy gaps decrease, causing a redshift to emitted light because of absorption band broadening. Larger PAHs are found higher in the flame and smaller PAHs are found lower in the flame, thus providing a mechanism for discrimination [58].

Following excitation via a laser pulse (see Figure 2.2, step 1) the molecule undergoes internal relaxation because of rotational and vibrational energy transfer. Thus, there is relaxation to a lower energy band, while still within the upper energy electronic level (see Figure 2.2, step 2). After the



emission of fluorescence, however, the molecule loses enough energy to fall back to ground state (see Figure 2.2, step 3). The energy released is less than the energy absorbed; therefore, the wavelength of the emitted light is longer than the wavelength of the excitation. The emission is confined to specific wavelengths because of the quantisation of the energy levels.

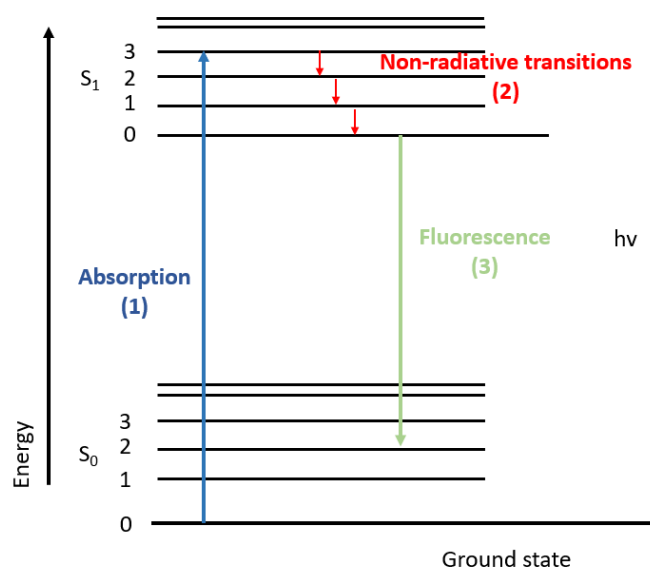


**Figure 2.2:** Energy level diagram showing fluorescence emission: (1) excitation, (2) internal relaxation and (3) fluorescent emission, where  $h$  = Planck's constant  $\nu$  = frequency and  $S_x$  = electronic energy level.

There may be complications when making fluorescent measurements. For example, there may be other contributions to the relaxation of the molecule, including processes such as quenching, and this must be taken into account. This makes LIF more suited to the identification of small radicals such as OH, NO and CH, as they are well known and thus data concerning their spectroscopy, quenching and transfer rates already exist. This is why studying species for which these data are unknown can suffer from many problems [10].

Fluorescence occurs predominantly at wavelengths longer than the excitation wavelength as discussed above. However, there is very little fluorescence because of the anti-Stokes fluorescence that occurs at high temperatures when some of the heat or thermal energy is converted into light. The excitation wavelength should be strategically chosen to excite particular target PAHs [59]. Measurements designed to simultaneously observe PAHs, OH and other small molecules while exciting with short wavelengths in the ultraviolet (UV) range are also possible [60]. As highlighted by Desgroux in the 2013 review paper, the PAH concentration is not proportional to the LIF signal [10]. The structure of PAHs and the measurement environment affect the

fluorescence level because of the effects of collisional quenching [60]. One of the main limitations of LIF measurement is that it cannot quantify individual species because it reflects the sum of contributions of a number of different PAH molecules. It is known that PAHs are sensitive to the excitation wavelength used. Although not species selective, it is accepted that shorter wavelengths excite smaller PAHs than longer wavelengths.

PAHs fluoresce mainly in the UV–visible spectrum (250–450 nm) as discussed previously [61, 62]. Longer fluorescence wavelengths are emitted from larger PAH species with more rings. The number of rings (aromatic island size) increases with the fluorescence emission spectrum [63, 64]. However, fluorescence spectra with peak wavelengths above 450 nm are difficult to attribute to PAHs larger than coronene, because their relative concentration in flames is quite low compared with that of smaller PAH species [65]. A redshifted spectrum can indicate structure evolution towards a more stacked arrangement. In summary, an increase in fluorescent lifetime and a redshift are indicative of nanostructure growth favouring physical dimerisation, while bluer spectra and shorter/constant lifetimes indicate growth through chemical polymerisation. In controlled environments and conditional on a sufficiently low optical density to avoid reabsorption effects, molecular species concentration is proportional to fluorescence intensity [66]. The same is true for fluorescent nanostructures within non-sooting premixed flames [67]. In premixed flames, particle evolution is curtailed as coagulation is limited in low concentrations and the flame front downstream has a relatively constant temperature.

#### 2.4.1.3 Chemiluminescence

Reactions at excited states cause the generation of chemical species and spontaneous intra-flame emissions, also known as chemiluminescence. Oscillations of heat emanating from combustion systems is one process fostered as a result. Chemiluminescence investigation can provide information that is fundamental to combustion processes such as local heat release and equivalence ratios.

Spectroscopy uses emission and absorption spectra to differentiate each molecule. Transitions can take place between the lowest (E1) and the highest (E2) energy levels and vice versa. As emission and absorption cause electromagnetic radiation, spectrally resolved radiation must be measured by a suitable device to obtain the spectrum. The frequency of the emitted radiation is calculated using the following equation:

$$v = \frac{\Delta E}{h} (H_z) \tag{2.8}$$

Where  $\nu$  is the frequency of the emitted radiation,  $\Delta E$  is the energy difference between two energy states and  $h$  is Planck's constant.

Post-excitation, the molecules fall back to a lower, stable energy state. The emission of radiation, and in turn the chemiluminescent intensity, varies according to the gas fuel, the flame temperature and the number and density of excited molecules—thus on the equivalence ratio. Molecules investigated in the current study were the carbogen (CH) and the diatomic carbon (C<sub>2</sub>). Radiation is emitted mainly because of the electronic transition of molecules; therefore, all measurements were taken from the UV–visible region.

Flame structure in a hydrocarbon flame is important for combustion-related research ranging from essential reaction kinetics to industry system optimisation. Flame-emission spectroscopy is a simple method to apply in combustion diagnostics and its use in flame diagnostics has increased recently because of its ability to provide a clear understanding of flame process. It is an important technique for investigating flame characteristics in the combustion location and at the flame front; the thickness of the layer of CH\* and C<sub>2</sub>\*; and soot temperature during the combustion process. Soot temperature is a very useful property in the understanding of the soot formation process as the actual mechanism that results in soot formation is quite intricate, involving many complex chemical and physical processes [19, 21]. The spatially resolved emission spectroscopy (SRES) technique is based on the process of electronically exciting the radicals produced from a flame's chemical reactions measured at well-defined different locations. Theoretically, the major excited radical radiations come from OH\*, CH\* and C<sub>2</sub>\*. The primary emission of CH\* bands is at 430 nm, and for C<sub>2</sub>\* bands, 436–560 nm (the so-called Swan bands). Gaydon provided a useful description of flame reactions in premixed flames [68]. In addition, recent experimental and theoretical studies have employed spectrometry of CH\* and C<sub>2</sub>\* to characterise flames by investigating the relationships between luminescence intensity and various process factors, for instance, equivalence ratio fuel type and flame structure [69-72]. Comparing CH\* emissions from various flames leads to the conclusion that CH\* is not directly formed by a breakdown of C<sub>2</sub>H<sub>2</sub> but by a side reaction. In the reaction zone, it can be observed that CH\* usually occurs at higher levels than C<sub>2</sub>\* [68]. However, there is ongoing debate about the formation of an excited CH\* and C<sub>2</sub>\* flame.

Chemiluminating species are considered important intermediates that characterise the reaction zone because of their presence in the flame front as potential markers for heat release; and in the reaction zone in combustion systems. However, the CH\* radical is commonly used as a flame marker because it is relatively short lived, is present over a narrow zone in flame [73, 74] and is

of eminent interest because of its involvement in prompt NO formation. Moreover, the CH excited radical plays a crucial role in the formation of other radicals which influences the outcome of experiments in different ways [75]. C<sub>2</sub> radicals are also useful in the development of CH\* radicals and the C<sub>2</sub>\* radical is a possible intermediate in the polymerisation dehydrogenation of hydrocarbon fuel. However, unsaturated C<sub>2</sub>\* hydrocarbon radicals are key precursors in the formation of aromatic and polyaromatic molecules in both combustion processes and planetary atmospheric environments.

#### 2.4.1.3.1 Carbon–hydrogen chemiluminescence

The  $A^2\Delta \rightarrow X^2\Pi$  (at ~431 nm) and  $B^2\Sigma^- \rightarrow X^2\Pi$  (at ~390 nm) transitions, in which the 431 nm band is usually dominant, cause the primary CH\* emission in the UV–visible region [68, 76]. CH\* chemiluminescence mechanism has some requirements:

1. State formation reactions and rates of excitation
2. Collisional quenching and radiative relaxation rates that remove the excited state.

Quenching data and radiative rates are available for CH\* by major species of hydrocarbon combustion [77]. However, for OH\*, the accuracy of information may be variable. There have been attempts to explore CH\* formation reactions and their rate parameters. Of the various proposed sources, research has focussed on the following:



Gaydon [76], who suggested reaction Equation 2.9, was challenged by Grebe and Homann [78]. After experimentation, Brenig backed an earlier proposal that the reaction of ground state ethynyl radicals (C<sub>2</sub>H) with O atoms forms CH\* [79]. A recent shock tube study with methane (CH<sub>4</sub>)–hydrogen mixtures has supported that Equation 2.9 and 2.10 are the dominant CH\* formation pathways. This is true for conditions ranging from 1200–2300 K and 0.6–2.2 atm [80]. However, because of inadequate information on C<sub>2</sub> kinetics, there are many uncertainties in the rate parameters. Equation 2.9 may also be important in high-order hydrocarbon (liquid) fuel systems where C<sub>2</sub> is more abundant. Devriendt et al. [81] determined that the majority of CH\* is produced

by Equation 2.10 in a temperature-dependent fashion using a pulsed-laser equation photolysis study at low pressure. In addition, it was found that excess O<sub>2</sub> or its addition in the reaction actually decreased the CH\* yield in pulsed-laser photolysis [81] and shock tube studies [80] eliminating the O<sub>2</sub> step (Equation 2.11) in the analysis. However, Renlund et al. [82] indicated that C<sub>2</sub>H should be with O<sub>2</sub> and not atomic oxygen (Equation 2.10). In a recent photolysis study at low pressure of C<sub>2</sub>H<sub>2</sub> [83], the temperature dependence of Equation 2.11 was evaluated. The study determined that there would be a significant contribution of Equation 2.11 to CH\* chemiluminescence in hot flames and under lean fuel conditions. Absolute excited state concentrations of CH\* were measured in low-pressure CH<sub>4</sub>-air premixed flames, and rate parameters for Equation 2.10 and 2.11 were determined [84] and recently re-analysed [85]. The Equation 2.10 rate constant showed temperature independence, while Equation 2.11 showed weak temperature dependence.

#### 2.4.1.3.2 C<sub>2</sub>\* chemiluminescence

Under fuel-rich conditions  $\Phi \geq 1.0$ , C<sub>2</sub>\* chemiluminescence occurs in the blue-green spectrum between 436 and 564 nm from the C<sub>2</sub> D<sup>3</sup>Σ<sup>-</sup> → A<sup>3</sup>Π transition, or Swan bands. Therefore, it is useful to highlight areas susceptible to soot formation. The reaction CH<sub>2</sub> + C = C<sub>2</sub>\* + H<sub>2</sub> to form C<sub>2</sub>\* was suggested by Gaydon [68]. Savadatti and Broida [86] subsequently put forward the reaction C<sub>3</sub> + O = C<sub>2</sub>\* + CO. Smith and team observed various premixed hydrocarbon flames and the contained C<sub>2</sub>\* formation via LIF imaging measurements [87]. A sub-mechanism for C<sub>2</sub>\* kinetics was developed. They also recommended rate coefficients for the two formation reactions stated in the section above. More recently, Kathrotia et al. [88] studied C<sub>2</sub>\* formation among others in various premixed CH<sub>4</sub>-air flames. Their findings included the reproducibility of their flame experiments considering the aforementioned recommended reactions from [68] and [86]. However, because of the lack of reliable precursor concentrations, their results suffer from simulation uncertainties.

#### 2.4.1.4 Thermocouples

There are many different types of thermocouple with regard to the set of material combinations that can be made from metals used in the thermo-elements that form the thermocouple (the positive and negative thermo-elements). These types have different measurable temperature ranges, which is clearly associated to voltage drop and other material characteristic factors that are directly related to metal properties. Various thermocouple types and temperature ranges are

listed in Table 2.1 [89]. Thermocouples are typically selected because of their low cost, high temperature limits, wide temperature ranges and durable nature.

Table 2.1: Thermocouple types.

Number	Thermocouple type	Materials making up the thermocouple	Temperature range (°C)
1	S	Pt-10% Rh v. Pt	-50 to 1480
2	R	Pt-13% Rh v. Pt	-50 to 1480
3	B	Pt-30% Rh v. Pt-6%	0 to 1700
4	E	Ni-10% Cr v. constantan	-270 to 870
5	J	Fe v. constantan	-210 to 760
6	K	Ni-10% Cr v. Ni-5% (Al,Si)	-270 to 1260
7	N	Ni-14% Cr-1.5% Si v. Ni-4.5% Si-0.10 Mg	-270 to 392
8	T	Cu v. constantan	-270 to 370

A thermocouple is made of two metals for which the voltage differences under a thermal gradient are dissimilar. A measurement of this varying potential difference is correlated with temperature. This makes thermocouples useful for combustion measurements at high temperatures. Platinum–rhodium alloys are often used in the manufacture of thermocouples. The temperature of the flow is then determined as a result of an energy balance problem, as seen in Equation 2.12. The thermocouple bead is heated up to gas temperature by convective heat transfer. However, the thermocouple does not reach that temperature simply because of conduction through the wires and radiation loss from the bead. Assuming that the probe volume does not have strong temperature gradients, exposure of the wire to a combustion environment can minimise conduction losses [90]. Additional uncertainty is added because of enhanced surface reactions via the bead’s catalytic effects. With respect to that coatings can mitigate the artificial increase of local temperature that is measured by the probe [91]:

$$Q_{conduction} + Q_{convection} + Q_{radiation} + Q_{catalytic} = 0 \quad (2.12)$$

Particle deposition on the thermocouple bead because of sooting flames further complicates measurements and energy balance equations. The roughness diameter and emissivity of the bead change as a direct consequence of this. Using the diameter and temperature time history, emissivity values of the particles inside the flame can be extracted according to thermocouple particle densitometry (TPD) [92, 93]. These measurements further contrast the spectroscopic properties of early flame particles with soot.

Thermal inertia does not always allow thermocouples to track fluctuations in gas temperature accurately, for instance in turbulent flames. Therefore, only time-averaged measurements can be made with a thermocouple.

## 2.5 Literature Review

### 2.5.1 Soot formation under low-pressure conditions

Several recent studies investigating soot formation under low-pressure conditions have been carried out on premixed and non-premixed flames to improve understanding of the process of soot formation. These studies chose low-pressure flames, due to having the advantage that the reaction time resolution in flames at this pressure help in examining the early steps in soot formation. Mouton et al [8] specifically studied the formation of soot particles in low-pressure CH<sub>4</sub> flames using LII. They kept the pressure constant (26.6 kPa) and changed the equivalence ratio ( $\phi = 1.95, 2.05, 2.15$  and  $2.32$ ) to record the evolution of LII signal with laser fluence (fluence curve), time (temporal decay) and emission wavelength at different height above burner (HAB). They specifically took advantage of the low-pressure conditions to probe with good spatial resolution in the soot inception zone of the flames. They concluded that the different behaviours of fluence curves were related to the probed region of the flame and  $\phi$ . At high levels of  $\phi$ , the process of surface growth was accompanied by an increase in the LII decay times. At lower  $\phi$ , the decay times became shorter until they reached a constant value along the flame at  $\phi = 1.95$ . These behaviours are appropriate for the detection of the smallest incandescent particles in flames as such particles have very weak surface growth [8]. Desgroux et al [15] demonstrated that the LII time decays are almost constant within the first millimetres, whereas an increase in the decay was correlated with the growth of the primary soot particle. They also found that the soot volume fraction still increases after a given HAB and becomes stable in burnt gases. The reaction time resolution is a property in low-pressure flames that helps in examining the early steps of soot formation. At the beginning of the soot formation process, the variation in the LII signal with laser energy before the LII ‘plateau’ zone will be weaker than at any other time. This means that in the first few millimetres, the time decay of LII will be constant as the primary soot particle begins growing then the LII time decay begins increasing [15]. The same result was reported by Bladh et al. in their experiments: the first used CH<sub>4</sub>/oxygen/N<sub>2</sub> flames ( $1.95 < \phi < 2.32$ ) at 26.7 kPa; the second used atmospheric C<sub>2</sub>H<sub>4</sub>-air flames ( $1.77 < \phi < 2.00$ ). Both experiments produced the same results: at elevated HAB and elevated  $\phi$  the mature soot fluence curve changes, but the change in nascent soot linear behaviour found at low HAB and low  $\phi$  is considered to reflect LII decay time

and particle size decrease [14]. Bockhorn also measured the distribution of particle size in sooting flat hydrocarbon oxygen flames for several fuels at low pressure, noting that the soot particle aerosols had size distributions in light scattering and extinction measurements that could be approximated by log normal distributions. This result agreed well with results in other studies mentioned above [94]. Another study by Wersborg et al. used the attenuation of a laser beam to determine the soot concentration at various positions for premixed C<sub>2</sub>H<sub>2</sub>–oxygen flat flame at a pressure of 20 mm Hg. They then compared the resulting concentration with that of measured previously under the same flame conditions using molecular beam sampling and electron microscopy of beam deposits; the concentrations observed were larger in the regions of particle nucleation and rapid surface growth, but in good agreement farther downstream in the region of predominant particle coagulation [95].

### 2.5.2 Effect of pressure on soot formation

The main effect of pressure is taken as the increase in soot formation with a proportionality degree of  $P^n$ , where  $1 < n < 3$ . This is expressed by the power law:

$$f_v = kP^n \quad (2.13)$$

This directly implies that with a lower value of  $n$ , soot formation is reduced or hindered whereas an increase in the value of  $n$  increases soot formation considerably rises. Soot formation under low-pressure conditions is minimal as it tends to be inhibited. In contrast, an increase in pressure corresponds to an increase in soot production as expressed by the relationship.



Table 2. 2: Summary of previous studies (pressure exponent  $n$  in soot  $\propto P^n$ ).

Pressure (bar)	Pressure Low/high	HAB (mm)	Fuel	Burner	Type	Diagnostic method	Pressure exponent $n$ in soot $\propto P^n$	Ref
1–3	High		n-Heptane	High-pressure vessel and laminar burner (HPVB)	Laminar diffusion flames	LII	$P^{1.38 \pm 0.32}$	[96]
4, 8,12 and 16	High		N <sub>2</sub> -diluted C <sub>2</sub> H <sub>4</sub>	Co-flow burner	Co-flow laminar diffusion flames	LOSA and scattering	$P^{1.8}$	[97]
1–7 1–20	high		C <sub>2</sub> H <sub>4</sub> diluted with N <sub>2</sub>	Circular co-flow laminar diffusion type burner	Co-flow laminar diffusion flames	Abel-type inversion algorithm	$P^{2.8}$	[18]
1– 3	High		n-Heptane	HPVB	Laminar diffusion	LII calibrated by means of the LOSA technique	$P^{3.4 \pm 0.3}$	[98]
0.20–0.28	Low	30	CH <sub>4</sub> -oxygen Co-flow N <sub>2</sub>	McKenna burner	Laminar premixed	LII calibration performed by cavity ring-down spectroscopy	$P^{11}$	[15]
5–40	High		CH <sub>4</sub>			Spectral soot emission (SSE), LOSA and numerical technique	$P^2$	[99]
1.0–2.0 2.0–7.3	High		Propane–air	Annular	Co-flow laminar diffusion	SSE and LOSA	$P^{3.4}$ $P^{1.4}$	[100]
5–20 20–40	High		CH <sub>4</sub> –air	Annular	Laminar non-premixed	SSE and LOSA	$P^2$ $P^{1.2}$	[101]
1–16 1–25	High		CH <sub>4</sub> C <sub>2</sub> H <sub>4</sub>	annular	Axisymmetric diffusion	LOSA and LII	$P^{1.2}$ $P^{1.7}$	[102]
5–20 20–40	High		CH <sub>4</sub> –air		Laminar co-flow diffusion	LOSA	$P^1$ $P^{0.1}$	[103]
1–4	High	20	C <sub>2</sub> H <sub>4</sub>	annular	Diffusion	Two-colour method and thermocouple	$P^2$	[104]
1–60	High		Propane–oxygen–inert gas		Premixed	In situ laser extinction		[105]

1-70	High	30	C <sub>2</sub> H <sub>4</sub> -air	a) Porous plates made from bronze particles; 1 cm thick b) Burners made from aluminium sheets into which channels were engraved. These sheets were pressed together	Premixed	Optical methods and chemical analysis	$\sim P^2$	[106]
1-8	High		C <sub>2</sub> H <sub>4</sub> -air		Diffusion turbulent	Laser light scattering	$P^{1.4}$	[107]
1-5	High	30	C <sub>2</sub> H <sub>4</sub> -air and C <sub>6</sub> H <sub>6</sub> -air flames	The central flat flame burners were surrounded by a flat shielding burner	Premixed		$P^2$	[108]
1-5	High		C <sub>2</sub> H <sub>4</sub> -air	Water-jacketed tubular burner	Premixed	Laser light absorption and scattering	$P^{1.5-2.0}$	[109]
1-25	High	20 30 40	C <sub>2</sub> H <sub>4</sub>	Annular	Laminar diffusion	LOSA	$p^{1.7\pm 0.3}$	[110]

The literature in which several parameters are associated from the perspective of previous researchers is summarised in Table 2.2. These were pressure range values, fuel types, burners and types, the diagnostic methods used and the pressure exponential. In one study [97], the line-of-sight attenuation (LOSA) and scattering diagnostic approaches were employed with a co-flow burner, and a pressure exponential of 1.8 was estimated by the authors. The flame type employed in the study was laminar co-flow of diffusion flames for pressure bar ranges of 4, 8, 12 and 16 bar. A 2.8 pressure exponent emerged for a pressure ranges of 1–7 bar and 1–20 bar for dilute C<sub>2</sub>H<sub>4</sub> fuel. Karataş and Gülder [18] employed a circular co-flow burner type using an Abel-type inversion approach with a co-flow diffusion flame type. Another study on C<sub>2</sub>H<sub>4</sub> flame laminar diffusion at pressures ranging between 0 and 10 bar was determined through measurement of temperature and the ‘integrated soot volume’s’ line of sight. The authors reported pressure scaling to be a maximum volume fraction of the integrated soot with a 1.26 exponent for the laminar C<sub>2</sub>H<sub>4</sub> flames between 1 and 4 bar [108]. In another study [104], it was found that above the rim of the burner (~20 mm) there was a square pressure-dependence of the volume fraction on the maximum local soot.

### 2.5.3 Soot surface growth

Soot formation involves various physical and chemical mechanisms and reactions. C<sub>2</sub>H<sub>2</sub> was found to be responsible for particle growth in the gas phase, where most particle reactions occur. Models were developed and experiments were performed to define the rate of particle surface growth. Early models were based on the assumption that particle surface growth rate is dependent on either the surface area of the soot particle or the soot volume fraction. An early expression of this relationship was proposed by Wanger to express the relationship between the rate of particle surface growth and the soot volume fraction, as shown in Equation 2.14. Harries and Weiner developed a model that helped in presenting a formulation to identify the rate of particle surface growth [111]:

$$df_v/dt = k_{SG}(f_v^\infty - f_v) \quad (2.14)$$

where  $f_v^\infty$  represents the final soot volume fraction reached at various reaction times and  $k_{SG}$  is an apparent first-order rate constant [15].

From the previous models and expressions, it is known that the rate of particle surface growth decreases with increase in particle size. Frenklach and Wang investigated this fact and defined a chemical reaction path for the surface reaction [112]. An active site on soot particles was proposed. This parameter helps in identifying the reaction activity on the soot surface that further allows the soot particle to be involved in chemical reactions in the gas phase. Using PAHs helps in defining a surface reaction constant, which then helps in calculating the rate of particle surface growth with the following formulation. Previous models showed that particle surface growth changes with time. The surface reaction activity of bigger (older) particles differs from that of smaller (younger) particles. This introduces the concept of soot particle aging. As a soot particle grows in size (getting older), it tends to lose reactivity and becomes inert in the gas phase reaction. This fact has been established since 1973 [113] and later models supposedly addressed this fact. However, a model built by Colket and Hall ignored this fact in a way that simplified the model, but raised critical questions concerning the process involved [114]. As most of the latest models run with premixed flames, Wersborg studied the carbon-formation process in a premixed oxygen-acetylene flame; his findings confirmed that the increase in soot particles will decrease surface growth, as smaller particles tend to react faster [113]. Harris and Weiner stated that particle surface growth is responsible for the mass of the soot produced in the combustion process. They concluded that the increased rate of mass growth found in richer flames is caused by the increased surface area as a result of particle inception and not a larger amount of growth species [44, 115, 116]. Another model was established by Bockhorn to describe soot formation, identify a different relationship between soot inception, particle surface growth, PAH and oxidation and examining how these might affect soot particle appearance and growth rate.

The effect of low pressure on the soot volume fraction increases with almost the same magnitude as the increase in the peak value of  $df_v/dt$ . This corresponds to a slope change in  $df_v/dt$  as a function of  $f_v$ . This further indicates slowing or completion of the soot inception process [15].

#### **2.5.4 Effect of gas additives on soot formation**

Soot is a type of particulate matter that is produced during combustion. Soot suppression has become a significant area of research as soot pollutes the environment, adversely affects public health and influences the efficiency of the thermal processes involved which ultimately reduces the capacity for energy savings [117]. Much research has been carried out on suppressing soot formation by introducing additives to the diffusion flame, such as N<sub>2</sub>, Ar, He and CO<sub>2</sub>, along with

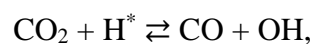
the fuels such as  $C_2H_4$ ,  $C_3H_4$  and  $C_4H_4$ . Such studies have included reactive species ( $CO_2$ ,  $H_2$ ), highly diffusive species ( $He$ ,  $H_2$ ) and non-reactive near equidiffusive species ( $Ar$  and  $N_2$ ). These studies have helped to identify the mechanisms by which additives affect soot inception. In one experiment, measurement of the limiting strain rate for complete suppression of soot, or the soot particle inception limit ( $k_p$ ), was undertaken [118]. Laser excitation measurement of the soot volume fraction was also carried out in counter flow. The sooting limit was observed to decrease with the addition of inert gases because of a decrease in fuel concentration and temperature.  $He$  gas was found to be the most effective. Addition of  $H_2$  increased the flame temperature but significantly decreased  $k_p$ . Selective diffusion was responsible for these observations, and also decreased PAH formation. The addition of  $CO$  was found to decrease  $k_p$  [118]. Studies have revealed that the influence of gaseous fuel additives on soot formation is highly complex even when an additive like the inert gas  $Ar$  is used.

It has been observed that the inclusion of additives in a diffusion flame is capable of influencing soot formation in several ways. Primarily it dilutes the fuel concentration and reduces the flame temperature and residence time. Moreover, chemistry plays a vital role in such combustion processes by influencing the inception, growth and oxidation stages. All these factors have a cumulative effect on soot formation directly through fuel dilution; subsequent modification of the flame temperature and residence time reduces soot formation. Other than that, additives take part in chemical reaction mechanisms. Du et al [118] specifically attempted to identify the chemical role of  $H_2$  and  $CO$  and showed that the role of  $H_2$  is complicated; Additives such as  $Ar$  and  $N_2$  provided an important understanding of the additive effects of fuel dilution and temperature. Highly mobile and diffusive additives such as  $He$  exhibited more effective soot suppression as the fuel concentration was highly reduced in the soot region. Addition of  $CO$  had a weak suppression effect on soot [118]. Haynes et al [119] reported an effect on soot formation in an  $C_2H_4$ -air flat flame as a result of addition of 3%  $N_2$ ,  $H_2O$ ,  $H_2$ ,  $NH_3$ ,  $NO$ ,  $H_2S$ ,  $SO_3$ ,  $SO_2$ ,  $HCl$ ,  $CH_4$ ,  $C_2H_4$  and  $O_2$ . These additives did not influence soot particle coagulation, but soot volume fraction was reduced significantly. Addition of  $SO_3$  showed no such evidence of a pre-soot effect on aliphatic or aromatic flames. The behaviour of  $NH_3$  was not clearly understood but it was believed that one molecule of  $NH_3$  acted via removal of one C atom by rapid formation of inert  $HCN$ . Effects of the addition of  $CH_3NH_3$  were not very fast or significant. The addition of  $CO$  generated a slightly luminous flame. Soot suppression was much stronger with the addition of  $H_2O$  and  $CO_2$ . The influence of added  $H_2$  was complex, but it could change the shape of the flame completely [119]. Tang et al. reported the effect of the addition of  $CO_2$  and suggests that it promoted the flame and

as a result soot yield was reduced. It was also claimed that the addition of CO<sub>2</sub> changed flame temperature and the composition of both the fuel and oxidiser, and thus could reduce soot build up via the combined effects of these factors [120]. Liu Fengshan et al [121] studied the effect of CO<sub>2</sub> addition and tried to establish the chemical mechanism of soot suppression. As per this experiment the chemical reactions:



Were proposed to explain the chemical effects of CO<sub>2</sub> addition that suppress soot formation, and the following equation was assumed to be particularly responsible for soot suppression:



The activity of CO<sub>2</sub> reduced the flame temperature and slowed the soot nucleation process. In this reaction, H<sup>\*</sup> radical was consumed, which then slowed C<sub>6</sub>H<sub>6</sub> ring and PAH formation. Laser-induced microscopy was used to observe the effect of reduction of soot, suppressed growth of soot particle size and number density in a laminar propane diffusion flame diluted with CO<sub>2</sub> [122]. As mentioned earlier PAH contributed to soot build up. It was believed that PAHs in the flame zone collided with one another and became associated by Van der Waals interactions. Thus, they kept increasing in size. An experiment was undertaken using a highly diluted flame sample particle, a scanning mobility particle sizer and a differential mobility analyser. They were considered the soot precursors. The absorbed chemical species were detected by laser desorption and laser ionisation followed by time-of-flight spectroscopy (TOF-MS) [121]. Experiments were undertaken by Du et al [118] to investigate the effect of CO<sub>2</sub> and O<sub>2</sub>. Addition of O<sub>2</sub> was found to reduce soot [16]. Chen Linghong et al [123] investigated the effect of CO<sub>2</sub> addition on soot particle size and its distribution. Additionally, the flame height and absorption function of soot particles was studied. It was observed using LII that CO<sub>2</sub> addition diluted the fuel gas, suppressed the nucleation of soot particles and reduced their growth; to achieve a satisfactory signal the flame position in the experiment must have a high soot volume fraction. It was detected that strong signals were obtained between 18 and 40 mm HAB. The signal measured from the soot particles was averaged over 128 laser shots, and the peak LII signal used for plotting curves were averaged over 50 laser shots [123]. The addition of CO<sub>2</sub> was believed to reduce PAH formation because of the chemical reaction discussed above. Thus, soot generation was suppressed mainly through destruction of its precursors [124].

It was observed that fatty acid methyl ester bio fuels did not produce PAH [117]. An investigation of the effect of CO<sub>2</sub> and H<sub>2</sub>O addition on PAH was undertaken using laminar premixed C<sub>2</sub>H<sub>4</sub>-O<sub>2</sub>-Ar flames while keeping the flame temperature constant. It was observed that less PAH was formed on addition of CO<sub>2</sub> and H<sub>2</sub>O and thus a lower fluorescent signal was obtained [125]. LIF was employed to probe the existence of PAHs in an atmospheric sooting flame; only a fraction of PAHs had the characteristics of a spectral feature and only those with these characteristics can be detected. Usually, large PAHs are unable to generate spectral signals [62]. Various experiments have shown that fuel oxidation and the 1–4-ring aromatic hydrocarbons formed generally contribute to soot formation. It was also believed that the pathway for each such type of PAH formation is extremely important for fuel decomposition. Furthermore, it was known that even a small amount of aromatic hydrocarbon formation could be rate controlling in soot formation steps.

Various models for investigation of PAH formation and specific fuel decomposition have been developed but these phenomena are in need of better explanation. In particular, the accuracy of previous models was affected by the lack of spatially resolved quantitative data concerning concentration profiles of PAHs containing several rings. Another important issue that remained poorly understood was the reformation of some aromatic species in the flame zone, where soot particles were present. El Bakali et al [126] designed a detailed kinetic model for the investigation of aromatic and first PAH formation pathways in sooting CH<sub>4</sub> premixed flames, operating at two equivalence ratios (2.05, 2.32) and various pressures (0.211–0.263 atm). The proposed model was able to predict quite accurately the C<sub>6</sub>H<sub>6</sub> mole fraction in both the reaction and post-flame zone where soot particles were produced. Formation of naphthalene was also modelled and the corresponding pathways were discussed. Pyrene formation was also investigated in previous study, as pyrene plays a vital role in soot particles formation [126]. However, the model they used was not sufficient to explain the pathway of pyrene formation as they lack crucial information about these species throughout the experiment.

Zhang et al [125] investigated the chemical effect of CO<sub>2</sub> and H<sub>2</sub>O addition on formation of PAHs in laminar premixed C<sub>2</sub>H<sub>4</sub>-O<sub>2</sub>-Ar flames using the LIF technique. For this purpose, the equivalence ratio, dilution ratio and maximum flame temperature were kept constant and the blending ratios of CO<sub>2</sub> and H<sub>2</sub>O were varied. The experimental results indicated that the fluorescent signal intensities of different PAHs monotonically decreased with higher blending ratios of both CO<sub>2</sub> and H<sub>2</sub>O. It was also observed that the suppression effect of PAHs was stronger when H<sub>2</sub>O was added, compared with addition of CO<sub>2</sub>. The kinetic analysis was carried out to

clarify the experimental phenomenon using a chemical kinetic model in the Chemkin-Pro software coupled with a PAH formation mechanism proposed by Appel et al [127]. It was observed that CO<sub>2</sub> addition increased the reaction rate for  $\text{CO} + \text{OH} \rightleftharpoons \text{CO}_2 + \text{H}$ , resulting in a decrease in the H<sup>\*</sup> radical concentration and increase in OH<sup>\*</sup> concentration. In contrast, the addition of H<sub>2</sub>O significantly increased the reverse rates for the  $\text{OH} + \text{OH} \rightleftharpoons \text{O} + \text{H}_2\text{O}$  and  $\text{CH}_3 + \text{OH} \rightleftharpoons \text{CH}_2 + \text{H}_2\text{O}$  reactions, promoting the formation of OH radicals. In the following steps, the PAH growth pathway from C<sub>6</sub>H<sub>6</sub> to large PAHs still needed to be completed via a more accurate PAH mechanism, which required more accurate data from LIF technique [125].

## 2.6 Motivation for the Study

Although, several approaches have been used to explain the early process of soot formation, a gap remains in fully determining the steps and precursors involved. In a combustion system, soot formation has been described generally as involving five processes: soot nucleation, surface growth, coagulation, aggregation and oxidation. Although the order of these processes is generally accepted, some questions remain unanswered related to the inception or nucleation process due to the limited knowledge available to fully explain this process, such as experimental information about nascent particles and soot precursor particles.

The transition from gaseous species to nascent solid soot particles is still poorly understood. The production of polycyclic aromatic hydrocarbons (PAHs) is assumed throughout the early steps of combustion as result of fuel pyrolysis [128]. PAHs play a vital role, as they are considered the precursors for soot formation. Knowledge about PAHs formation, growth and transformation to nascent soot particles through the soot nucleation process is essential, but data describing this process are limited in the literature [128-130]. Therefore, the combined measurement of PAHs and temperature associated with nascent soot particles production is very valuable to the soot modelling community.

The utilization of low pressure laminar premixed flames provides advantages to understanding the mechanisms of soot formation because the larger reaction zone offers a bigger window for examining the early soot formation zone. However, the total number of soot particles formed in low pressure laminar premixed flames was assumed to be lower than the total number in flames at atmospheric pressure. Therefore, sensitive techniques are required to facilitate detection of the



early steps of soot formation and measure newly formed precursors and soot particles. LII and LIF possess advantages over other intrusive techniques (e.g., probing) to detect and identify PAH and early formed soot particles as these diagnostic techniques are capable of detecting the particles with a size of 2–3 nm [14].

In this context, this thesis studies the range of applicability of laser diagnostics for the detection of PAHs and measurement of the soot volume fraction in low pressure laminar premixed flames. The aim of this work is to gain information about the combustion process by detecting and characterising soot particles, their PAH precursors and their growth at different flame conditions under a wide pressure range. This will be achieved by connecting different techniques to predict the results. The main benefits of performing such experiments are to:

- Realise the advantages of using optical diagnostics to provide useful data relating to soot formation in flames.
- Better understanding the soot inception zone and growth rate under low-pressure conditions.
- Quantify the dependence of the soot volume fraction on the pressure (P) and illustrate the strong sensitivity of soot formation.
- Establish the temperature of soot inception.
- Identify the soot surface growth rate constant.
- Identify spatially the phenomenological removing rate constant of PAHs.
- Identify the possible link between PAHs consumption and soot particles production.

## Chapter 3: Experimental

### 3.1 Equipment Used Throughout the Experiments

In this research four experiments were conducted using the same set of laboratory equipment for the purposes of studying the soot formation through the burning process. Only the detection technique varied between experiments and was either flame emission spectroscopy, LII or LIF.

The flames used in this research were premixed C<sub>2</sub>H<sub>4</sub> –air (plus other additives) flames stabilised on a McKenna burner. The flames' composition is reported in Table 3.1. This study was concerned with two equivalence ratios  $\Phi = 2.1$  and 2.3 at low pressure of 27–48 kPa, in burns conducted on a McKenna burner with a bronze plug and a steel plate with 60 mm diameter. This criterion was followed to determine the flow rates and the ranges of pressure, which are dependent on achieving excellent stability situations for the flame.

The reason for selecting these flames in which the C<sub>2</sub>H<sub>4</sub> flames considered a typical flame, were often investigated by the soot society and because of the availability of temperature information.

Table 3.1: Flow composition of premixed C<sub>2</sub>H<sub>4</sub> –air.

Flame no	Gas flow parameters						Dilution blending ratio (%)	Total flow rate (l/min)	$\Phi$
	Fuel flow rate C <sub>2</sub> H <sub>4</sub>	Oxidant flow rate air	Dilution CO <sub>2</sub>	Dilution N <sub>2</sub>	Dilution Ar	Co-flow flow rate N <sub>2</sub>			
	(l/min)	(l/min)	(l/min)	(l/min)	(l/min)	(l/min)			
1	0.64	4.35	--	--	--	1.0	--	5	2.1
2	0.69	4.30	--	--	--	1.0	--	5	2.3
3	0.90	6.09	--	--	--	0.5	0	7	2.1
4	0.90	6.09	0.6	--	--	0.5	11	7.6	2.1
5	0.90	6.09	--	0.6	--	0.5	11	7.6	2.1
6	0.90	6.09	--	--	0.6	0.5	11	7.6	2.1

### 3.1.1 Burner and gas handling

#### 3.1.1.1 Mc-Kenna burner

Many types of burners are currently used in chemical laboratories, including Meker, Hencken, and McKenna burners, each with its own specifications.

McKenna burner is used frequently in combustion processes. The main target when using this burner is the production of flat, premixed flames. These premixed flames are used in the study of soot and the way in which it is formed. The assumption is made of uniform characteristics of both concentrations and temperatures, along with a radial direction in relation to the flame's axis. Thus, measurements are usually conducted along the axis of the flame to ensure homogeneous and precise results [131].

A sectional view of the McKenna burner is depicted in Figure 3.1. The premixed flames produced by this type of burner are supported on a sintered matrix fabricated from stainless steel or bronze, with 6 cm diameter tubes to provide fluid cooling. The reactant mixture (fuel and oxidiser) is distributed within this sintered matrix.

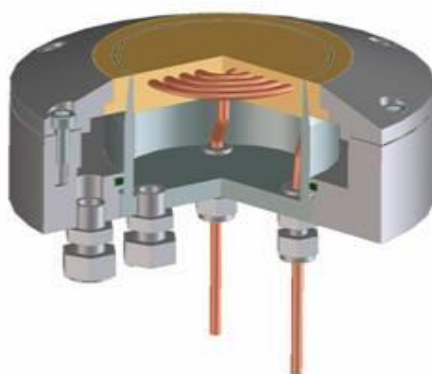


**Figure 3.1:** The construction of the McKenna burner (L. Holthuis, Holthuis & Associates Flat Flame Burners. <http://www.flatflame.com/home.html> 2017).

#### 3.1.1.2 Mass flow controller

C<sub>2</sub>H<sub>4</sub> and air were the reactants in the combustion reaction flowing inside the McKenna burner at certain mass flow rates controlled by the use of valves before the gases enter the burner. Fuel

mixing was achieved by three mass flow controllers (Bronkhorst). This study used a special mass controller with pressure at the input and exit sides at 760 Torr (1 atm) and 200 Torr (~0.26 atm), respectively. The calibration data for the mass flow controller are presented in Appendix A. The flow rates for C<sub>2</sub>H<sub>4</sub> and air were within the ranges of 0–4 l/min and 0–10 l/min, respectively. N<sub>2</sub> co-flow was used to stabilise the flame inside the chamber; the total flow rate of N<sub>2</sub> was 0–1 l/min. The mass flow controller is shown in Figure 3.2.

To study the effect of gas additives on soot formation, a mass flow controller (Bronkhorst) was used for each gas, N<sub>2</sub>, Ar and CO<sub>2</sub>. The calibration data for these three mass flow controllers are provided in Appendix A.

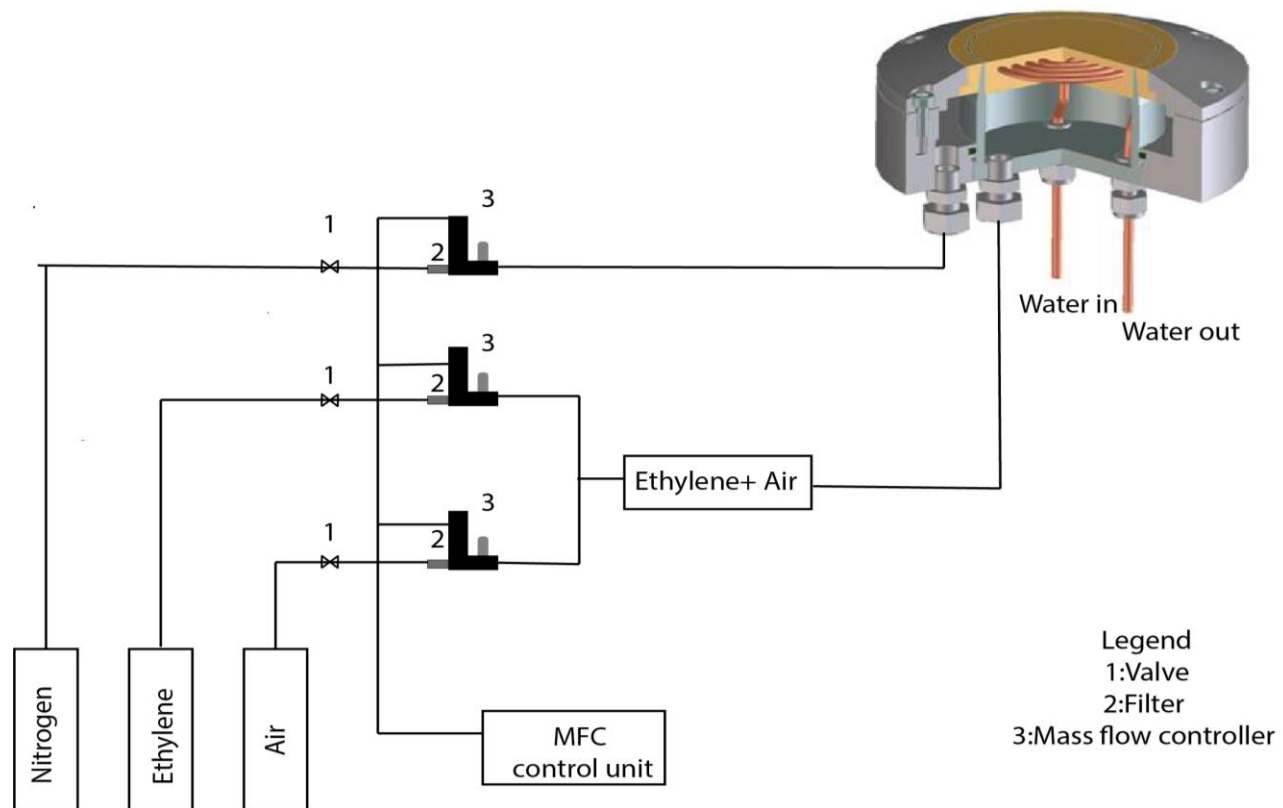


**Figure 3.2:** Schematic diagram of the mass flow controller for the reactants flowing into the McKenna burner.

### 3.1.2 Vacuum chamber

A sealed vacuum chamber was constructed to achieve the particular low-pressure values at which the soot formation process was studied. Pressure is a key player in the rate of soot formation, as described in previous studies [15, 132], thus low-pressure environment was chosen to help extending the flame length, which would help to provide a bigger window for our studied region. The chamber's total capacity was 39 L, and it was made by connecting six plates to form the final shape, as presented in Figure 3.4. The first lower part of the chamber is a cylindrical tube 220 mm high and 700 mm in diameter and containing six pores (holes) to allow delivery of gases and water to the burner. It holds the burner and a steel plate 80 mm in diameter employed at a height of 25 mm above the burner surface to stabilise the flames, as shown in Figure 3.3 Present the schematic diagram of burner with stabilizer attached. However, to achieve measurements at different heights along the flame centreline, the burner was traversed vertically with a spatial resolution of 0.5 mm.

The second (middle) part is next, with a height of 170 mm and a similar diameter to the lower part (700 mm). This section contains four windows, each pair of two opposes the other, with a diameter of 50mm each. Two opposing windows were used as a path for delivering a laser beam, and the other two were used for data collection. This section also contains a pore (hole) to allow insertion of a thermocouple, as shown in Part B of Figure 3.5. The second part is connected to the third part, which is an empty cylindrical tube with a height of 240 mm and a diameter of 420 mm which allows the end products of flame to evaporate out of the chamber.

The fourth and fifth parts provided cooling to the system. Both parts contained two holes (in and out) to allow the drainage of water from the system. Both parts were connected with a cylindrical tube, 340 mm long and 250 mm in diameter, allowing evaporating gases to travel through the parts prior being exposed to water in the fifth part. The sixth part is a condenser used to condense the evaporation into water drops for easy extraction out of the system through the exit hole attached at the end of this part, as presented in the Figure 3.3.

To ensure low pressure environment inside the chamber, a vacuum bump (Edwards, EDM 12) was used and connected to the last part (the condenser) by a 1 m flexible hose. Pressure was measured by using a Baratron (MKS, 122AA-0100AB) and was regulated with a pressure regulator to ensure a steady pressure with accuracy of 0.66 kPa. Both pressure reader and regulator were connected to the system through pressure transducer as shown in Part A of Figure 3.5. Information about the pressure regulating controller is presented in the next sub section.

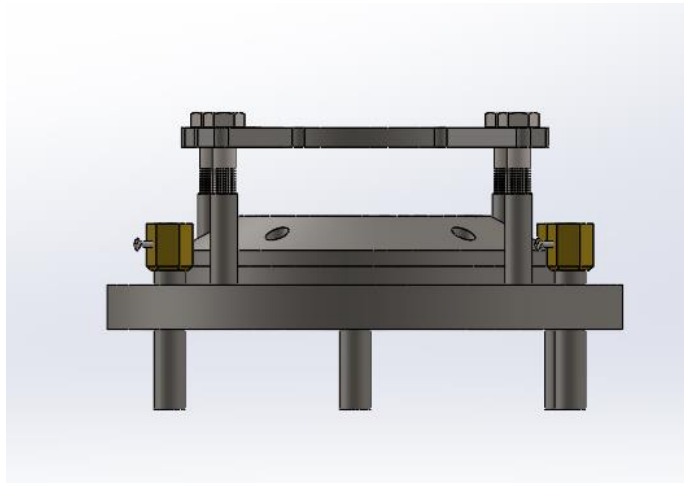


**Figure 3.3:** Schematic diagram of the burner with stabilizer.

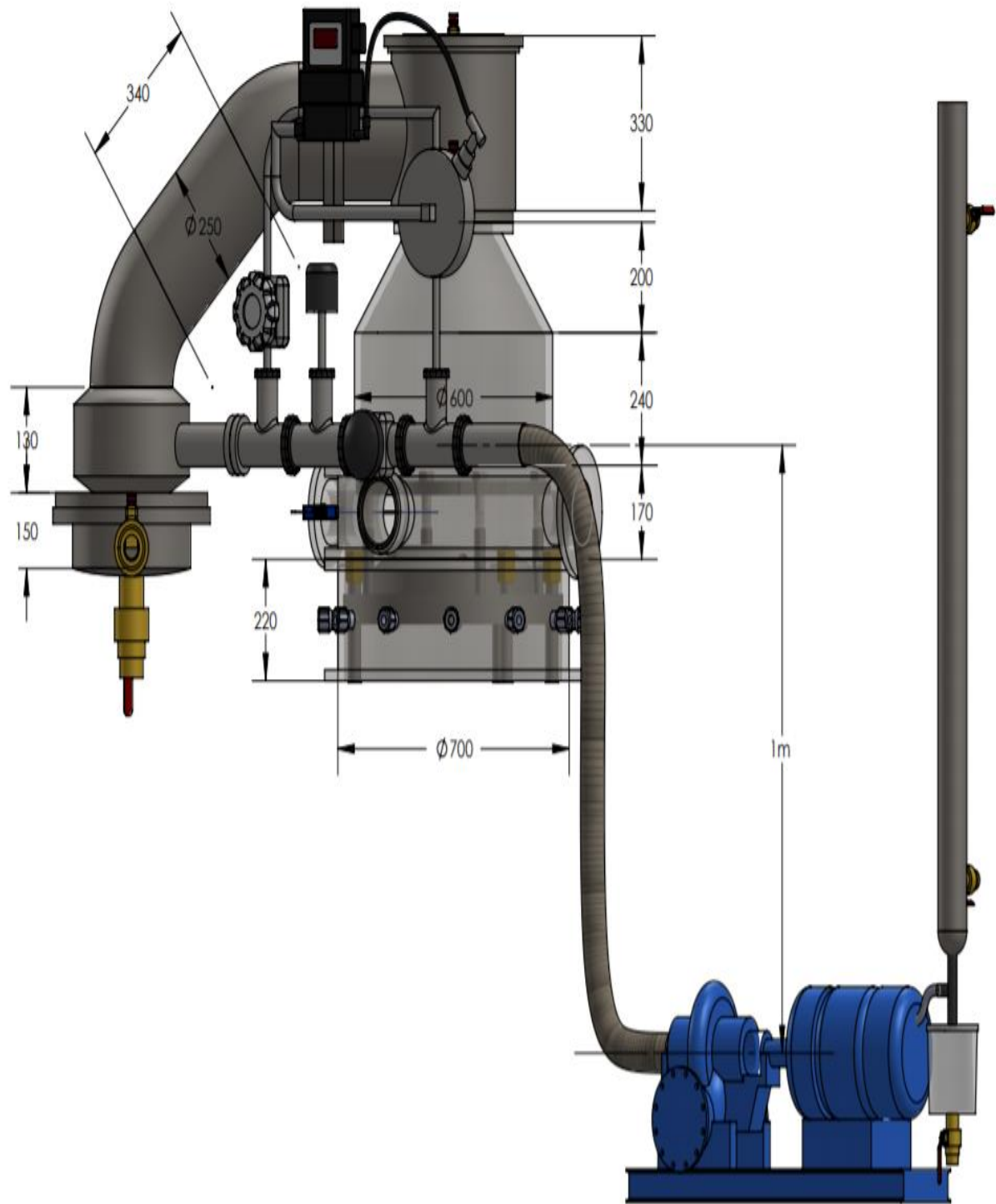


**Figure 3.4:** Schematic diagram of the vacuum chamber



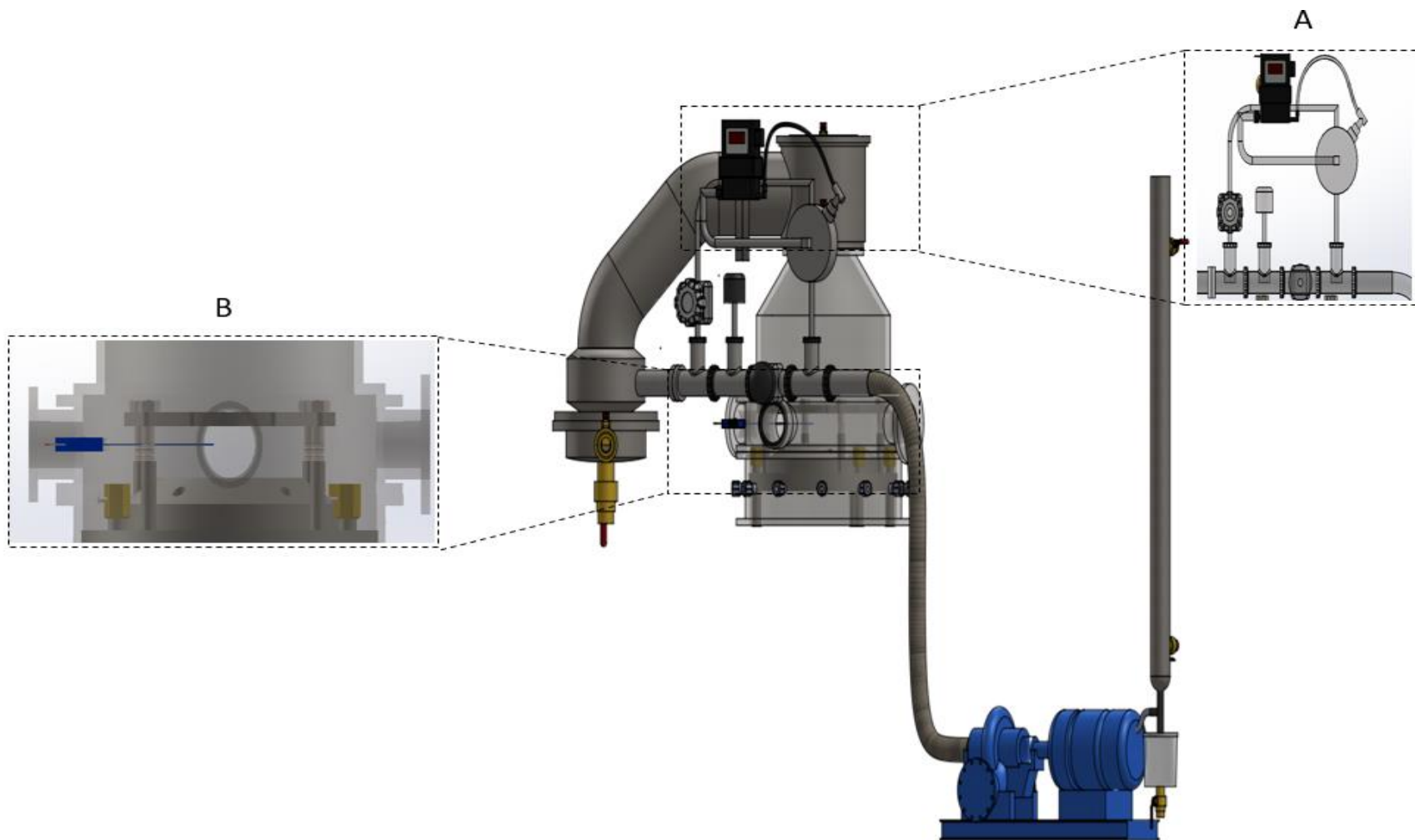


**Figure 3.5:** Schematic diagram of the vacuum chamber connected to the burner: A, pressure controller and B, inside the chamber.

### *3.1.2.1 Pressure controller*

As soot formation is very sensitive to pressure, a pressure controller system, the Equilibar® Precision Back Pressure Regulator, was used to control back pressure down to approximately 0.02 psig / 1.38 millibar (g). The back-pressure regulator was attached to a QPV electronic pressure regulator to control the pressure as it accepts an analogous voltage (0–10 V) to that used by the controlled unit (TENMA Power Supply). The unit-controlled pressure is proportional to the signal received; for example, 0–10 V = 0–760 Torr units, so giving the unit a command of 5 V tells it to go to 380 Torr.

The QPV series electronic pressure regulator has calibration ranges as low as 0–2 in H<sub>2</sub>O (0–500 Pa, 0–5 millibar(g)) with an accuracy of  $\pm 0.25\%$  of full-scale calibration for pressures above 1 psig / 68 millibar(g) and an accuracy of 1% of full scale for pressures of 1 psig / 68 millibar(g) and below.

The QPV1 will go to the desired pressure accurate to within  $\pm 1\%$  of the full-scale calibrated range (for pressures <1 psig / 68 millibar(g)). However, the repeatability spec of  $\pm 0.2\%$  may be more applicable. This means that when given the same command, the unit will always be within a  $\pm 1\%$  range of the chosen pressure but will also be within 0.2% (of full scale) of the same pressure. For example, for a 0–500 Pa calibrated unit the accuracy is as followed: a command of 5 VCD (or 12 mA) tells the unit to go to 250.0 Pa and it could land anywhere between 245 Pa and 255 Pa for an accuracy of  $\pm 5$  Pa. With regards to repeatability, say the unit hits 250.625 Pa it will then always be within  $\pm 0.2\%$  of that number or,  $\pm 1$  Pa, representing a very high degree of repeatability.

### **3.1.3 Radiation source**

A laser is described as light amplification caused by radiation emission. Each light has a certain wavelength measured in nanometres. This research used a Nd:YAG solid-state laser Neodymium in YAG lasers. In this laser, lasing occurs in  $\text{Nd}^{3+}$  trivalent neodymium ions housed in yttrium aluminium garnet ( $\text{Y}_3\text{Al}_5\text{O}_{12}$ ) crystalline. This laser is optically pumped using a flash lamp for high energy or a diode laser for low power applications. This work used a flash lamp as the pumped Nd:YAG lasers that are used to measure the concentration of some light-absorbing substances, typically emitting light with a wavelength of 1064 nm, in the infrared region. However, this work used a fundamental wavelength of 1064 nm to measure the soot volume fraction and a fourth harmonic (266 nm) was used to measure the PAH LIF.

### 3.1.4 Detection

#### 3.1.4.1 Digital camera

A Nikon camera (Model D5500) with a micro lens (TAMRON F004 \_SP90 mm) attached was used to take the flame photographs. The details of the camera setup are provided in Table 3.2.

Table 3.2: Camera setup

F-stop	f/8
Exposure time	¼ sec
ISO speed	ISO-640
Focal length	90 mm
Filch mode	No

#### 3.1.4.2 ICCD camera

The generated LII or PAH LIF signal was measured by use of an ICCD (Andor I star camera) set at an angle of  $\sim 87^\circ$  in relation to the laser beam. At LII, ICCD was then set to operate at gate delay and gate width of 100 ns and 200 ns, respectively. While at PAH LIF the ICCD was set at 30 ns without delay to avoid detecting LII signals. Once the pressure was stable, 200 images were recorded with a short pass filter (900 nm, 50 mm).

#### 3.1.4.3 Spectroscopy

A spectrometer is an instrument used to split light emitted by a source into different components depending on their wavelength. The spectrometer used in this study was an Andor Shamrock 500i, equipped with a second ICCD camera (Andor, iStar). The grating used in the experiments had 150 lines  $\text{mm}^{-1}$ . Spectroscopic measurements were used to recode the chemiluminescence of CH, C<sub>2</sub>, soot luminosity and PAHs.

## 3.2 Methodology

### 3.2.1 Laser-induced incandescence

The optical configuration for the LII measurements is shown in Figure 3.7. A Nd:YAG (Surelite II) laser was used as the heating source, controlled at 1046 nm. The laser radiation was directed towards a half-wave plate and then to a Glen laser polariser, which provided accurate control of the laser pulse energy without adjusting the time between the flash lamp and the Q-switch. A CW

530 nm from diode laser was overlapped with  $\sim 1064$  nm beam to visualise the path of the beam at  $\sim 1064$  nm within the chamber. Moreover, the cylindrical lens used a 750-mm focal length was used without decreasing the vertical spatial resolution through weak signal. As illustrated in Figure 3.6 a horizontally oriented laser sheet of  $\sim 1 \times 5$  mm was formed by focussing the beam in the vertical axis oriented by the cylindrical lens with focal length of  $\sim 750$  mm. Then, the generated LII signal was measured through an ICCD camera, utilising a short pass filter (900 nm, 50 mm), to suppress the 1046 nm radiation to the laser beam. The ICCD was set to operate at gate delay and gate width of 100 ns and 200 ns, respectively. Once the pressure was stable, 200 images were recorded when the laser was set to above the burner, as shown in Figure 3.8. The LII signal intensity was obtained by adding counts at each pixel, where the LII was recorded and the background subtracted. The laser fluence was kept constant at  $1.3 \text{ J cm}^{-2}$ .

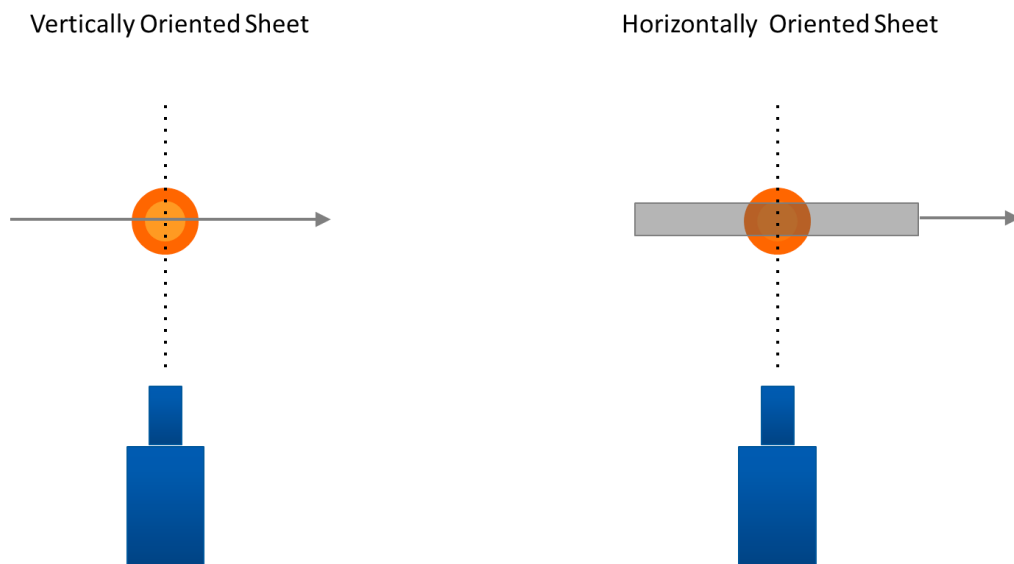


**Figure 3.6:** LII signal sheet.

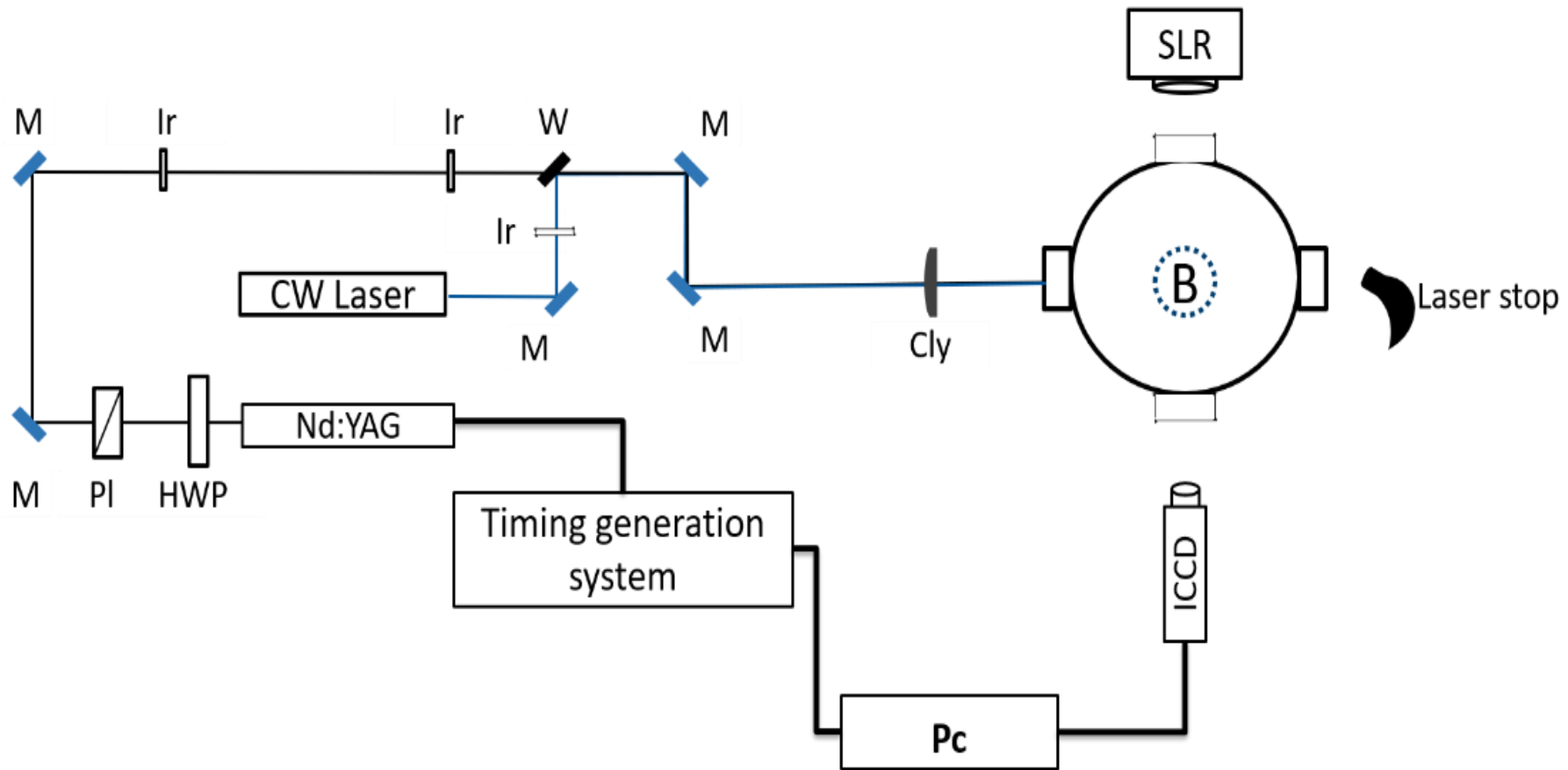


**Figure 3.7:** LII experimental setup; HWP, half-wave plate; PI, polariser; M, mirror; Ir, iris; W, window; Cly, cylindrical lens  $f = 750$  mm; B, McKenna burner; SLR, single-lens reflex camera.

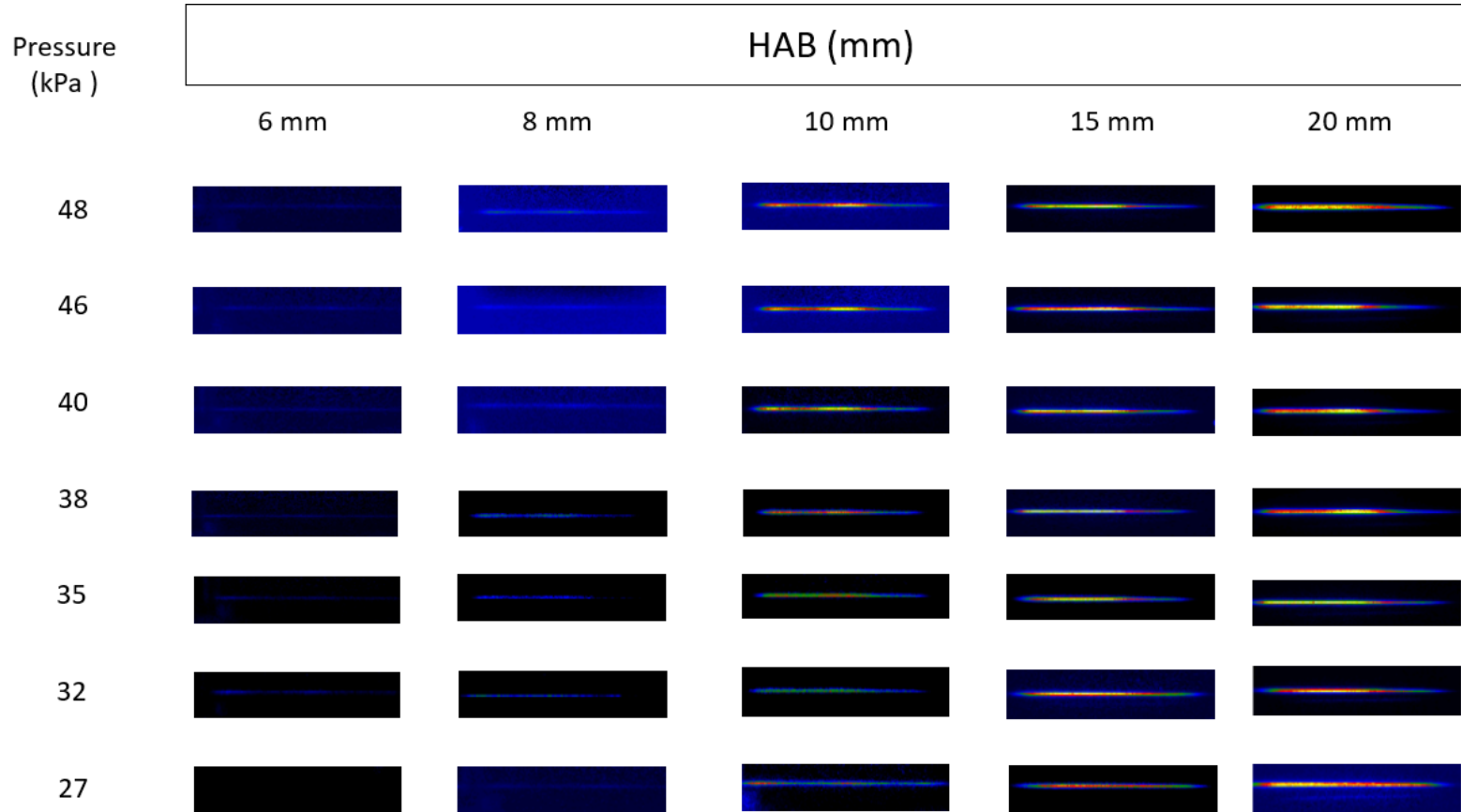


**Figure 3.8:** Typical LII imaging set for different pressure and HAB  $\Phi = 2.1$ .

### 3.2.1.1 Laser-induced incandescence calibration methods

In this research, the data were collected using the LII technique, as it was considered one of the most widely used techniques in recent years in research in this field. However, it was important to ensure that the data resulting from this and the other measurement techniques was reliable. Thus, calibration issues must be taken into account when dealing with measurement techniques.

Calibration of signals resulting from LII is one of the most important steps as the data collected via these measurements were to be utilised to obtain soot volume fractions. Many methods are available for LII calibration, including the light extinction, cavity ring-down (CRD) and gravimetric techniques. The light extinction technique is the method that was used throughout this research.

#### 3.2.1.1.1 Laser extinction method

This method is based on the assumption that there is a light size limit within which soot particles should lie, with reference to the source of light. This method is suitable for many types of flames including steady flames (premixed and diffusion) and unsteady flames. Figure 3.9 shows a schematic diagram of the experimental setup for the extinction measurements used for LII calibration.

For the purposes of obtaining the soot volume fraction, the following equations were used:

$$\frac{I}{I_0} = \exp \frac{(K_{ext} \cdot f_v \cdot L)}{\lambda} \quad (3.1)$$

$$f_v = -\frac{\lambda}{K_{ext} \cdot L} \ln \left( \frac{I}{I_0} \right) \quad (3.2)$$

Where  $I/I_0$  is the ratio of transmitted laser radiation at 1064 nm;  $K_{ext}$  is the extinction coefficient;  $\lambda$  is the wavelength of laser at 1064 nm;  $f_v$  is the volume fraction; and  $L$  is the optical path length in the flame.

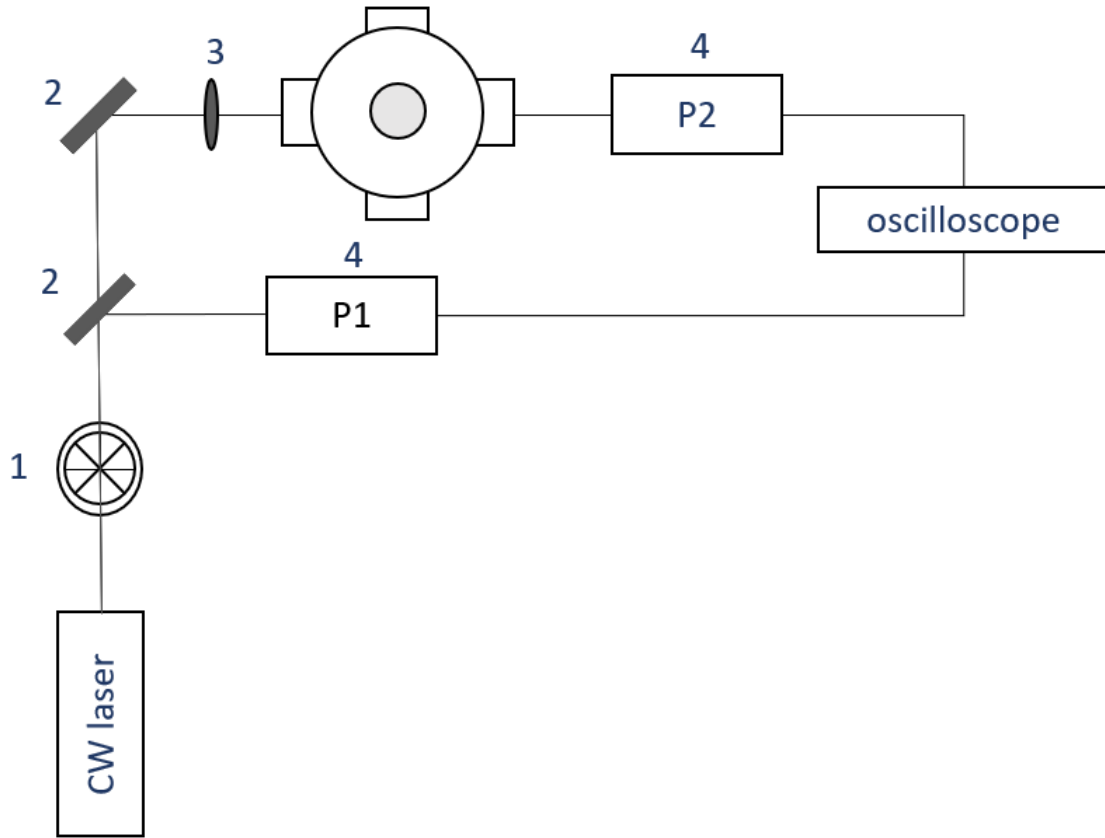


**Figure 3.9:** Calibration by the laser extinction method; 1, chopper; 2, mirror; 3, lens (f = 1000 mm); 4, photodetector1.

Table 3.3: Laser extinction method parameter.

E(m)	$K_{ext}$	Soot volume fraction	Refs
1.60–0.59 i.	5.01	$\frac{I}{I_0} = \exp \left( \frac{K_{ext} \cdot f_v \cdot L}{\lambda} \right)$ $\frac{I}{I_0} = \text{ratio of transmitted}$ $\lambda = \text{wavelength of light}$ $L = \text{optical path length in flame}$ $f_v = -\frac{\lambda}{K_{ext} \cdot L} \ln \left( \frac{I}{I_0} \right)$	[133, 134]

It is generally considered that the degree of agreement between measurements obtained from LII and those obtained from the laser extinction method can lie within 10% at regions and locations within the flame itself, because of the high soot concentration in these regions. Sometimes, the



signals generated through LII are calibrated at heights that are near to the middle of diffusion laminar flames. Thus a deviation is predicted between LII and laser extinction derived volume fractions of soot when conducting experiments at heights above or below the middle of the flame because the soot particles at these locations are smaller and thus tend to exhibit lower sensitivity [135].

### **3.2.2 Spatially resolved emission spectroscopy setup**

Spatially resolved emission spectroscopy was achieved by two methods to confirm the data: with and without fibre optics.

#### *3.2.2.1 Flame emission with fibre optics*

A schematic diagram of the experimental spatially resolved spectroscopy setup used in this work is presented in Figure 3.10. The light emitted from the flame was collected using a lens (L1;  $f = 300$  mm) focussed by a mirror and directed by another lens (L2;  $f = 250$  mm) to focus the emission from a single point of light onto the end of a linear-fibre bundle (Thorlabs, BFL200HS02). The fibre was stabilised on the axis of the equipment to allow for free up-and-down motion. In the test, the identified filaments were placed precisely at focus-to-focus separations running 23 mm high from the light fibre. The brightening fibre conveyed light from the McKenna burner source to the spectrometer (Andor, Shamrock 500i; 150 lines  $\text{mm}^{-1}$  diffraction grating) equipped with an ICCD camera (Andor, iStar). The gate width was 50 ms and the gain = 100. Figure 3.11 shows a typical spatially resolved emission spectroscopy of 27 kPa, at  $\Phi$  2.1.

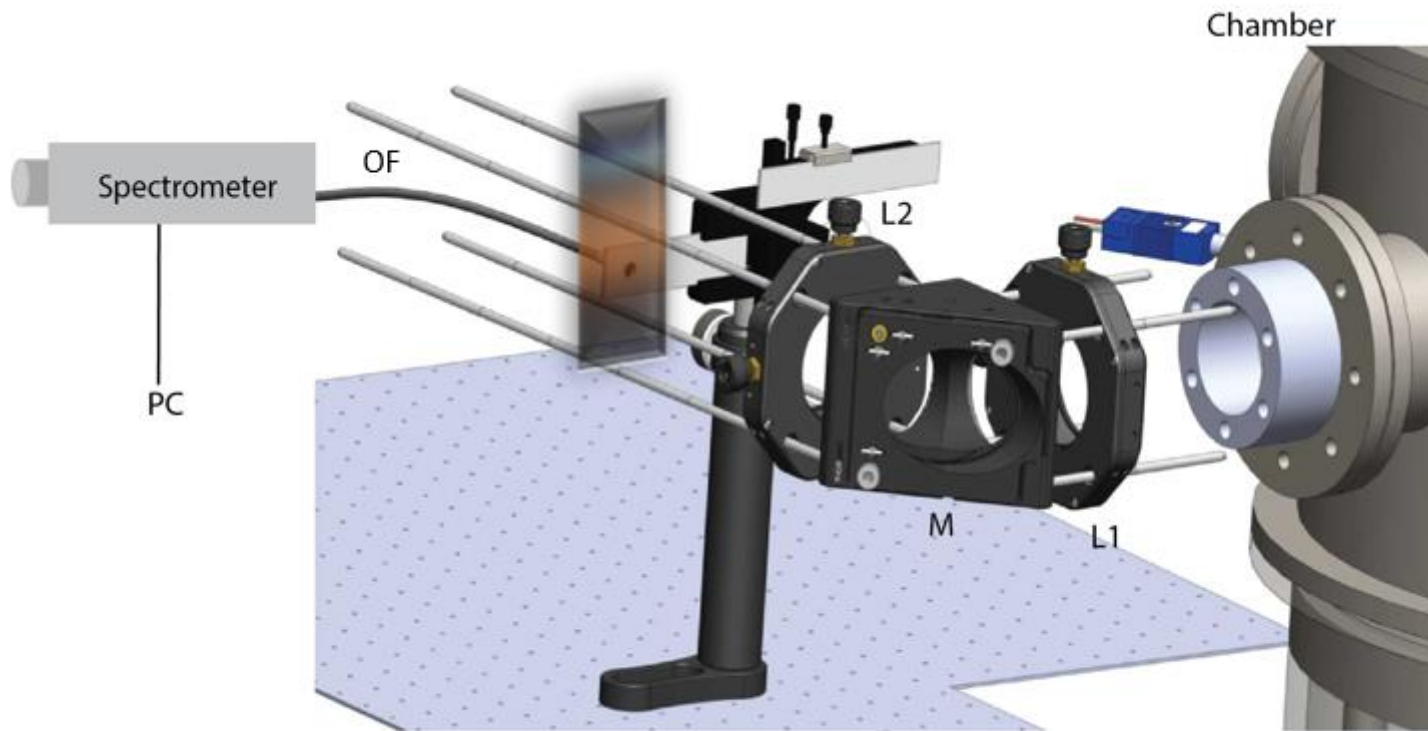


**Figure 3.10:** Experimental setup, where B is a McKenna burner and L1 and L2 represent lenses ( $f = 300$  mm and  $f = 250$  mm, respectively); OF is an optical fibre.

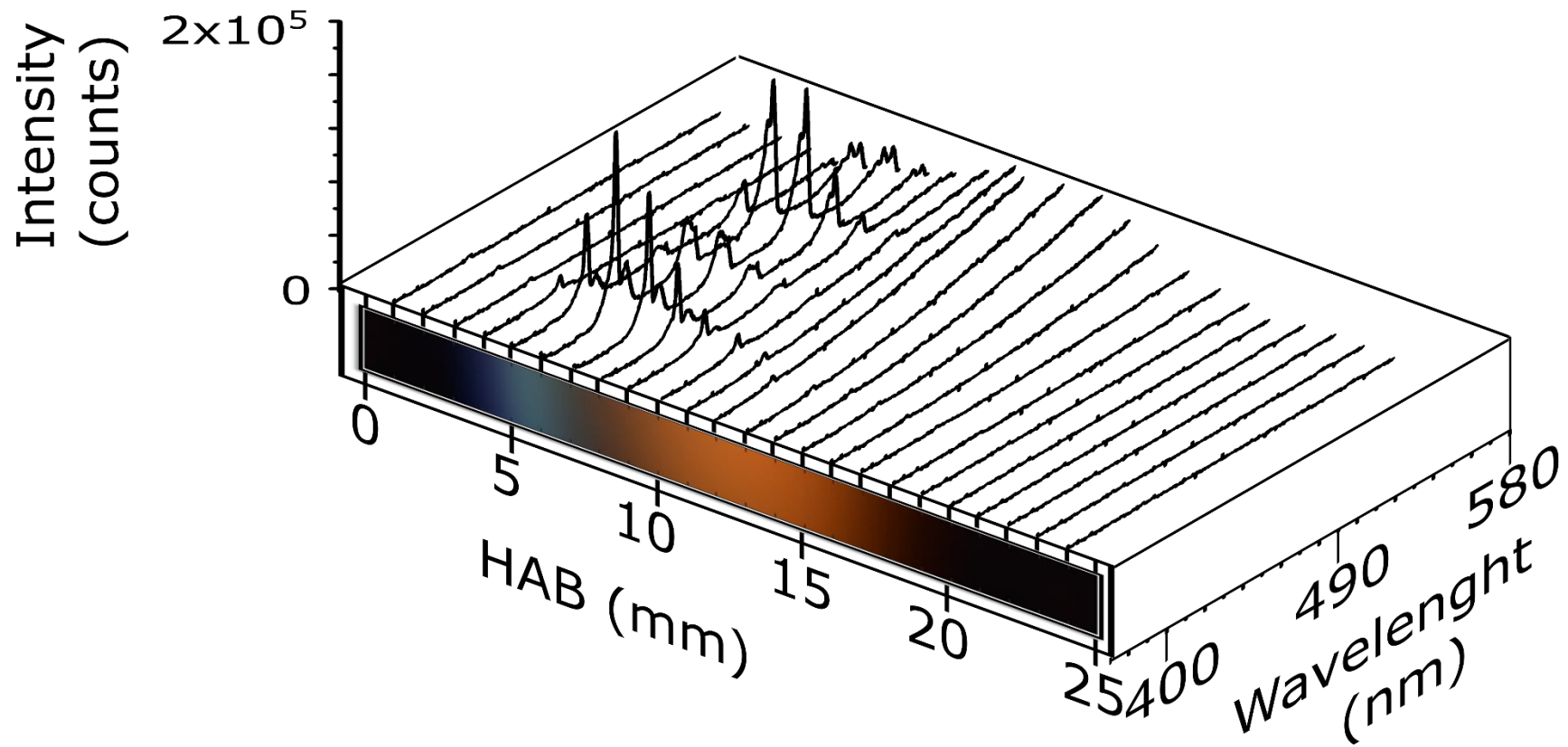


**Figure 3.11:** A typical spectrum for pressure of 27 kPa at  $\Phi = 2.1$ .

### 3.2.2.2 Flame emission without fibre optics

Spatially resolved emission spectroscopy was achieved by scanning the burner, in this set up, the flame emission was imaged using one lens where the flame emission was focussed onto the slit of the spectrometer through the lens ( $f = 100$  mm) as shown in the setup in Figure 3.12. And then guided to the detector. Figure 3.13 and 3.14 present the results for a flame image at different pressure and different  $\Phi$ .

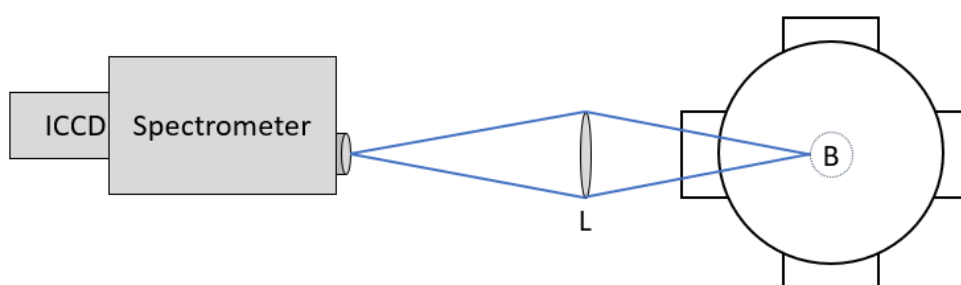


**Figure 3.12:** Flame emission without fibre optics set up.

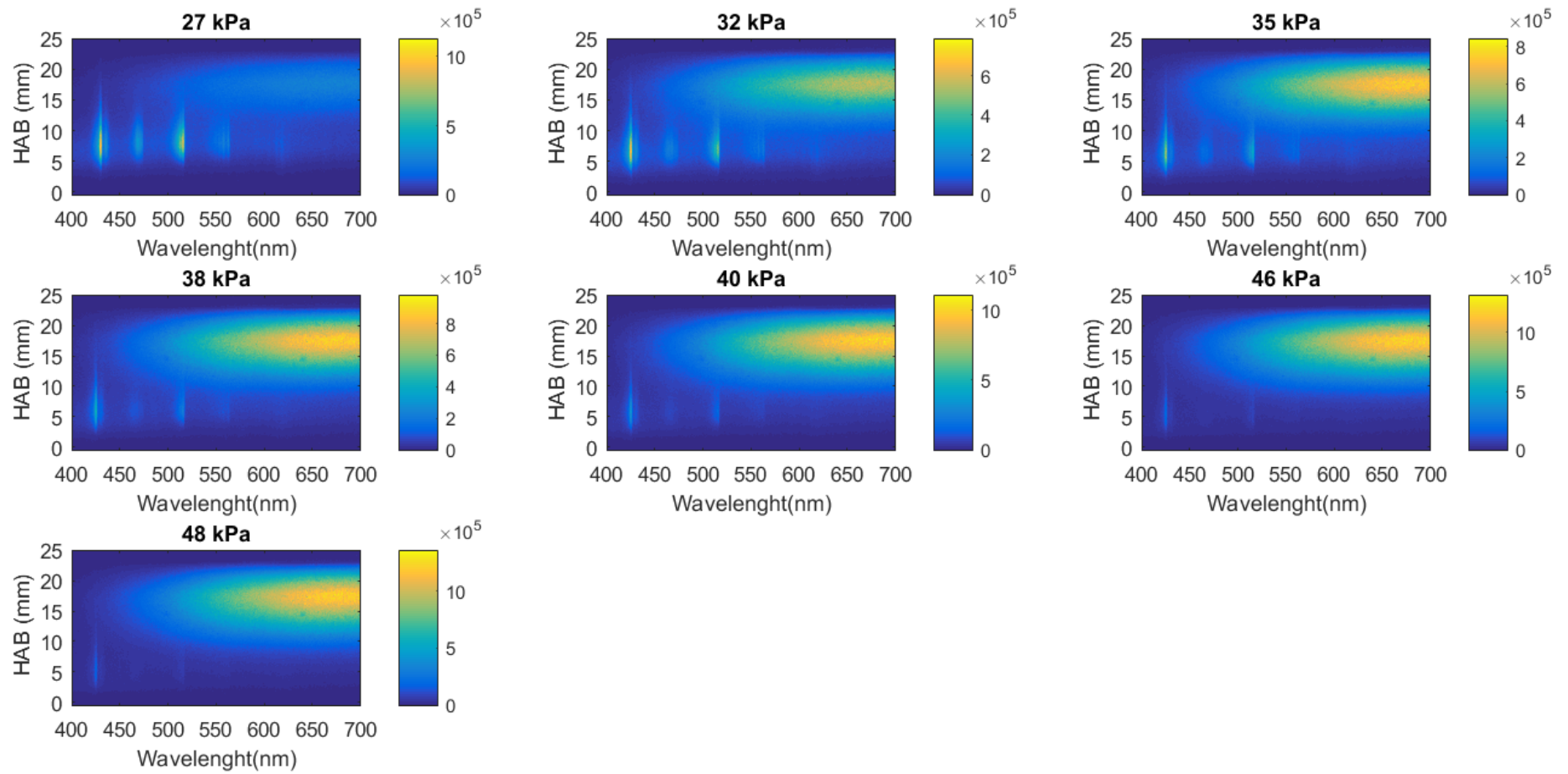


**Figure 3.13:** Flame emission image at  $\Phi = 2.1$ .

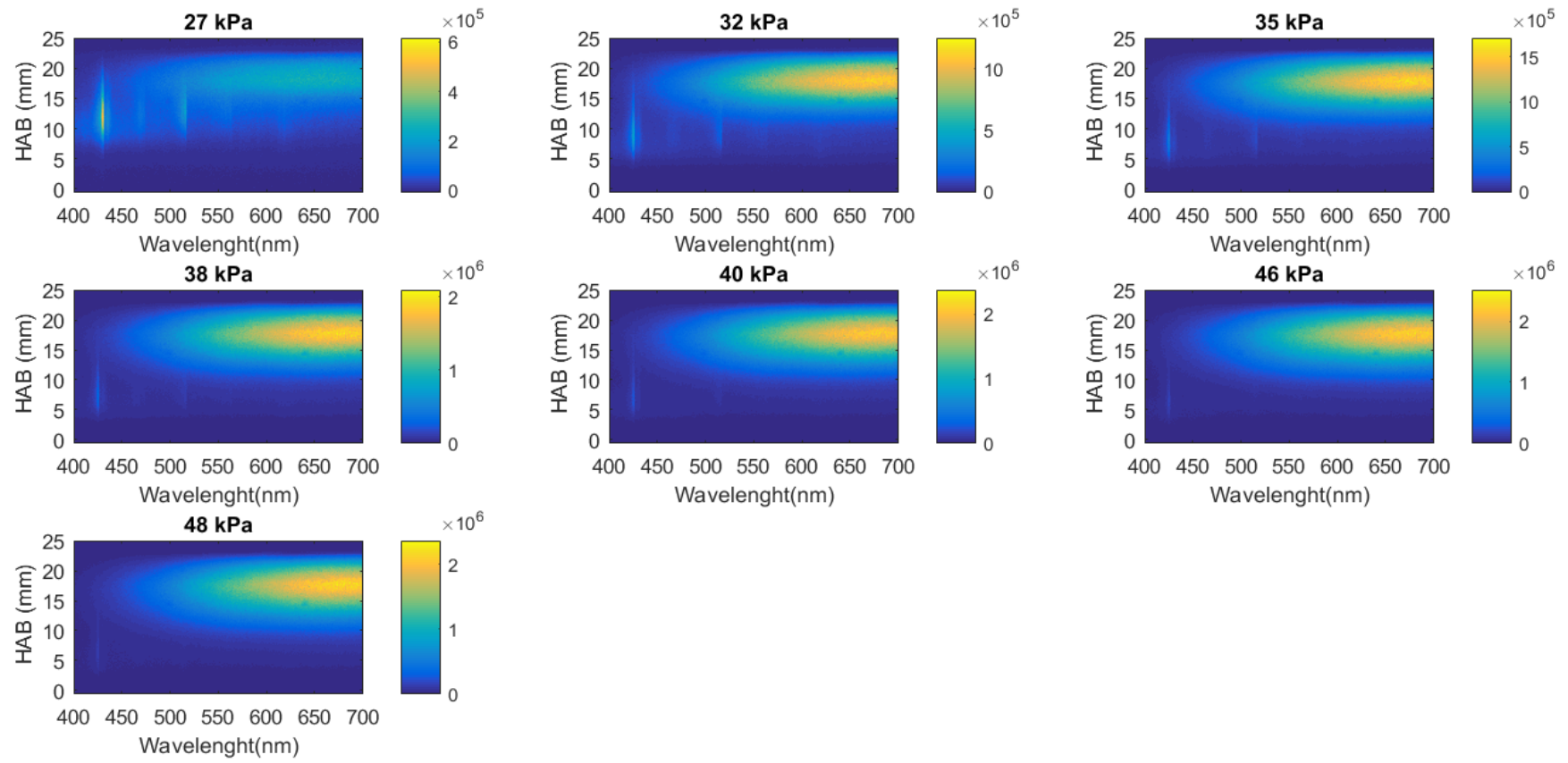
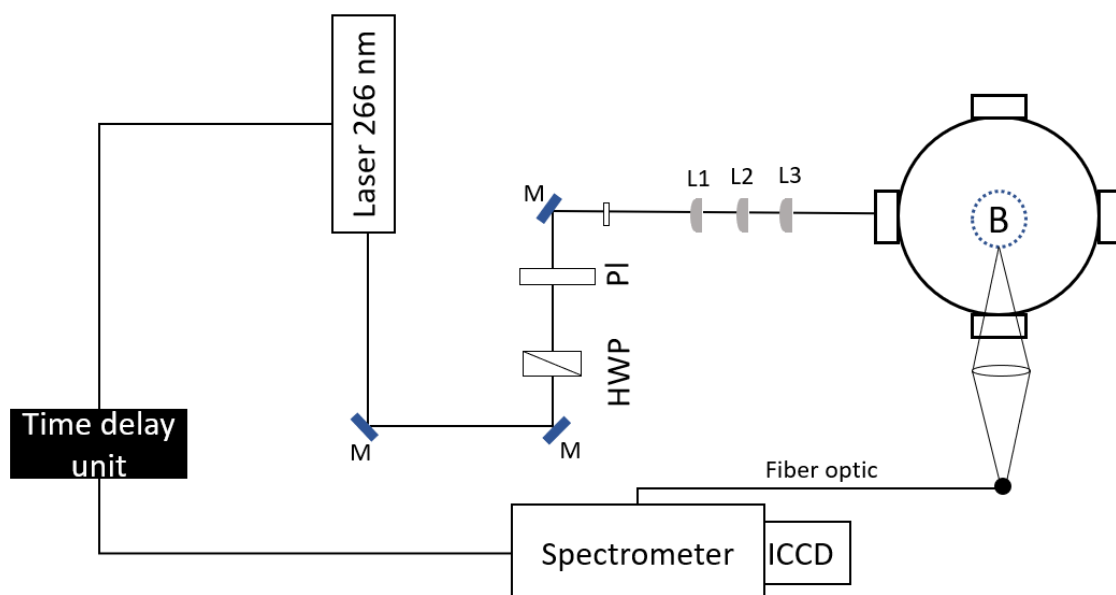


Figure 3.14: Flame emission image at  $\Phi = 2.3$ .

### 3.2.3 Laser-induced fluorescence of PAHs

In the Laser induced fluorescence (LIF) measurements, the fourth harmonic (266 nm) of a pulsed Nd:YAG laser (Quantel) was used as laser source to induce fluorescence from PAHs in flames. The incident laser energy was kept at  $23.3 \text{ mJ cm}^{-2}$  per pulse to avoid LII signal from soot being induced by a laser energy that was too great and the laser was operated at 10 Hz.

Figure 3.15 illustrates the experimental setup: the laser beam was transmitted via a half-wave plate and a Glen laser polariser, through which the laser power was varied. The round laser beam was then reformed into a horizontal laser sheet using three cylindrical lenses. The LIF signals were conveyed to a spectrometer (Andor, Shamrock 500i) with a  $150 \text{ lines mm}^{-1}$  grating via an optical fibre placed at right angles to the laser propagation. The fibre was fixed at the same plane while the burner was moved vertically to obtain LIF signals along different HABs. In this way, the incident laser energy could be kept almost constant as the HAB changes. An ICCD (Andor, iStar) camera was linked to the exit of the spectrometer to register the LIF signals. As LIF signals are far shorter lived than LII signals from soot in a flame, the gate width of the ICCD was set at 30 ns without delay to avoid detecting LII signals. To deal with flame fluctuation, every point was measured 200 times to calculate the average values.



**Figure 3.15:** PAH experimental setup.

Figure 3.16 present a typical of PAH LIF spectra for a pressure of 40 kPa at different HAB. The emission wavelength of PAHs increases along with an increase in aromatic ring size; hence, in several previous studies the detection wavelength was varied to distinguish the relative size groups of PAHs. Three detection wavelength bands were used to distinguish three kinds of PAHs [125, 136].

PAH LIF signals in the range 320–360 nm are due to 2–3-membered PAHs. After that, signals in the wavelength range 370–410 nm indicate the presence of 4-aromatic-ring-membered species. PAH LIF signals above 500 nm indicate the presence of PAHs with 5-membered ring structures, where the individual rings consist of five carbon atoms. Hence, PAH LIF signals of 500–550 are indicative of the presence of 5 membered PAHs. The signal strengths roughly indicate the concentration of the corresponding PAHs.

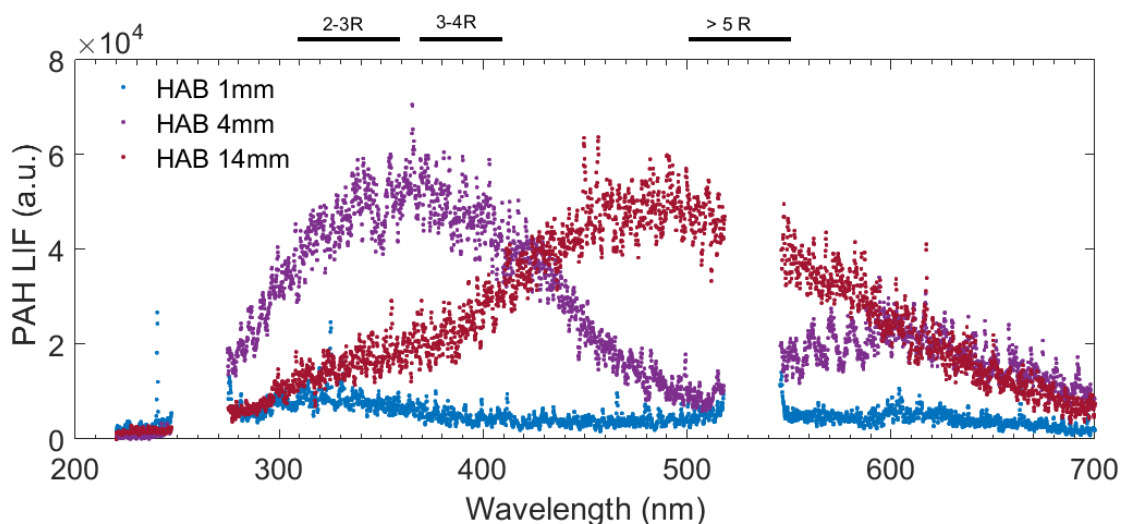


**Figure 3.16:** PAH LIF spectra recorded at pressure of 40 kPa at different HAB at  $\Phi = 2.1$ .

### 3.2.4 Flame temperature

#### 3.2.4.1 Thermocouple (gas phase)

The gas temperatures were measured using an uncoated Pt/Pt<sup>+</sup> 13% Rh (R type, Omega) thermocouple with a diameter of 75  $\mu\text{m}$  and a junction diameter of  $\sim 175 \mu\text{m}$  (see Figure 3.18). This thermocouple was set inside the chamber with the bead of the thermocouple located in the centreline of the burner. To prevent leakage in the chamber, sealant was applied to the end of the thermocouple as shown in Figure 3.17. The gas temperatures were then measured from the distance of the flame surface to a height of 20 mm. To change the height for each position,



adjustments were made to the burner axial heights via a moveable vertical traverse; the accuracy of the position was estimated as  $\pm 0.50$  mm. To mitigate soot deposits on the junction, the thermocouple was rapidly swept into the blue region (soot free) of the flame and held there for 2 s. The data were collected with a thermocouple reader calibrated for the R type. However, thermocouple measurement errors must be corrected to avoid serious deviations of measured temperature values from the actual value. Three correction methodologies are available in the literature: the extrapolation method (using wires of different diameters); the multi-element correction method; and the numerical correction method. In this work the temperature value was corrected by the heat radiation loss method. A thin, 75- $\mu\text{m}$ -diameter wire thermocouple was used to minimise conductivity and radiation effects. Catalytic effects of the junction and errors because of conduction along the wires were expected to be negligible. Radiation losses from the surface of the thermocouple were calculated using the method suggested by Shaddix [137]. In the steady state condition Equation 3.3 given by Shaddix describes the heat balance for a thermocouple:

$$T_g = T_m + \frac{\varepsilon \sigma (T_m^4 - T_w^4)}{h_c} \quad (3.3)$$

where  $T_g$  is the gas temperature (K);  $T_m$  is the measured temperature (K);  $T_w$  is the wall (ambient) temperature to which heat is radiated (300 K);  $\varepsilon$  is the emissivity of the surface of the thermocouple junction;  $\sigma$  is the Stefan–Boltzmann constant ( $5.67 \times 10^{-08} \text{ W/m}^2 \cdot \text{K}^4$ ); and  $h_c$  is the convective heat transfer coefficient.

The convective heat transfer coefficient can be expressed as:

$$h_c = \frac{k \text{Nu}}{\varepsilon} \quad (3.4)$$

Where  $K$  is the thermal conductivity of the gas (W/m K) and  $Nu$  is the Nusselt number, given by:

$$Nu = (0.43 + 0.48) Re^{0.5} \quad (3.5)$$

To estimate local values of the Reynolds number ( $Re$ ), knowledge of local flow velocity,  $v$ , density,  $\rho$ , gas kinematic viscosity,  $\mu$ , and diameter,  $d$ , of the thermocouple junction are required:

$$Re = \frac{v d}{\mu} \quad (3.6)$$

Where viscosity of the mixture,  $\mu$ , may be calculated by [138]

$$\sum_{\alpha=1}^N \frac{x_{\alpha} \mu_{\alpha}}{\sum_{\beta} x_{\beta} \mu_{\beta} \phi_{\alpha\beta}}$$

Where is N is the number of chemical species in the mixture,  $x_{\alpha}$  is the mole fraction of species,  $\mu_{\alpha}$  is dynamic viscosity.

Finally, the energy balance on Equation 3.3 can be solved for the actual flame temperature.

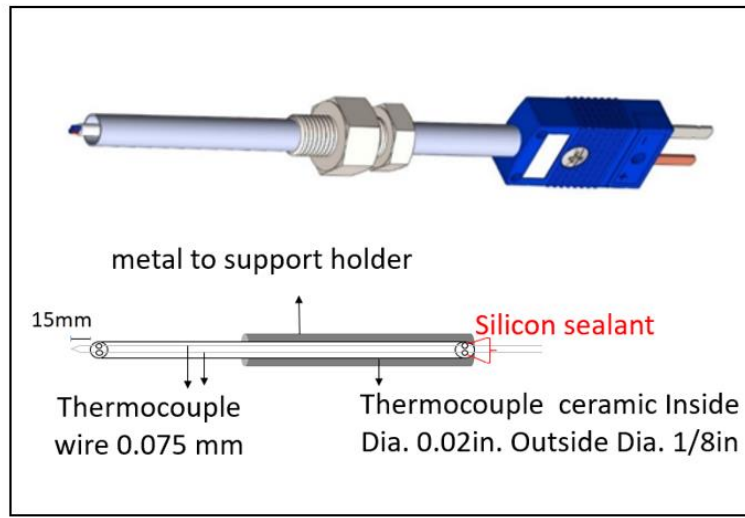


**Figure 3.17:** Cross-section of the type R thermocouple.

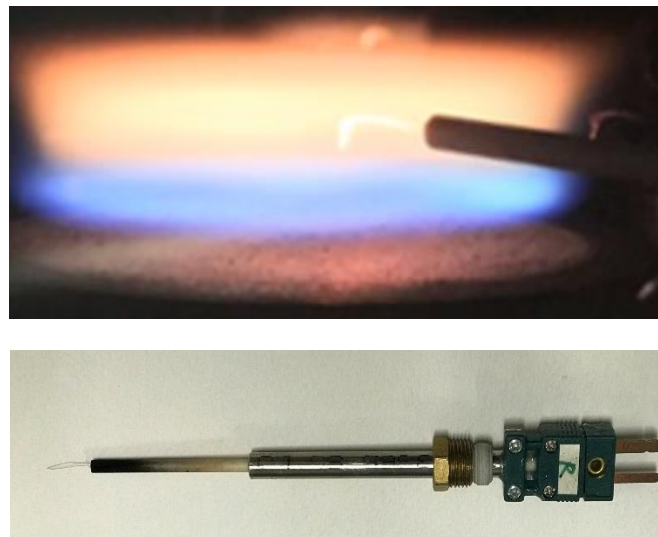


**Figure 3.18:** The thermocouple junction.

### 3.2.4.2 Soot Particles temperature derivation from flame luminosity (solid phase)

Spatially resolved spectroscopy was applied to determine the soot particle temperature at different HABs. With the use of integrated Planck relationship over all solid angles, soot temperature was computed from spatially resolved spectra following Equation 3.8 [139].

$$M(\lambda) = \varepsilon_{\lambda} \frac{2\pi^2 D^2 hc^2}{\lambda^5 e^{\frac{hc}{\lambda kT} - 1}} \quad (3.8)$$

where  $M(\lambda)$  is radiative emission,  $T$  is temperature,  $\lambda$  is wavelength,  $h$  is Planck's constant,  $c$  is speed of light and  $D$  is primary particles diameter [139].

The emissivity of soot can be calculated using:

$$\varepsilon_{\lambda} = \frac{4(\pi D)}{\lambda} \cdot E(m) \quad (3.9)$$

where  $E(m)$  is the absorption function of soot particles in flames, which is a function of the complex index of refraction  $m$ , expressed as:

$$E(m) = -Im \frac{m^2 - 1}{m^2 + 1} \quad (3.10)$$

In the present work, a value of  $m = 1.63 + 0.7i$  was adopted, corresponding to a value of  $E(m) = 0.30$ . [140].

Utilisation of the recorded spatially resolved spectra to measure the soot particle temperature calls for the correction of the entire optical system wavelength response using a stabilised broad band tungsten light source (THROLAB, SLS201, SLS201/M). The property in Equation 3.8 was utilised by varying the input temperature values utilised to fit each spectrum, upon correction. Figure 3.19 displays a typical fitting curve and recorded spectra as well as the corresponding radiance in arbitrary units against the wavelength in nm, displaying the exponential relationship that can be developed from Equation 1. It is clear that the source has adjusted the wavelength accordingly to obtain a unique modulation frequency. The result is a signal that is very sensitive to the modulated radiation. As such, the emitted and the reflected radiation does not necessarily interfere with the measurement exercise. Thus, the results obtained in the experiment remain not only reliable but also accurate.

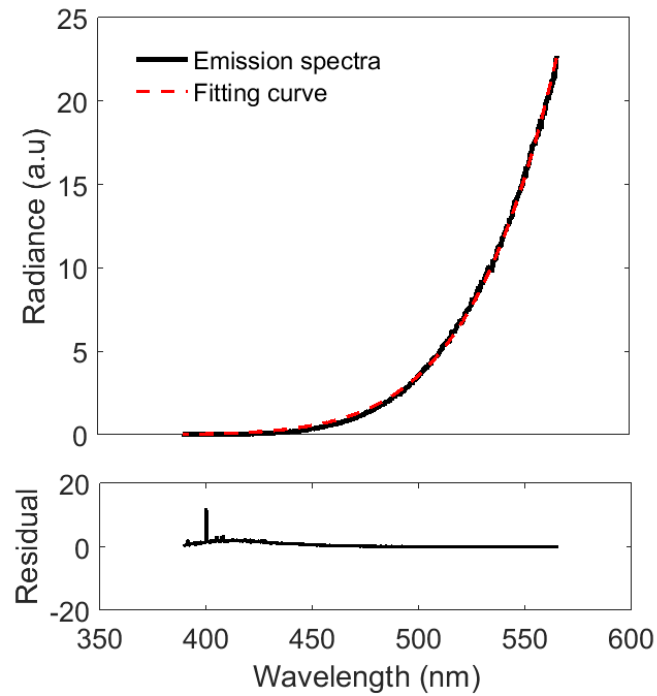


**Figure 3.19:** Typical example of flame emission spectra at HAB of 13 mm and pressure 46 kPa. The fitting curve, red, of the emission spectra, black, are shown. Based on the Planck function the soot particle temperature was calculated at  $1340 \pm 65$  K.

## Chapter 4: Velocity field in a McKenna burner

This chapter presents a detailed information about velocity simulation and measurement in a McKenna burner. The first part in this chapter shows in detail the full steps for experimental measurement of the velocity. The second part describes a computational fluid dynamics (CFD) model, explains the geometry used to model the McKenna burner and gives details for boundary conditions.

In this thesis, flame velocity was simulated through a CFD model using the Ansys-Fluent software package, version 18.0. The velocity profile is crucial in calculating reaction time. Direct velocity measurement was not achievable throughout the experiment since the equipment to measure this was not available. Therefore, a CFD simulation model was the approach chosen to predict the velocity profile. However, the CFD model should be tested to ensure accurate and precise simulated results. To validate the model, the velocity profile was measured in real-time in a cold flow setting. This setting was then modelled to simulate the velocity profile. The simulated profile was compared to the measured values, where the error margin was within 20%. Therefore, the flame velocity profiles were simulated through the CFD modelled, after validating it as described above.

### 4.1 Velocity measurement in a McKenna burner

#### 4.1.1 Cold flow velocity

The air velocity,  $V^{\text{cold flow}}$ , at room temperature 295 K was measured at 10 l/min and 5 l/min by using the VelociCalc® Air Velocity Meter 9545-A (TSI), which has an accurate measurement range of 0 –30 m/s. At 5 l/min the velocity measurement was not sensitive; thus, the velocity profile at 10 l/min was measured and scaled to be applied at 5 l/min. Table 4.1 presents the measured velocity at cold flow with flow rate of 10 and 5 l/min. Figure 4.6 presents a schematic graph for the measured velocity using cold flow with a flow rate of 10 and 5 l/min.

#### 4.1.2 Flame velocity

The flame velocity values were converted based on the density ratio, with the assumption that the flame area does not change. The actual gas velocity for each flame was calculated by:

$$V^{flame} = V^{cold\ flow} \cdot \frac{T_{flame}}{T_{room}} \quad (4.1)$$

Where  $V^{cold\ flow}$  is measured air velocity,  $T_{room}$  is room temperature 298K and  $T_{flame}$  is flame temperature. The details measurement of flame temperature is fully explained on chapter 5. Figure 4.8 presents the actual flame velocity,  $V^{flame}$  of a premixed flame at  $\Phi$  2.1 and pressure 27 and 46 kPa.

## 4.2 Computational fluid dynamics (CFD) model

### 4.2.1 Geometry and boundary conditions

A full geometric description of the McKenna burner was provided in Figure 3.1 and explained previously (Chapter 3). The flame simulation was performed using the Ansys-Fluent software package, version 18.0. The computational domain representing the burner geometry is shown in Figure 4.1. A two-dimensional domain was generated to model the McKenna burner geometry. The domain includes three different zones: the burner plug, shrouding ring and combustion zone.

The well-premixed ethylene and air is released to the burner plug and shrouding nitrogen gas enters the shroud ring. The combustion occurs above the burner surface ( $z = 0$ ) in the combustion zone. A stabilizer is present at 25 mm vertically above the burner surface. This stabilizer is made of 5mm thick steel. The computational domain was discretized into 5347 nodes with the structure mesh generation

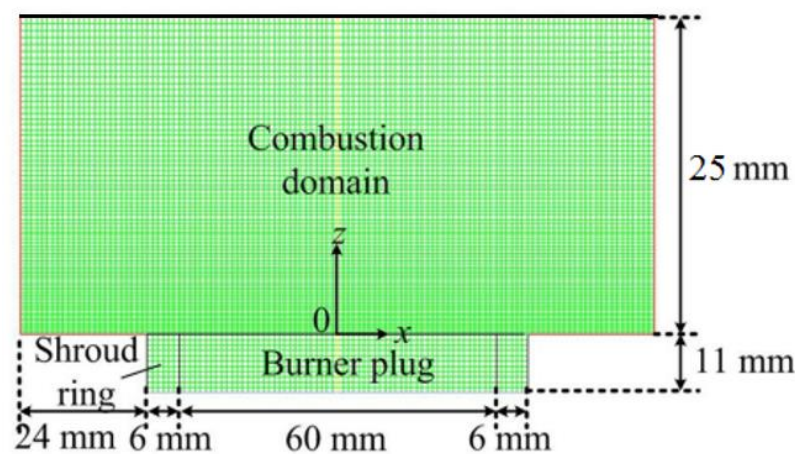


**Figure 4.1:** Computational domain

The velocity inlet boundary condition was set for the inlet premixed fuel and shrouding nitrogen gas, since the flow rate and the inlet area were known. Each velocity inlet surface was specified by the species mass fractions, inlet temperature and a velocity magnitude. The flow direction was kept normal to the surface. The output boundaries of the computational domain were set as the pressure outlet with gauge pressure setting. The operating pressure was set to 101.325 kPa. The stabilizer was defined as the wall boundary condition with steel material of 5 mm thickness. A non-slip condition was selected for the walls.

#### **4.2.2 Computational fluid dynamics (CFD) model**

A steady state pressure-based solver was defined for the CFD model. Since the flame parameters are related to the heat transfer, the energy equation was activated in the simulation. The viscous model was laminar regarding the flow rate of the inlet premixed fuel and nitrogen gas and the inlet areas.

The species transport model was selected for flame simulation. Mixture material was set as premixed ethylene–air, which is available in the Fluent database. However, for the cases of additional gas combustion, the species are selected separately from the database. Laminar finite rate is selected for the turbulence chemistry interaction with the volumetric reactions model. The volumetric species are the multi-species used in the volumetric reactions.

There are significant time scale differences between the general flow characteristics and the chemical reactions in the reacting flows. In order to manage the numerical difficulties that arise from these differences, the Stiff – Chemistry solver was activated in Fluent. This solver integrates the reaction rate of each individual species over a time scale of the same order of magnitude as the general fluid flow.

The radiation model was not activated in this simulation due to the high computational cost. In general, this model is used for simulation of industrial furnaces, gas fired heaters and other equipment which involves combustion in an enclosed domain. For the combustions which are open to air, such as industrial flares and lab-scale burners, the generated heat is dissipated into the atmosphere. For such a cases, the radiation model can improve the simulation results but increases the computational time.

It should be mentioned that all the simulation runs were performed as a cold flow first, which means that the combustion chemistry was disabled at this stage. Once the cold flow simulation was converged, a region above the burner surface in the computational domain was patched with a temperature of 3000 K in the second stage. This process represents the spark to initiate the flame in the combustion zone.

The simulation in this thesis was performed in three phases. The first phase was C<sub>2</sub>H<sub>4</sub>-air with  $\Phi$  of 2.1 with 7 different outlet pressures of 27 kPa, 32, 35, 38, 40, 46 and 48 kPa. The second phase was again C<sub>2</sub>H<sub>4</sub>-air with the same outlet pressures as for the first phase but  $\Phi$  of 2.3. The last phase was C<sub>2</sub>H<sub>4</sub>-air with additional gas Ar, N<sub>2</sub> and CO<sub>2</sub> with  $\Phi$  of 2.1 and an outlet pressure of 40 kPa.

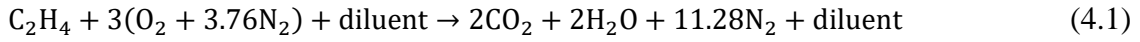
As already mentioned, the C<sub>2</sub>H<sub>4</sub>-air premixed fuel was selected from the Fluent database for the simulation of the first and second phases. In this case, five relevant species including ethylene (C<sub>2</sub>H<sub>4</sub>), oxygen (O<sub>2</sub>), carbon dioxide (CO<sub>2</sub>), water (H<sub>2</sub>O) and nitrogen (N<sub>2</sub>) were involved in the chemical reaction. The reaction was defined as the stoichiometric coefficients of C<sub>2</sub>H<sub>4</sub>, O<sub>2</sub>, CO<sub>2</sub> and H<sub>2</sub>O with 1, 3, 2 and 2, respectively. It was set based on equation 2.1, which was mentioned in previous chapter (Chapter2).

N<sub>2</sub> was not involved in the chemical reactions. However, this gas was defined separately as the shrouding gas to enter the shroud ring. The flow rate of premixed C<sub>2</sub>H<sub>4</sub>-air was 5 l/min for the first phase of simulation, given a velocity of 0.07 m/s at the entrance of the burner plug. With the  $\Phi$  of 2.1, the flow rate was 0.64 l/min in ethylene and 4.36 l/min in air. The flow rate of shrouding nitrogen was 1 l/min. The mass fraction of species was required for the velocity inlet boundary condition. For each species, the mass fraction was calculated based on the percentage of fuel and air in the premixed fuel, the molar mass of the species and the stoichiometric coefficient. The mass fraction of ethylene was set to 0.09, oxygen to 0.19 and nitrogen to 0.72.

For the second phase, the total flow rate and, therefore, inlet velocity was the same as the first simulation phase. However, the  $\Phi$  was 2.3. The flow rate was 0.69 l/min for ethylene and 4.3 l/min for air. The mass fraction of the species was calculated based on the explanations for the first phase.

For the third phase of simulation, additional gases of Ar, CO<sub>2</sub> and N<sub>2</sub> were added to the reactants based on the stoichiometric coefficient in the chemical equation, which was set as 1 for these gases.

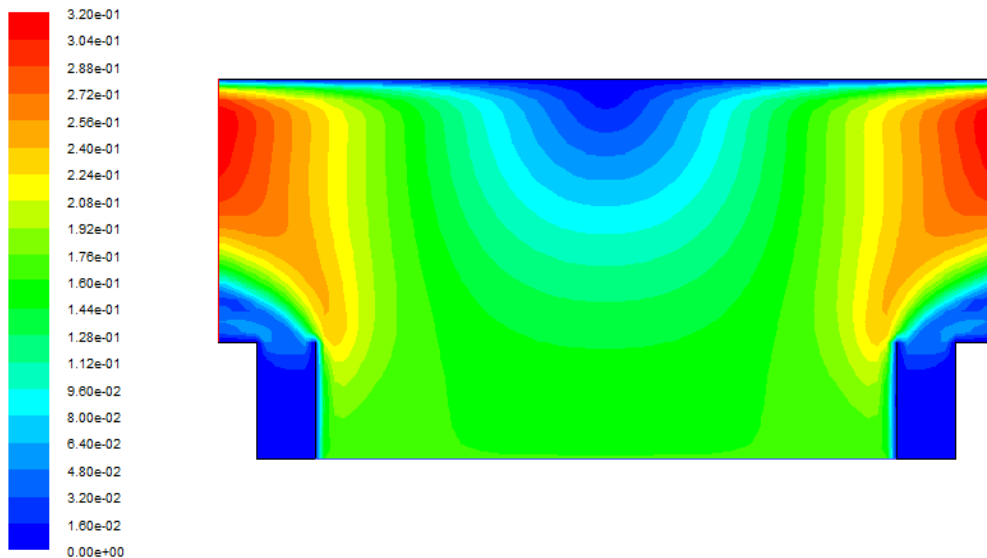




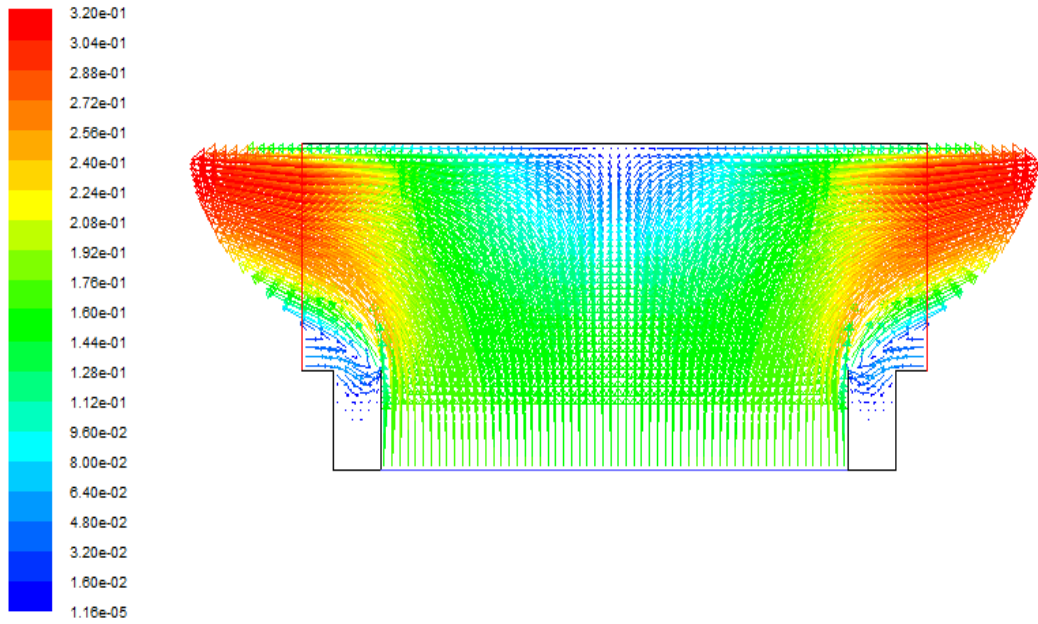
Since there is no database in Fluent for this set of premixed fuels, the reactants and products were selected individually from the database and then set in the mixture species panel to form the chemical reactions. The mixture properties were set as the Fluent default. The mass fraction of the species was calculated as explained in the previous phases. In this phase, the flow rate was 7 l/min for the case of C<sub>2</sub>H<sub>4</sub> -air, 0.9 l/min ethylene and 6.1 l/min air, giving a velocity of 0.1 m/s. The flow rate for the cases of diluent gas was 7.6 l/min, 0.9 l/min ethylene and 6.1 l/min air and 0.6 l/min diluent, with an inlet velocity of 0.106 m/s. The shrouding gas was again nitrogen, with the flow rate of 0.5 l/min.

### 4.2.3 Cold flow velocity

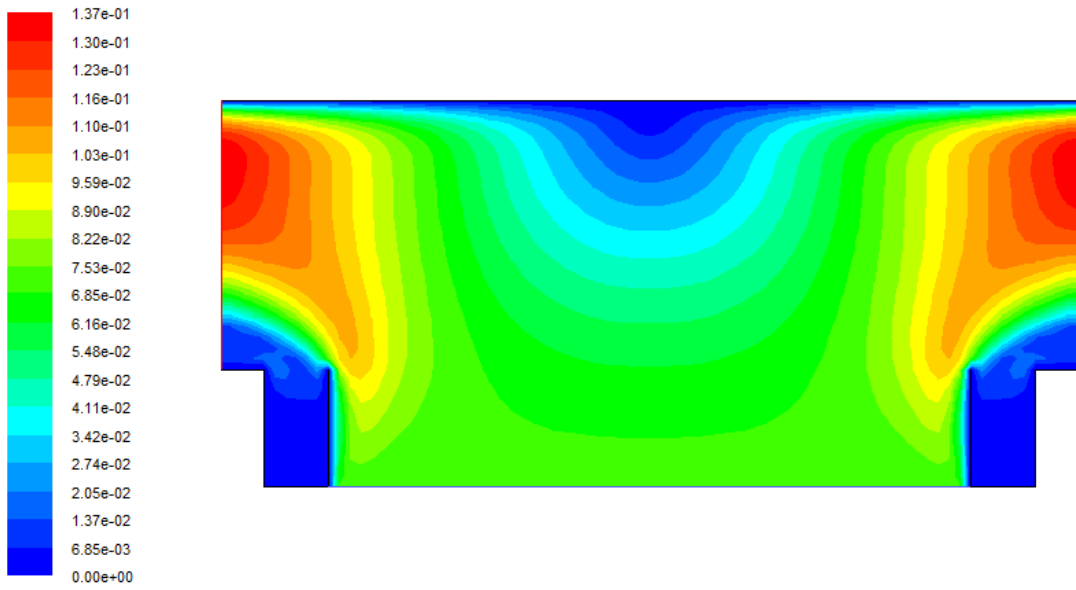
Figure 4.2 presents a velocity contour for cold flow at 10 l/min, where figure 4.3 presents the velocity vector for the same setting. Similarly, figures 4.4 and 4.5 present velocity contours and vectors for cold flow at 5 l/min. the velocity simulated values are presented in table 4.1 and figure 4.6.



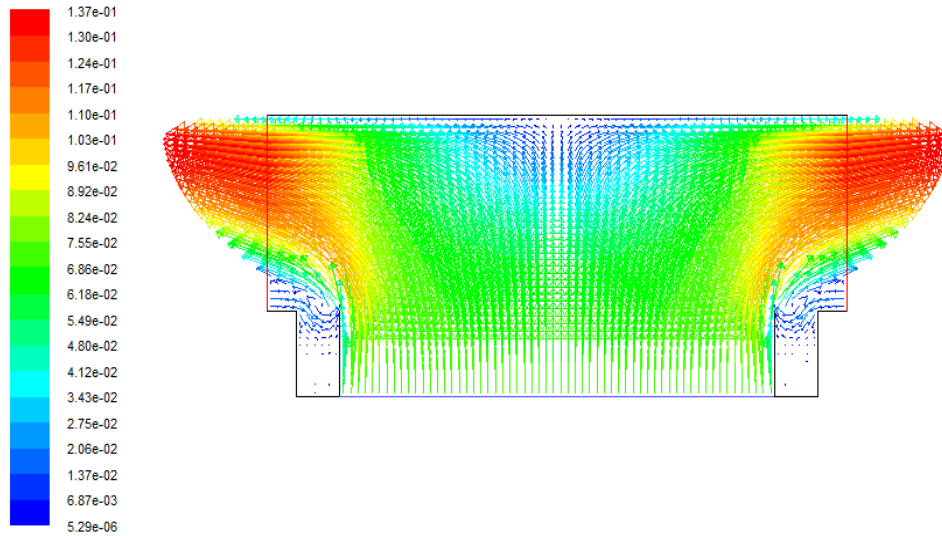
**Figure 4.2:** Cold flow velocity Contour profile at 10 l/min



**Figure 4.3:** Cold flow velocity vector profile at 10 l/min



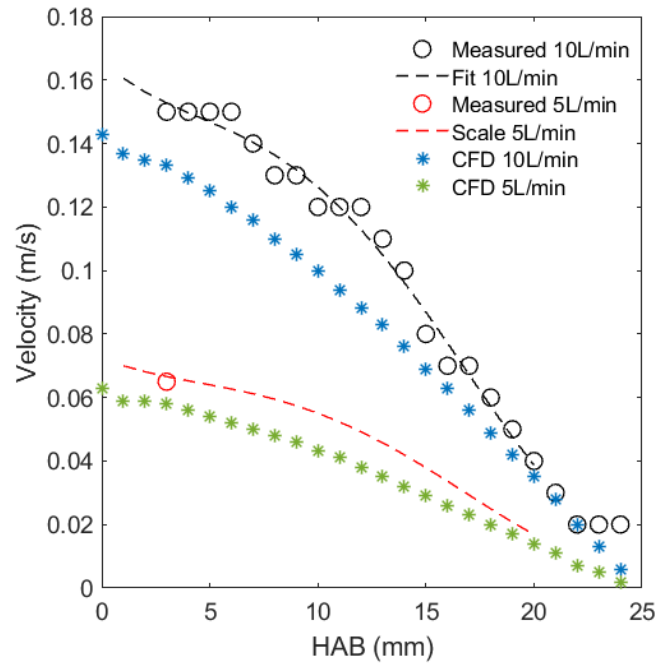
**Figure 4.4:** Cold flow velocity Contour profile at 5 l/min



**Figure 4.5:** Cold flow velocity vector profile at 5 l/min

Table 4.1: Cold flow velocity as measured, scaled and modelled at 10 l/min and 5 l/min

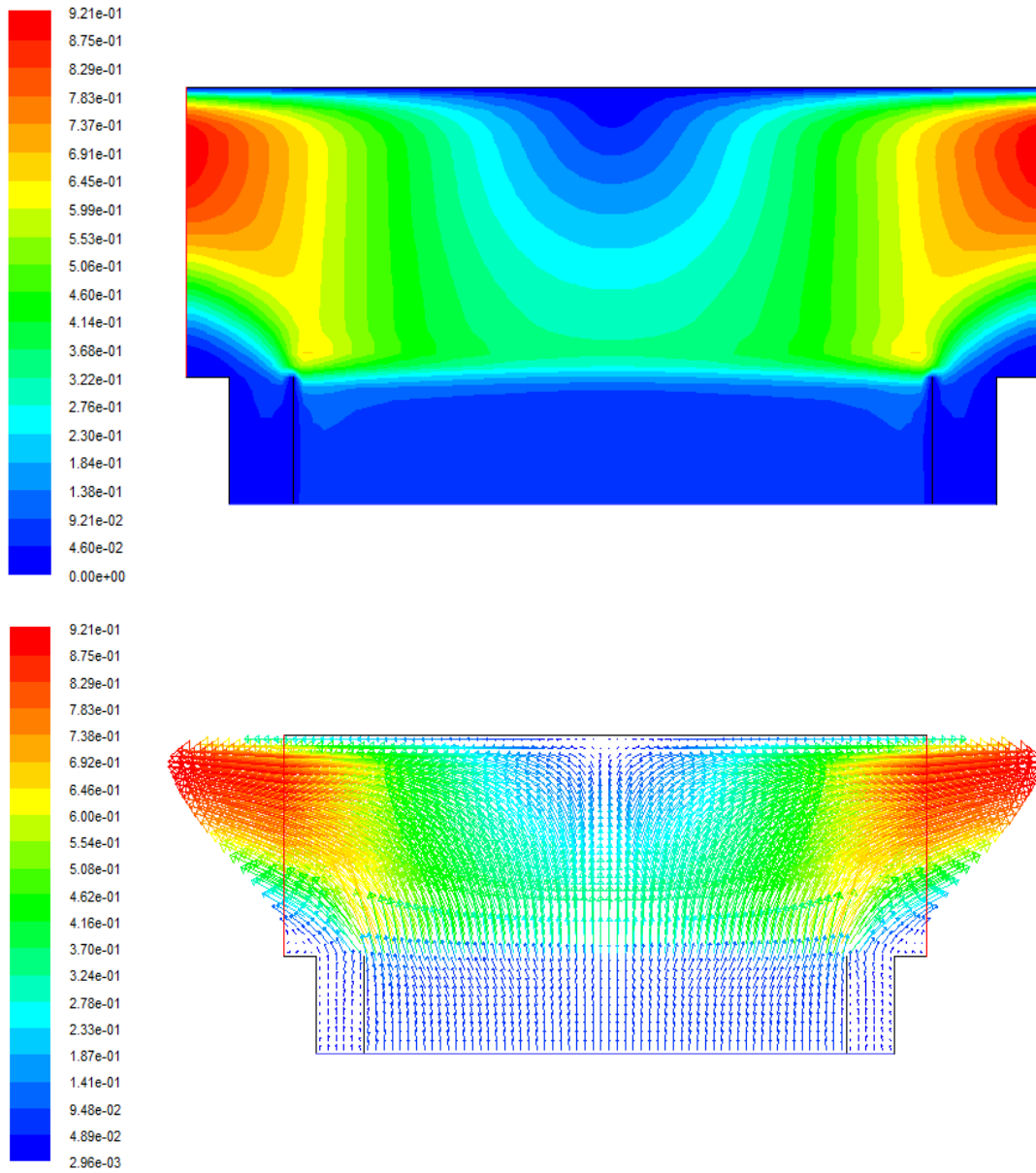
HAB (mm)	Measured velocity (m/s) 10 l/min	Measured velocity (m/s) 5 l/min	Fit velocity (m/s) 10 l/min	Scaled velocity (m/s) 5 l/min	Model velocity (m/s) 10 l/min	Model velocity (m/s) 5 l/min
0	-	-	-	-	0.143	0.063
1	-	-	0.161	0.0700	0.137	0.059
2	-	-	0.156	0.0681	0.135	0.059
3	0.15	0.065	0.153	0.0666	0.133	0.058
4	0.15	-	0.150	0.0653	0.129	0.056
5	0.15	-	0.147	0.0640	0.125	0.054
6	0.15	-	0.144	0.0627	0.120	0.052
7	0.14	-	0.140	0.0612	0.116	0.050
8	0.13	-	0.136	0.0595	0.110	0.048
9	0.13	-	0.132	0.0574	0.105	0.046
10	0.12	-	0.126	0.0551	0.100	0.043
11	0.12	-	0.120	0.0523	0.094	0.041
12	0.12	-	0.113	0.0492	0.088	0.038
13	0.11	-	0.105	0.0457	0.083	0.035
14	0.1	-	0.096	0.0420	0.076	0.032
15	0.08	-	0.087	0.0379	0.069	0.029
16	0.07	-	0.077	0.0336	0.063	0.026
17	0.07	-	0.067	0.0293	0.056	0.023
18	0.06	-	0.057	0.0250	0.049	0.020
19	0.05	-	0.048	0.0208	0.042	0.017
20	0.04	-	0.039	0.0169	0.035	0.014
21	0.03	-	-	-	0.028	0.011
22	0.02	-	-	-	0.020	0.007
23	-	-	-	-	0.013	0.005
24	-	-	-	-	0.006	0.002



**Figure 4.6:** Cold flow velocity profile as measured, modelled and scaled at 10 l/min and 5 l/min

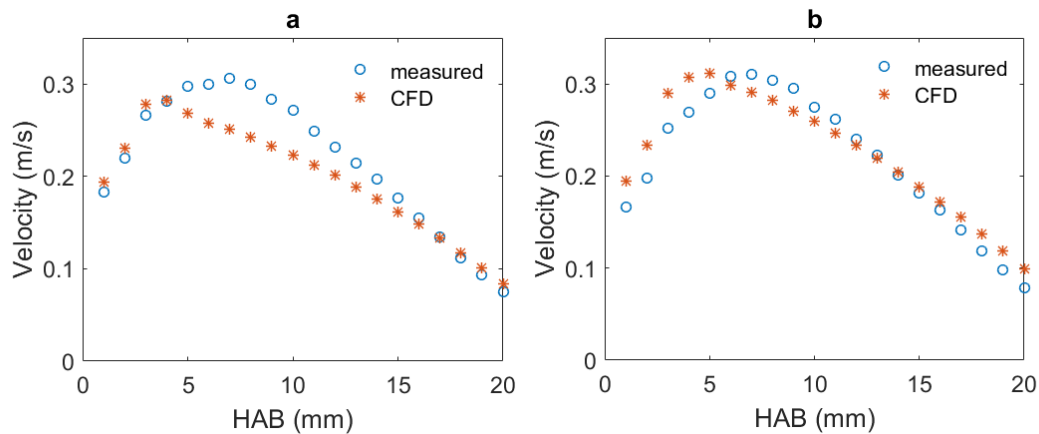
#### 4.2.4 Flame Velocity

Figure 4.7 presents a CFD simulated result for velocity contours and vectors for premixed flame at  $\Phi$  2.1 and pressure 46 kPa.



**Figure 4.7:** Contour of velocity (top) and vector (bottom) profile at  $\Phi$  2.1 with total flow rate 5 l/min at a pressure of 46 kPa

Figure 4.8 presents the actual and the modelled flame velocity,  $V^{\text{flame}}$  of a premixed flame at  $\Phi$  2.1 and at pressure 27 and 46 kPa. Figure 4.9 clearly shows that the velocity profile modelled with this flame condition is consistent with a measurement done in a flat stabilizer burner at atmosphere pressure by Aamir.et al [141], However, the velocity model values agree with the velocity measured values for a pressure of 27 kPa, while some discrepancies were observed at a pressure of 46 kPa, as shown on Figure 4.8.



**Figure 4.8:** Axial flame velocity profile as modelled and after converted at different pressures a; 46 kPa and b: 27kPa at  $\Phi$  2.1

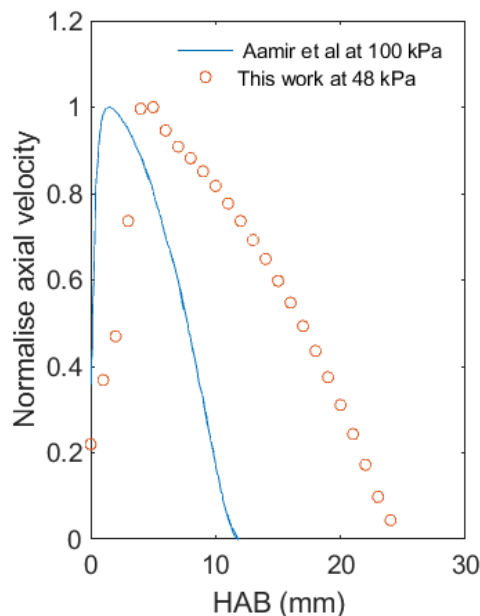


**Figure 4.9:** Normalise axial velocity profile with pressure 48 kPa at  $\Phi$  2.1 and compared to the published study [141]

## Chapter 5: Premixed Ethylene-Air at $\Phi$ 2.1

This chapter presents a study on soot formation in laminar premixed  $C_2H_4$ -air flames at different HABs and with a chamber pressure operating at pressures of 27–48 kPa with an equivalence ratio of  $\Phi = 2.1$ . Measurements included flame front,  $f_v$ , using LII, PAHs using LIF,  $T_s$  and  $T_g$ .

### 5.1 Results and Discussion

#### 5.1.1 Low pressure flames photography

For this study, a steel plate was employed at a height of 25 mm to stabilise the flames, and the chamber pressure varied in a range of 27–48 kPa with an equivalence ratio of  $\Phi = 2.1$ . Figure 5.1 shows a series of photographs that recorded the flames in the experiment. It was found that soot luminosity decreased with a decrease in pressure, which may directly imply the pressure dependence of soot formation in these premixed  $C_2H_4$ -air flames. This is consistent with the results presented by Desgroux and others showing that the study of soot formation at low pressure is affected by many factors. In these pressure conditions, the soot volume fraction is sensitive to both pressure and the equivalence value  $\Phi$  for  $CH_4$  fuel [15, 132].

In addition, a quasi-one-dimensional structure is clearly demonstrated in the photographs in Figure 5.1, which may be divided into three regions. The blue flame at the front is divided into two regions: light blue, which refers to a  $C_2^*$  radical; and dark blue, which indicates  $CH^*$ . In addition, the non-luminous soot inception layer, in which the production of soot begins, is shown in blue combined with orange; this region is not evident in atmospheric pressure or in the above conditions. The luminous soot region and the ‘dark’ region close to the stabiliser are particularly clear in the photographs recorded at 27 kPa.

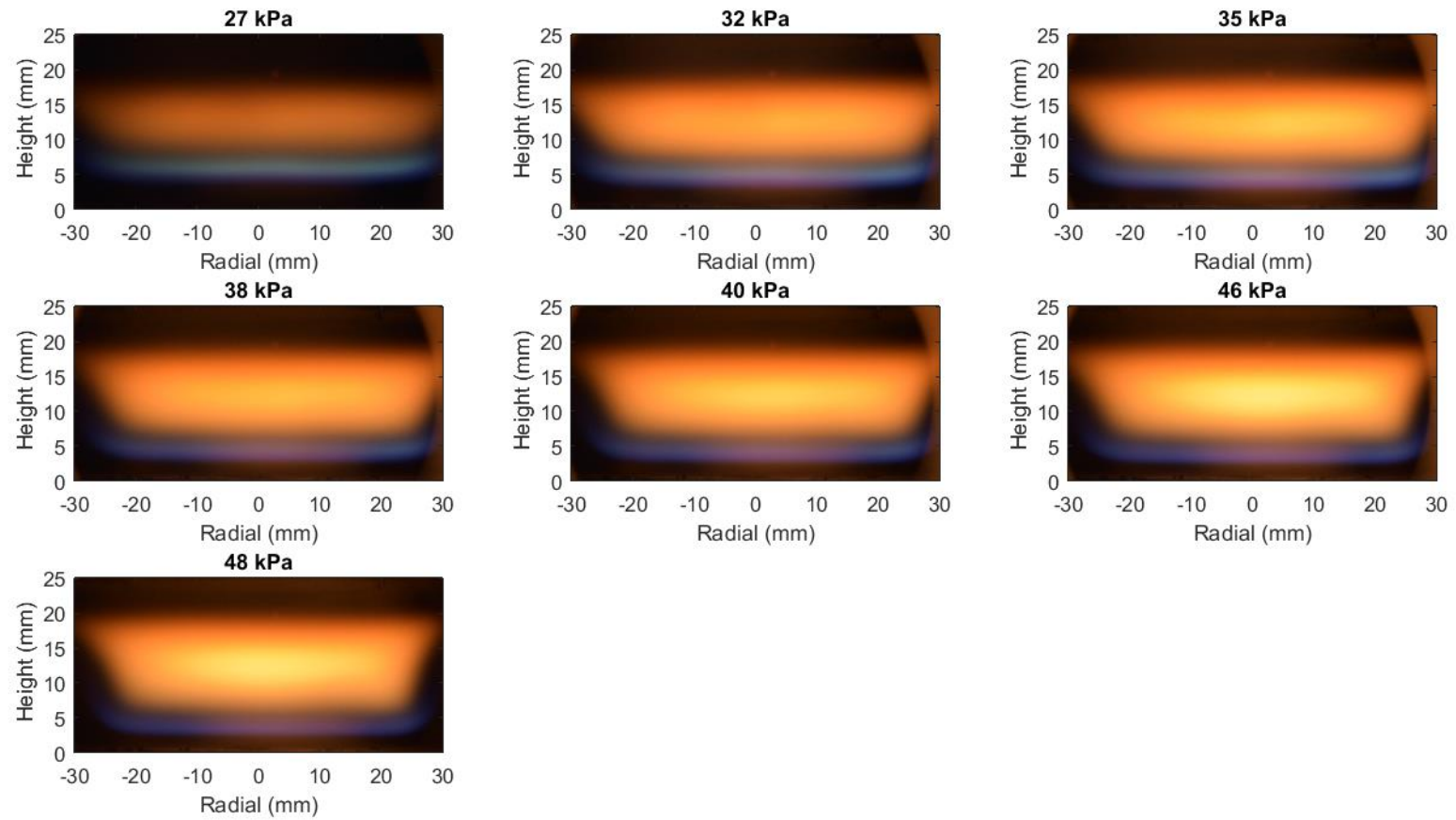


**Figure 5.1:** Photographs of flat, rich premixed laminar flames at different pressures with  $\Phi = 2.1$ .



### 5.1.2 Spatially resolved emission spectra of CH\* and C<sub>2</sub>\* radicals

For heights of 0–23 mm above the burner surface, 200 spectra were collected at each HAB at increasing steps of 1 mm, and then averaged for that HAB. Typical spectra are shown in Figure 5.2.

Calculations were based on the configuration of the optical collection system and showed that the measurements below 2.2 mm were only minimally influenced by the blocking edge of the burner; by ~12%. Accordingly, the correction of this effect barely changed the results. Also, as shown in Figure 5.1, the flame images were collected using a digital camera, and no clear blue emission was found below a HAB of 2 mm.

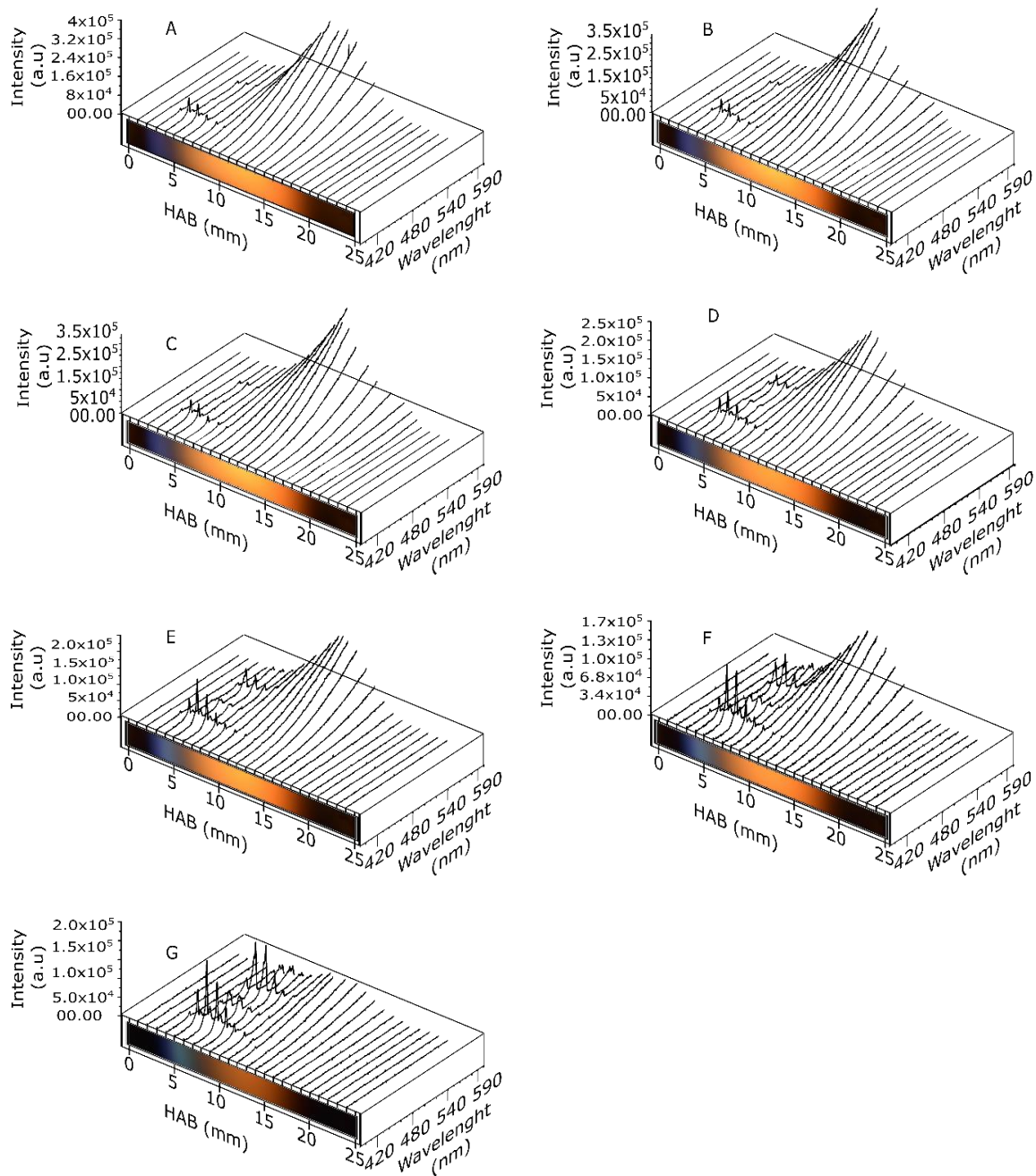


**Figure 5.2:** Flame photographs and spatially resolved emission spectra recorded at  $\Phi = 2.1$  for different pressures; A, 48 kPa; B, 46 kPa; C, 40 kPa; D, 38 kPa; E, 35 kPa; F, 32 kPa; G, 27 kPa.

The  $\text{CH}^*$  chemiluminescence was measured from 418 to 430 nm, where  $\text{C}_2^*$  was 500–525 nm. Figure 5.2 presents emission spectra for laminar  $\text{C}_2\text{H}_4$ –air premixed flames at low-pressure conditions from 48 to 27 kPa. At a pressure of 48 kPa, the  $\text{CH}^*$  radicals began to form at a height of 2 mm; the  $\text{C}_2^*$  radicals appeared at 3 mm. The peaks of  $\text{CH}^*$  and  $\text{C}_2^*$  increased from 3–5 mm; the soot emission profile at 4 mm was shown beside the  $\text{CH}^*$  and  $\text{C}_2^*$ . After that, the  $\text{C}_2^*$  disappeared at 5 mm, and the  $\text{CH}^*$  peak decreased until it disappeared at 8 mm. Thus, at 10 mm, the emission of soot increased in intensity until it reached 13 mm; then, this emission decreased until the signal disappeared at 19 mm. However, at a pressure of 46 kPa, the spectra were similar to those at 48 kPa: other than differences in intensity value, mean and the spectra profile (from where the radical started), the spectra were the same. At a pressure of 40 kPa at 2 mm,  $\text{CH}^*$  began to form and at 3 mm,  $\text{CH}^*$  and  $\text{C}_2^*$  were observed. Then, the peak of  $\text{CH}^*$  and  $\text{C}_2^*$  increased until 5 mm, when the emission of soot appeared at a height of 5 mm. Afterwards, the peak representing  $\text{C}_2^*$  disappeared at 6 mm with the peak for  $\text{CH}^*$  remaining beside the emission of the soot profile; the  $\text{CH}^*$  peak decreased until a height of 9 mm. At a height of 10 mm, only the emission of the soot profile was shown, and the emission of soot was increased until 13 mm. After that, the emission decreased until the signal disappeared at 19 mm.

At a pressure of 38 kPa, the  $\text{CH}^*$  radicals began at a height of 2 mm when  $\Phi = 2.1$ . The  $\text{C}_2^*$  began to form at 4 mm and emitted a clear signal, with the peak increasing up to a height of 5 mm. At this height, soot emission was shown beside  $\text{CH}^*$  and  $\text{C}_2^*$  radicals. The  $\text{C}_2^*$  vanished at 6 mm, and only  $\text{CH}^*$  was seen at this height in the soot emission. Then, the peak of  $\text{CH}^*$  diminished until a height of 9 mm was reached, where only the emission of the soot profile can be seen; it then decreased until it reached 13 mm, decreasing further until the signal disappeared at 17 mm. At 35 kPa,  $\text{CH}^*$  radicals began to form at a height of 2 mm and then  $\text{C}_2^*$  radicals appeared at 3 mm; at 6 mm, the soot emission profile was shown beside the  $\text{CH}^*$  and  $\text{C}_2^*$ . After that, the  $\text{C}_2^*$  disappeared at 7 mm, and the  $\text{CH}^*$  peak decreased until it disappeared at 10 mm. At 11 mm, it was evident that the emission of soot increased in intensity until it reached 13 mm; the emission then decreased until the signal disappeared.

At 32 kPa,  $\text{CH}^*$  radicals began to appear at a HAB of 2 mm, and  $\text{C}_2^*$  began to form at 3 mm HAB. They emitted a clear signal at 4 mm, and the peak increased until 6 mm HAB. At 6 mm HAB, a soot emission was shown beside the  $\text{CH}^*$  and  $\text{C}_2^*$  radicals. The  $\text{C}_2^*$  vanished at 8 mm HAB, while  $\text{CH}^*$  and soot emission were recorded at this height. The peak of  $\text{CH}^*$  diminished once a height of 11 mm was reached: at this height only the emission of the soot profile was seen. The soot emission began to decrease from 12 mm and disappeared at 17 mm.

At a pressure of 27 kPa, the  $\text{CH}^*$  radicals began at 3 mm, but the signal was too weak. At 4 mm, the  $\text{CH}^*$  and  $\text{C}_2^*$  were evident. The peak of these radicals increased very clearly with a strong intensity value. At 7 mm, peaks of the  $\text{CH}^*$ ,  $\text{C}_2^*$  and soot emission profiles were observed. The  $\text{C}_2^*$  peak decreased until its disappearance at 9 mm and the  $\text{CH}^*$  peak decreased until 12 mm; after this height, the peak of  $\text{CH}^*$  had limited value beside the emission profile of soot until the signal disappeared at 17 mm.

#### 5.1.2.1 Excited $\text{CH}^*$ radical

Figure 5.3 shows the intensity of  $\text{CH}^*$  chemiluminescence as a function of HAB, presented as actual recorded data with a Gaussian line of best fit to describe and differentiate different pressure settings. It is clear that the intensity of the  $\text{CH}^*$  spectra decreased with increasing pressure. At the 27 kPa pressure point, the highest intensity of the spectra was noted. A sharp spike in intensity was noted for all pressure points from 2 mm, peaking at 3 mm with pressure at 48 kPa. At a pressure of 32 kPa, it reached its peak at 4 mm (fast reaction HAB). After 5 mm, there was a gradual decline in the intensity for all pressure points. The intensity was constant from around 10 mm HAB.

Increasing the pressure from 27 to 48 kPa had a strong effect on the distribution of the  $\text{C}_2\text{H}_4$  flame components (e.g.  $\text{CH}^*$ ). This is presented as a higher peak intensity as recorded at the lowest pressure setting, while a lower and wider peak area represents flames recorded at higher pressure settings. The effect of increasing the pressure could therefore be seen in the reduction of the flame temperature, which may be an indicator of the flame intensity. To satisfactorily quench the  $\text{CH}^*$ , the side reactions ran in a similar manner, with higher pressure points determining the rate at which combustion took place, if the fuel content was constant.

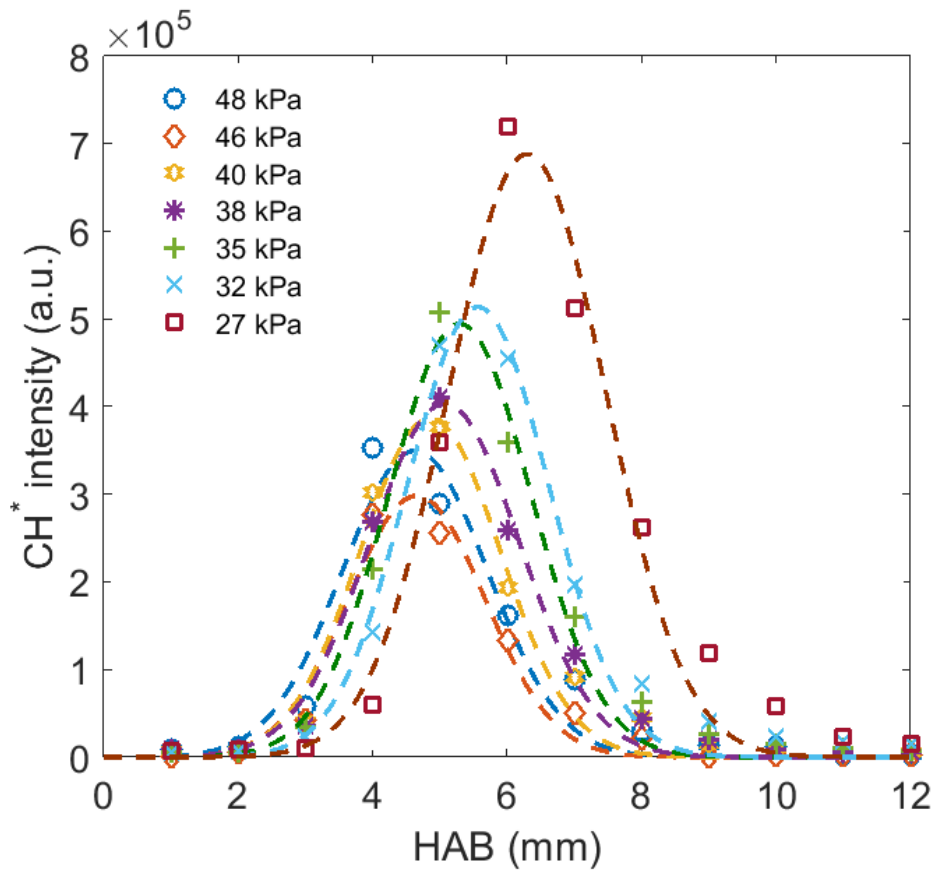


**Figure 5.3:** The intensity of  $\text{CH}^*$  at different pressures as a function of the HAB  $\Phi = 2.1$

#### 5.1.2.2 Excited $\text{C}_2^*$ radical

Figure 5.4 presents the intensity of  $\text{C}_2^*$  chemiluminescence as a function of HAB.  $\text{C}_2^*$  inception shifted at around 1 mm at a level comparable to  $\text{CH}^*$  inception at all recorded pressures. The figure shows the actual recorded data with a Gaussian line of best fit to describe and differentiate different pressure settings. A spike in intensity was noted for all pressure points from 3 mm HAB. The levels of intensity were considerably different at higher distances from the burner. Increasing the pressure resulted in compaction of the fuel components, which then led to reduced flame intensity regardless of the HAB. Since the formation of  $\text{C}_2^*$  was part of the chain reaction that characterises the combustion process, it was noted that an increase in pressure had a concurrent effect on the distribution of the fuel components. At 5 mm HAB, increasing pressure had a much stronger effect on the flame intensity than at 10 mm.

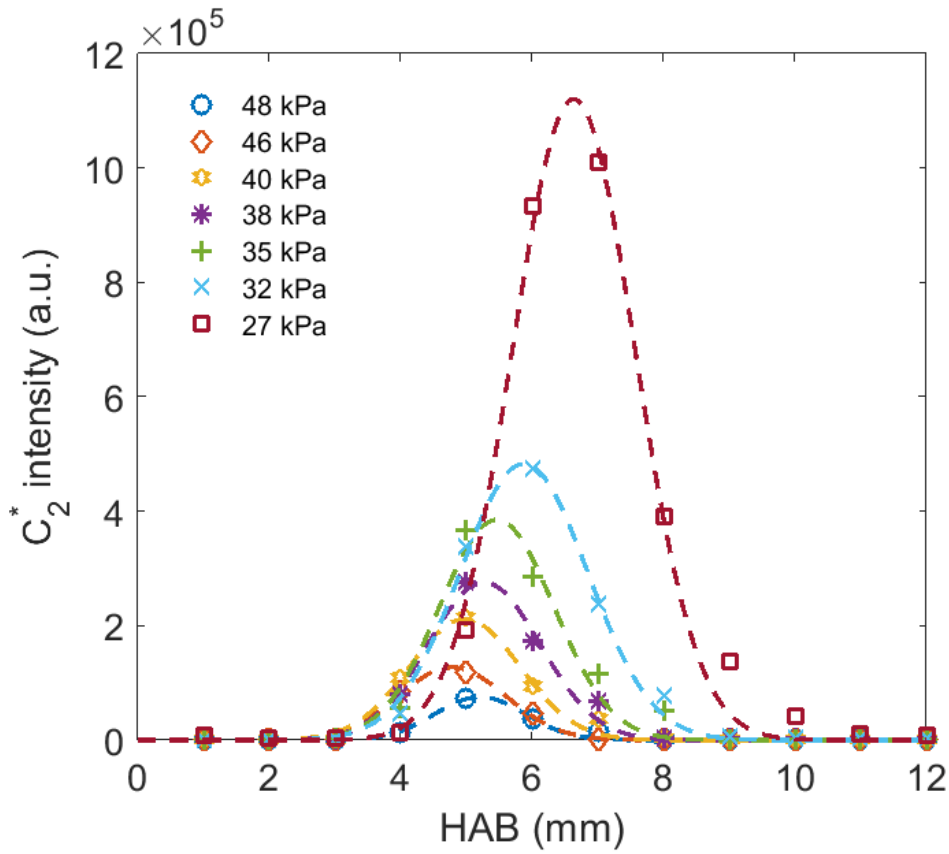


**Figure 5.4:** The intensity of  $C_2^*$  at different pressures as a function of the HAB at  $\Phi = 2.1$ .

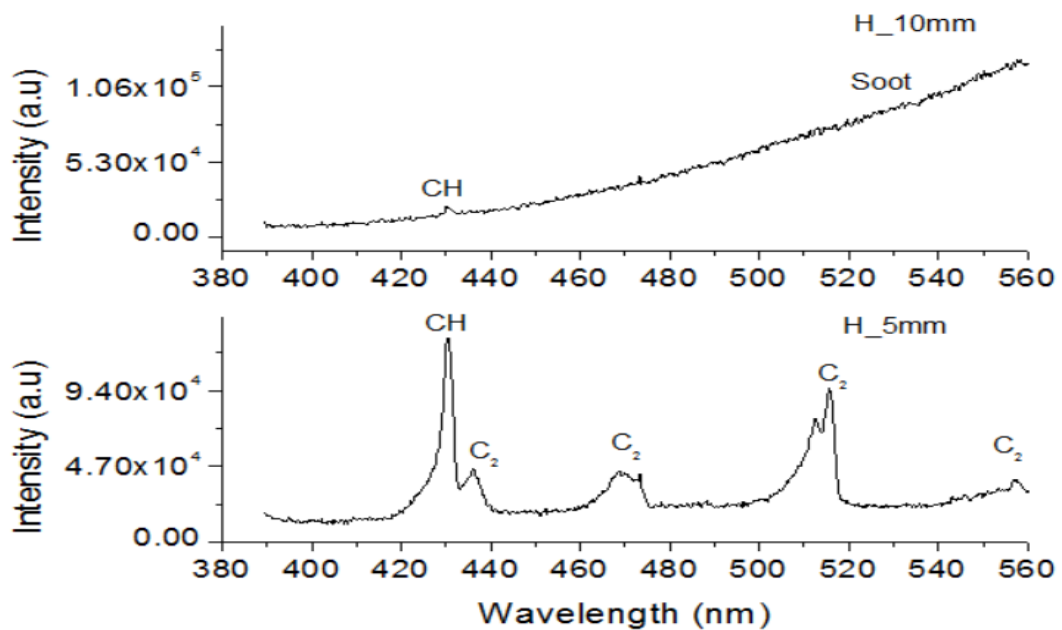


**Figure 5.5:** Flame emission at pressure 32 kPa at HAB of 5 and 10 mm, at  $\Phi = 2.1$ .

There is sufficient evidence to show that the various compounds formed from combustion varied in chemical composition, size, nanostructure and chemicals, depending on the conditions of combustion [142, 143]. The results of the laminar premixed C<sub>2</sub>H<sub>4</sub>–air flame experiments carried out under well-controlled pressure indicated a distinct presence of CH\* and C<sub>2</sub>\* excited hydrocarbon radicals. Generally, it has been noted that an increase in pressure reduces the distributional distance of the fuel material components, thus driving down the flame intensity. This was evidenced by a reduction in the intensity of the flame. Figure 5.5 demonstrates a strong presence of CH\* at 430 nm wavelength. This observation is consistent for 5 mm and 10 mm HAB. CH\* was formed as a product of a side reaction of C<sub>2</sub>H<sub>4</sub> and not from direct breakdown as expected in the combustion process, and can be used as a marker for the flame front [68].

Bimolecular reactions in the fast reaction zone could also yield CH\* radicals, which were evidenced by a blue flame colour. This reaction took place in an environment where oxygen levels were higher than specified by stoichiometric proportions. The 430-nm wavelength CH\* band was the strongest when analysed from a flame intensity point of view. The CH excited radical played a crucial role in the formation of other radicals, which influenced the outcome of the experiment in different ways [75]. There were several uncertainties in the manner in which the excitation reaction rate constants for CH\* production were evaluated [144]. Figure 5.5 shows a spectrogram of the results obtained, with C<sub>2</sub>\* bands observed in the 436–560 nm wavelength range for 5 mm HAB. These bands of excited C<sub>2</sub>\* emissions are also known as Swan bands. The degraded diatomic species of the C<sub>2</sub>\* band systems were formed as a result of the transition between triplet levels, or between singlet levels [68]. It is important to note that there was no inter-combination of any kind between the singlet and triplet levels. The wavelength of the C<sub>2</sub>\* Swan band made the flame turn an intense greenish–blue colour. The Swan band system is a core part of the triplet side system, and typically exists in the range of 435–686 nm. This means that the results obtained for the laminar premixed C<sub>2</sub>H<sub>4</sub>–air flame were consistent with previous experiments carried out. The spectral characteristics of the Swan band have been similar for a wide array of experimental sources [144]. The excitation mechanism was therefore expected to be the same, and the resultant flame colour confirmed this assumption. The C<sub>2</sub>\* radicals were formed in an experimental environment where oxygen levels were below specified stoichiometric proportions. The energy transfer process accounted for the reduction in the flame intensity at high pressure. There was no apparent difference in the wavelength of the CH\* excited radicals; hence a consistent blue flame was observed at 5 and 10 mm HAB. The C<sub>2</sub>\* Swan band was only observed in the 5 mm HAB,

while the 10 mm HAB was characterised by soot formation. Therefore, spectra-resolved emission spectroscopy can be very useful in understanding the process of soot particle formation. Figure 5.2 shows that soot particle formation increased sharply from 5 mm HAB intensity, peaking at 13 mm then beginning to decrease as the HAB increased. Of note is that the absorption became more visible as soot formation aged along the  $C_2H_4$  flame, in line with known effects of temperature on soot formation [145].

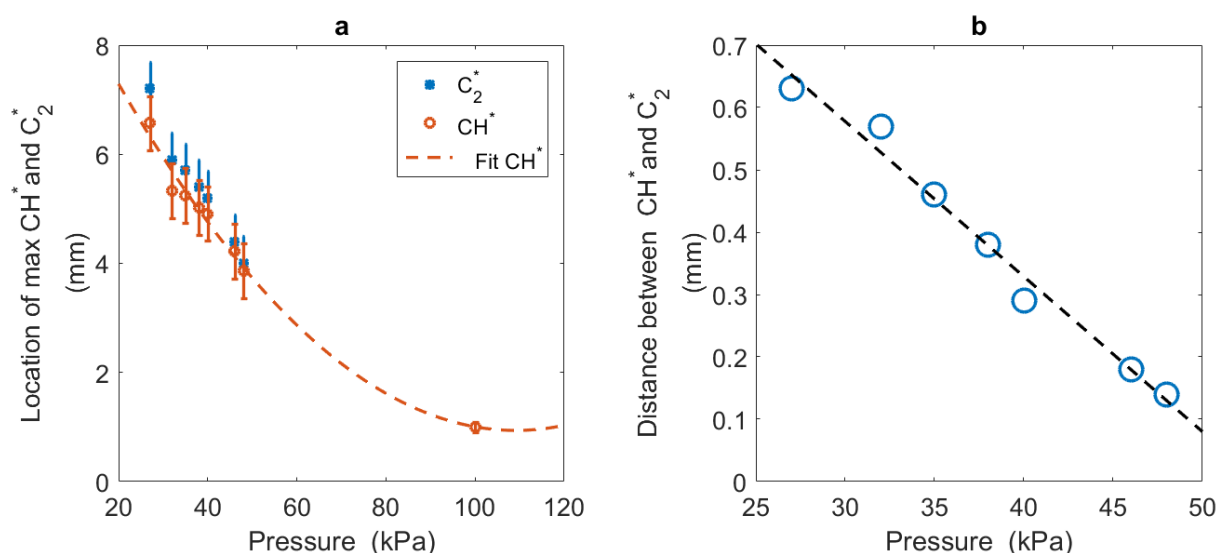


**Figure 5.6:** (a) HAB of the locations with maximum  $CH^*$  and  $C_2^*$  emission in different pressure flames; and (b) the distance between the locations with maximum  $CH^*$  and  $C_2^*$  emission at  $\Phi = 2.1$ .

$CH^*$  and  $C_2^*$  layers became thick with a decrease in pressure; they also moved away from the burner surface, as shown in Figure 5.6 (a). This figure represents data recorded with a Gaussian line of best fit for  $CH^*$  maximum emission locations HAB to help to easily correlate it to atmospheric pressure.  $CH^*$  and  $C_2^*$  layers almost overlapped each other at atmospheric pressure, while separation between them could be seen in the pressure-reduced flames, particularly for pressures less than 40 kPa. It was also interesting to find a separation between the  $C_2^*$  and  $CH^*$  layers at reduced pressures. As shown in Figure 5.6 (a), the peak strength of  $CH^*$  and  $C_2^*$  emissions appeared at different heights when the pressure was lower than  $\sim 50$  kPa, while in the atmospheric pressure flame, the peak of two layers overlapped each other. At low pressure, the peak strength of  $C_2^*$  appeared later (or higher in space) than that of  $CH^*$ , showing a distance of  $\sim 0.6$  mm at 27 kPa. Moreover, the distance between the two peaks decreased linearly with the increase in pressure: as shown in Figure 5.6 (b), intensity of  $CH^*$  and  $C_2^*$  decreased linearly with increasing



pressure with a slope of  $25 \times 10^{-9} \pm 0.062 \times 10^{-9}$  (mPa<sup>-1</sup>) indicating that the distance approached zero at 53 kPa.

### **5.1.3 Flame temperature**

#### *5.1.3.1 Gas temperature ( $T_g$ )*

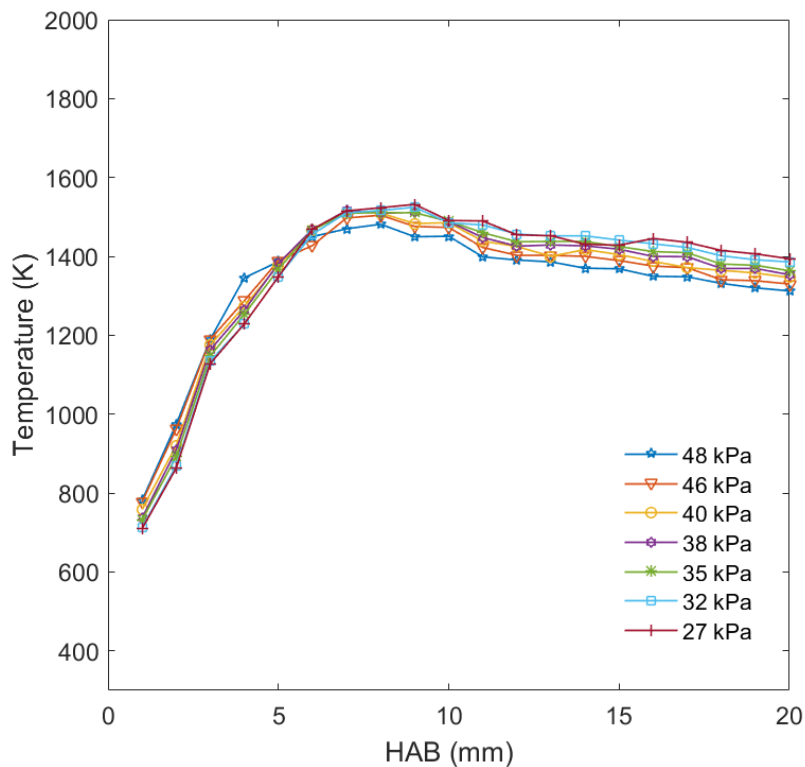
For the first method to test the pressure effect on the formation of soot, a Pt/Pt–Rh uncoated thermocouple was used to measure temperatures along the flame axis. To mitigate soot deposits on the junction, the thermocouple was rapidly swept into the blue region (soot free) of the flame and held there for 20 s. The thermocouple measurement errors must be corrected to avoid serious deviations of measured temperature values from the actual value. In this work the temperature value was corrected by the heat radiation loss method. A thin, 75  $\mu\text{m}$  diameter wire thermocouple was used to minimise conductivity and radiation effects. Catalytic effects of the junction and errors because of conduction along the wires were expected to be negligible. Further details into the radiation correction procedure are described in Chapter 3. The next step involving applying appropriate correction to account for radiation heat losses effect. The temperature correction for 46 kPa was presented on Table 5.1. The temperatures for all flames are presented in appendix B.

Table 5. 1: Axial temperature after radiation correction at 46 kPa.

HAB (mm)	Measured temperature (K)	$v_{flame}$ (m/s)	kinematic viscosity ( $m^2 s^{-1}$ )	Thermal conductivity (W/mK)	Re	Nu	$h_c$ (W/m <sup>2</sup> K)	Corrected temperature (K)
1	773	0.194	1.05E-05	0.0563	27.68	2.96	876.19	777.30
2	954	0.231	1.1E-05	0.065	31.52	3.12	1081.53	962.18
3	1174	0.278	1.2E-05	0.0768	34.81	3.26	1319.02	1189.46
4	1268	0.282	1.2E-05	0.0816	35.1	3.27	1406.89	1287.74
5	1363	0.268	1.24E-05	0.0866	32.47	3.17	1444.02	1388.69
6	1399	0.258	1.25E-05	0.0886	30.94	3.10	1446.48	1427.47
7	1464	0.251	1.26E-05	0.0923	29.76	3.05	1481.22	1497.36
8	1470	0.243	1.28E-05	0.0926	28.58	3.00	1461.08	1504.38
9	1443	0.233	1.27E-05	0.0911	27.6	2.95	1415.62	1475.94
10	1440	0.223	1.26E-05	0.0909	26.44	2.90	1387.28	1473.33
11	1392	0.212	1.26E-05	0.0882	25.29	2.84	1321.16	1422.56
12	1373	0.201	1.24E-05	0.0872	24.28	2.80	1283.31	1402.77
13	1372	0.188	1.24E-05	0.087	22.72	2.72	1246.97	1402.55
14	1369	0.176	1.24E-05	0.0870	21.28	2.64	1211.08	1400.18
15	1358	0.162	1.24E-05	0.0864	19.65	2.56	1163.39	1389.42
16	1344	0.148	1.23E-05	0.0856	18	2.47	1112.67	1375.52
17	1339	0.133	1.23E-05	0.0853	16.22	2.36	1062.14	1371.53
18	1309	0.117	1.22E-05	0.0837	14.39	2.25	992.79	1340.78
19	1305	0.101	1.22E-05	0.0835	12.44	2.12	933.93	1338.37
20	1295	0.084	1.21E-05	0.0830	10.37	1.98	863.86	1329.98

Figure 5.7 displays the corrected temperature values after correction using the heat radiation method (described in chapter 3). The measurement of temperature was undertaken along the flame axis, reaching HAB = 20 mm. An identical trend was presented by the curves that paralleled the seven pressure flames. There was a rapid increase in temperature that began from the burner surface for the first 5 mm, reaching a maximum temperature and slightly decreasing in the presence of soot. This was the result of radiation loss at elevated soot level.

An evaluation of the gas temperature was made in an attempt to define criteria for selection of the precise junction temperature and application of the procedure at different HAB while taking radiation losses into consideration. Measured temperatures in the high-pressure flames were found to be lower than those derived from low-pressure flames. Therefore, it was evident that they overlapped. Thus, the temperature field appears not to be affected by pressure in C<sub>2</sub>H<sub>4</sub> flames.



**Figure 5.7:** Temperature measured by a thermocouple for flames with different pressures and HAB at  $\Phi = 2.1$ .

### 5.1.3.2 Soot particle temperature ( $T_s$ )

Soot particle temperature was calculated by using Planck relationship over all solid angles which was extensively described in chapter 3. From Figure 5.2, soot spatially resolved emission spectra data were obtained for this calculation to generate a fitting which then was used to identify soot particles temperature. Figure 5.8 shows soot resolve spectre emission including the fitting reading for pressure setting at 32 kPa and at different high above burner.

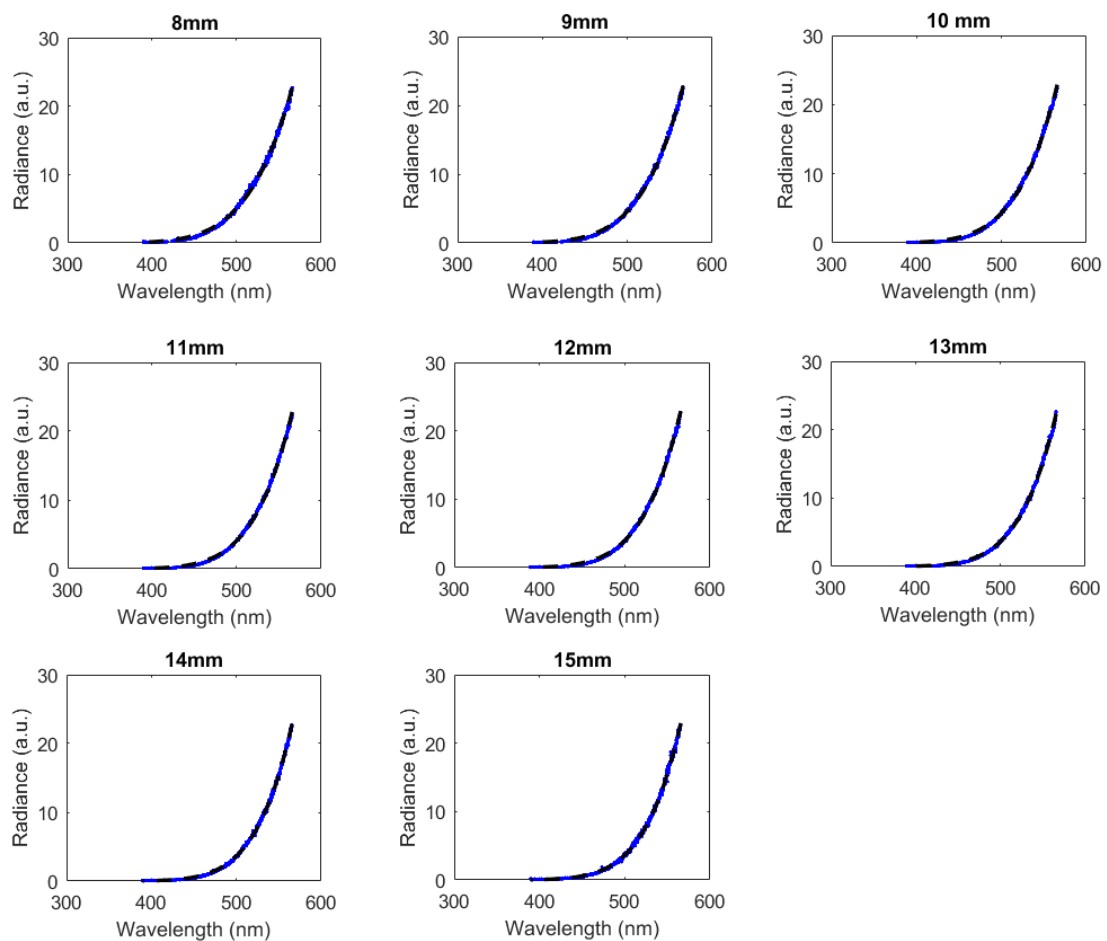


**Figure 5.8: Typical example of flame emission spectra at different HAB and pressure 32 kPa. The fitting curve, black, of the emission spectra, blue, are shown. Based on the Planck function the soot particle temperature**

Figure 5.9 presents soot particle temperature at different high above burner and for different pressure setting. An identical trend of temperature versus HAB was observed for the flames. The data below 8 mm was not reliable due to weak soot emission signal. The particle temperature decreased with the increase in HAB. Interestingly, in the soot growth region, the soot particle temperature decreased from 1500 K and appeared not to be affected by pressure.

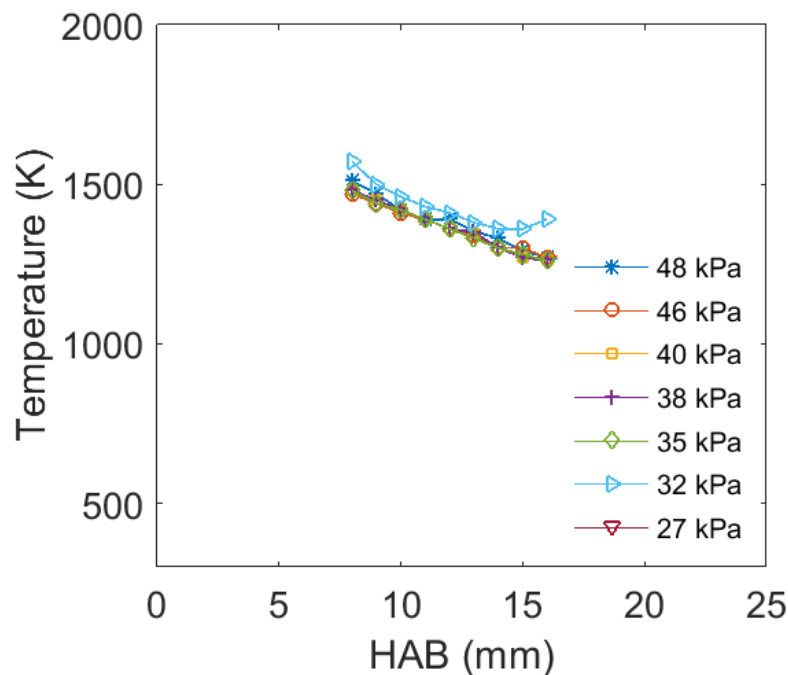


**Figure 5.9:** Soot particle temperature at different HABs and pressures at  $\Phi = 2.1$ .

### 5.1.3.3 Temperature of first soot inception

Figure 5.10 illustrates the temperature points at which soot inception was observed: the corresponding gas temperature was  $\sim 1465 \pm 66$  K. These results are similar to and consistent with observations of [143] that showed that soot inception occurs at a nearly uniform temperature of  $\sim 1600$  K. Further, similar to other research findings the first soot inception temperature seems to be independent of fuel type. Similar results were reported in previous studies. Gomez and colleagues [146] reported that the first soot inception temperature for  $C_2H_2$  varied between 1388 and 1398 K;  $C_4H_6$  varied between 1345 and 1370 K; and  $C_4H_8$  varied between 1337 and 1380 K. Saito et al. [147] reported that the first soot inception temperatures for  $CH_4$ ,  $C_2H_2$ ,  $C_2H_4$  and  $C_2H_6$  were 1390 K, 1350 K, 1385 K, 1399 K, respectively while McEnally and Pfefferle [148, 149] reported this temperature as 1600 K and 1750 K, respectively, for  $CH_4$ .

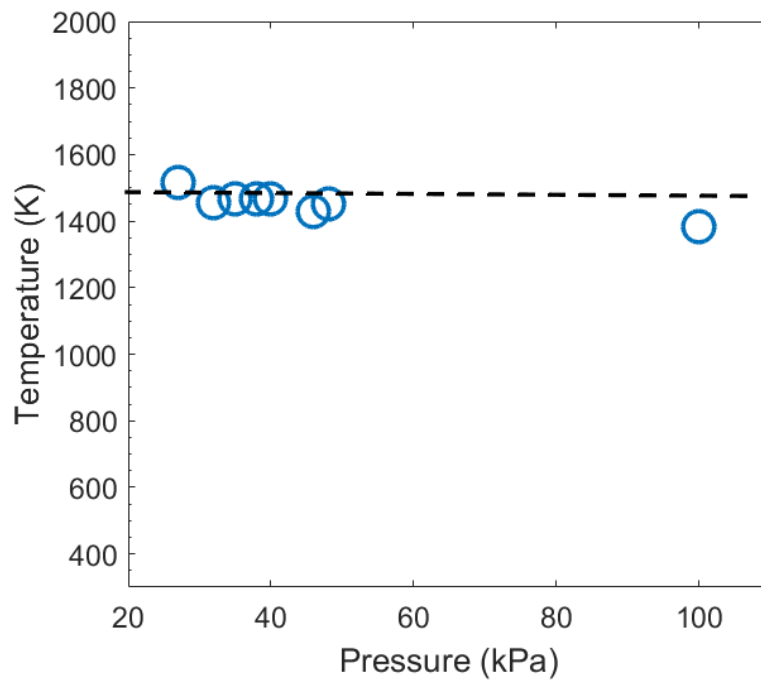


**Figure 5.10:** Temperature of first soot inception, as measured by the thermocouple, at  $\Phi = 2.1$ , the data at 100 kPa [147].

## 5.1.4 Laser-induced incandescence

### 5.1.4.1 Excitation curves relating laser signal to laser energy

From this measurement, it was possible to relate the dependence of the LII signals on laser power. The relationship between the LII signal and the excitation fluence is referred to as the excitation curve. In this study, once the flame had stabilised the relationship between the LII signal and the laser energy was investigated. The selected flame was stabilised at 46 and 38 kPa at 16 mm HAB, with an equivalence ratio  $\Phi = 2.1$ . The laser energy was varied from 32 to 132 mJ per pulse. It was seen that the LII signal was non-linearly dependent on the laser power. This finding conformed with prior literature findings [99]. The LII approach is weakly dependent on the laser's energy after a threshold has been attained [101]. The spatial distribution of laser light fluence can have a significant effect on the measured LII signal level, as shown in the excitation curves presented in Figure 5.11. Regardless of the spatial fluence profile, as the energy of the laser light increases there is an initial sharp increase in LII signal.

The stability of the flame and avoiding of soot sublimation and wing effects are the main factors that should be taken into consideration when determining the value of laser energy. According to previous investigations and observations of the optimal conditions at which the experiment should be carried out, it is important to keep the laser energy values below soot sublimation conditions. Previously studied LII profiles obtained at 60 and 100 mJ pulse<sup>-1</sup> are very close, while the LII profile obtained at high fluence (200 mJ pulse<sup>-1</sup>) is clearly distorted because of the contribution of wing effects, and likely sublimation [15]. In this study, the thickness of the laser sheet was 600  $\mu\text{m}$ , which resulted in a corresponding laser fluence of 1.3 J cm<sup>-2</sup>. This fluence was in the plateau region as can be seen in Figure 5.11. It was found that a laser fluence of 1.3 J cm<sup>-2</sup> was sufficient to maintain an adequate LII signal-to-noise ratio. Figure 5.11 presents the excitation curves relating laser signal to laser energy. These results describe the first known appearance of C<sub>2</sub>H<sub>4</sub> gas at a low pressure setting.

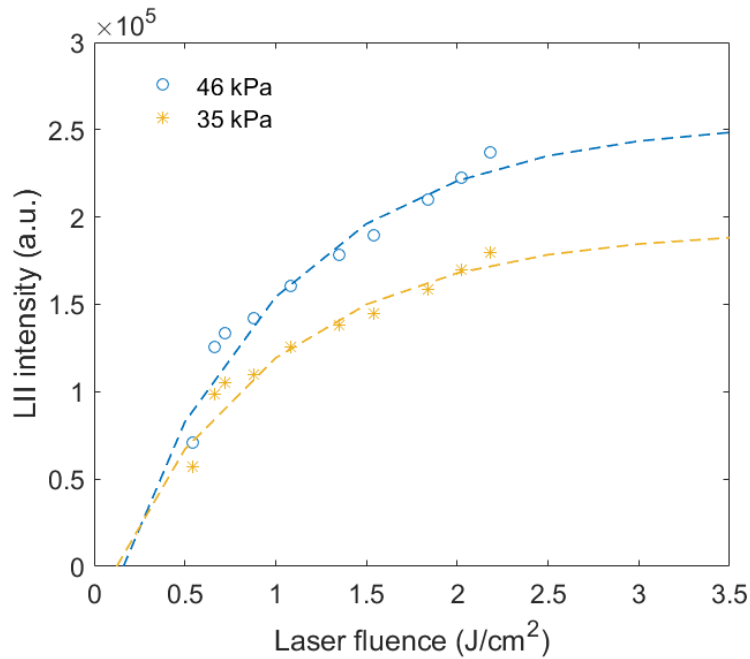


**Figure 5.11:** Laser induces Incandescence intensity as a function of incident laser fluence at HAB 16 mm under different pressures at  $\Phi = 2.1$ .

#### 5.1.4.2 The relationship between low-pressure application and soot volume fraction

The LII signal generated was measured through an ICCD camera, 200 images were recorded for each image. Figure 5.12 present the LII images for different pressure and HAB. The LII signal intensity was obtained by adding counts at each pixel, where the LII was recoded and the background subtracted. The LII signal was recorded at different HAB, by scanning the flame along HAB at positions from 1 to 5 mm, with an estimated error around  $\pm 0.5$  mm. No LII signal could be recoded, as LII appeared at  $5.50 \pm 0.5$  mm, at pressures of 48–40 kPa; while at pressures of 38–32 kPa, the LII signal began from  $6 \pm 0.5$  mm and at 27 kPa, the LII signal began from  $7 \pm 0.5$  mm. The soot volume fraction was then calculated via LII and calibration by the laser extinction method. A very weak soot volume fraction was calculated, around 0.0003 ppm at first soot inception; this value is 37% smaller than that reported by Desgroux for a CH<sub>4</sub> flame at the same pressure value with  $\Phi = 2.3$  [15].



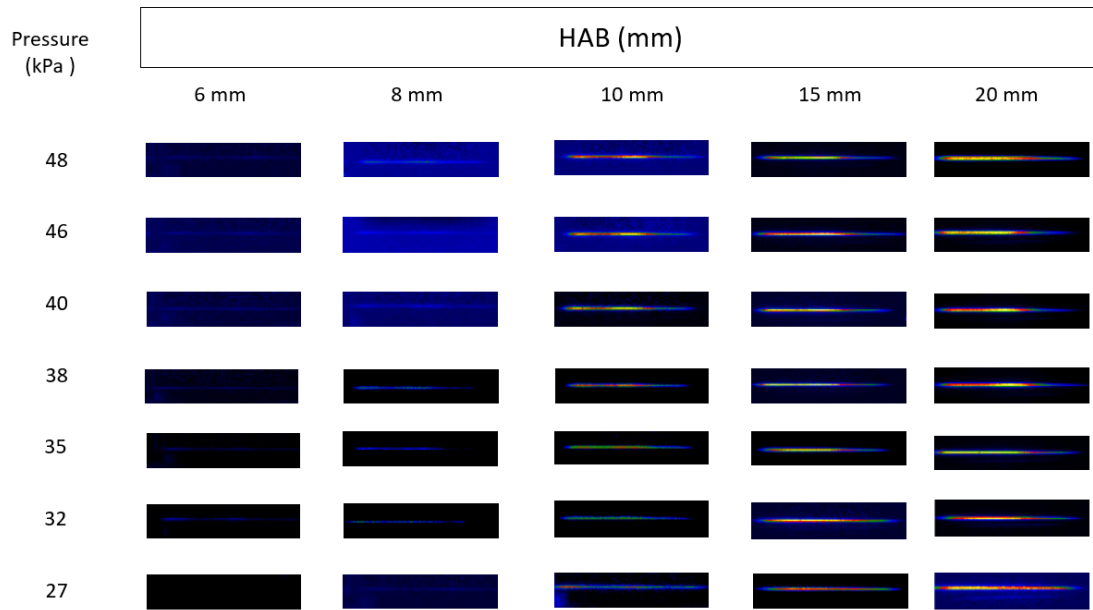


**Figure 5.12:** LII imaging set for different pressures and HAB at  $\Phi = 2.1$ .

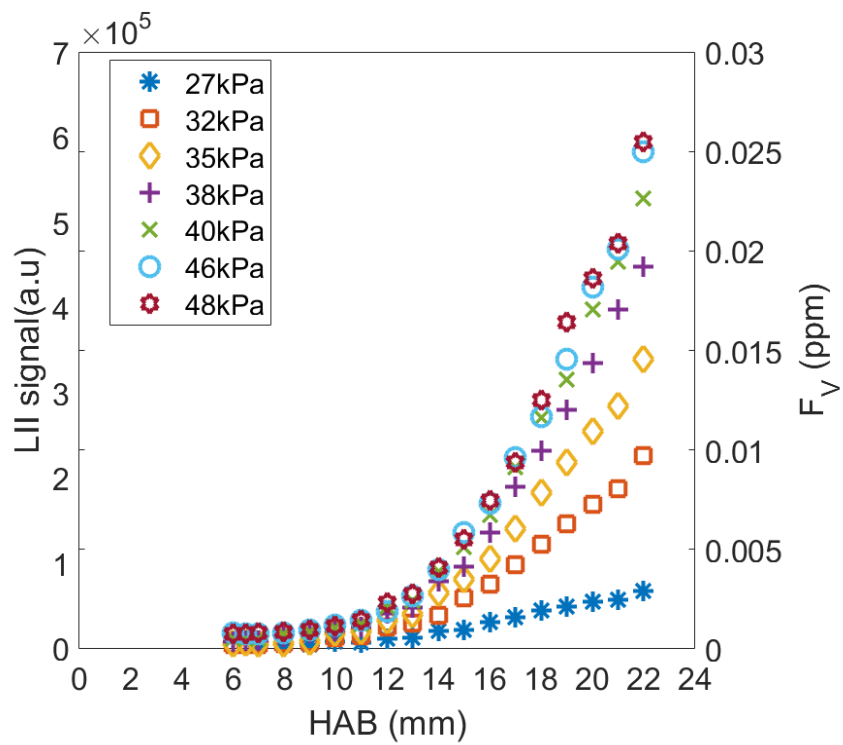


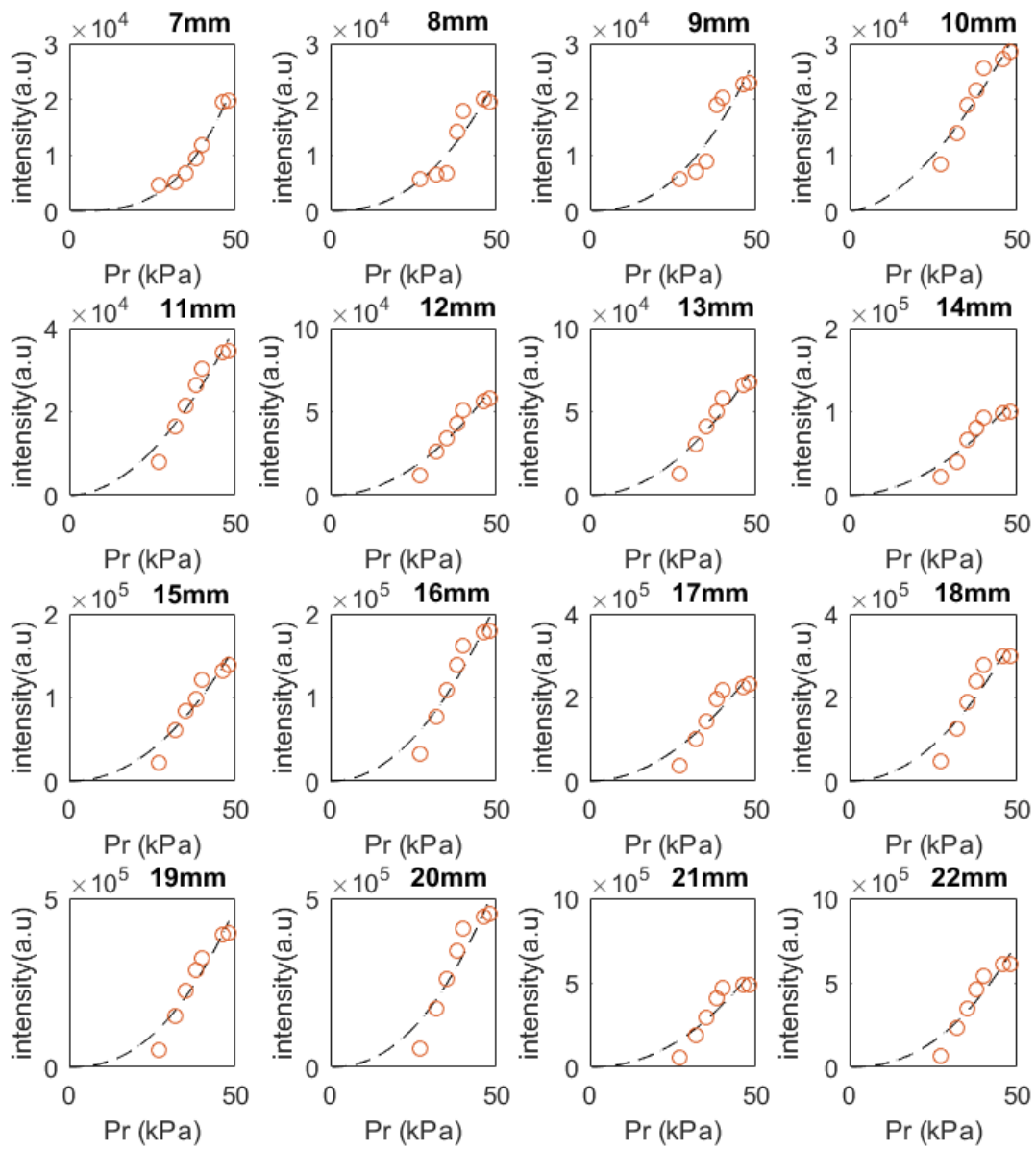
**Figure 5.13:** Soot volume fraction and LII signal along HAB with different pressures at  $\Phi = 2.1$ .

The results from the LII measurements are presented in Figure 5.13. Soot volume fractions are presented as a function of HAB; the soot volume fraction significantly increased with increasing pressure. At very low pressures the soot volume fraction was almost insignificant.

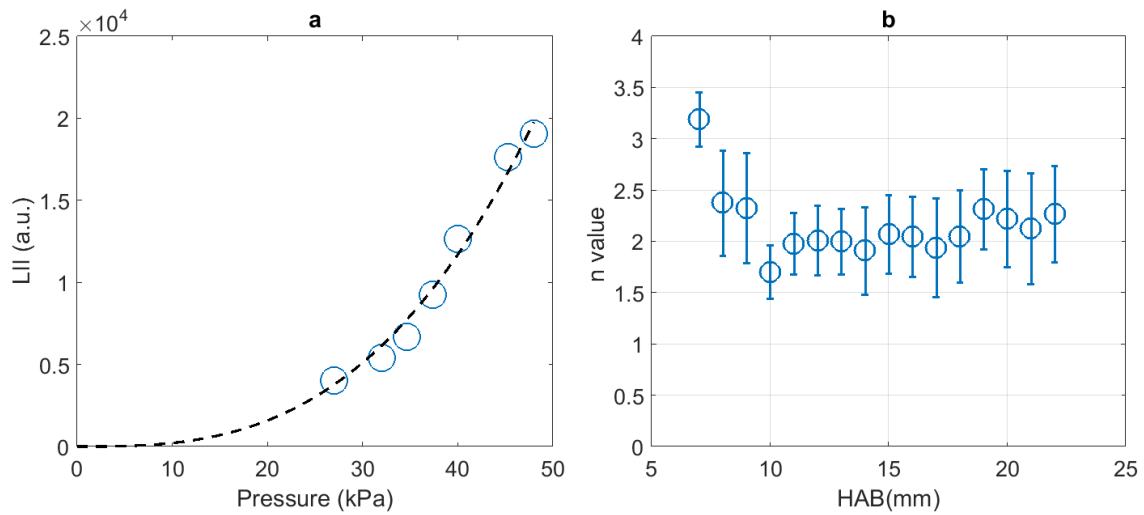
The soot volume fraction increased with increasing pressure. The LII signals indeed followed the same relationship with pressure as for soot volume fraction and attained stability at lower pressure. The relationship was found to be exponential with pressure following the pressure law, given information on the soot volume fraction,  $f_v = kP^n$ . Examples of power fit are presented in Figure 5.14 and Figure 5.15 (a).

Figure 5.15 (b) presents the pressure exponent ( $n$ ) value at different HAB. Different pressure exponent values were obtained as a result of changing the experimental parameters for LII with regard to HAB. However, a few fluctuations were visible. This specific behaviour is evident in Figure 5.15 (b). The pressure exponential ( $P^n$ ) is weakly dependent on the HAB. This slight increase in the exponential factor may also be caused by the influence of the stabiliser plate at HAB = 25 mm, which can influence the flow fields when the flames propagate to the stagnation plate.

The results of the experiment show that the LII signal scales with the pressure to the power. As the soot volume fraction,  $f_v$ , scales linearly with the LII, it was concluded that  $f_v = kP^{2.15 \pm 0.7}$  where  $k$  is the scaling factor. These findings were not very different from those reported in most previous studies.



**Figure 5.14:** LII (circles) and an exponential fit curve (dashed line).



**Figure 5.15:** (a) LII (circles) measured at HAB = 7 mm in different flames and an exponential fit curve (dashed line) with a factor of  $n$ ; (b) The exponential factors fitted at different HAB at  $\Phi = 2.1$ .

From the range of reviewed technologies and literature, it was found that the pressure exponentials employed by most previous researchers at different pressure ranges, fuel type and diagnostic technology ranged between 1.2 and 3.7. Figure 5.16 provides a summary of previous studies carried out to determine the value and variation of the pressure exponent with regard to the soot volume fraction. For  $N_2$ -diluted  $C_2H_4$  with co-flow laminar diffusion flames under high-pressure ranges, the exponent  $n$  was estimated as 1.8. using  $CH_4$ ,  $CH_4$ -air,  $C_2H_4$  or  $C_2H_4$ -air. For  $C_6H_6$ -air the pressure exponent value  $n$  was estimated as 2.0 for high-pressure ranges [99, 101, 104, 106, 108]. Karataş and Gülder [18] employed a circular co-flow burner type using an Abel-type inversion approach on a co-flow laminar diffusion flame type in their study on  $C_2H_4$  flames diluted with  $N_2$  at pressures ranging between 0 and 20 bar; they estimated the exponent  $n$  as 2.8. In [98, 100], pressure scaling was reported at the maximum volume fraction of the integrated soot with an exponent of  $n = 3.4$  estimated for laminar diffusion n-heptane and co-flow laminar diffusion propane-air flames from 1 to 3 bar. Similarly, and also in accordance with the experimental results reported here, variation in the pressure exponential function of the soot volume fraction is very high when the experiment is conducted at low pressure. This was previously reported by Desgroux *et al* [15] who subjected  $CH_4$ -oxygen to low pressure (0.2–0.28 bar) at 30 mm HAB. The referenced study has shown that the soot volume fraction varies with the pressure exponent and estimated the exponent  $n$  as 11.0 [15]. Following previous studies and in accordance with the results obtained in this research, soot volume fraction is indeed proportional to the exponential function of the pressure to which combustion is subjected. However, the value of the pressure exponent is dependent on a number of functions such as the fuel under investigation, HAB (which

results in different radiance, thus affecting carbon vaporisation and consequently soot emission), the burner used, the diagnostic method (which determines the error accrued during experimentation and hence directly determines the accuracy of approximation), the combustion pressure range zone and the type with respect to the flow and diffusion.

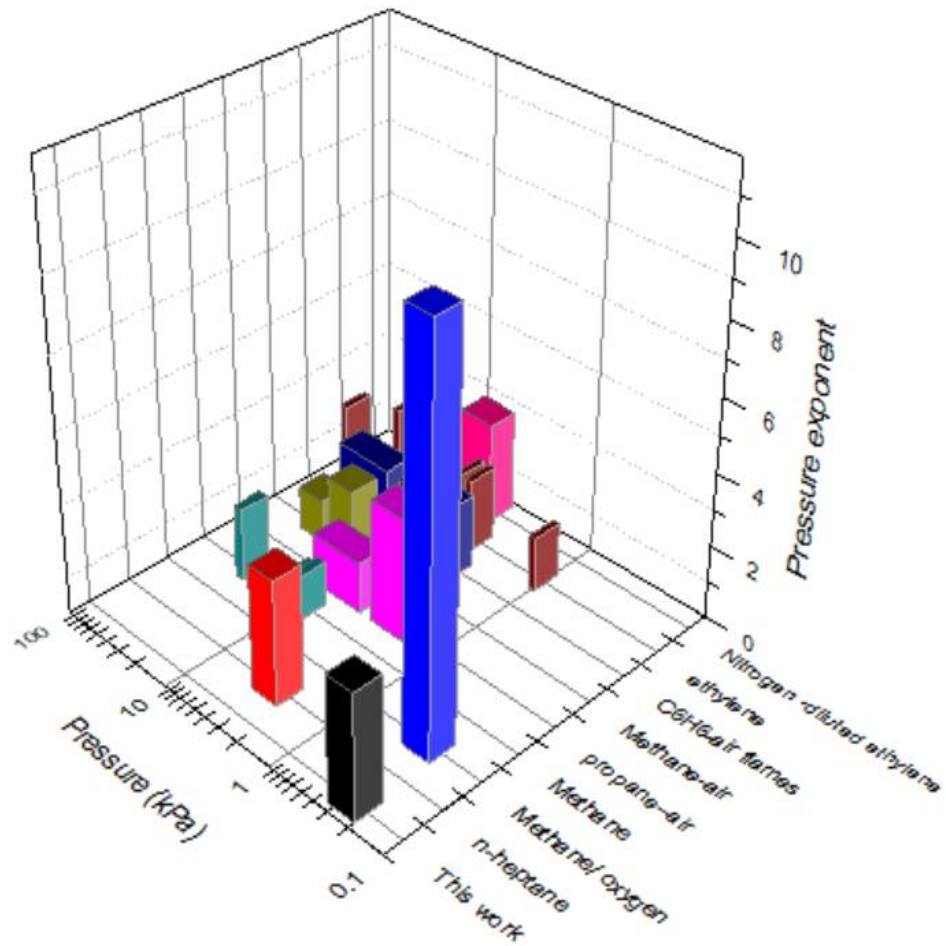


**Figure 5.16:** Summary of previous studies' pressure exponent  $n$  values in soot.

### 5.1.4.3 Reaction time

To obtain reaction time, the flame velocity was modelled by CFD as described previously (Chapter 4). The total reaction time at each high above burner level,  $t(\text{HAB})$ , was calculated using equation 5.1:

$$t(\text{HAB}=i) = \left( \sum_{\text{HAB}=0}^{\text{HAB}=i} dt_{\text{HAB}=i} \right) \quad (5.1)$$

Where;  $t(\text{HAB}=i)$  = The total reaction time at location  $\text{HAB}=i$  and  $dt_{\text{HAB}=i}$  = The local reaction time at location  $\text{HAB}=i$

The local reaction time ( $dt_{\text{HAB}=i}$ ) was calculated based on equation 2;

$$dt_{\text{HAB}=i} = \frac{x_{\text{HAB}=i+1} - x_{\text{HAB}=i}}{v_{\text{HAB}=i}} \quad (5.2)$$

Where;  $x_{\text{HAB}=i+1} - x_{\text{HAB}=i}$  is the distance between location  $x_{\text{HAB}=i+1}$  and  $x_{\text{HAB}=i}$ , which equals to 1mm, and  $v_{\text{HAB}=i}$  is the velocity at location  $\text{HAB}=i$

The calculation based on the above method is presented in table 5.2 for pressure 46 kPa.

Table 5. 2: Reaction time calculation at 46 kPa

<b>HAB (mm)</b>	<b><math>v_{\text{flame}}</math> (mm/s)</b>	<b>dt (ms)</b>	<b>Total reaction time (ms)</b>
0	72	0	0
1	194	5.15	5.15
2	231	4.33	9.48
3	278	3.60	13.08
4	282	3.55	16.63
5	268	3.73	20.36
6	258	3.88	24.23
7	251	3.98	28.22
8	243	4.12	32.33
9	233	4.29	36.63
10	223	4.48	41.11
11	212	4.72	45.83
12	201	4.98	50.80
13	188	5.32	56.12
14	176	5.68	61.80
15	162	6.17	67.98
16	148	6.76	74.73
17	133	7.52	82.25
18	117	8.55	90.80
19	101	9.90	100.70
20	84	11.90	112.60

#### 5.1.4.4 Soot surface growth

In this study, the aim was to carry out an analysis of how low pressure affects the growth of a soot volume fraction in premixed ethylene/air flames. Variables used were differential functions of soot volume fractions with respect to time ( $df_v/dt$ ).

The state of the  $f_v$  profile after the situation of soot rise has been found to follow the following first-order rate law, which was proposed by Bockhorn et al [12]:

$$df_v/dt = k_{SG}(f_v^\infty - f_v) \quad (5.3)$$

In Equation 5.3,  $f_v^\infty$  is the soot volume fraction at a vast distance away from the burner surface (i.e., plateau value) and  $k_{SG}$  is a rate constant describing the time of active soot growth. The variable  $t$  is the ‘reaction time’, which describes the progress of measurable soot formation.

In order to determine whether the pressure has some influence on  $k_{SG}$ , a graphical representation was prepared by plotting  $df_v/dt$  as function of  $f_v$  (see Figure 5.17). Figure 5.17 shows the axial profiles of  $df_v/dt$  as a function of  $f_v$  for C<sub>2</sub>H<sub>4</sub> flames stabilised at 27 and 48 kPa. Only at the lowest pressure (27 kPa), measurement of soot growth was possible. The soot surface growth rate constant  $k_{SG}$  was calculated to be 20 s<sup>-1</sup>. This is considered as 80% lower compared to the values reported in previous published literature [12, 15, 109, 150-152].

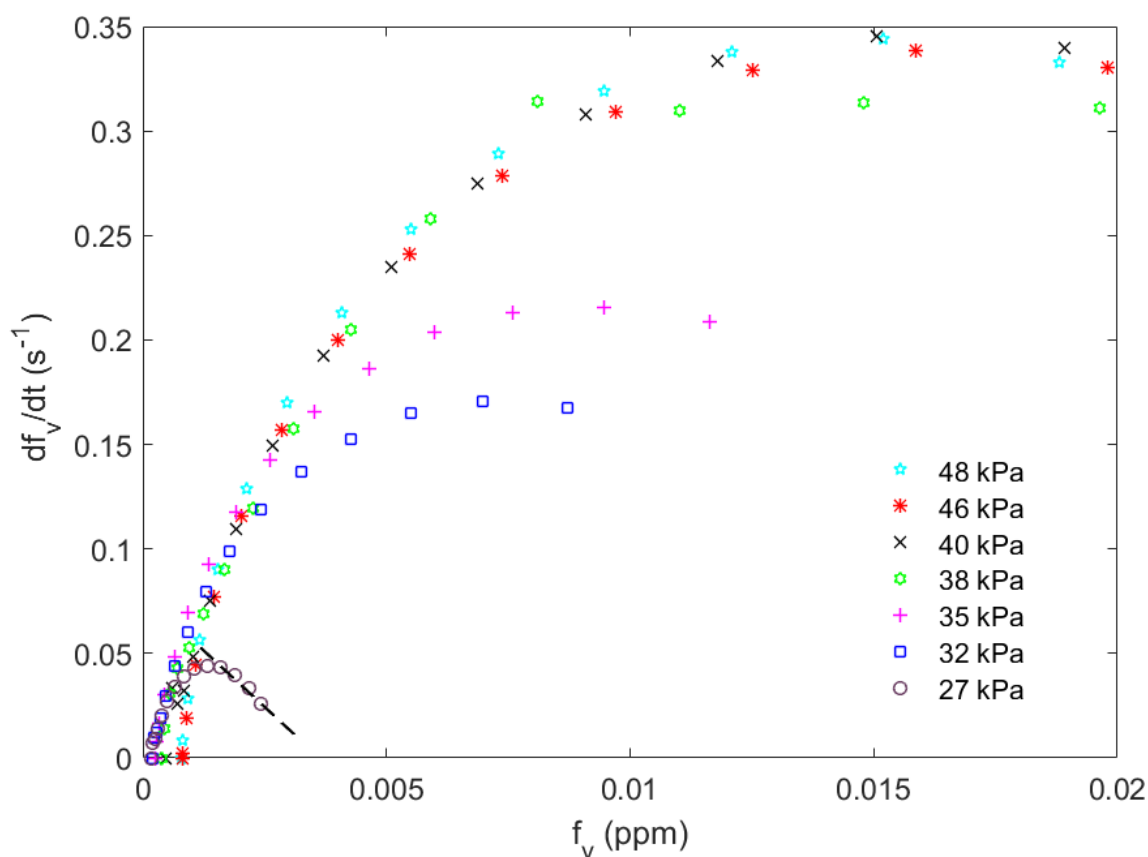


**Figure 5.17:** Derivative function  $df_v/dt$  as a function of soot volume fraction and linear fit (dashed line) at  $\Phi = 2.1$ .

### 5.1.5 Laser-induced fluorescence of PAHs

PAHs formed during burning of fossil fuels are carcinogenic [153]. Further, PAHs are precursors of soot particles, which are generally considered one of the more fundamental segments of atmospheric suspended particulate matter. The arrangement instruments of PAHs and soot have received increasing attention of late [59, 154-157]. There is some agreement regarding the route of PAH formation. For instance, the first aromatic ring is the premise of PAH growth and is essentially shaped by expansion reactions among small radical species produced from fuel pyrolysis. When just formed, the first aromatic ring can grow into bigger PAHs following the HACA mechanism [158, 159]. Some bigger PAHs can get by at flame condition and are viewed as the nucleation core of soot particles in soot models. In this way, the accuracy of soot models mostly relies on the accuracy of PAH concentration profiles.



Laser-induced fluorescence (LIF) was utilised to measure PAHs. PAH-LIF spectroscopic studies were performed at 40 kPa and 27 kPa pressure from wavelengths range of 200–700 nm. A typical spectrum of different pressure and at different HAB is presented in Figure 5.18

The emission wavelength of PAHs increases with an increase in aromatic ring number; hence, in several studies, the detection wavelength was varied to distinguish the relative sizes of PAHs. According to the quantum chemistry calculations in [125, 136], three detection wavelength bands were used to distinguish three kinds of PAHs. PAH LIF signals in the range 320–360 nm are caused by the presence of PAHs with 2–3 aromatic rings. Similarly, signals in wavelength ranging from 370 to 410 nm indicate the presence of 3-4 aromatic-ring-membered species. PAH LIF signals above 500 nm indicate the presence of PAHs with 5-membered ring structures, in which the individual rings consist of five carbon atoms. PAH LIF signals of 500–550 are indicative of the presence of 5-membered PAHs. Signal strengths qualitatively indicate the concentrations of the corresponding PAHs.

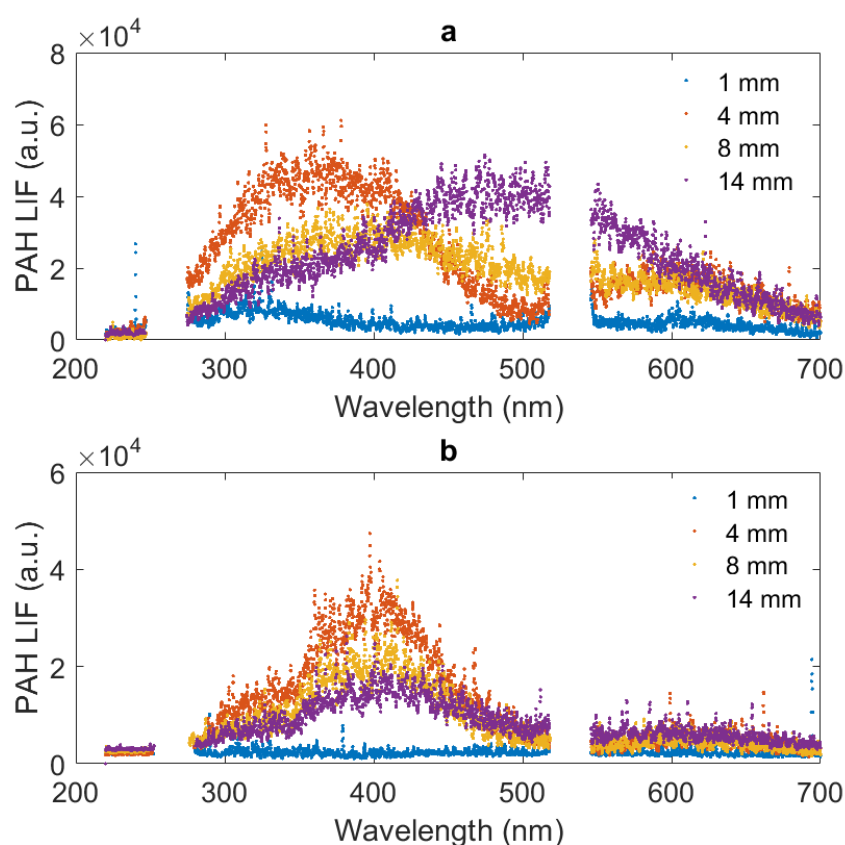


**Figure 5.18:** PAH LIF spectra for different pressure a; 40 kPa and b; 27 kPa at different HAB

Figure 5.19 (a) and (b) show the PAH LIF over HAB (1–16 mm) at pressures of 40 kPa and 27 kPa, respectively, through three wavelengths range, 320–360 nm, 370–410 nm and 500–550 nm. From Figure 5.19 (a) with pressure 40 kPa, the wavelength range of 500–550 nm resulted in lower PAH LIF at low HAB than other wavelengths range, but PAH LIF increased after HAB = 12 mm and was higher than other wavelengths range. However, in the results shown in Figure 5.19 (b) where pressure was 27 kPa, the wavelength range of 500–550 nm produced lower PAH LIF than did other wavelengths range over all values of HAB, and the wavelength range of 370–410 nm produced higher values of PAH LIF than did other wavelengths range for all values of HAB, but it decreased along HAB.

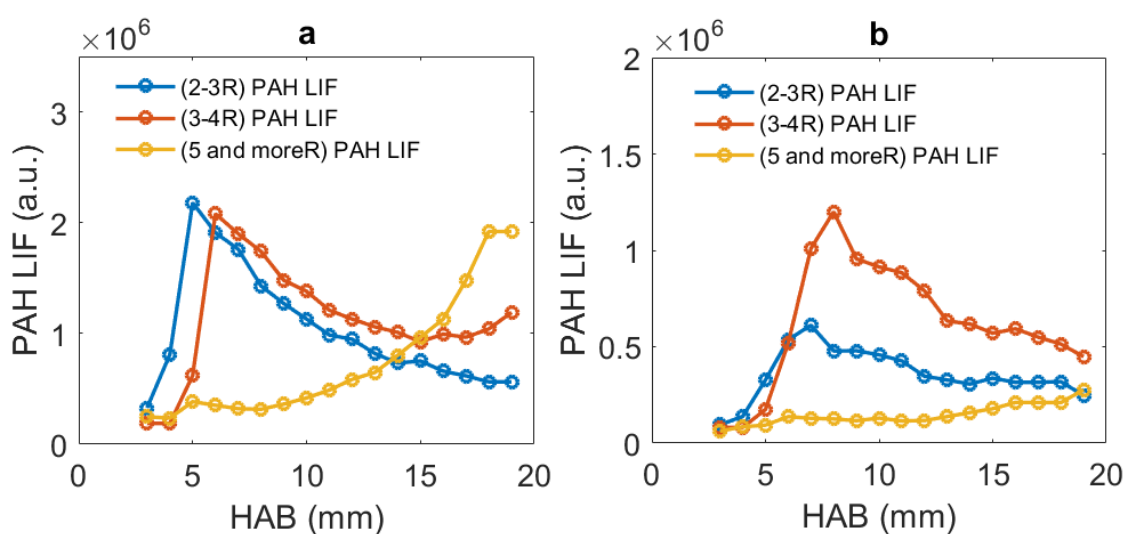


**Figure 5.19:** Three kinds of PAH LIF at different pressures; (a) 40 kPa and (b) 27 kPa.

From Figure 5.19 (a) and (b), the peak spatial distributions of (2-3R) PAH LIF were followed by the peak spatial distributions of (3-4R) PAH LIF with a difference of 1 mm HAB at both pressure settings. The peak intensity of (3-4R) PAH LIF was greater than (2-3R) PAH LIF at pressure of 27 kPa, where the peaks were close to each other at pressure 40 kPa. The spatial distribution of >5R PAH LIF signals started to form when the (2-3R) PAH LIF signals reached their peaks. It is hard to determine the peak spatial distribution of >5R PAHs LIF signals, as these signals kept increasing inside the soot growth region which indicated soot and PAHs formation.

Figure 5.20 a and Figure 5.20 b show that the signals for (2-3R) PAH LIF and (3-4R) PAH LIF attained a peak for each type of flame and then declined over time. Table 5.3 summarised the spatially phenomenological removing rate constant of PAHs with 2–3 rings ( $k_{phen}^{2-3R}$ ) and 3–4 rings

$(k_{phen}^{3-4R})$ . From this table, the  $(k_{phen}^{2-3R})$  and  $(k_{phen}^{3-4R})$  were found to be  $24.61 \text{ s}^{-1}$  and  $21.64 \text{ s}^{-1}$ , respectively, at a pressure of 40 kPa. At a pressure of 27 kPa,  $(k_{phen}^{2-3R})$  and  $(k_{phen}^{3-4R})$  were measured as  $15.29 \text{ s}^{-1}$  and  $18.26 \text{ s}^{-1}$  respectively. This indicates that  $(k_{phen}^{2-3R})$  is faster than  $(k_{phen}^{3-4R})$  by a factor of 1.14 at a pressure of 40 kPa. At a pressure of 27 kPa,  $(k_{phen}^{3-4R})$  is faster than  $(k_{phen}^{2-3R})$  by a factor of 1.19. The determination of the spatially phenomenological removing rate of soot formation was key for this study, presumably due to the PAHs being consumed to increase soot amounts [160]. This simply shows that, at low pressure, the removing rate is very slow, while at high pressure, the removing rate is much faster. At the same time, removing the different rings that form the PAHs around the soot also differs at different pressures. As seen from the experimental results, the removing rate of  $(k_{phen}^{2-3R})$  rings is lower at low pressure of 27 kPa than the removing of  $(k_{phen}^{3-4R})$  rings. This may be due to the fact that the PAHs are themselves formed at low pressures, thus the removing rate would tend to decrease with a decrease in pressure. Another reason for this could be coagulation of the gases that form the PAHs in the soot. The coagulation rates of these gases are very weak in  $(k_{phen}^{3-4R})$  at a low pressure than they are in  $(k_{phen}^{2-3R})$ . At a high pressure, the removing rate of the PAHs from the soot is higher in  $(k_{phen}^{2-3R})$  rings than in  $(k_{phen}^{3-4R})$  rings as shown in table 5.3. These factors all depend on the oxidation and reduction rate of the reactants and their coagulation rates.

It is worth noting that the PAHs removing rate constant value is close to the soot growth rate constant. This another novel finding which has not been previously reported.

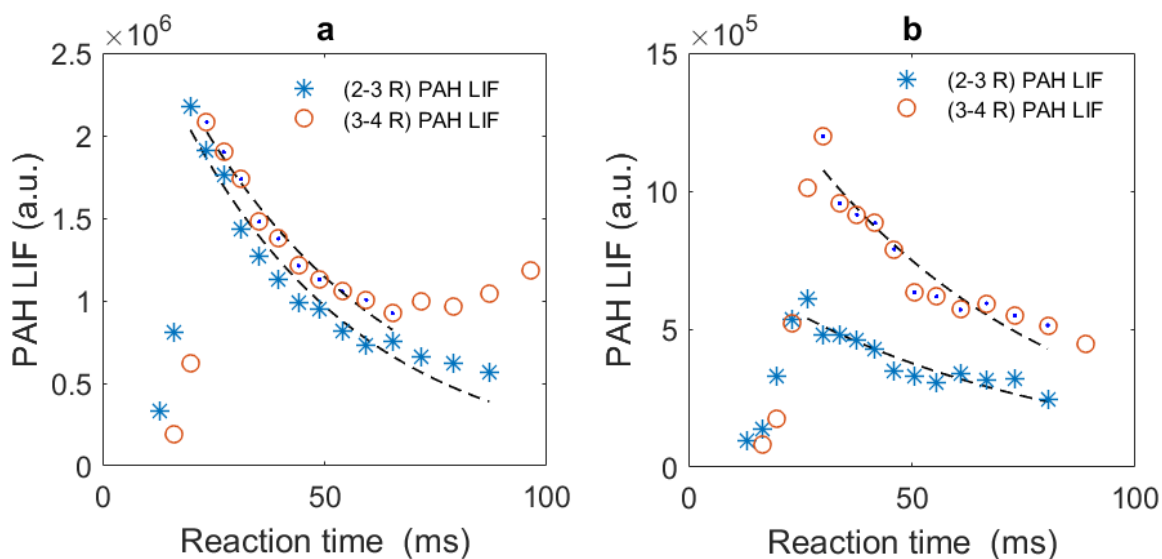


**Figure 5.20:** Different types of PAH LIF as a function of reaction time at different pressures; (a) 40 kPa and (b) 27 kPa, exponential fit curve (dashed line)

Table 5. 3: The spatially phenomenological removing rate constant of PAHs

Pressure (kPa)	Spatially phenomenological removing rate constant (s <sup>-1</sup> )	
	( $k_{phen}^{2-3R}$ )	( $k_{phen}^{3-4R}$ )
40	24.61	21.64
27	15.29	18.26

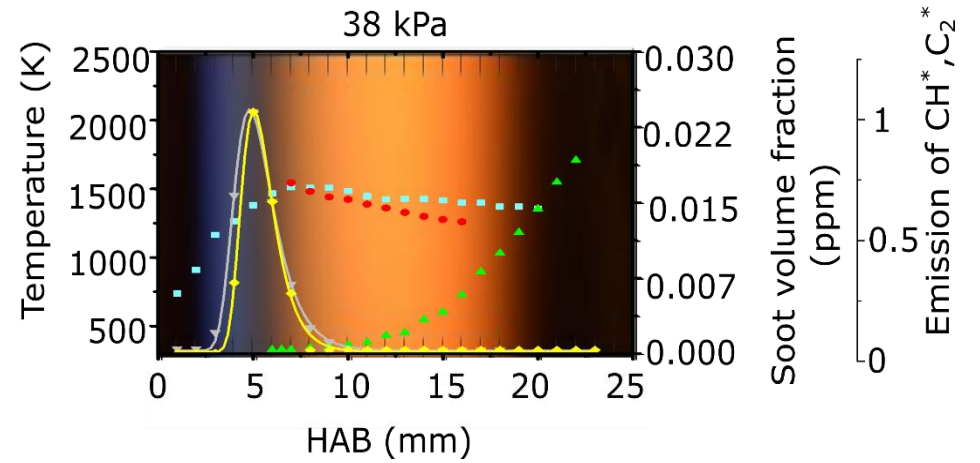
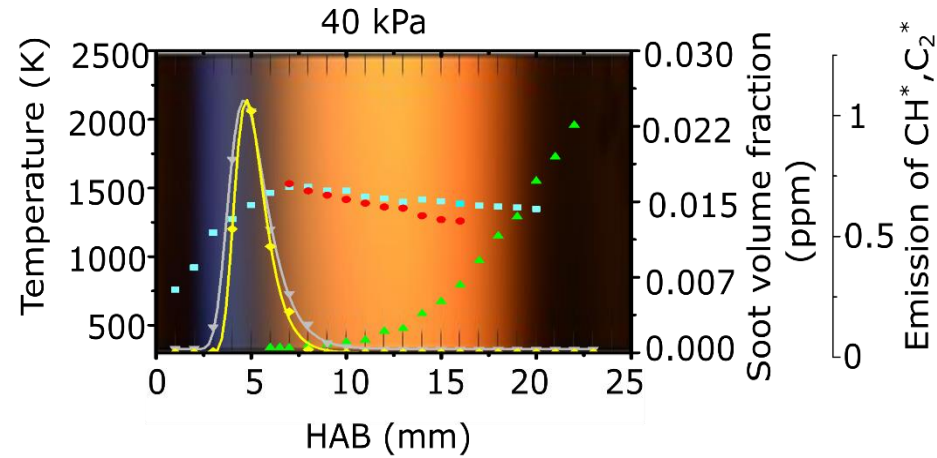
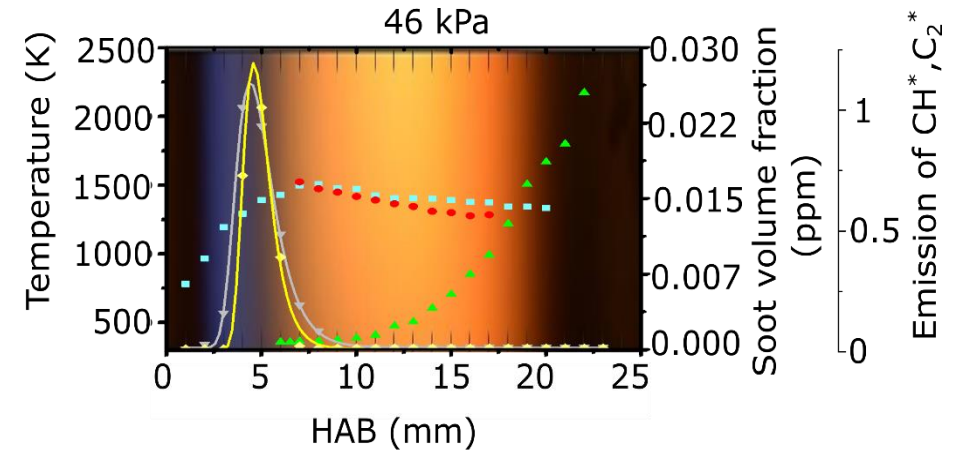
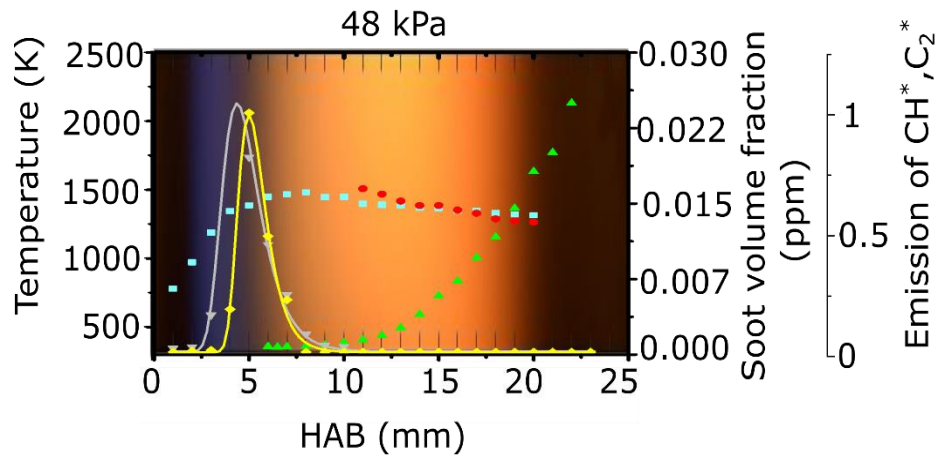
### 5.1.6 Spatial correlation among the measured parameters

Figure 5.21 presents superimposition of the parameters on the corresponding flame photographs to reveal the spatial relationships among the parameters measured. The flame photographs show four regions from the burner surface upwards to the stagnation plate: the invisible pre-combustion region; the blue region with CH\* and C<sub>2</sub>\* emissions; the yellow sooting region; and the dark sooting region with low temperature. At low pressure, for example 27 kPa, a dark yellow layer is evident above the blue layer, indicating the slow process of soot formation at low pressure.

Figure 5.21 also presents the spatial distributions of the measured parameters including the radicals, soot and flame temperature. This figure highlights the spatial relationships among these parameters. It was found that the formation of soot, which was detectable, began immediately after the peak region of the radicals. Soot particles were evidently formed within the descent region of the radical emissions, forming an overlap region of the radicals with soot. Above this region, a significant increase in soot volume fraction can be seen in Figure 5.13, indicating a higher soot formation rate than in the region of overlap with the radicals. It is notable that the flame temperature also peaks in this soot radical overlap region, indicating that this layer may be a critical region for understanding soot formation in this kind of premixed flame.

Figure 5. 21 also reveals the temperature for soot emergence; that is, the temperature at the lowest location with detectable soot in the different flames. Figure 5.10 summarises the values of flame temperature for soot emergence, revealing a critical temperature around 1465 K, and that the value of the critical temperature for soot formation decreases slightly with pressure.





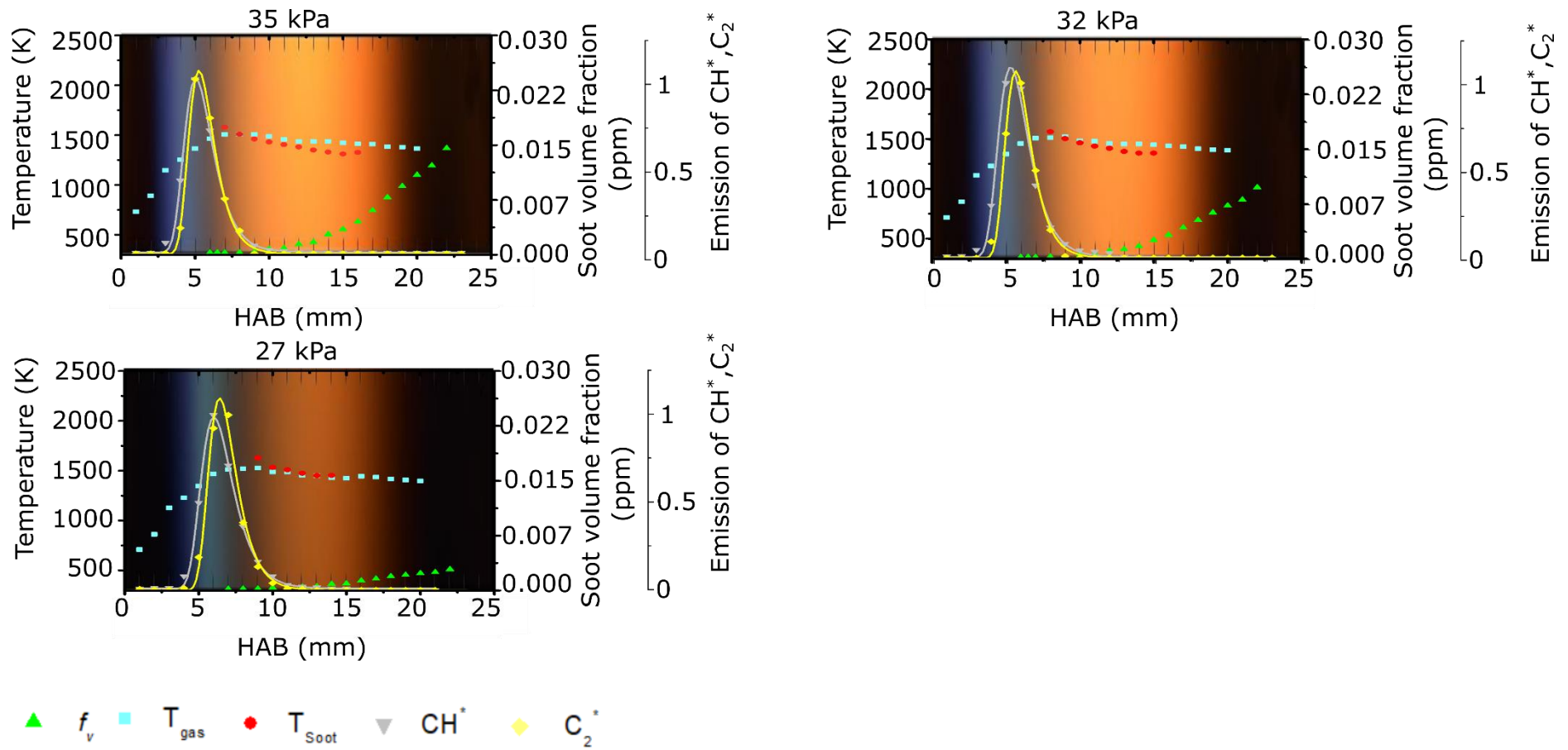
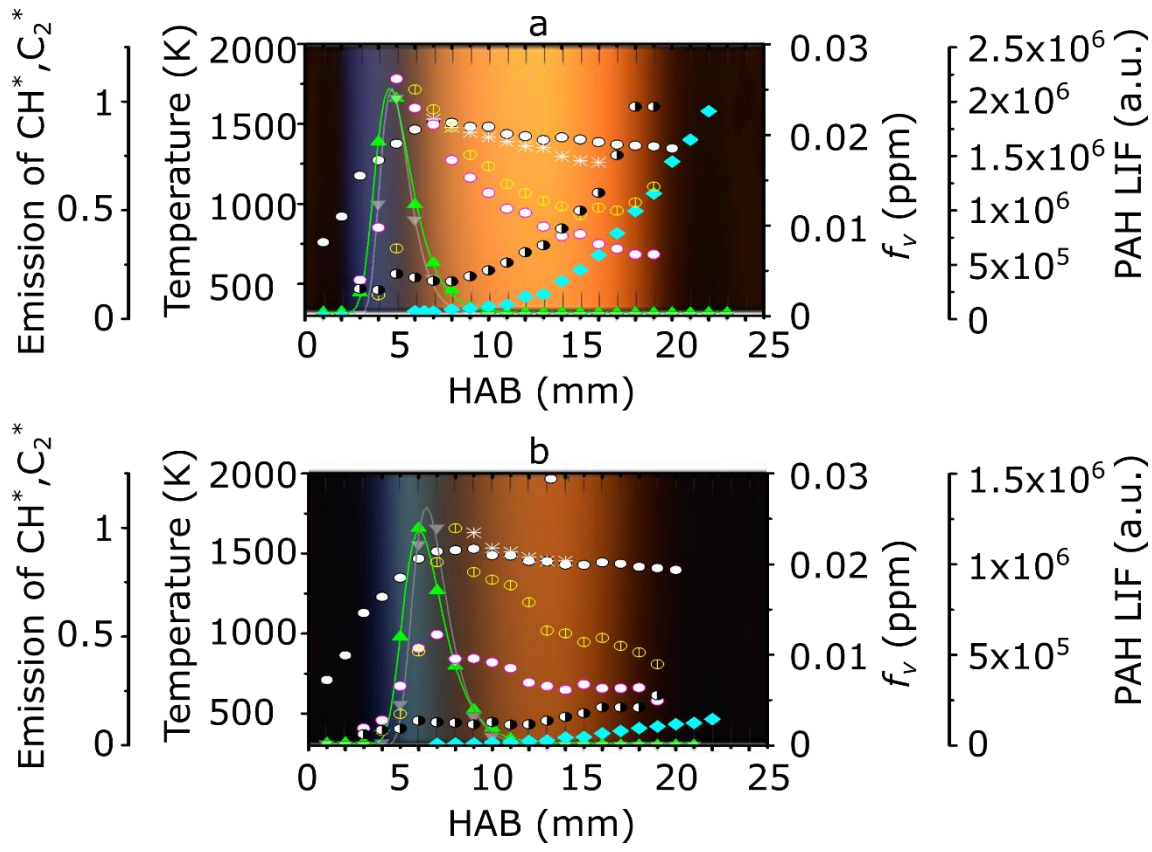


Figure 5.21: Superimposition of the measured profiles for  $f_v$ , normalise  $CH^*$  and  $C_2^*$  emissions,  $T_s$  and  $T_g$  onto flame photographs.

Figure 5.22 illustrates superimposition of the measured profiles onto the flame photograph, including flame and soot temperatures,  $\text{CH}^*$  and  $\text{C}_2^*$  emissions, soot volume fractions and PAHs at  $\Phi = 2.1$  for pressures of 40 and 27 kPa. For the most part, the profiles display a regular pattern: the beginning of soot formation at some separation downstream of the burner, trailed by enduring ascent because of surface and coalescence growth, culminating in a plateau region. Here, particle growth ceased even though the concentration of  $\text{C}_2/\text{CH}$  as a representative growth species was resolved to be very high in the burnt gases of comparable flames. This has been ascribed to a lessening in soot particle activity [161].

The superimposition of the measured profiles was summarised on Table 5.4. The distance between the max intensity of  $\text{CH}^*$  and the max intensity of  $\text{C}_2^*$  is  $\sim 1$  mm as discussed at the beginning; the max intensity of  $\text{C}_2^*$  had a peak at the same value of HAB as did the max intensity of PAHs with (2-3R) PAH LIF. The correlation has been observed for the first time and may be useful in understanding soot formation. However, it was found that the maximum peak for (2 - 3R) PAH LIF occurred before the maximum for (3 - 4R) PAH LIF, at  $\sim 1$  mm. PAHs with 5 or more rings are formed at the same peak as (2 - 3R) PAH LIF; thus, it is difficult to identify the location of PAHs with 5 or more rings as the signal increased in the region of soot growth, indicating the signal included emission from both soots particles and PAHs.





### legend

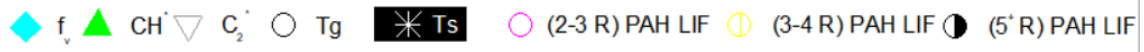


**Figure 5.22:** Superimposition of measured profiles for  $f_v$ , PAH LIF, normalised of  $\text{CH}^*$  and  $\text{C}_2^*$  emissions,  $T_s$  and  $T_g$  onto the flame photographs at different pressure; (a) 40 kPa and (b) 27 kPa.

Table 5. 4: Superimposition of the measured profiles

Chemical species	Spatial location Max intensity (mm)	
	40 (kPa)	27 (kPa)
$\text{CH}^*$	4	6
$\text{C}_2^*$	5	7
(2-3 R) PAH LIF	5	7
(3-4 R) PAH LIF	6	8
Soot inception	$6 \pm 0.5$	$8 \pm 0.5$

## 5.2 Summary

Flame structures for a quasi-one-dimensional laminar premixed C<sub>2</sub>H<sub>4</sub>–air flame burnt on a McKenna burner at  $\Phi$  of 2.1 were studied experimentally using optical methods. The work described in this chapter was based on the study of the dependence of soot particle formation on pressure in the range of 48–27 kPa.

Soot volume fractions ( $f_v$ ) were measured using LII, and the spatial distribution of two key radicals (CH\* and C<sub>2</sub>\*) was measured via chemiluminescence in the soot inception region with a spatial resolution of 1 mm along the flame height. Soot particle temperature ( $T_s$ ) was evaluated by fitting spectrally resolved soot luminosity, while flame gaseous temperature ( $T_g$ ) was measured using a thermocouple. PAHs were measured via LIF taking advantage of the extended flame structure at low pressure. Thus, the spatial profiles of CH\*, C<sub>2</sub>\*,  $f_v$ , PAH LIF, and temperature as a function of the HAB, were well resolved.

From the measurements performed under different premixed conditions the following conclusions were drawn:

- The distance between  $CH_{max}^*$  and  $C_{2_{max}}^*$  decreased linearly with increasing pressure with a slope of  $-25 \times 10^{-9} \pm 0.062 \times 10^{-9}$  (mPa<sup>-1</sup>).
- The soot volume fraction followed a power function with pressure; that is,  $f_v = kp^n$  and  $n = 2.15 \pm 0.7$ . It was also found that the value of  $n$  was weakly dependent on the HAB.
- The gas temperature and soots particles temperatures agreed very well within  $\pm 70$  degree.
- A common temperature of  $1465 \pm 66$  K was found at the early stage of soot inception (i.e., where with  $f_v = 0.3$  ppb). This is then termed as soot inception temperature. The results were similar and consistent with the observations at atmospheric pressure [147].
- The soot surface growth rate  $k_{SG}$  was calculated to be  $20 \text{ s}^{-1}$ . This is 80% lower than previously published values recorded at elevated pressure [109, 150], atmospheric pressure [151, 152] and low pressure [12, 15].
- From the PAH LIF study, three wavelength ranges were selected to identify the number of PAH rings: 320–360, 370–410 and 500–550 nm, to identify PAH LIF with 2–3 rings, PAH LIF 3–4 rings and PAH LIF 5<sup>+</sup> rings, respectively. It was found that the maximum value for (2–3R) PAH LIF occurred at  $\sim 1$  mm before the maximum value of (3–4R) PAH LIF.
- For the first time, it was observed that the location of maximum (2–3R) PAH LIF coincided with the location of maximum of intensity of C<sub>2</sub>\* for all measurements.

- The spatially phenomenological removing rate of PAHs with 2–3 rings ( $k_{phen}^{2-3R}$ ) and 3–4 rings ( $k_{phen}^{3-4R}$ ), ( $k_{phen}^{2-3R}$ ) and ( $k_{phen}^{3-4R}$ ) were found to be 24.61 s<sup>-1</sup> and 21.64 s<sup>-1</sup>, respectively, at pressure of 40 kPa. At pressure of 27 kPa ( $k_{phen}^{2-3R}$ ) and ( $k_{phen}^{3-4R}$ ) were measured as 15.29 s<sup>-1</sup> and 18.26 s<sup>-1</sup> respectively. This indicates that ( $k_{phen}^{2-3R}$ ) is faster than ( $k_{phen}^{3-4R}$ ) by factor of 1.14 at pressure 40 kPa, where at pressure 27 kPa ( $k_{phen}^{3-4R}$ ) is faster than ( $k_{phen}^{2-3R}$ ) by factor of 1.19.
- The value of the PAH removing rate, 18.26 s<sup>-1</sup>, was found to be almost identical to the soot growth rate, 20 s<sup>-1</sup>.

## Chapter 6: Premixed Ethylene-Air at $\phi$ 2.3

As in the previous chapter, soot formation was studied in the experiments reported in this chapter within laminar premixed  $C_2H_4$ -air flames along different HAB and with chamber pressure operating at different pressure from 27 kPa to 48 kPa, but this time with an equivalence ratio of  $\Phi = 2.3$ . In this pressure range, the soot volume fraction ( $f_v$ ), the location of the flame front ( $y^{ff}$ ), PAH LIF, the gas temperature ( $T_g$ ) and soot particle temperature ( $T_s$ ) were carefully measured.

### 6.1 Results and Discussion

#### 6.1.1 Low pressure flames photography

A steel plate was employed at a height of 25 mm to stabilise the flames, and the chamber pressure varied between 27 and 48 kPa with an equivalence ratio of  $\Phi = 2.3$ . Figure 6.1 presents a series of photographs that record the flames in the experiment. It was found that soot luminosity decreased with a decrease in pressure, as in the experiments presented in Chapter 5. This is also consistent with the results presented by Desgroux and others [15, 132]; the study of soot formation is affected by many factors at low pressure. The soot volume fraction in these pressure conditions for  $CH_4$  fuel is dependent upon both the pressure and equivalence value,  $\phi$  [15, 132].

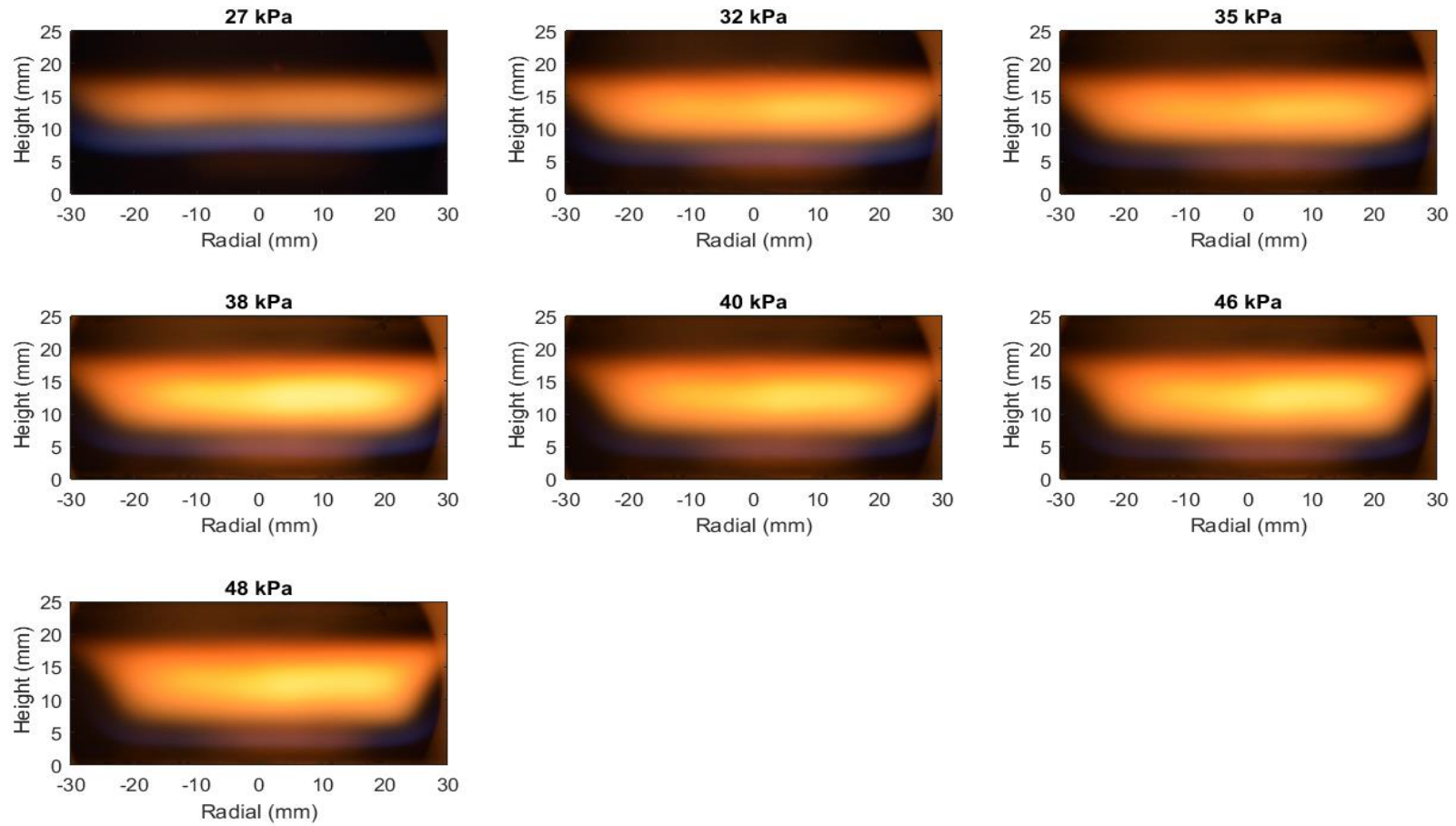


**Figure 6.1:** Photographs of flat rich premixed laminar flames at different pressures, at  $\Phi = 2.3$ .

## 6.1.2 Spatially resolved emission spectra of CH\* and C<sub>2</sub>\* radicals

At HAB of 0–23 mm with increasing steps of 1 mm, at each height 200 spectra were collected and averaged. Typical spectra are shown in Figure 6.2.

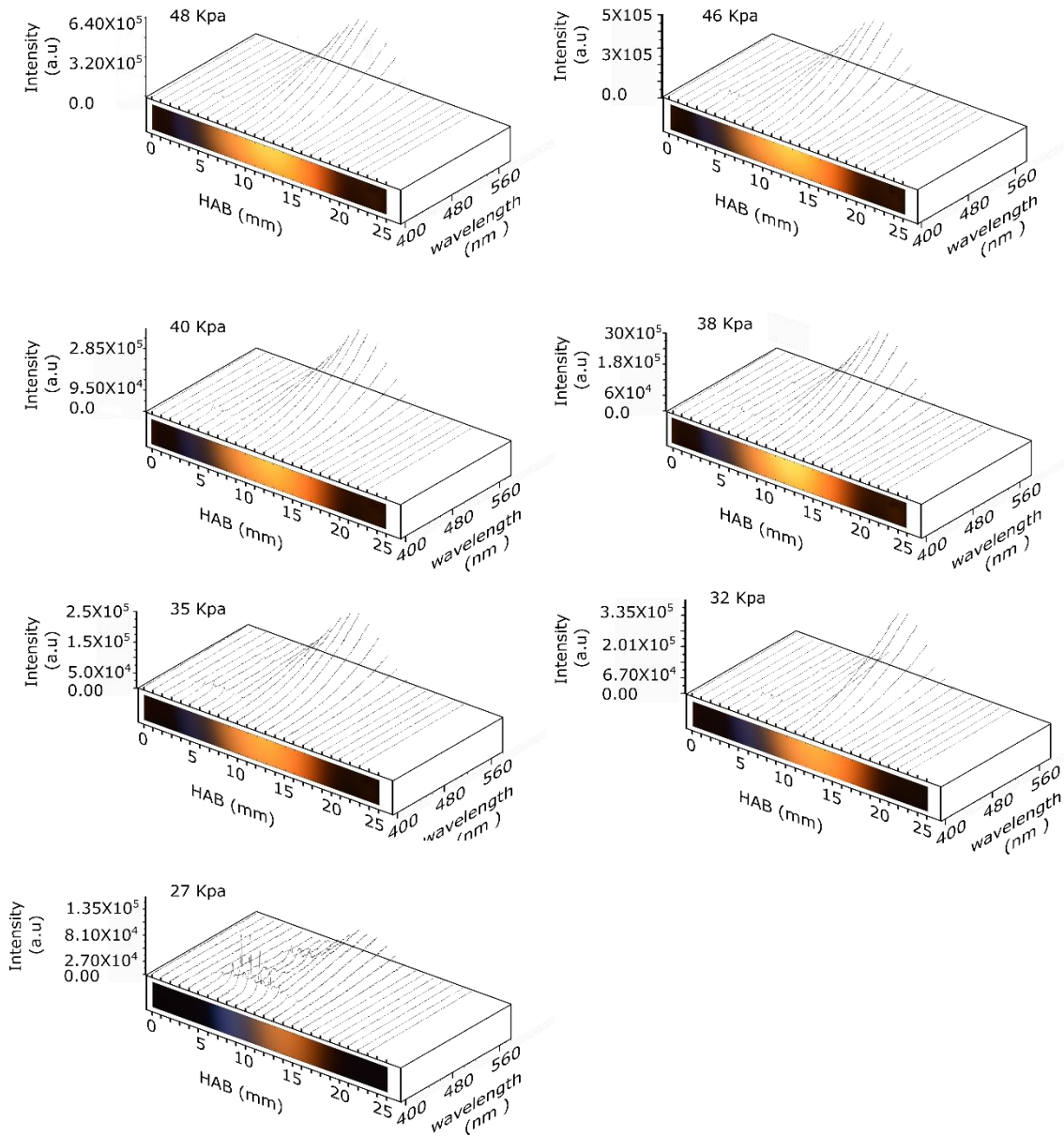


**Figure 6.2:** Flame photographs and spatially resolved emissions spectra recorded at  $\Phi = 2.3$  for different pressures.

The  $\text{CH}^*$  chemiluminescence ranged from 418 to 430 nm, and the  $\text{C}_2^*$  was from 500 to 525 nm. Figure 6.2 presents the emission spectra for laminar  $\text{C}_2\text{H}_4$ -air premixed flames under low-pressure conditions from 48 to 27 kPa with an equivalence ratio of  $\Phi = 2.3$ . At a pressure of 48 kPa, for  $\Phi = 2.3$ , there was a slight difference in the early formation of  $\text{CH}^*$  compared with  $\Phi = 2.1$ , when the  $\text{CH}^*$  radical started to form at 3 mm, and the  $\text{C}_2^*$  radical was seen at 4 mm. At a pressure of 46 kPa and  $\Phi$  of 2.3, the spectra were similar to those of 48 kPa: other than differences in the intensity value, mean and the spectra profile (from where the radical started), these spectra were the same. At 40 kPa pressure, in contrast,  $\Phi = 2.3$  produced the same spectra but with a different form of  $\text{CH}^*$  than  $\Phi = 2.1$ , when it began to form at 3 mm and ended at 9 mm and of  $\text{C}_2^*$ , which started at 4 mm and ended at 6 mm. At pressures of 38 kPa, the  $\text{CH}^*$  formed at 3 mm and the  $\text{C}_2^*$  started to form at 4 mm. It emitted a clear signal and the peak increased up to a height of 5 mm. At this height, soot emission was shown beside  $\text{CH}^*$  and  $\text{C}_2^*$  radicals. The  $\text{C}_2^*$  vanished at 6 mm, as was seen for  $\text{CH}^*$  at this height and soot emission. Then, the peak of  $\text{CH}^*$  diminished until a height of 9 mm was reached, where on the high only the emission of the soot profile was evident, and then decreased until it reached 13 mm, and then further until the signal disappeared at 17 mm. At 35 kPa for  $\Phi = 2.3$ , there was a slight difference from  $\Phi = 2.1$  in that at  $\Phi = 2.3$  the  $\text{CH}^*$  radical started to form at 4 mm, and the  $\text{C}_2^*$  radical was shown at 5 mm. At 31.99 kPa, the  $\text{CH}^*$  started from 4 mm and disappeared at 11 mm, whereas  $\text{C}_2^*$  began at 5 mm and ended at 8 mm, and soot emission began at 6 mm. At a pressure of 27 kPa,  $\text{CH}^*$  was formed at 5 mm, and at 6 mm the peak of  $\text{C}_2^*$  was evident beside the  $\text{CH}^*$  (it was very clear). Also, these peaks increased until a height of 10 mm, where the emission of the soot profile appeared beside the  $\text{CH}^*$  and  $\text{C}_2^*$  radicals. Subsequently, the peak of  $\text{C}_2^*$  diminished until a height of 11 mm, and the  $\text{CH}^*$  peak decreased until the value was not observable. Finally, at 17 mm, there was no signal under these conditions.

#### 6.1.2.1 Excited $\text{CH}^*$ radical

The intensity of  $\text{CH}^*$  chemiluminescence was presented as recorded data with a Gaussian line of best fit to describe and differentiate data from different pressure settings. This is shown in Figure 6.3 as a function of the HAB at  $\Phi = 2.3$ . At the 27 kPa pressure point, the highest intensity for spectra was noted at 9 mm with a large separation from the second height point pressure ( $\sim 3 \times 10^5$ ) at 48 kPa. At pressures of 46 and 48 kPa,  $\text{CH}^*$  chemiluminescence reached its peak at 5 mm (fast reaction HAB). The intensity became constant at zero from around 15 mm HAB.

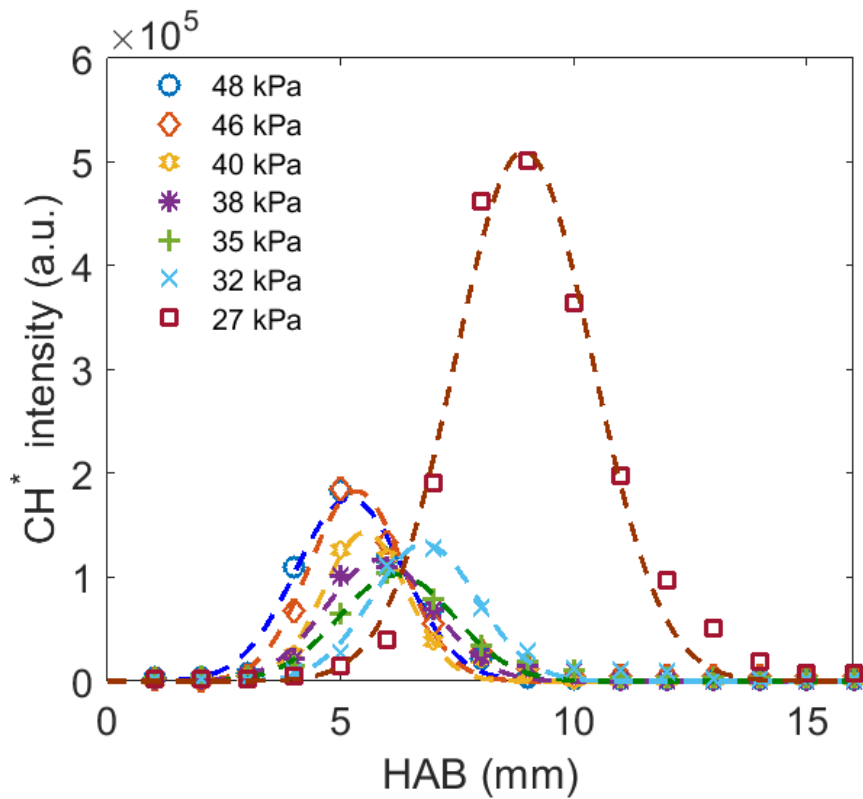


**Figure 6.3:** The intensity of  $\text{CH}^*$  at different pressures as a function of the HAB at  $\Phi=2.3$ .

#### 6.1.2.2 Excited $\text{C}_2^*$ radical

Figure 6.4 presents the recorded data of the intensity of  $\text{C}_2^*$  with a Gaussian line of best fit to describe and differentiate data from different pressure settings as a function of HAB at  $\Phi = 2.3$ . A spike in intensity was noted at 46 kPa of pressure at 5 mm HAB. The levels of intensity were considerably different at greater HAB. Increasing the pressure resulted in the compaction of the fuel components, which then led to reduced flame intensity regardless of the HAB. At 9 mm HAB, a pressure setting of 27 kPa had a maximal intensity reading compared with other pressure settings.



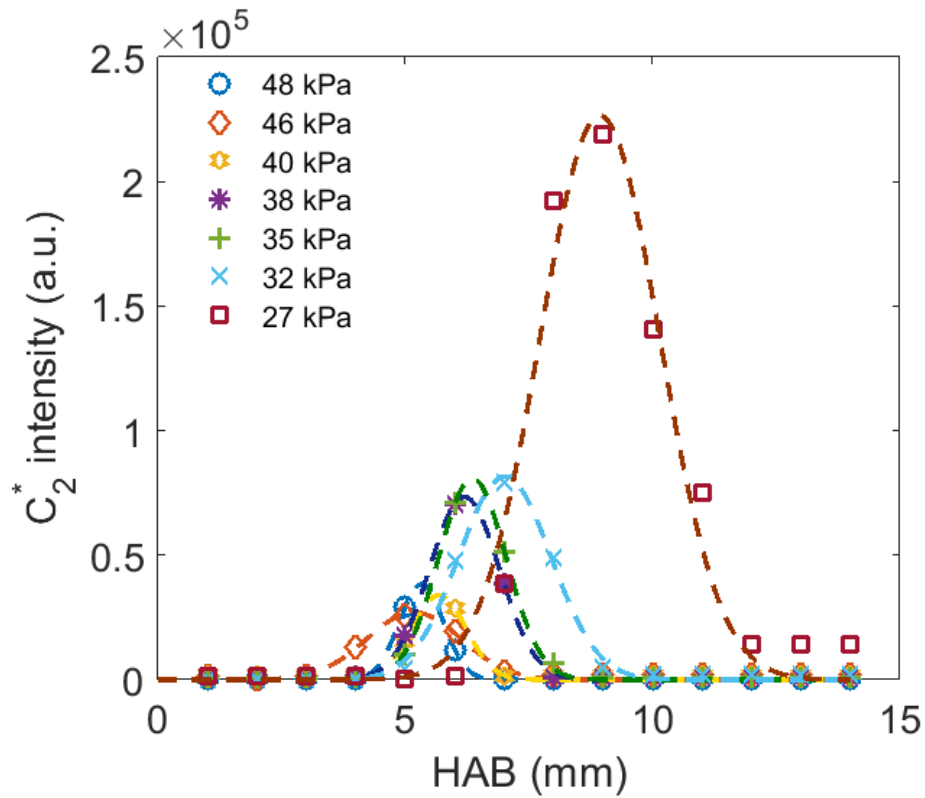


**Figure 6.4:** The intensity of  $C_2^*$  at different pressures as a function of the HAB at  $\Phi = 2.3$ .

Figure 6.5 shows the distance between the locations with maximum  $CH^*$  and  $C_2^*$  emission at  $\Phi = 2.3$ .  $CH^*$  and  $C_2^*$  layers almost overlap each other at atmospheric pressure, but the separation between them increased at lower pressures, particularly 27 kPa, and the distance decreased at higher pressures, particularly 46 kPa. It was also interesting to observe a separation between the  $C_2^*$  and  $CH^*$  layers at reduced pressures. Further, it was observed that the distance between the maximum recorded intensity of  $CH^*$  and  $C_2^*$  decreased linearly with increasing pressure, with a slope of  $28 (\pm 0.048) \times 10^{-9} (\text{mPa}^{-1})$ .

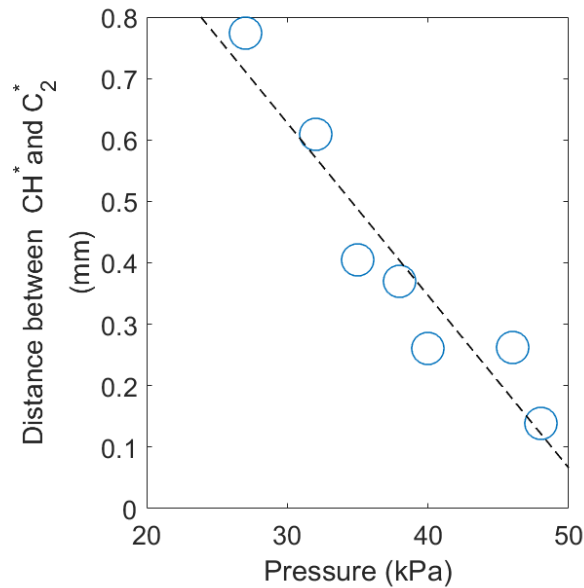


**Figure 6.5:** The distance between the locations with maximum CH\* and C<sub>2</sub>\* emissions.

### 6.1.3 Flame temperature

#### 6.1.3.1 Gas temperature ( $T_g$ )

The corrected temperature of axial profiles of flames are displayed in Figure 6.6. The temperature measurements were assumed with the flame axis, arriving at HAB = 20 mm at  $\Phi = 2.3$ . A similar direction is indicated by the curves that parallel the seven pressure flames. There was a quick rise in temperature beginning from the surface of the burner for the first 17 mm, arriving at the maximum temperature and decreasing a little in the presence of soot. Figure 6.6 provides an evaluation of the gas temperature, which increased at different HAB, while taking radiation losses into consideration. Detected temperatures in the high-pressure flames were found to be lower than those derived from low-pressure flames as in Chapter 5. Therefore, they overlap, as can be seen. With only a slight temperature decrease, they became quite low in doped flames.

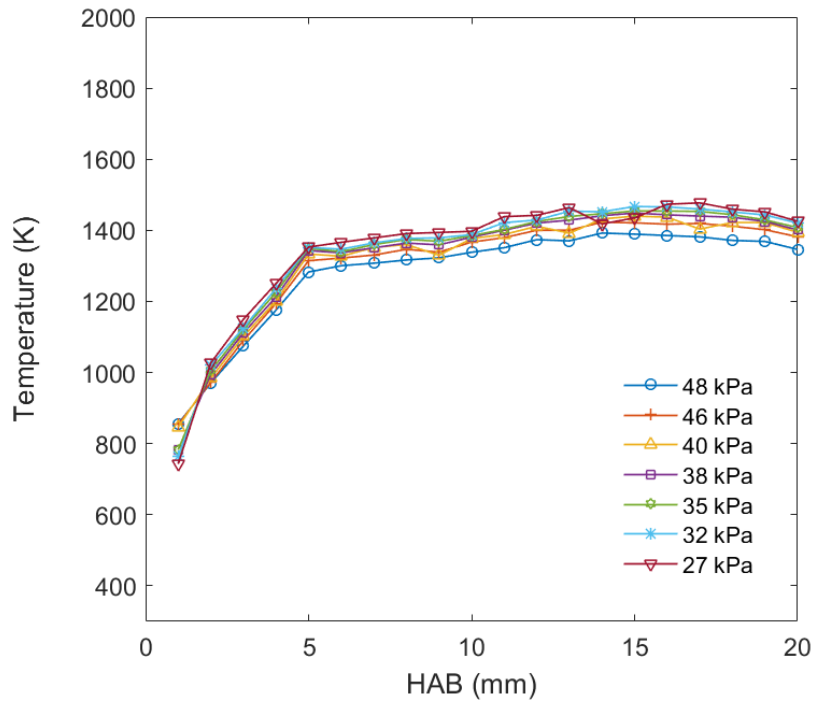


**Figure 6.6:** Temperature profiles measured by a thermocouple for flames with different pressures and HAB.

### 6.1.3.2 Soot Particle Temperature

Similar to chapter 5, Plank relationship over all solid angles was used to generate a fitting reading which then was used to calculate soot particles temperature. Data for this calculation were obtained from Figure 6.2. Figure 6.7 shows soot resolve spectre emission including the calculated fitting reading for pressure setting at 32 kPa and at different HAB.

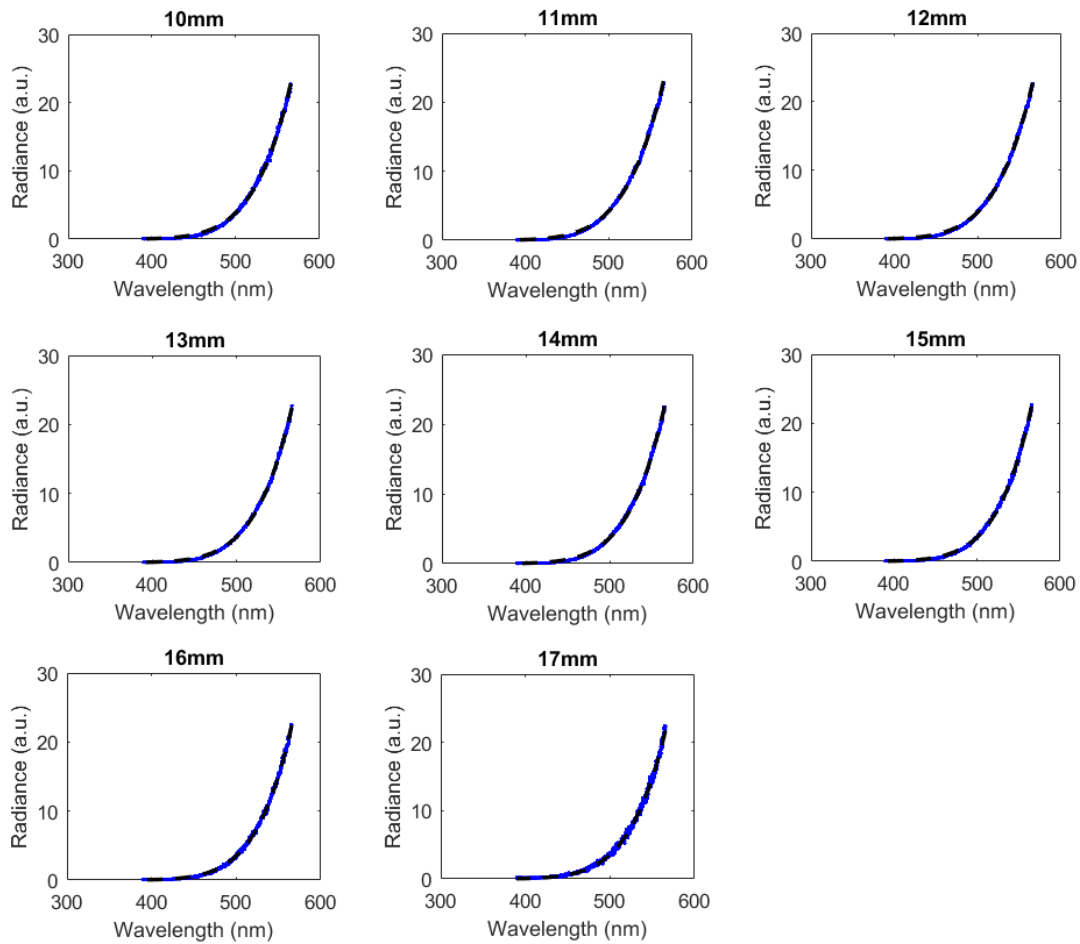


**Figure 6.7:** Typical example of flame emission spectra at different HAB and pressure 32 kPa. The fitting curve, black, of the emission spectra, blue, are shown. Based on the Planck function the soot particle temperature.

The soot particle temperature was derived utilising the fitting process above as introduced in Figure 6.8. Interestingly, in the soot growth region, soot particle temperature decreased to  $\sim 1400$  K, but pressure had no effect. The temperature at soot inception was  $\sim 1332 \pm 62$  K for all pressures at  $\Phi = 2.3$  and was similar to that at  $\Phi = 2.1$ . Higher pressures (48 kPa) produced lower temperatures than did the minimum pressure value (27 kPa), as reported in Chapter 4.

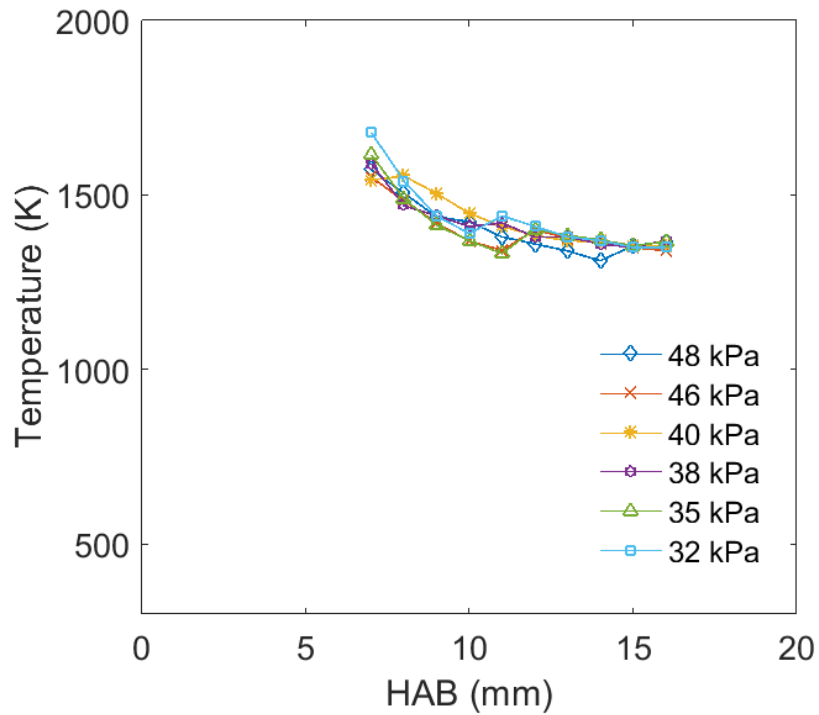


**Figure 6.8:** Soot particles temperature at different HAB for seven pressures as indicated.

#### 6.1.4 Laser-induced incandescence

The LII signal generated was measured through an ICCD camera, 200 images were recorded for each LII image. Figure 6.9 presents the LII images for different pressure and HAB. The LII signal intensity was obtained by adding counts at each pixel, where the LII was recorded and the background subtracted.

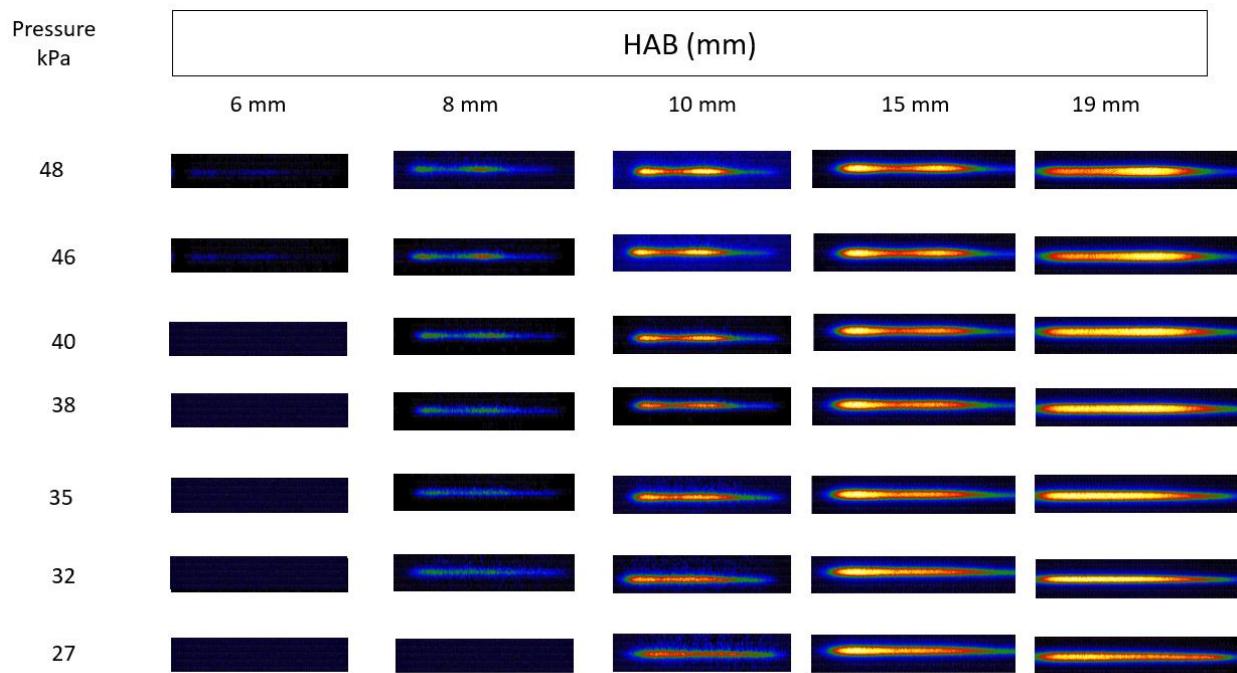


**Figure 6.9:** LII imaging set for different pressure and HAB  $\Phi = 2.3$ .

The strength of LII signals at different HAB in the different low-pressure flames investigated, together with soot volume fractions converted from the LII signal strengths were shown in Figure 6.10. The soot volume fraction increased with HAB at  $\Phi = 2.3$ , and it was higher than the soot fraction obtained at  $\Phi = 2.1$ . An increase in pressure had a significant enhancing effect on soot formation. A rapid increase in soot volume fraction began at HAB around 10–12 mm, where  $C_2^*$  and  $CH^*$  emissions faded away. It is worth noting that the LII signals in Figure 6.10 reveal the distribution of all soot particles only if they were heated efficiently by the laser up to a high temperature, while spontaneous soot luminosity depended greatly on both temperature and soot volume fraction, which causes the difference between the profiles of LII in Figure 6.10 and the soot luminosity spectra as a function of HAB.

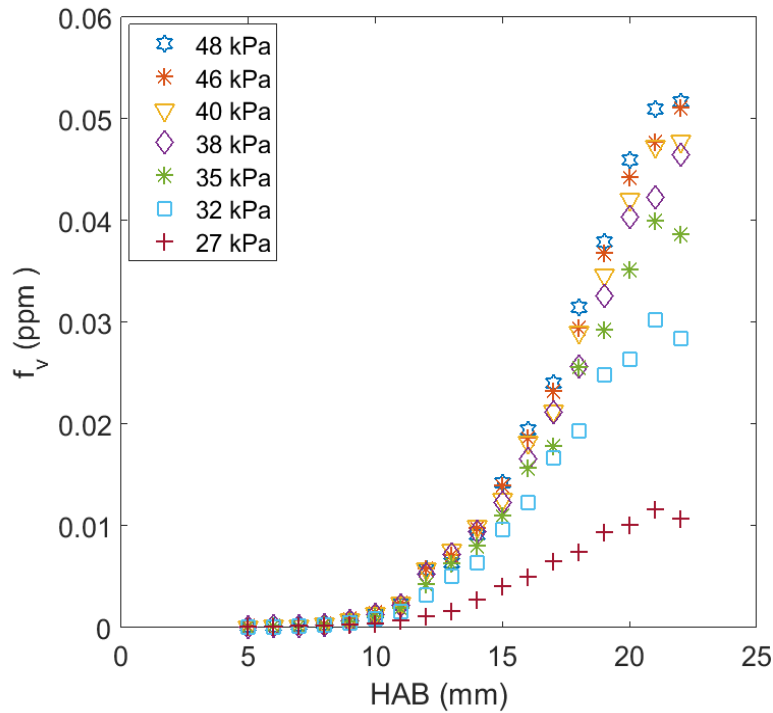
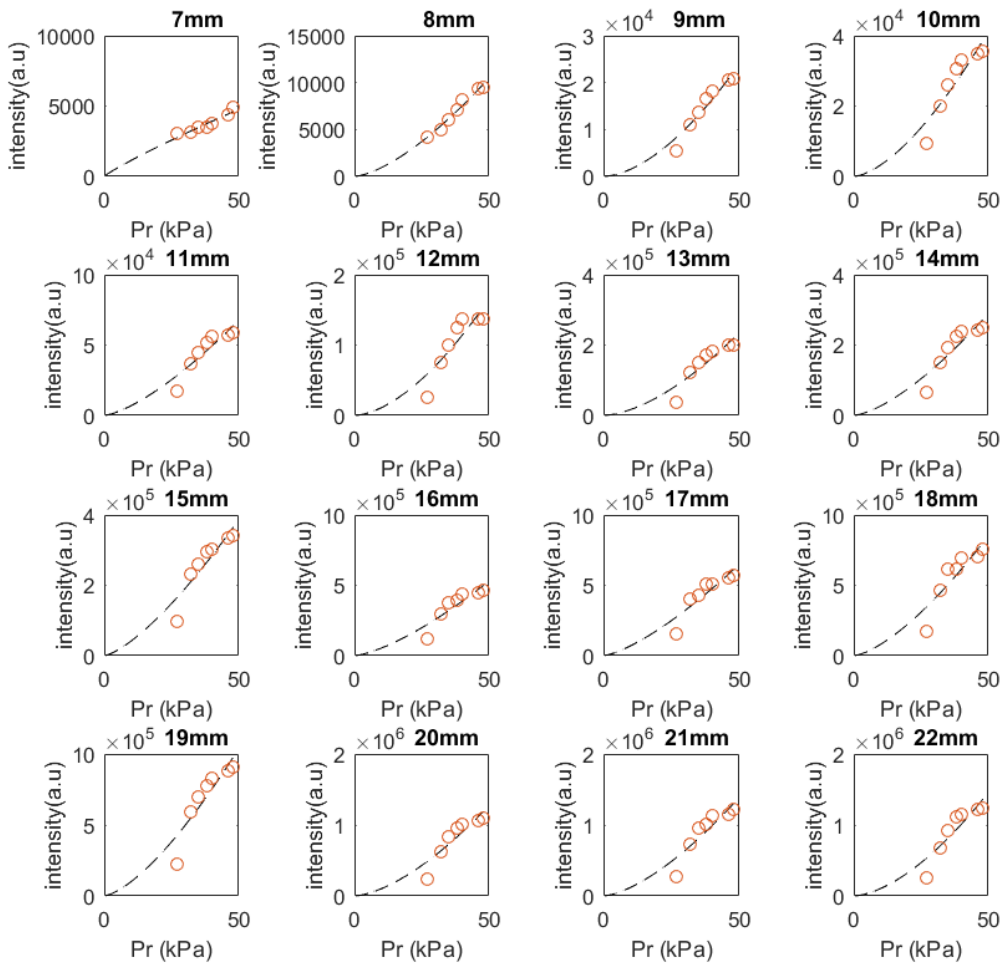


**Figure 6.10:** Axial profiles of soot volume fractions in the flames investigated under different pressures at  $\Phi = 2.3$ .

As in chapter 5, Figure 6.11 a present the power fit at different HAB. An exponential fitting to the measured values reveals a dependence of soot volume fraction  $f_v = Kp^{1.5 \pm 0.4}$  on pressure, suggesting a significant influence of pressure on soot formation. From Figure 6.11b, the exponential factor ( $n$ ) slightly increased with HAB revealing a weak dependence on the HAB. This slight increase in the exponential factor may also be caused by the influence of the stabiliser plate at HAB = 25 mm, which can influence the flow fields when the flames propagate to the stagnation plate.

**a**



**b**

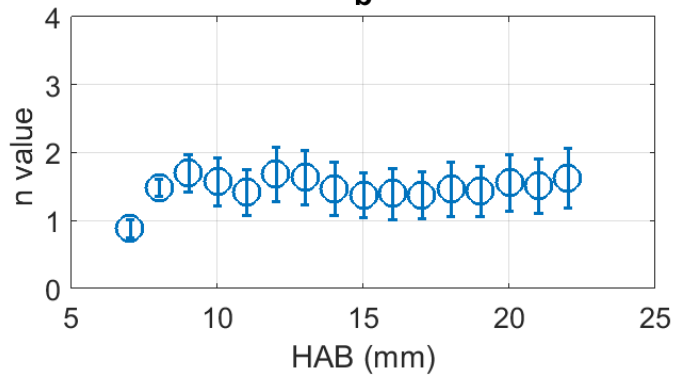
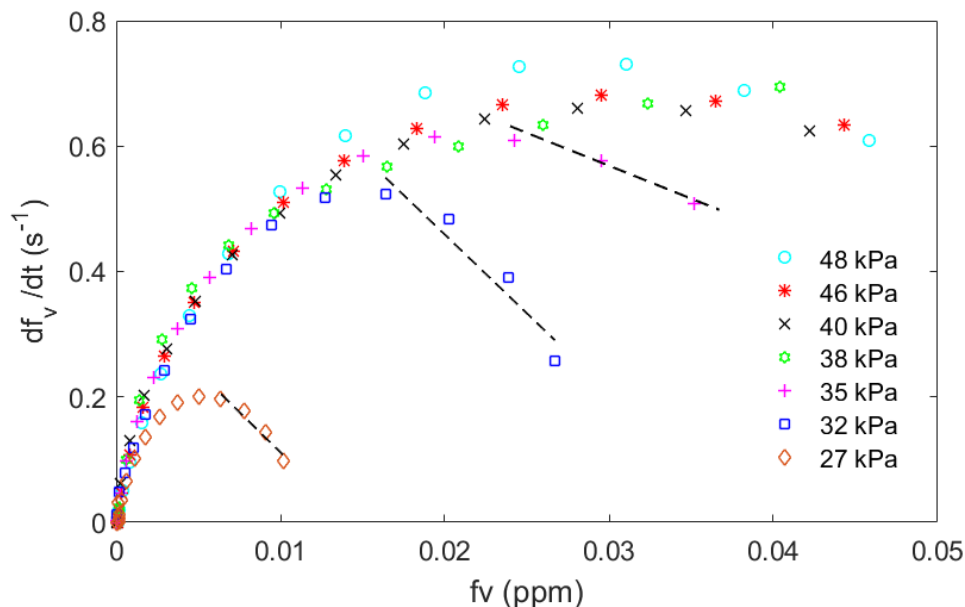


**Figure 6.11:** (a) LII (circles) and an exponential fit curve (dashed line), (b) The exponential factors  $n$  fitted at different HAB at  $\Phi = 2.3$ .

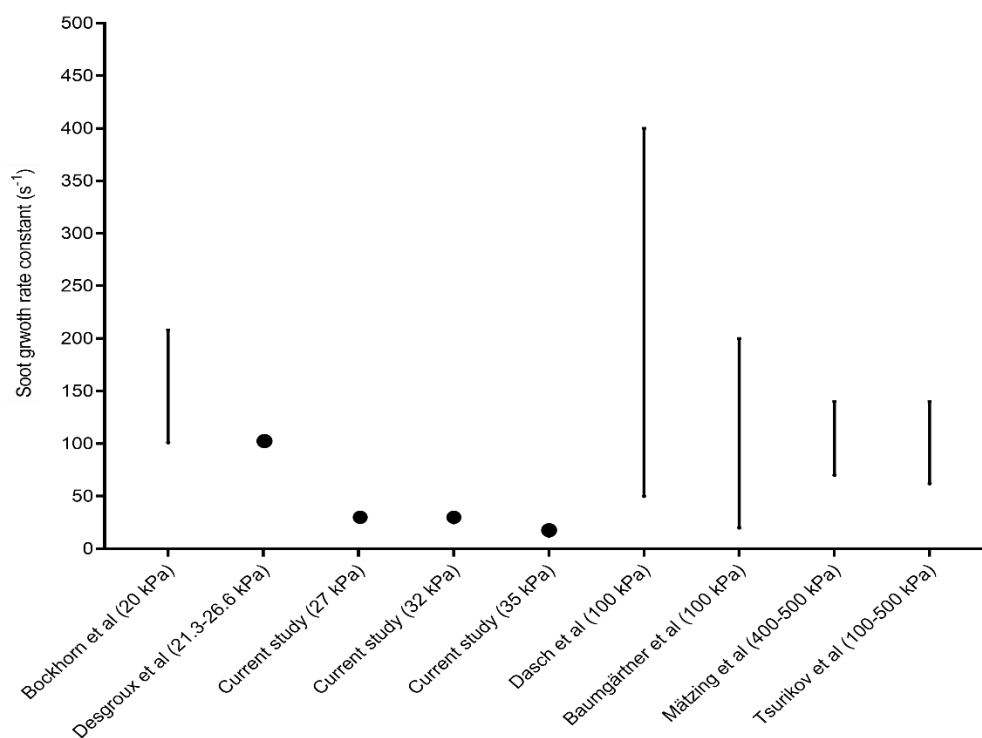


### 6.1.4.1 Soot surface growth

To determine the  $k_{SG}$  values for different flames used in the experimental protocol under discussion, a graphical representation was prepared by plotting  $df_v/dt$  along the y-axis and the corresponding soot volume fraction along the x-axis (see Figure 6.12). The resultant values for  $k_{SG}$  at different pressures (27, 32 and 35 kPa) were  $32 \text{ s}^{-1}$ ,  $25.13 \text{ s}^{-1}$  and  $12.11 \text{ s}^{-1}$ , respectively (shown in figure 6.13). These are the lowest reported values recorded, as compared to previously published literature at elevated pressure [109, 150], atmospheric pressure [151, 152] and low pressure [12, 15]. These results showed that the rate of soot growth slightly increased with a decrease in pressure, as shown in Figure 6.13. The soot growth rate was shown to be weakly dependent on the amount of pressure involved. However, there is a slight change in the soot surface growth constant as compared to the equivalence ratio of  $\Phi = 2.1$ , which gave a constant pressure of  $20.0 \text{ s}^{-1}$ . This constant is lower compared to the equivalent ratio of  $\Phi = 2.3$ . Thus, the soot surface growth constant changes with the equivalence ratio, confirming that the soot surface growth rate constant increases slightly with an increase in equivalence ratio. This increase could be due to the fact that there is an excess quantity of fuel at a higher equivalence ratio compared a lower ratio.



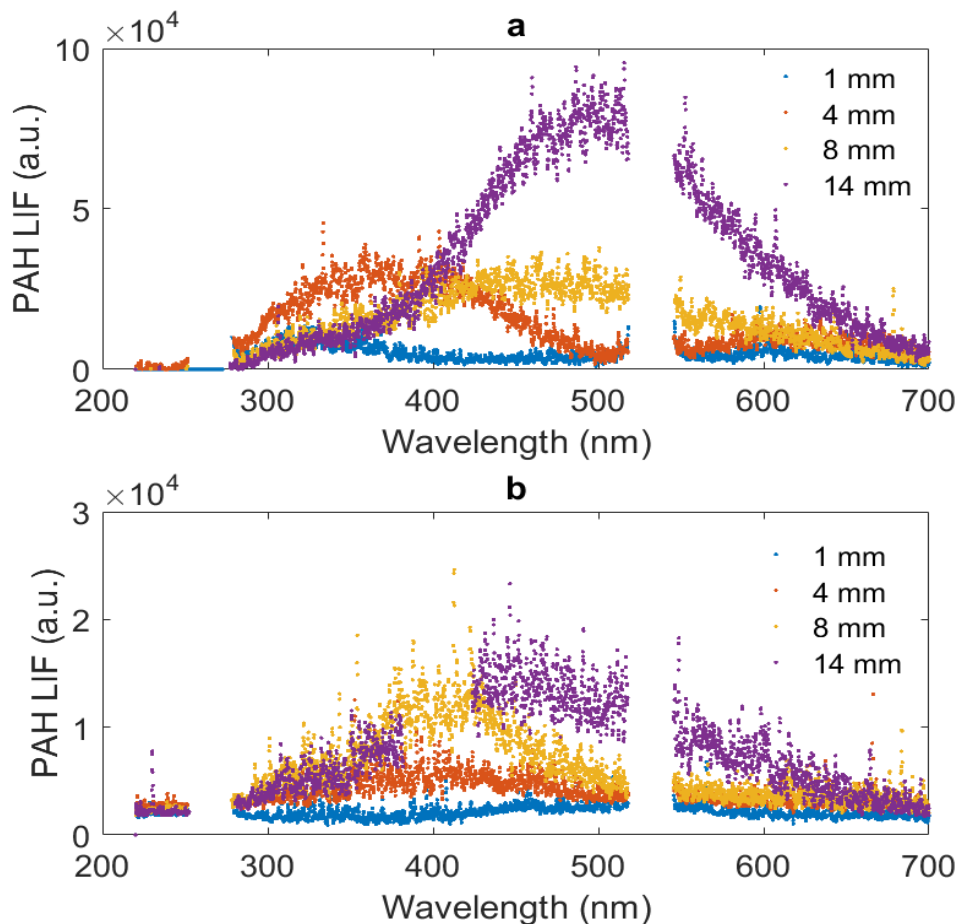
**Figure 6.12:** Derivative function  $df_v/dt$  as a function of soot volume fraction at  $\Phi = 2.3$ .



**Figure 6.13:** Summary of previous studies' soot growth rate constant  $k_{SG}$ '

### 6.1.5 Laser-induced fluorescence of PAHs

Similarly, to chapter five, laser-induced fluorescence (LIF) was used to measure PAHs. The emission wavelength of PAH LIF will increase with an increase in aromatic ring sizes; hence, according to the quantum chemistry calculations in [125, 136], three detection wavelength bands were used to distinguish three kinds of PAHs. PAH-LIF spectroscopic studies were conducted at two pressure setting; 40 kPa and 27 kPa, from wavelengths range of 200 – 700 nm. Three different wavelength bands were used to identify three kinds of PAHs. Figure 6.14 presents a typical spectrum of wavelength bands at different pressure, at different HAB and at  $\Phi = 2.3$ . PAH LIF signals in the range 320 – 360 nm are caused by the presence of PAHs with 2 - 3 aromatic rings, while signals in wavelength ranging from 370 to 410 nm indicate the presence of 3 - 4 aromatic-ring-membered species, and signals above 500 nm indicate the presence of PAHs with 5 - membered ring structures. Signal strengths qualitatively indicate the concentrations of the corresponding PAHs.



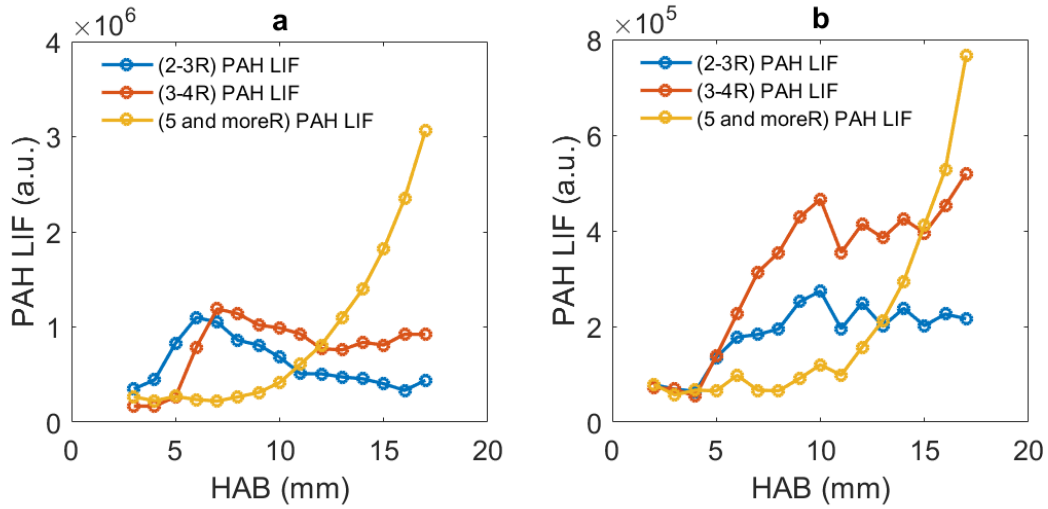
**Figure 6.14:** PAH LIF spectra for different pressure a; 40 kPa and b; 27 kPa at different HAB at  $\Phi = 2.3$ .

Figure 6.15 (a) shows results for PAH LIF spectroscopic studies performed at a pressure of 40 kPa at three ranges of wavelength (320–360, 370–410 and 500–550 nm) with different HAB. The signals from the emissions from combustion products were measured at different HAB ranging from 1 to 16 mm.

Figure 6.15 (b) shows results for PAH LIF spectroscopic studies performed at 27 kPa pressure at three values of wavelength (320–360, 370–410 and 500–550 nm) with different HAB. The signals from the emissions from combustion products were measured at HAB from 1 to 16 mm. Figure 6.15 b also shows that the best values of PAH LIF were at wavelengths range from 370–410 nm and HAB from 1–14 mm; PAH LIF then increased from 15 mm at 500–550 nm.

The best spatial distribution of PAHs was recorded at  $\Phi = 2.3$ . A well separation of (2-3R) PAHs LIF from (3-4R) PAHs LIF was achieved. This is comparable to results obtained from a previous experiment (chapter 5), as the best spatial distributions were recorded at  $\Phi = 2.1$ . Figure 6.15

shows that at  $\Phi = 2.3$ , there was clear separation at each pressure between (2–3 R) PAH LIF and (3–4 R) PAH LIF at  $\sim 1$  mm HAB.



**Figure 6.15:** PAH LIF as a function of HAB at different pressures; a, 40 kPa and b, 27 kPa.

As seen in Figure 6.16, the signals for (2-3R) PAH LIF and (3-4R) PAH LIF attained a peak for each type of flame and subsequently started to decline, Table 6.1 summarised the spatially phenomenological removing rate constant of PAHs with 2–3 rings ( $k_{phen}^{2-3R}$ ) and 3–4 rings ( $k_{phen}^{3-4R}$ ). From these data, the ( $k_{phen}^{2-3R}$ ) and ( $k_{phen}^{3-4R}$ ) were found to be  $23.33 \text{ s}^{-1}$  and  $16.9 \text{ s}^{-1}$ , respectively, at a pressure of 40 kPa. This indicates that ( $k_{phen}^{2-3R}$ ) is faster than ( $k_{phen}^{3-4R}$ ) by a factor of 1.38 at a pressure of 40 kPa.

The removing rate of the PAHs at the equivalence ratio of 2.3 also differs from the rate at the 2.1 equivalence ratio. When the equivalence ratio increases from 2.1 to 2.3, there is an increase in the removing rate of PAHs with ( $k_{phen}^{2-3R}$ ) and a reduction in the removing rate with ( $k_{phen}^{3-4R}$ ), measured at the high pressure of 40 kPa.

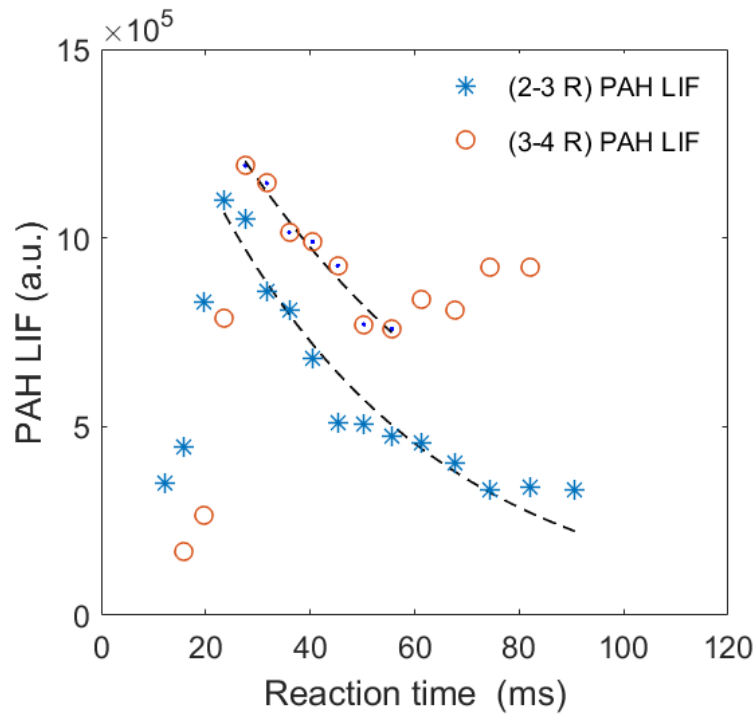


**Figure 6.16:** PAH LIF as a function of reaction time at a pressure of 40 kPa.

Table 6. 1: The spatially phenomenological removing rate constant of PAHs

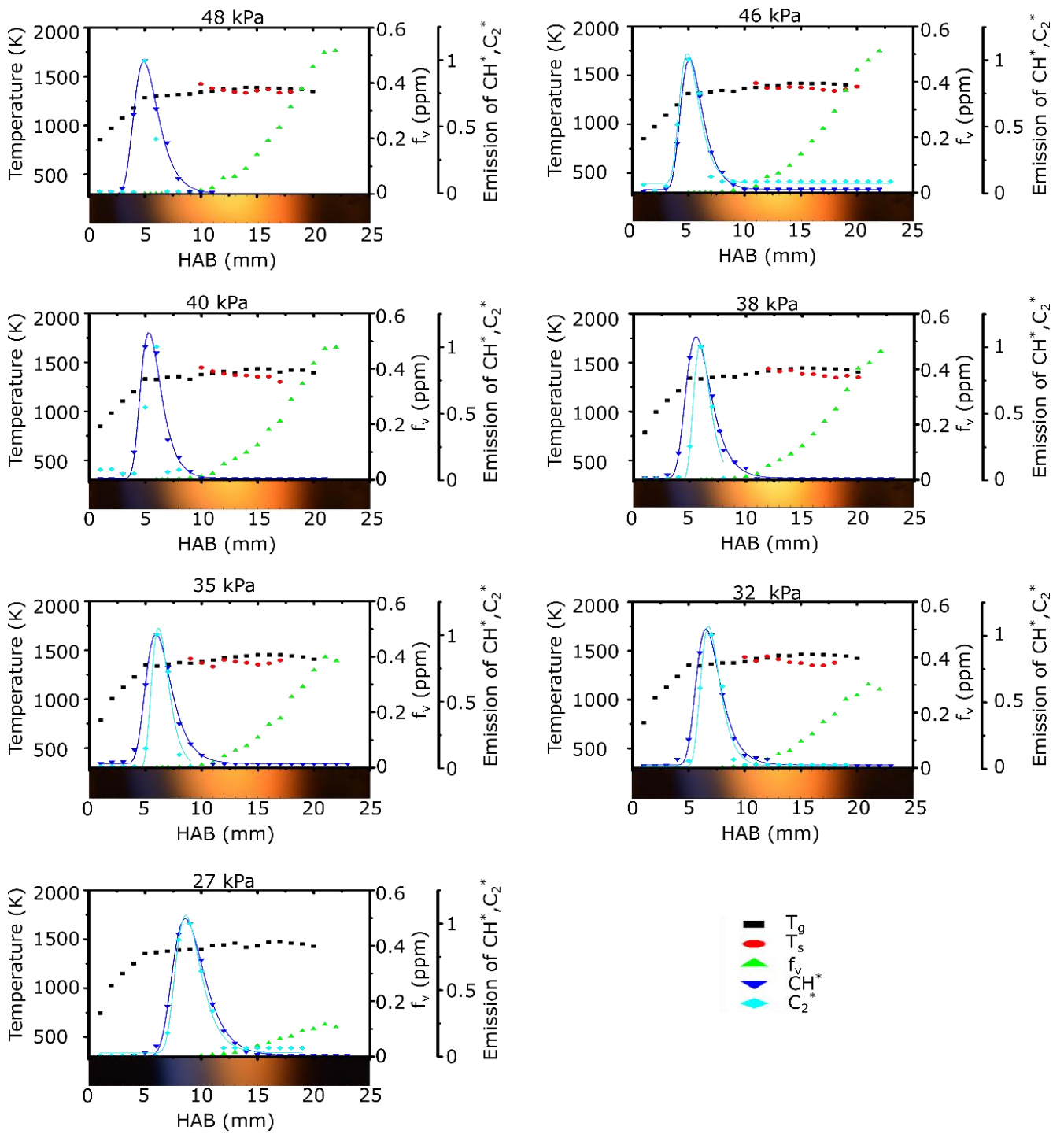
Pressure (kPa)	Spatially phenomenological removing rate constant (s <sup>-1</sup> )	
	( $k_{phen}^{2-3R}$ )	( $k_{phen}^{3-4R}$ )
40	23.33	16.9
27	–	–

As seen in Table 6.1 and Table 5.3, the removing rate of the aromatic compounds in soot formation decreases with an increase in pressure. At the same time, the removing rate of PAHs increases with an increase in the equivalence ratio.

### 6.1.6 Spatial correlation among the measured parameters

Figure 6.17 presents the spatial distributions including the visual presentation of the flame and HAB (in mm) along the  $x$ -axis, and measured results for concentrations of  $\text{CH}^*$  and  $\text{C}_2^*$  radicals,

soot and flame temperature and volume fraction of soot along the  $y$ -axis. The graphical presentation highlights the spatial relationships among these parameters. It was found that the detectable formation of soot began immediately after the peak region where the radicals were generated. Detectable soot particles were formed within the near flame regions of the radical emissions, forming a region of overlap between the radicals and soot. Above this region, a significant increase in soot volume fraction was found, indicating faster soot formation than in the region of overlap with the radicals. Flame temperatures also peaked in this soot radical overlap region, indicating that this layer might be a critical region for understanding soot formation in the case of premixed flames as utilised in the experimental setup. The spatial plot also revealed the temperature of soot emergence; that is, the temperature at the lowest location with detectable soot in the different flames. It may be clarified by reducing the concentration of hydrogen atoms or reducing the particle surface brought about by coagulation. Reducing the temperature of flame because of irradiative losses and the cooling influence of the stabilisation plate may add to this effect as discussed in Chapter 5.



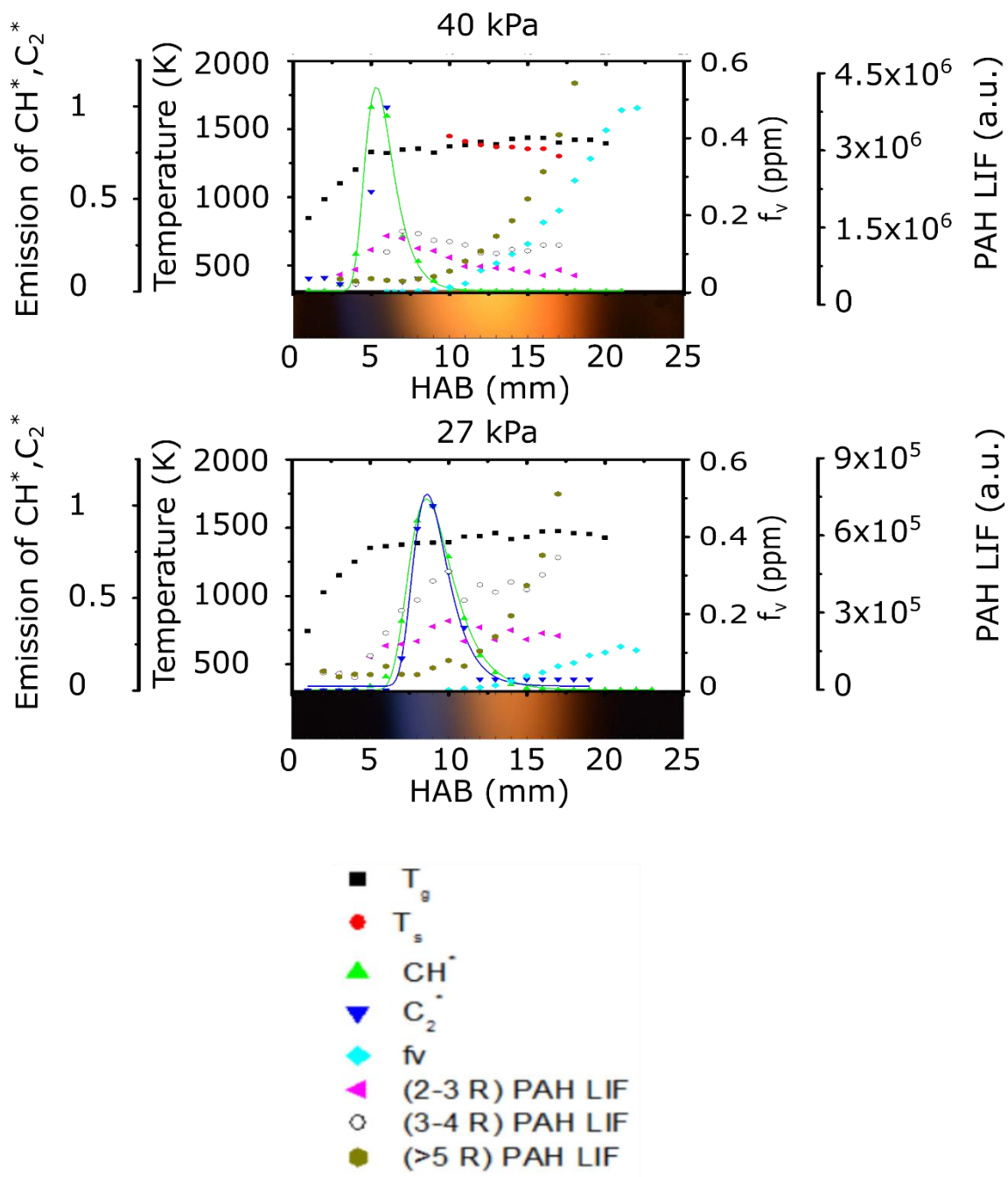
**Figure 6. 17:** Superimposition of the measured profiles for flame and soot temperatures, normalise of  $\text{CH}^*$  and  $\text{C}_2^*$  emissions and soot volume fractions onto flame photographs.

Figure 6.18 presents the spatial distributions for all measurements including PAH LIF for pressures of 40 and 27 kPa. The max intensity of  $C_2^*$  location was found to be coincides with (2–3R) PAH LIF for each pressure. Thus, for the first time a link has been found between (2–3R) PAH LIF and  $C_2^*$ , indicating a potentially critical area on which to focus to understand soot formation. (> 5R) PAH LIF were found to be formed but it was difficult to identify where PAH LIF with (>5R) PAH LIF occurred as the signal increased in regions of soot growth, indicating the signal included (soot) and (PAH LIF), as also seen for  $\Phi = 2.1$ . Also, it was clear that the starting location of soot formation coincided with the location of the observed decrease in PAHs.

Table 6. 2: Superimposition of the measured profiles

Chemical species	Spatial location max intensity (mm)	
	40 (kPa)	27 (kPa)
CH*	5	8
C <sub>2</sub> *	6	9
(2-3 R) PAH LIF	6	9
(3-4 R) PAH LIF	7	10
Soot inception	7±0.5	10±0.5





**Figure 6.18:** Superimposition of the measured profiles for flame and soot temperatures, normalise of  $\text{CH}^*$  and  $\text{C}_2^*$  emissions, soot volume fractions and PAH LIF onto flame photographs.

## 6.2 Summary

Soot volume fraction, chemiluminescence of  $\text{CH}^*$  and  $\text{C}_2^*$ , flame temperature and particle temperature were measured in a series of flat premixed  $\text{C}_2\text{H}_4$ –air flames with a constant equivalence ratio of 2.3 and at low pressures of 27 to 48 kPa. The spatially resolved measurements revealed that:

1. The distance between the max intensity of  $\text{CH}^*$  and max intensity of  $\text{C}_2^*$  increased linearly with decreasing pressure according to a slope of  $28 \times 10^{-9} \pm 0.048$  ( $\text{mPa}^{-1}$ ).
2. Soot volume fraction increased with HAB at  $\Phi = 2.3$  and was higher than the soot fraction at  $\Phi = 2.1$ ; the increase in pressure had a significant enhancing effect on soot formation.
3. Soot volume fraction followed a power function with pressure; that is,  $f_v \propto kp^n$  and  $n = 1.5 \pm 0.4$ . It was also found that the value of  $n$  was weakly dependent on the HAB.
4. The gas temperature and soot particles temperature agreed very well within  $\pm 93$  degree. A common temperature of  $1332 \pm 62$  K was found at the early stage of soot inception. The results were similar and consistent with the observations of Glassman and co-workers at atmospheric pressure [143].
5. The soot growth rate constants  $k_{SG}$  ( $\text{s}^{-1}$ ) for pressures 27 kPa, 32 kPa and 35 kPa are  $32 \text{ s}^{-1}$ ,  $25.13 \text{ s}^{-1}$  and  $12.11 \text{ s}^{-1}$ , respectively. This is a change in the soot surface growth constant as compared to the equivalence ratio of  $\Phi = 2.1$ , which gave a constant rate at a pressure of 27 kPa is  $20.0 \text{ s}^{-1}$ . Thus, the soot surface growth constant changes with the equivalence ratio, however, the soot surface growth rate constant increases slightly with decrease in pressure. For all pressures, there is an indication that  $k_{SG}$  is weak dependence of pressure and equivalence ratio.
6. At a pressure of 40 kPa, the spatially phenomenological removing rate constants ( $k_{phen}^{2-3R}$ ) and ( $k_{phen}^{3-4R}$ ) were found to be  $23.33 \text{ s}^{-1}$  and  $16.9 \text{ s}^{-1}$ , respectively.

## Chapter 7: Effect of gases additive

CO<sub>2</sub> is an important compound for the inhibition of combustion flames. The study reported in this chapter investigated the effects of CO<sub>2</sub>, N<sub>2</sub> and Ar addition on soot particles in laminar premixed C<sub>2</sub>H<sub>4</sub>–air flames, as determined by soot volume fraction using LII and PAHs using PAH LIF.

The gases added to the flame had three ruling effects on PAH and soot formation: a dilution effect of changing the segment concentrations; a thermal effect of changing the heat capacity; and a chemical effect of participating in the reactions specifically. Previous examinations for the most part were centred on the effects of CO<sub>2</sub> and N<sub>2</sub> as the principle segments of exhaust gas on PAH and soot formation. Teini et al. [162] studied the influence of CO<sub>2</sub> on PAH and nascent soot particle formation under the homogeneous conditions of a quick compression facility. They found that CO<sub>2</sub> upgraded the soot inception rate in C<sub>2</sub> which responded with stable species to deliver radicals that accelerated the growth process of PAHs but had no effect in CH<sub>4</sub> flames. Wang and Chung [163] numerically and experimentally explored the effect of CO<sub>2</sub> dilution in C<sub>2</sub>H<sub>4</sub> counter-flow laminar premixed flames and found that the formation of PAHs was repressed by the chemical effects of CO<sub>2</sub>.

Another study investigated the effects of fuel dilution by CO<sub>2</sub> and N<sub>2</sub> on soot formation and the flame structure in laminar co-flow ethylene/air diffusion flames at high pressures [161]. The study reported that fuel mass flow rate was fixed, and the flame was buoyancy-dominated. The flame height was nearly independent of pressure. Properties of each flame under different conditions and different pressures were comparable to one another. At atmospheric pressure, the luminous zone appeared only at the flame tip as result of nitrogen or carbon dioxide addition. Dilution by either nitrogen or carbon dioxide at a 1:2 ratio was very effective in reducing flame sooting tendency, so flames remained non-smoking even at 20 atm. It was noted that the ethylene/air diffusion flame becomes smoking at 9 atm, when nitrogen or carbon dioxide were not added. The visible flame height of the nitrogen diluted flame was consistently slightly higher than that of the carbon dioxide-diluted flames.

In this chapter, laminar premixed ethylene air with a total flow rate of 7 l/min and at pressure 40 kPa was chosen because it was the best setting for stabilising the flame inside the chamber after testing different conditions (pressure and flow rate). The three different gasses (CO<sub>2</sub>, N<sub>2</sub>, Ar) were selected to dilute the main flame as each one has a different effect on soot formation, as discussed in in previous studies. The maximal volume of each gas to be added was established. Ar with a

volume exceeding 0.6 l/min disturbed flame stabilisation, leading to extinguishing of the flame, whereas CO<sub>2</sub> and N<sub>2</sub> exceed this maximum volume with less of an effect on the flame stability. Therefore, a flow rate of 0.6 l/min for each added gas was chosen to compare the effect of each gas on soot formation and PAHs. The pressure was set to 40 kPa, as this will allow for a bigger dilution factor compared to other pressure settings, allowing examination of the effects of gas addition.

## **7.1 Results and Discussion**

### **7.1.1 Flame photographs**

Photographs of laminar premixed flames of C<sub>2</sub>H<sub>4</sub>-air at 40 kPa pressure and diluted with Ar, N<sub>2</sub> and CO<sub>2</sub> are shown in Figure 7.1; photographs of laminar flames premixed with gaseous additives such as CO<sub>2</sub>, N<sub>2</sub> and Ar at pressure of 40 kPa were taken for comparison. It was observed that the flame height was reduced with premixed fuel compared with the C<sub>2</sub>H<sub>4</sub>-air. The flame height and combustion were reduced to a maximum in the presence of Ar premixed fuel. In the case of Ar premixed fuel, the luminous zone of the flame was reduced, as was soot formation. Flame propagation was also restricted when premixed fuel was used.

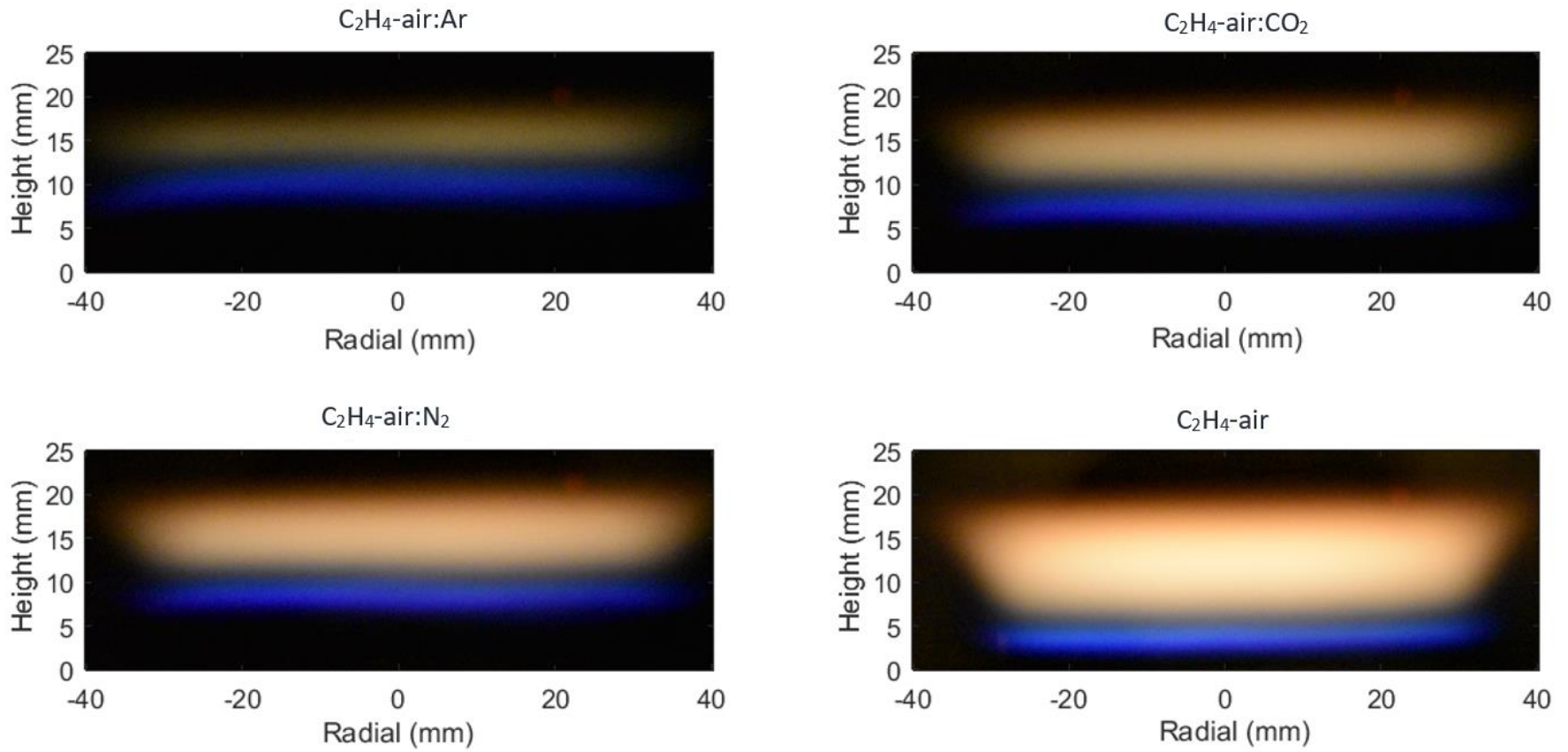


**Figure 7.1:** Photographs of C<sub>2</sub>H<sub>4</sub>-air with different additive of Ar, CO<sub>2</sub> and N<sub>2</sub> at pressure of 40 kPa

### 7.1.2 Spatially resolved emission spectra of $\text{CH}^*$ and $\text{C}_2^*$

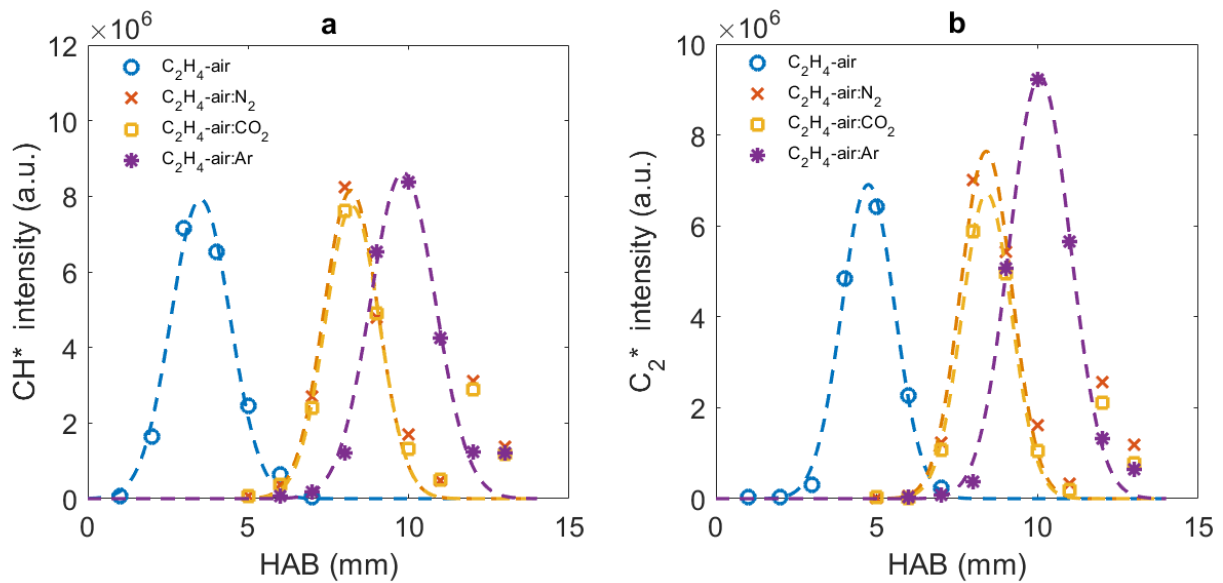


**Figure 7.2:** Flame emission for two radicals; a,  $\text{CH}^*$  and b,  $\text{C}_2^*$  as a function of HAB with different dilution gases at pressure of 40 kPa.

With chemiluminescence, the investigation of fluctuations of the base of the flame demonstrated an increase in fluctuation of the length of the flame, as shown by the two variables. The influence of  $\text{CO}_2$  in a  $\text{C}_2\text{H}_4$ -air flame was focussed on experimentally in laminar premixed flame structure at 40 kPa pressure and PAH and soot formation investigations. Several changes in PAH and soot in-flame concentrations were noticed in the  $\text{CH}^*$  and  $\text{C}_2^*$  doped flame. PAH and soot suppression indexes can be useful to highlight how the presence of  $\text{CH}^*$  and  $\text{C}_2^*$  can globally reduce pollutant emissions. Figure 7.2 shows the intensity of  $\text{CH}^*$  and  $\text{C}_2^*$  with HAB of  $\text{C}_2\text{H}_4$ -air and  $\text{C}_2\text{H}_4$ -air diluted with Ar,  $\text{N}_2$  and  $\text{CO}_2$  at pressure of 40 kPa. It is shown that the higher intensity was for the  $\text{CH}^*$  case with diluted Ar, while in the  $\text{C}_2^*$  case, the best intensity was for  $9 \times 10^6$  at 10 mm HAB with diluted Ar. Highly spectrally resolved local  $\text{CH}^*$  and  $\text{C}_2^*$  chemiluminescent spectra were obtained at the near flame zone in the case of the  $\text{C}_2\text{H}_4$ -air. The soot yield was directly proportional to the concentration of  $\text{CH}^*$  and  $\text{C}_2^*$  in the near flame zone. The same signal was obtained at higher HAB in the case of a premixed flame. The signal from chemiluminescent spectra indicated that the presence of  $\text{C}_2^*$  was found at the largest HAB in the case of the Ar premixed flame; and the presence of  $\text{CH}^*$  was found almost at the same HAB in the case of  $\text{N}_2$ ,  $\text{CO}_2$  and Ar premixed flames.

A second peak was obtained when  $N_2$  and  $CO_2$  were added for both  $CH^*$  and  $C_2^*$ ; however, this could be a false signal or perhaps a new mechanism which sits outside the scope of this study.

### 7.1.3 Laser-induced incandescence

In this work, various experimental examinations were carried out concerning the utilisation of  $CO_2$ ,  $N_2$  and Ar as an additive in laminar premixed  $C_2H_4$ -air flames at pressure of 40 kPa.

The LII signal generated was measured through an ICCD camera, 200 images were recorded for each image. Figure 7.3 presents the LII images for different gas additive and HAB at pressure of 40 kPa. The LII signal intensity was obtained by adding counts at each pixel, where the LII was recorded and the background subtracted. To acquire LII signals with appropriate signal to noise ratios, the position identified in the flames should have a high soot volume fraction, so that the signals are sufficient. Thus, the LII signals to be examined were identified at 4–19 mm HAB.

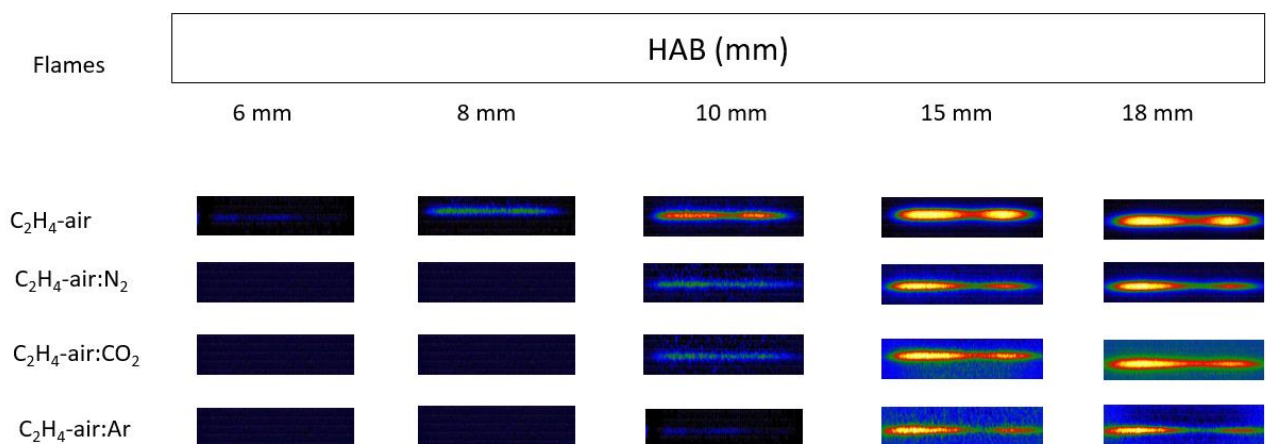


**Figure 7.3:** LII imaging at different gas addition at 40 kPa pressure

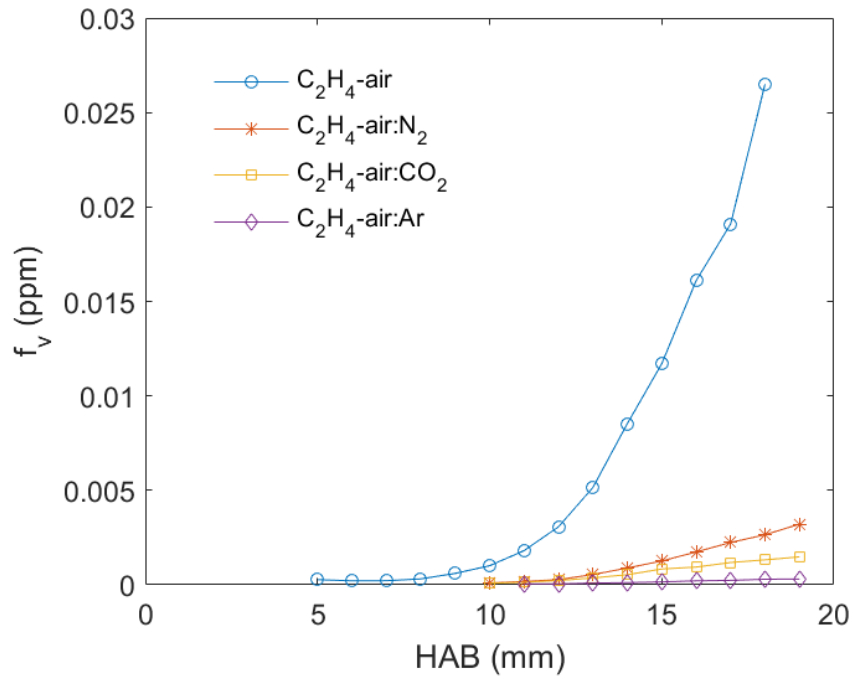


**Figure 7.4:** Soot volume fraction as a function of HAB with different gas additives at 40 kPa pressure

Figure 7.4 presents soot volume fraction as a function of HAB with different gas additives at 40 kPa of pressure. Ar addition produced minimal soot emission compared to the addition of other gasses. These results were inconsistent with previously reported studies [124, 164]. These studies used computational work that permits recognition of the relative contribution of the thermal and chemical effects brought about by additions of gas to flames. The first examination of experimental and modelling discoveries suggested that CO<sub>2</sub> is able to chemically decrease PAH and soot emissions.



### 7.1.3.1 Soot surface growth

This study was conducted to analyse the effects of CO<sub>2</sub>, Ar and N<sub>2</sub> dilution at pressure of 40 kPa. As a rule, Ar and CO<sub>2</sub> dilution can reduce soot formation. Prior work has centred on the three effects of CO<sub>2</sub>, which are dilution, temperature and direct chemical participation [165]. More recently, scientists have typically considered the effect of CO<sub>2</sub> dilution on soot formation specifically, without investigating the three specific effects. Liu et al. [166], for example, claimed that it was difficult to absolutely isolate these three effects experimentally, so they researched the nucleation, surface growth and oxidation of soot particles.

Most results have demonstrated that CO<sub>2</sub>/N<sub>2</sub> dilution has a negative effect on the nucleation of incipient soot and almost no effect on the oxidation of soot particles. Regarding the surface growth of soot particles, [119] found no change in the surface growth rate, while Gu et al. [167] concluded in their simulation results that CO<sub>2</sub> dilution on the fuel side strongly reduced surface growth. Consequently, an experimental study was required to clarify the influence of CO<sub>2</sub>/N<sub>2</sub>/Ar addition on soot formation, and the flame structure of a laminar C<sub>2</sub>H<sub>4</sub>-air flame.

Figure 7.4 illustrates the case of using Ar as a diluent rather than CO<sub>2</sub> or N<sub>2</sub>, at 40 kPa pressure demonstrating that the soot volume fraction abruptly decreased. The suppression of soot volume fraction in the Ar diluted case resulted from two processes: the short residence time in the inception region caused by late nucleation; and the decrease of surface growth distance by the low flame temperature resulting from the higher thermal capacity and the chemical change of Ar.

To determine the soot surface growth constant  $k_{SG}$  values for the different flames at a pressure of 40 kPa, a graphical representation was prepared by plotting  $df_v/dt$  along the  $y$ -axis and the corresponding soot volume fraction along the  $x$ -axis (see Figure 7.5).

Soot growth rates were calculated to compare soot growth rates in flames under different nucleation conditions. The results suggested that the soot growth rate had a relatively weak dependence on the change of conditions. Using the method described above, the derived  $k_{SG}$  values were found to be 8.3 s<sup>-1</sup>, 15.35 s<sup>-1</sup>, 35.65 s<sup>-1</sup> and 60.35 s<sup>-1</sup> for C<sub>2</sub>H<sub>4</sub>-air, C<sub>2</sub>H<sub>4</sub>-air:N<sub>2</sub>, C<sub>2</sub>H<sub>4</sub>-air:CO<sub>2</sub> and C<sub>2</sub>H<sub>4</sub>-air:Ar, respectively. This can be seen in Figure 7.5. Therefore, the results show that the soot growth rate constant was high with the addition of Ar.

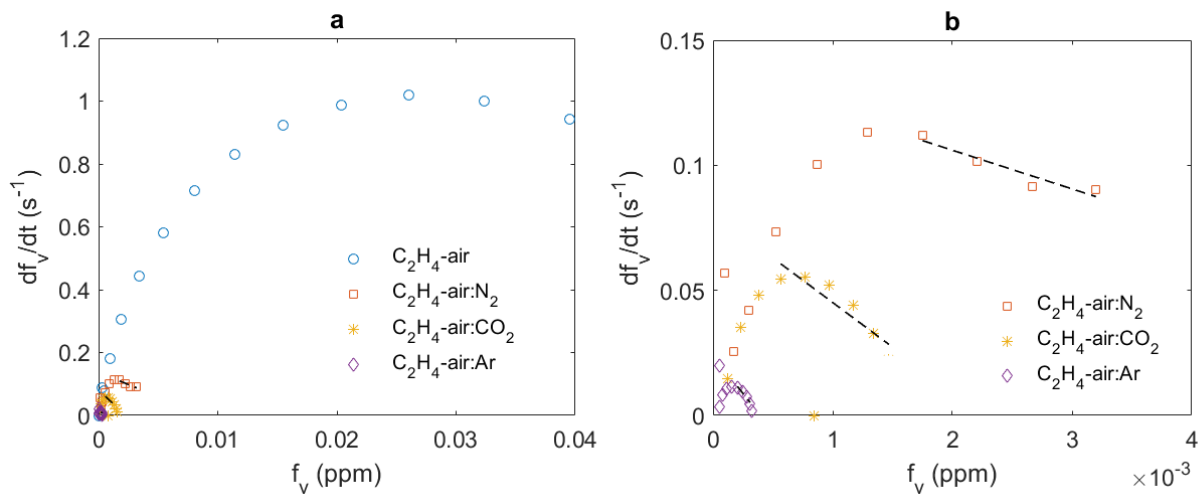


**Figure 7.5:** Derivative function  $df_v/dt$  as a function of soot volume fraction, at pressure of 40 kPa; a = the whole flame condition, b= with gas additives

#### 7.1.4 Flame temperature

It is crucial to keep the temperature profiles constant in the investigation of the chemical effects of  $N_2$ ,  $CO_2$  or Ar additions at pressure of 40 kPa. Comparisons of different diluted flame temperature profiles are shown in Figure 7.6. The results showed that the diluted Ar had lower temperature values than the  $C_2H_4$ -air and flames diluted with  $CO_2$  and  $N_2$  at (blue region) low HAB (2–10 mm).

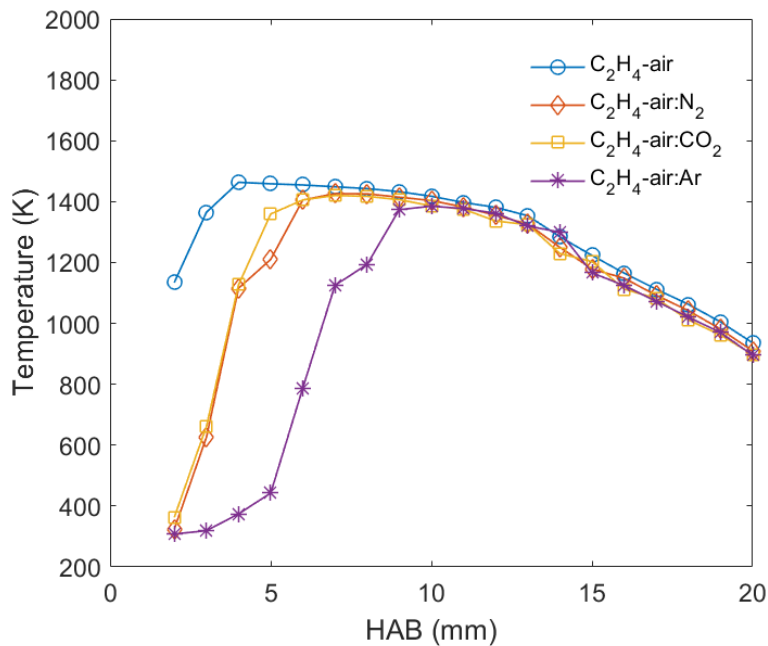


**Figure 7.6:** Temperature profile of different diluted flames at 40 kPa pressure

According to the reaction rate discussed in the following sections, the reactions mainly happened at HAB less than 10 mm, indicating that these deviations in the post flame region were acceptable. Hence, the temperature profiles were thought to be nearly constant and the thermal effects of C<sub>2</sub>H<sub>4</sub>-air, N<sub>2</sub>, CO<sub>2</sub> and Ar should be excluded. The temperature at the first soot inception was 1458.52 K, 1414.51 K, 1406.21 K, and 1377.16 K for C<sub>2</sub>H<sub>4</sub>-air, C<sub>2</sub>H<sub>4</sub>-air:N<sub>2</sub>, C<sub>2</sub>H<sub>4</sub>-air:CO<sub>2</sub> and C<sub>2</sub>H<sub>4</sub>-air:Ar, respectively. Thus, the soot inception temperature was affected when a gas was added to the flame as the temperature became lower.

### 7.1.5 Laser-induced fluorescence of PAHs

Similarly to previous chapters, laser-induced fluorescence (LIF) was used to measure PAHs. The emission wavelength of PAH LIF will increase with an increase in aromatic ring sizes; hence, according to the quantum chemistry calculations in [125, 136], three detection wavelength bands were used to distinguish three kinds of PAHs. PAH-LIF spectroscopic studies were conducted at two pressure setting; 40 kPa and 27 kPa, from wavelengths range of 200 – 700 nm. Three different wavelength bands were used to identify three kinds of PAHs. Figure 7.7 presents a typical spectrum at 40 kPa pressure in respect to different gas additive and different HAB. PAH LIF signals in the range 320 – 360 nm are caused by the presence of PAHs with 2 - 3 aromatic

rings, while signals in wavelength ranging from 370 to 410 nm indicate the presence of 3 - 4 aromatic-ring-membered species, and signals above 500 nm indicate the presence of PAHs with 5 - membered ring structures. Signal strengths qualitatively indicate the concentrations of the corresponding PAHs.

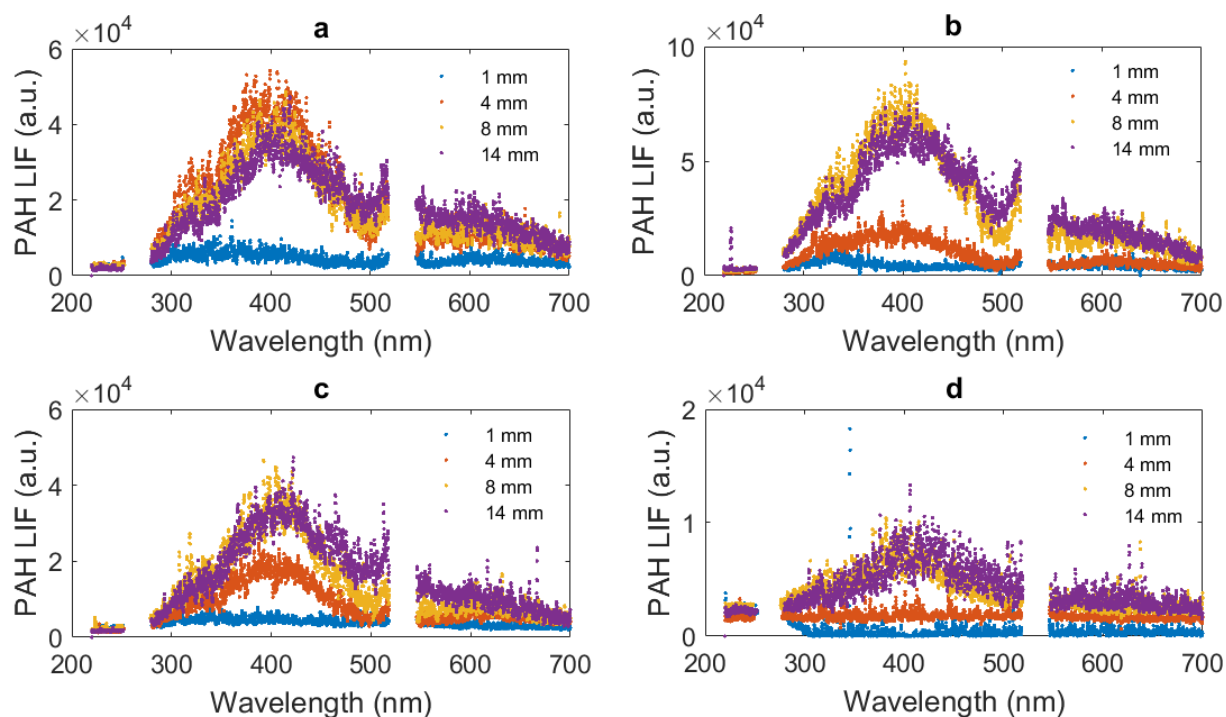


**Figure 7.7:** PAH LIF spectra for different flames at 40 kPa pressure a; C<sub>2</sub>H<sub>4</sub>-air, b; C<sub>2</sub>H<sub>4</sub>-air:N<sub>2</sub> c; C<sub>2</sub>H<sub>4</sub>-air:CO<sub>2</sub> and d; C<sub>2</sub>H<sub>4</sub>-air:Ar at different HAB

Figure 7.8 presents PAH LIF as a function of HAB. It was found that, the PAH LIF decreased with Ar addition more so than with CO<sub>2</sub>, N<sub>2</sub> or C<sub>2</sub>H<sub>4</sub>-air for all values of HAB at pressure of 40 kPa. Thus, it was concluded that addition of Ar to the laminar premixed flames slowed down the nucleation rate and thus compressed the formation of nascent soot and a slight reduction in the absorbency of soot particles was observed. This demonstrated that Ar dilution made the soot particles less mature.

The PAH LIF signals were measured along the axial line of the series of flames in two detection wavelength bands, 320–360 and 370–410 nm, at various different gas additive and at pressure of 40 kPa, as shown in Figure 7.8 (a) and (b). PAHs was measured up to 17 mm HAB. This height was sufficient to show the distribution of PAH LIF concentrations along the flame. As shown in

Figure 7.8 (a) and (b), the signal profiles indicated that the relative concentrations of (2–3R) PAH LIF and (3–4R) PAH LIF gradually increased along the HAB and then levelled off at ~5, 9, 9 and 11-mm HAB with the C<sub>2</sub>H<sub>4</sub>-air, C<sub>2</sub>H<sub>4</sub>-air:N<sub>2</sub>, C<sub>2</sub>H<sub>4</sub>-air:CO<sub>2</sub> and C<sub>2</sub>H<sub>4</sub>-air:Ar, respectively. Further, the PAH LIF signals of different PAHs monotonically decreased with additive gases which indicates that CO<sub>2</sub>, N<sub>2</sub> and Ar additions chemically suppressed PAH formation.

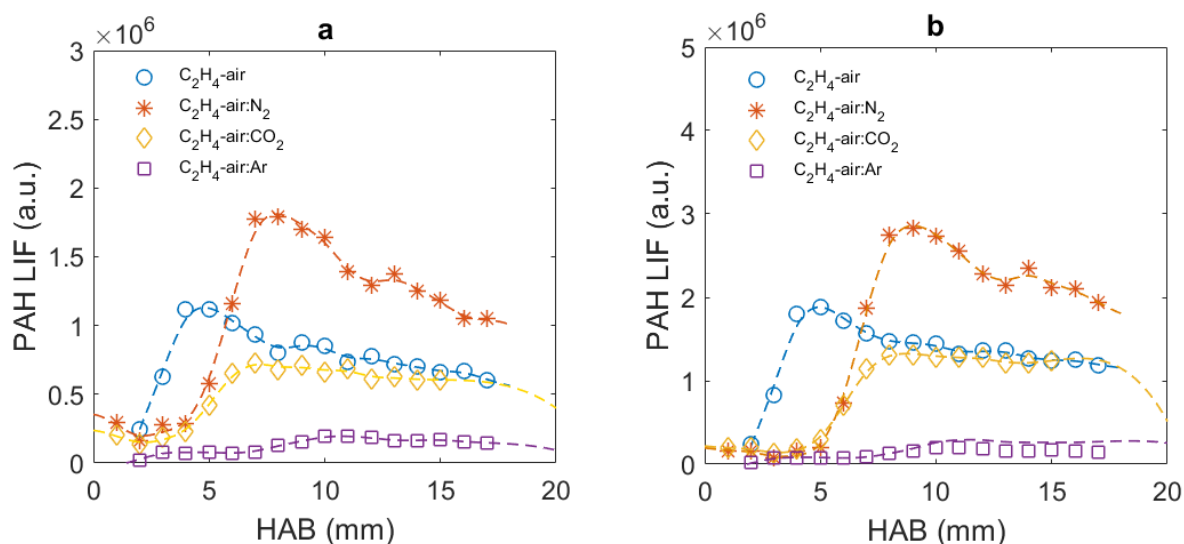


**Figure 7.8:** PAH LIF as a function of HAB; a, (2–3R) PAH LIF and b, (3–3R) PAH LIF with different gas additive at 40 kPa pressure

From Figure 7.9 a and Figure 7.9 b. The spatially phenomenological removing rate at 40 kPa of pressure was calculated using exponential fitting and the values were presented on Table 7.1. For ( $k_{phen}^{2-3R}$ ), the values were 14.1 s<sup>-1</sup>, 20.58 s<sup>-1</sup>, 7.87 s<sup>-1</sup> and 11.2 s<sup>-1</sup> for C<sub>2</sub>H<sub>4</sub>-air, C<sub>2</sub>H<sub>4</sub>-air:N<sub>2</sub>, C<sub>2</sub>H<sub>4</sub>-air:CO<sub>2</sub> and C<sub>2</sub>H<sub>4</sub>-air:Ar, respectively. The values for ( $k_{phen}^{3-4R}$ ) were 10.3 s<sup>-1</sup>, 14.53 s<sup>-1</sup>, 4.7 s<sup>-1</sup> and 3.9 s<sup>-1</sup> for C<sub>2</sub>H<sub>4</sub>-air, C<sub>2</sub>H<sub>4</sub>-air:N<sub>2</sub>, C<sub>2</sub>H<sub>4</sub>-air:CO<sub>2</sub> and C<sub>2</sub>H<sub>4</sub>-air:Ar, respectively.

The C<sub>2</sub>H<sub>4</sub>-air:Ar had the lowest effect on the removing rate on ( $k_{phen}^{3-4R}$ ), as compared to ( $k_{phen}^{2-3R}$ ), where C<sub>2</sub>H<sub>4</sub>-air:N<sub>2</sub> had the highest effect on the removing rates of PAHs on both the rings.

It is worth noting that the PAH removing rate for C<sub>2</sub>H<sub>4</sub>-air and C<sub>2</sub>H<sub>4</sub>-air:N<sub>2</sub> was close to the soot growth rate constant. In comparison, the PAHs removing rate constant for C<sub>2</sub>H<sub>4</sub>-air:CO<sub>2</sub> and C<sub>2</sub>H<sub>4</sub>-air:Ar was lower than the soot growth rate.

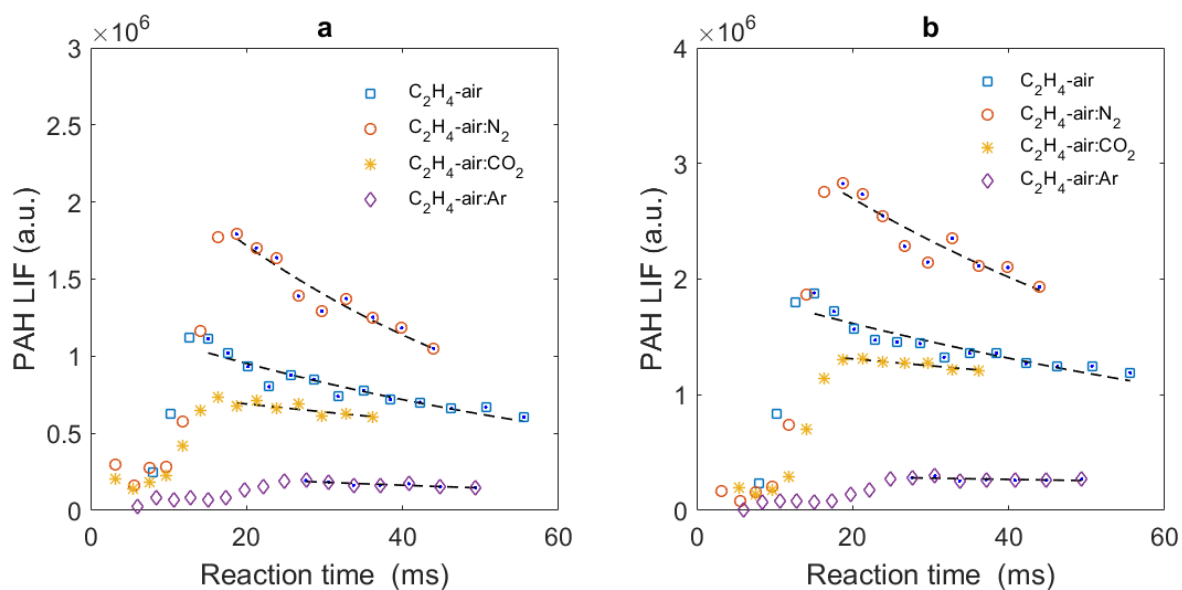


**Figure 7.9:** PAH LIF as a function of time and a fit curve (dashed line) with different PAH LIF a; (2–3R) PAH LIF and b; (3–4-R) PAH LIF at 40 kPa pressure.

Table 7.1: The spatially phenomenological removing rate constant of PAHs at 40 kPa pressure

Flame	The spatially phenomenological removing rate constant ( $s^{-1}$ )	
	( $k_{phen}^{2-3R}$ )	( $k_{phen}^{3-4R}$ )
$C_2H_4$ -air	14.1	10.3
$C_2H_4$ -air: $N_2$	20.58	14.53
$C_2H_4$ -air: $CO_2$	7.874	4.709
$C_2H_4$ -air:Ar	11.2	3.978

### 7.1.6 Spatial correlation among the measured parameters

Figure 7.10 shows superimposition of measured profiles including flame and soot temperatures,  $CH^*$  and  $C_2^*$  emissions, soot volume fractions and PAH LIF onto flame photographs at 40 kPa pressure. From spatial resolution as shown at Table 7.2. It was found that a separation occurs between the two radicals  $CH^*$  and  $C_2^*$ . However, it was interesting to find that the max intensity

of  $C_2^*$  radicals and (2–3R) PAH LIF overlapped. The locations of maximum (2–3R) PAH LIF were 4, 8, 8 and 10 mm HAB for the  $C_2H_4$ -air,  $C_2H_4$ -air: $N_2$ ,  $C_2H_4$ -air: $CO_2$  and  $C_2H_4$ -air:Ar, respectively. The soot formation locations also increased in the case of premixed flames. The soot formation locations were 5, 9, 9 and 11 mm HAB for the  $C_2H_4$ -air,  $C_2H_4$ -air: $N_2$ ,  $C_2H_4$ -air: $CO_2$  and  $C_2H_4$ -air:Ar flames, respectively. The soot volume fraction,  $f_v$ , decreased gradually in the case of  $C_2H_4$ -air: $N_2$ ,  $C_2H_4$ -air: $CO_2$  and  $C_2H_4$ -air:Ar flames. However, the locations for the soot volume fraction and removing of PAH LIF were found to be almost overlapping, corresponding temperatures remained unaffected for the types of flames under the experimental scheme.

It was inferred from the spatial representation that the location of maximum concentration of PAH LIF, the location of soot formation, the soot volume fraction and temperature were interconnected.

Table 7.2: Superimposition of the measured profiles.

Chemical species	Spatial location Max intensity (mm)			
	$C_2H_4$ -air	$C_2H_4$ -air: $N_2$	$C_2H_4$ -air: $CO_2$	$C_2H_4$ -air:Ar
$CH^*$	3	7	7	9
$C_2^*$	4	8	8	10
(2-3 R) PAH LIF	4	8	8	10
(3-4 R) PAH LIF	5	9	9	11
Soot inception	5	9	9	11

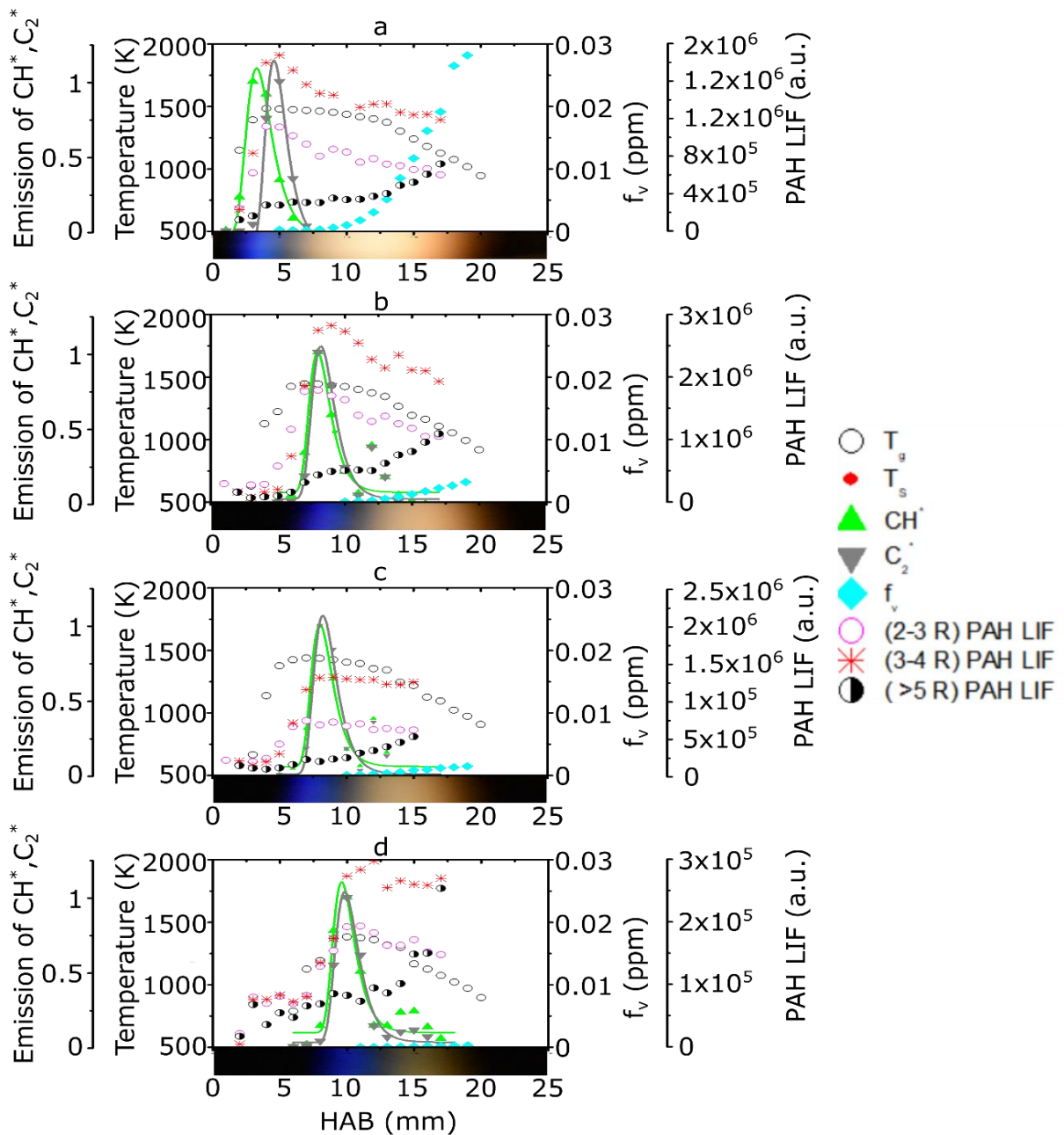


**Figure 7.10:** Superimposition of the measured profiles for flame and soot temperature, normalise of  $\text{CH}^*$  and  $\text{C}_2^*$  emissions, soot volume fractions and PAH LIF onto flame photographs at 40 kPa pressure for different gas addition; a,  $\text{C}_2\text{H}_4$ -air; b,  $\text{C}_2\text{H}_4$ -air: $\text{N}_2$ ; c,  $\text{C}_2\text{H}_4$ -air: $\text{CO}_2$ ; d,  $\text{C}_2\text{H}_4$ -air: $\text{Ar}$ .



## 7.2 Summary

Suppression of soot particle formation during combustion of gaseous fuels is particularly important as soot is harmful for the environment and human health. It was primarily observed that the introduction of some gases in the flame zone effectively suppressed soot formation although the exact mechanism is yet to be established in some cases. In the present experiment, premixed C<sub>2</sub>H<sub>4</sub> fuel with a constant equivalence ratio of 2.1 and at 40 kPa with the addition of CO<sub>2</sub>, N<sub>2</sub> and Ar gases was studied.

From the photographs of C<sub>2</sub>H<sub>4</sub>-air premixed flames, it can be concluded that the flame zone was reduced significantly by the addition of CO<sub>2</sub>, N<sub>2</sub> and Ar gases. Maximum reduction of the flame zone might be achieved by using Ar as an additive in fuel. It was known from previous studies that soot yield is proportional to the concentration of CH\* and C<sub>2</sub>\* near the flame zone. These could be expelled from the near flame zone by using premixed flames. Ar most effectively reduced the presence of those ions in the flame zone and thus soot suppression was achieved. The  $f_v$  decreased after addition of N<sub>2</sub>, CO<sub>2</sub> and Ar, but this was achieved most effectively with the addition of Ar.

Gaseous additives had no effect on the first soot initiation temperatures, which were 1458.52 K, 1414.51 K, 1406.21 K, and 1377.16 K for C<sub>2</sub>H<sub>4</sub>-air, C<sub>2</sub>H<sub>4</sub>-air:N<sub>2</sub>, C<sub>2</sub>H<sub>4</sub>-air:CO<sub>2</sub> and C<sub>2</sub>H<sub>4</sub>-air:Ar, respectively.

The soot surface growth rate constant ( $k_{SG}$ ) was found to be 8.3 s<sup>-1</sup>, 15.35 s<sup>-1</sup>, 35.65 s<sup>-1</sup> and 60.35 s<sup>-1</sup> for C<sub>2</sub>H<sub>4</sub>-air, C<sub>2</sub>H<sub>4</sub>-air:N<sub>2</sub>, C<sub>2</sub>H<sub>4</sub>-air:CO<sub>2</sub> and C<sub>2</sub>H<sub>4</sub>-air:Ar, respectively. The results show that the soot growth rate constant  $k_{SG}$  was high with the addition of Ar.

PAHs are known to be contributors to soot formation. The locations for the soot volume fraction and removal of PAH LIF were found to be almost overlapping. Ar was the most effective fuel diluent for shifting all types of PAH LIF and moving soot formation locations away from the flame zone. Thus, Ar proved to be the best additive for soot suppression even beyond the flame zone. The spatially phenomenological removing rate ( $k_{phen}^{2-3R}$ ) and ( $k_{phen}^{3-4R}$ ) were calculated. The values for ) were 14.1 s<sup>-1</sup>, 20.58 s<sup>-1</sup>, 7.87 s<sup>-1</sup> and 11.2 s<sup>-1</sup> with C<sub>2</sub>H<sub>4</sub>-air, C<sub>2</sub>H<sub>4</sub>-air:N<sub>2</sub>, C<sub>2</sub>H<sub>4</sub>-air:CO<sub>2</sub> and C<sub>2</sub>H<sub>4</sub>-air:Ar, respectively; while the values ( $k_{phen}^{3-4R}$ ) were 10.3 s<sup>-1</sup>, 14.53 s<sup>-1</sup>, 4.7 s<sup>-1</sup> and 3.9 s<sup>-1</sup> for C<sub>2</sub>H<sub>4</sub>-air, C<sub>2</sub>H<sub>4</sub>-air:N<sub>2</sub>, C<sub>2</sub>H<sub>4</sub>-air:CO<sub>2</sub> and C<sub>2</sub>H<sub>4</sub>-air:Ar, respectively. This indicates that N<sub>2</sub> has the highest effect on the removing rates of PAHs using ( $k_{phen}^{2-3R}$ ) and ( $k_{phen}^{3-4R}$ )

It is worth noting that the PAH removing rate for C<sub>2</sub>H<sub>4</sub>-air and C<sub>2</sub>H<sub>4</sub>-air:N<sub>2</sub> was close to the soot growth rate constant. In comparison, the PAH removing rate constant for C<sub>2</sub>H<sub>4</sub>-air:CO<sub>2</sub> and C<sub>2</sub>H<sub>4</sub>-air:Ar was lower than the soot growth rate

## Chapter 8: Conclusion

The objective of this study was to utilise optical laser diagnostics as a tool to better understand the inception phase and surface growth of soot particles. The work described in this thesis is based on the study of quasi-one-dimensional, premixed C<sub>2</sub>H<sub>4</sub>–air (plus another additive) flames stabilised on a McKenna burner under low-pressure conditions ranging from 27 – 48 kPa with equivalence ratios of 2.1 and 2.3.

The soot volume fraction, PAH LIF, chemiluminescence of CH\* and C<sub>2</sub>\*, flame temperature, and particle temperature were measured. Table 8.1 summarised the parameters that have been measured for all flame settings.

Chapter 5 and 6 focussed on the pressure dependence of soot formation in a series of flat premixed C<sub>2</sub>H<sub>4</sub>–air flames with a constant equivalence ratio of 2.1 and 2.3 at different pressures ranging from 27 to 48 kPa. It was found that the separation between CH\* and C<sub>2</sub>\*, measured as the distance between CH\*<sup>-max</sup> and C<sub>2</sub>\*<sup>-max</sup>, decreased linearly with an increase in pressure, with a slope of  $25 \times 10^{-9} \pm 0.062 \times 10^{-9}$  (mPa<sup>-1</sup>) and  $28 \times 10^{-9} \pm 0.048 \times 10^{-9}$  (mPa<sup>-1</sup>) at  $\Phi = 2.1$  and 2.3, respectively. Also, a very weak soot volume fraction ( $f_v$ ) of 0.0003 ppm was found at first soot inception; however,  $f_v$  scaled with pressure to the power range of  $2.15 \pm 0.7$  and  $1.5 \pm 0.4$  at  $\Phi = 2.1$  and 2.3, respectively. This is consistent with a previous study published with different fuel and pressure range conditions as the  $n$  value  $1 \leq n \leq 3$  [18, 96-110].

At  $\Phi = 2.1$  the soot growth rate constant,  $k_{SG}$ , was found to be 20 s<sup>-1</sup> at a pressure of 27 kPa. At  $\Phi = 2.3$ ,  $k_{SG}$  was found to be 32 s<sup>-1</sup>, 25.13 s<sup>-1</sup> and 12.11 s<sup>-1</sup> for pressures of 27 kPa, 32 kPa and 35 kPa, respectively. This is 80% lower as compared to the values reported in previous studies [12, 15, 109, 150-152]. However, the growth rate constant of the soot formation was found to be slightly higher at a high equivalence ratio and lower at a low equivalence ratio. The soot growth rate was also found to increase slightly with a decrease in pressure. This indicates that  $k_{SG}$  has a weak correlation with the pressure and equivalence ratio.

PAHs are known to contribute to soot formation. The starting location for soot formation coincides with the location of the observed decrease in PAHs. The spatially phenomenological removing rate constant of  $(k_{phen}^{2-3R})$  and  $(k_{phen}^{3-4R})$  were found to be 24.61 s<sup>-1</sup> and 21.46 s<sup>-1</sup>

respectively, at a pressure of 40 kPa. While at a pressure of 27 kPa,  $(k_{phen}^{2-3R})$  and  $(k_{phen}^{3-4R})$  were measured as  $15.29 \text{ s}^{-1}$  and  $18.26 \text{ s}^{-1}$  for  $(k_{phen}^{2-3R})$  and  $(k_{phen}^{3-4R})$ , respectively. For  $\Phi = 2.3$  and pressures of 40 kPa, the  $(k_{phen}^{2-3R})$  and  $(k_{phen}^{3-4R})$  were found to be  $23.33 \text{ s}^{-1}$  and  $16.9 \text{ s}^{-1}$ , respectively. The removing rates of PAHs were also found to be different at different pressures and equivalence ratios. The removing rates of the PAHs increase with increasing in pressure and with increases in the equivalence ratio.

For both at  $\Phi = 2.1$  and  $2.3$ , it was observed that the initial detection of soot particles took place at temperatures of  $\sim 1465 \pm 66 \text{ K}$ ,  $1332 \pm 62 \text{ K}$ , respectively.

Chapter 7 examined the effect of gas additives ( $\text{CO}_2$ ,  $\text{N}_2$  and Ar) on soot formation at a series of flat premixed  $\text{C}_2\text{H}_4$ -air flames with a constant equivalence ratio of 2.1 at 40 kPa. It was found that  $f_v$  decreased after the addition of  $\text{N}_2$ ,  $\text{CO}_2$  and Ar. The soot growth rate formation with additive gases differs based on the additive gas used. The results showed that  $\text{C}_2\text{H}_4$ -air created the lowest soot growth rate constant.  $\text{C}_2\text{H}_4$ -air diluted with Ar had the highest soot growth rate constant, as compared to other additive gases.

The spatially phenomenological removing rate  $(k_{phen}^{2-3R})$  and  $(k_{phen}^{3-4R})$  were calculated. For  $(k_{phen}^{2-3R})$  were  $14.1 \text{ s}^{-1}$ ,  $20.58 \text{ s}^{-1}$ ,  $7.8 \text{ s}^{-1}$  and  $11.2 \text{ s}^{-1}$  with  $\text{C}_2\text{H}_4$ -air,  $\text{C}_2\text{H}_4$ -air: $\text{N}_2$ ,  $\text{C}_2\text{H}_4$ -air: $\text{CO}_2$  and  $\text{C}_2\text{H}_4$ -air:Ar, respectively. The values for  $(k_{phen}^{3-4R})$  were  $10.3 \text{ s}^{-1}$ ,  $14.53 \text{ s}^{-1}$ ,  $4.7 \text{ s}^{-1}$  and  $3.9 \text{ s}^{-1}$  for  $\text{C}_2\text{H}_4$ -air,  $\text{C}_2\text{H}_4$ -air: $\text{N}_2$ ,  $\text{C}_2\text{H}_4$ -air: $\text{CO}_2$  and  $\text{C}_2\text{H}_4$ -air:Ar, respectively. With additive gases, the removing rates of the PAHs depended on the dilution of the soot, which later leads to loading of the soot. Additives gasses with high dilution rates saw the rate of soot loading increase, thus having a negligible effect on the removing of the PAHs at the different rings.

When the loading of soot is low, the dilution rate of the additive gasses was also shown to be low, which lead to a significant effect on the removing rate of the PAHs on the gases. Therefore, these results show that the formation of soot is dependent on the type of additive gasses used during the experimental process. This difference is based on the fact that each additive will have a different oxidation rate with the premixed ethylene air.

The determination of the spatially phenomenological removal rate of soot formation was key for this study, presumably due to the PAHs being consumed to increase soot amounts [160]. This study found that the value of the PAHs removing rate is found to be identical to the soot growth rate at  $\Phi = 2.1$ , but when Ar and  $\text{CO}_2$  were added, the PAHs removing rate became lower.

However, the temperature also was affected when a gas was added to the flame as the temperature became lower; as with gas additives, the soot particle detection occurred at temperatures of 1458.52 K, 1414.51 K, 1406.21 K and 1377.16 K for C<sub>2</sub>H<sub>4</sub>-air, C<sub>2</sub>H<sub>4</sub>-air:N<sub>2</sub>, C<sub>2</sub>H<sub>4</sub>-air:CO<sub>2</sub> and C<sub>2</sub>H<sub>4</sub>-air:Ar, respectively. This relationship between the PAHs removal rate and soot growth rate has been reported here for the first time. However, the observed correlation between (2–3 R) PAH LIF and C<sub>2</sub><sup>\*</sup> may be useful for understanding soot formation.

Table 8. 1: Summarised of parameter measured

Parameter measured	Technique Used	Note
Pr	Baratron (MKS, 122AA-0100AB)	Stable pressure by QPV1
f <sub>v</sub>	Spatially resolved Laser- induce incandescence (LII).	Change burner position
CH <sup>*</sup>	Spatially resolved emission spectroscopy.	Change fiber optic position
C <sub>2</sub> <sup>*</sup>	Spatially resolved emission spectroscopy.	Change fiber optic position
T <sub>s</sub>	Spatially resolved emission spectroscopy.	Change fiber optic position
T <sub>g</sub>	Thermocouple probe	Change burner position
(2-3R) PAH LIF	Spatially resolved Laser induced fluorescence.	Change burner position
(3-4R) PAH LIF	Spatially resolved Laser induced fluorescence.	Change burner position
(5and more R) PAH LIF	Spatially resolved Laser induced fluorescence.	Change burner position
C <sup>old flow</sup>	Hot wire probe	Change burner position
V <sup>flame</sup>	Modelled by CFD	

## References

1. Stocker TF, Qin D, Plattner G-K, Tignor M, Allen SK, Boschung J, et al. Climate change 2013: The physical science basis. Cambridge University Press Cambridge; 2013.
2. Jacobson MZ. Strong radiative heating due to the mixing state of black carbon in atmospheric aerosols. *Nature*. 2001;409(6821):695-7.
3. Johansen BE. The Encyclopedia of Global Warming Science and Technology: Greenwood Press/ABC-CLIO; 2009.
4. Blacha T, Di Domenico M, Gerlinger P, Aigner M. Soot predictions in premixed and non-premixed laminar flames using a sectional approach for PAHs and soot. *Combustion and Flame*. 2012;159(1):181-93.
5. Mansurov Z. Soot formation in combustion processes (review). *Combustion, Explosion and Shock Waves*. 2005;41(6):727-44.
6. Wersborg BL, Fox LK, Howard JB. Soot concentration and absorption coefficient in a low-pressure flame. *Combustion and Flame*. 1975;24:1-10.
7. Roth P, Hospital A. Twenty-Fourth Symposium on Combustion Mass growth and coagulation of soot particles in low pressure flames. *Symposium (International) on Combustion*. 1992;24(1):981-9.
8. Mouton T, Mercier X, Wartel M, Lamoureux N, Desgroux P. Laser-induced incandescence technique to identify soot nucleation and very small particles in low-pressure methane flames. *Applied Physics B*. 2013;112(3):369-79.
9. Mauss F, Schäfer T, Bockhorn H. Inception and growth of soot particles in dependence on the surrounding gas phase. *Combustion and Flame*. 1994;99(3):697-705.
10. Desgroux P, Mercier X, Thomson KA. Study of the formation of soot and its precursors in flames using optical diagnostics. *Proceedings of the Combustion Institute*. 2013;34(1):1713-38.
11. Desgroux P, Faccinnetto A, Mercier X, Mouton T, Aubagnac Karkar D, El Bakali A. Comparative study of the soot formation process in a “nucleation” and a “sooting” low pressure premixed methane flame. *Combustion and Flame*. 2017;184:153-66.
12. Bockhorn H, Fetting F, Heddrich A, Wannemacher G. Investigation of the surface growth of soot in flat low pressure hydrocarbon oxygen flames. *Symposium (International) on Combustion*. 1985;20(1):979-88.
13. Bockhorn H, Fetting F, Heddrich A. Twenty-First Symposium (International on Combustion) Investigation of particle inception in sooting premixed hydrocarbon oxygen low pressure flames. *Symposium (International) on Combustion*. 1988;21(1):1001-12.
14. Bladh H, Olofsson N-E, Mouton T, Simonsson J, Mercier X, Faccinnetto A, et al. Probing the smallest soot particles in low-sooting premixed flames using laser-induced incandescence. *Proceedings of the Combustion Institute*. 2015;35(2):1843-50.
15. Desgroux P, Mercier X, Lefort B, Lemaire R, Therssen E, Pauwels JF. Soot volume fraction measurement in low-pressure methane flames by combining laser-induced incandescence and cavity ring-down spectroscopy: Effect of pressure on soot formation. *Combustion and Flame*. 2008;155(1-2):289-301.
16. Faccinnetto A, Desgroux P, Ziskind M, Therssen E, Focsa C. High-sensitivity detection of polycyclic aromatic hydrocarbons adsorbed onto soot particles using laser desorption/laser ionization/time-of-flight mass spectrometry: An approach to studying the soot inception process in low-pressure flames. *Combustion and Flame*. 2011;158(2):227-39.
17. Haynes BS, Wagner HG. Soot formation. *Progress in energy and combustion science*. 1981;7(4):229-73.

18. Karataş AE, Gülder ÖL. Dependence of sooting characteristics and temperature field of co-flow laminar pure and nitrogen-diluted ethylene–air diffusion flames on pressure. *Combustion and Flame*. 2015;162(4):1566-74.
19. Wang H. Formation of nascent soot and other condensed-phase materials in flames. *Proceedings of the Combustion Institute*. 2011;33(1):41-67.
20. Michelsen HA, Schulz C, Smallwood GJ, Will S. Laser-induced incandescence: Particulate diagnostics for combustion, atmospheric, and industrial applications. *Progress in Energy and Combustion Science*. 2015;51:2-48.
21. D'Anna A. Combustion-formed nanoparticles. *Proceedings of the Combustion Institute*. 2009;32(1):593-613.
22. D'Anna A, Violi A, D'Alessio A, Sarofim AF. A reaction pathway for nanoparticle formation in rich premixed flames. *Combustion and Flame*. 2001;127(1):1995-2003.
23. Turns SR. *An introduction to combustion: McGraw-hill New York*; 1996.
24. Poinot T, Veynante D. *Combustion, Encyclopedia of Computational Mechanics*. John Wiley&Sons. 2004.
25. Vander Wal RL. Soot precursor carbonization: Visualization using LIF and LII and comparison using bright and dark field TEM. *Combustion and Flame*. 1998;112(4):607-16.
26. Dobbins RA, Fletcher RA, Chang HC. The evolution of soot precursor particles in a diffusion flame. *Combustion and Flame*. 1998;115(3):285-98.
27. Dobbins RA, Subramaniasivam H. Soot Precursor Particles in Flames. In: Bockhorn H, editor. *Soot Formation in Combustion: Mechanisms and Models*. Berlin, Heidelberg: Springer Berlin Heidelberg; 1994. p. 290-301.
28. Alfè M, Apicella B, Barbella R, Rouzaud JN, Tregrossi A, Ciajolo A. Structure–property relationship in nanostructures of young and mature soot in premixed flames. *Proceedings of the Combustion Institute*. 2009;32(1):697-704.
29. Elvati P, Dillstrom VT, Violi A. Oxygen driven soot formation. *Proceedings of the Combustion Institute*. 2017;36(1):825-32.
30. Commodo M, D'Anna A, De Falco G, Larciprete R, Minutolo P. Illuminating the earliest stages of the soot formation by photoemission and Raman spectroscopy. *Combustion and Flame*. 2017;181:188-97.
31. Russo C, Tregrossi A, Ciajolo A. Dehydrogenation and growth of soot in premixed flames. *Proceedings of the Combustion Institute*. 2015;35(2):1803-9.
32. Vander Wal RL, Ticich TM, Brock Stephens A. Can soot primary particle size be determined using laser-induced incandescence? *Combustion and Flame*. 1999;116(1):291-6.
33. D'Anna A, Commodo M, Sirignano M, Minutolo P, Pagliara R. Particle formation in opposed-flow diffusion flames of ethylene: An experimental and numerical study. *Proceedings of the Combustion Institute*. 2009;32(1):793-801.
34. Sirignano M, Collina A, Commodo M, Minutolo P, D'Anna A. Detection of aromatic hydrocarbons and incipient particles in an opposed-flow flame of ethylene by spectral and time-resolved laser induced emission spectroscopy. *Combustion and Flame*. 2012;159(4):1663-9.
35. D'Anna A, Commodo M, Violi S, Allouis C, Kent J. Nano organic carbon and soot in turbulent non-premixed ethylene flames. *Proceedings of the Combustion Institute*. 2007;31(1):621-9.
36. Omidvarborna H, Kumar A, Kim D-S. Recent studies on soot modeling for diesel combustion. *Renewable and Sustainable Energy Reviews*. 2015;48:635-47.
37. Karataş AE, Gülder ÖL. Soot formation in high pressure laminar diffusion flames. *Progress in Energy and Combustion Science*. 2012;38(6):818-45.
38. Bockhorn H. *Combustion Generated Fine Carbonaceous Particles: KIT Scientific Publishing*; 2009.

39. Karatas AE. Soot formation in co-flow and counterflow laminar diffusion flames of fuel mixtures: University of Toronto; 2009.
40. Kamp CJ. Multiscale methods for the fundamental understanding of diesel soot mitigation: Chalmers University of Technology; 2011.
41. McEnally CS, Pfefferle LD, Atakan B, Kohse-Höinghaus K. Studies of aromatic hydrocarbon formation mechanisms in flames: Progress towards closing the fuel gap. *Progress in Energy and Combustion Science*. 2006;32(3):247-94.
42. Naydenova II. Soot formation modeling during hydrocarbon pyrolysis and oxidation behind shock waves. Doktorarbeit, Ruprecht-Karls-Universität Heidelberg. 2007.
43. Mitchell P, Frenklach M, editors. Monte Carlo simulation of soot aggregation with simultaneous surface growth-why primary particles appear spherical. *Symposium (International) on Combustion*; 1998: Elsevier.
44. HARRIS SJ, WEINER AM. Determination of the rate constant for soot surface growth. *Combustion science and technology*. 1983;32(5-6):267-75.
45. Frenklach M, editor On surface growth mechanism of soot particles. *Symposium (International) on Combustion*; 1996: Elsevier.
46. Lou C, Chen C, Sun Y, Zhou H. Review of soot measurement in hydrocarbon-air flames. *Science China Technological Sciences*. 2010;53(8):2129-41.
47. Eckbreth AC. *Laser diagnostics for combustion temperature and species*: CRC Press; 1996.
48. Weeks R, Duley W. Aerosol-particle sizes from light emission during excitation by TEA CO<sub>2</sub> laser pulses. *Journal of Applied physics*. 1974;45(10):4661-2.
49. Eckbreth AC. Effects of laser-modulated particulate incandescence on Raman scattering diagnostics. *Journal of Applied Physics*. 1977;48(11):4473-9.
50. Melton LA. Soot diagnostics based on laser heating. *Appl Opt*. 1984;23(13):2201-8.
51. Bengtsson PE, Aldén M. Soot-visualization strategies using laser techniques. *Applied Physics B*. 1995;60(1):51-9.
52. Bladh H, Johnsson J, Bengtsson P-E. On the dependence of the laser-induced incandescence (LII) signal on soot volume fraction for variations in particle size. *Applied Physics B*. 2008;90(1):109-25.
53. Cignoli F, Benecchi S, Zizak G. Simultaneous one-dimensional visualization of OH, polycyclic aromatic hydrocarbons, and soot in a laminar diffusion flame. *Optics Letters*. 1992;17(4):229-31.
54. Jeffries JB, Copeland RA, Smith GP, Crosley DR. Multiple species laser-induced fluorescence in flames. *Symposium (International) on Combustion*. 1988;21(1):1709-18.
55. Kohse-Höinghaus K. Laser techniques for the quantitative detection of reactive intermediates in combustion systems. *Progress in Energy and Combustion Science*. 1994;20(3):203-79.
56. Rensberger KJ, Jeffries JB, Copeland RA, Kohse-Höinghaus K, Wise ML, Crosley DR. Laser-induced fluorescence determination of temperatures in low pressure flames. *Appl Opt*. 1989;28(17):3556-66.
57. McManus K, Yip B, Candel S. Emission and laser-induced fluorescence imaging methods in experimental combustion. *Experimental Thermal and Fluid Science*. 1995;10(4):486-502.
58. Schoemaeker Moreau C, Therssen E, Mercier X, Pauwels JF, Desgroux P. Two-color laser-induced incandescence and cavity ring-down spectroscopy for sensitive and quantitative imaging of soot and PAHs in flames. *Applied Physics B*. 2004;78(3):485-92.
59. Vander Wal RL, Jensen KA, Choi MY. Simultaneous laser-induced emission of soot and polycyclic aromatic hydrocarbons within a gas-jet diffusion flame. *Combustion and Flame*. 1997;109(3):399-414.



60. Smyth KC, Shaddix CR, Everest DA. Aspects of soot dynamics as revealed by measurements of broadband fluorescence and flame luminosity in flickering diffusion flames. *Combustion and Flame*. 1997;111(3):185-207.
61. Ossler F, Metz T, Aldén M. Picosecond laser-induced fluorescence from gas-phase polycyclic aromatic hydrocarbons at elevated temperatures. II. Flame-seeding measurements. *Applied Physics B*. 2001;72(4):479-89.
62. Bejaoui S, Mercier X, Desgroux P, Therssen E. Laser induced fluorescence spectroscopy of aromatic species produced in atmospheric sooting flames using UV and visible excitation wavelengths. *Combustion and Flame*. 2014;161(10):2479-91.
63. Hayashida K, Mogi T, Amagai K, Arai M. Growth characteristics of polycyclic aromatic hydrocarbons in dimethyl ether diffusion flame. *Fuel*. 2011;90(2):493-8.
64. Minutolo P, Gambi G, D'ALESSIO A, D'ANNA A. Optical and spectroscopic characterization of rich premixed flames across the soot formation threshold. *Combustion science and technology*. 1994;101(1-6):311-25.
65. Homann KH. Formation of large molecules, particulates and ions in premixed hydrocarbon flames; Progress and unresolved questions. *Symposium (International) on Combustion*. 1985;20(1):857-70.
66. Lakowicz JR. *Principles of Fluorescence Spectroscopy*: Springer US; 2007.
67. Bruno A, de Lisio C, Minutolo P, D'Alessio A. Evidence of fluorescent carbon nanoparticles produced in premixed flames by time-resolved fluorescence polarization anisotropy. *Combustion and Flame*. 2007;151(3):472-81.
68. Gaydon A. *The spectroscopy of flames*: springer science & business media; 2012.
69. Hardalupas Y, Orain M, S. Panoutsos C, Taylor AMKP, Olofsson J, Seyfried H, et al. Chemiluminescence sensor for local equivalence ratio of reacting mixtures of fuel and air (FLAMESEEK). *Applied Thermal Engineering*. 2004;24(11–12):1619-32.
70. Higgins B, McQuay MQ, Lacas F, Candel S. An experimental study on the effect of pressure and strain rate on CH chemiluminescence of premixed fuel-lean methane/air flames. *Fuel*. 2001;80(11):1583-91.
71. Kojima J, Ikeda Y, Nakajima T. Spatially resolved measurement of OH\*, CH\*, and C2\* chemiluminescence in the reaction zone of laminar methane/air premixed flames. *Proceedings of the Combustion Institute*. 2000;28(2):1757-64.
72. Zhang T, Guo Q, Liang Q, Dai Z, Yu G. Distribution Characteristics of OH\*, CH\*, and C2\* Luminescence in CH4/O2 Co-Flow Diffusion Flames. *Energy & Fuels*. 2012;26(9):5503-8.
73. Vagelopoulos CM, Frank JH. An experimental and numerical study on the adequacy of CH as a flame marker in premixed methane flames. *Proceedings of the Combustion Institute*. 2005;30(1):241-9.
74. Donbar JM, Driscoll JF, Carter CD. Reaction zone structure in turbulent nonpremixed jet flames—from CH-OH PLIF images. *Combustion and Flame*. 2000;122(1):1-19.
75. CThJ A, Hermann R. *Fundamentals of analytical flame spectroscopy*. Hilger, Bristol. 1979.
76. Gaydon AG, Wolfhard HG. *Flames, their structure, radiation, and temperature*: Halsted Press; 1979.
77. Tamura M, Berg PA, Harrington JE, Luque J, Jeffries JB, Smith GP, et al. Collisional quenching of CH (A), OH (A), and NO (A) in low pressure hydrocarbon flames. *Combustion and Flame*. 1998;114(3-4):502-14.
78. Grebe J, Homann K. Kinetics of the Species OH (A2Σ+), OH (X2Π and CH (X2Π) in the System C2H2/O/H. *Berichte der Bunsengesellschaft für physikalische Chemie*. 1982;86(7):581-7.
79. Glass GP, Kistiakowsky GB, Michael JV, Niki H. The oxidation reactions of acetylene and methane. *Symposium (International) on Combustion*. 1965;10(1):513-22.

80. Hall J, De Vries J, Amadio A, Petersen E, editors. Towards a kinetics model of CH chemiluminescence. 43rd AIAA Aerospace Sciences Meeting and Exhibit; 2005.
81. Devriendt K, Van Look H, Ceursters B, Peeters J. Kinetics of formation of chemiluminescent CH (A $2\Delta$ ) by the elementary reactions of C $2$ H (X $2\ \Sigma^+$ ) with O (3P) and O $2$  (X $3\Sigma_g^-$ ): A pulse laser photolysis study. *Chemical physics letters*. 1996;261(4-5):450-6.
82. Renlund A, Shokoohi F, Reisler H, Wittig C. Reaction of ethynyl radical with oxygen. Chemiluminescent products. *The Journal of Physical Chemistry*. 1982;86(21):4165-70.
83. Elsamra RM, Vranckx S, Carl SA. CH (A $2\Delta$ ) formation in hydrocarbon combustion: The temperature dependence of the rate constant of the reaction C $2$ H+ O $2$ → CH (A $2\Delta$ )+ CO $2$ . *The Journal of Physical Chemistry A*. 2005;109(45):10287-93.
84. Smith GP, Luque J, Park C, Jeffries JB, Crosley DR. Low pressure flame determinations of rate constants for OH(A) and CH(A) chemiluminescence. *Combustion and Flame*. 2002;131(1):59-69.
85. Smith GP, Park C, Luque J. A note on chemiluminescence in low-pressure hydrogen and methane–nitrous oxide flames. *Combustion and flame*. 2005;140(4):385-9.
86. Savadatti M, Broida H. Spectral study of flames of carbon vapor at low pressure. *The Journal of Chemical Physics*. 1966;45(7):2390-6.
87. Smith GP, Park C, Schneiderman J, Luque J. C $2$  Swan band laser-induced fluorescence and chemiluminescence in low-pressure hydrocarbon flames. *Combustion and flame*. 2005;141(1-2):66-77.
88. Kathrotia T, Riedel U, Seipel A, Moshhammer K, Brockhinke A. Experimental and numerical study of chemiluminescent species in low-pressure flames. *Applied Physics B*. 2012;107(3):571-84.
89. Kinzie PA, Rubin LG. Thermocouple temperature measurement. *Physics Today*. 1973;26:52.
90. Heitor MV, Moreira ALN. Thermocouples and sample probes for combustion studies. *Progress in Energy and Combustion Science*. 1993;19(3):259-78.
91. Kent J. A Noncatalytic Coating for Platinum-Rhodium Thermocouples. *Combustion and Flame*. 1970;14:279-82.
92. McEnally CS, Köylü ÜÖ, Pfefferle LD, Rosner DE. Soot volume fraction and temperature measurements in laminar nonpremixed flames using thermocouples. *Combustion and Flame*. 1997;109(4):701-20.
93. De Falco G, Commodo M, D'Anna A, Minutolo P. The evolution of soot particles in premixed and diffusion flames by thermophoretic particle densitometry. *Proceedings of the Combustion Institute*. 2017;36(1):763-70.
94. Bockhorn H, Fetting F, Heddrich A. Investigation of particle inception in sooting premixed hydrocarbon oxygen low pressure flames. *Symposium (International) on Combustion*. 1988;21(1):1001-12.
95. Wersborg BL, Fox LK, Howard JB. Soot concentration and absorption coefficient in a low-pressure flame. *Combustion and Flame*. 1975;24(C):1-10.
96. Zhou L, Xiong G, Zhang M, Chen L, Ding S, de Goey LPH. Experimental study of Polycyclic Aromatic Hydrocarbons (PAHs) in n-Heptane laminar diffusion flames from 1.0 to 3.0 bar. *Fuel*. 2017;209:265-73.
97. Steinmetz SA, Fang T, Roberts WL. Soot particle size measurements in ethylene diffusion flames at elevated pressures. *Combustion and Flame*. 2016;169:85-93.
98. Zhou L, Dam NJ, Boot MD, de Goey LPH. Measurements of sooting tendency in laminar diffusion flames of n-heptane at elevated pressure. *Combustion and Flame*. 2013;160(11):2507-16.

99. Liu F, Thomson KA, Guo H, Smallwood GJ. Numerical and experimental study of an axisymmetric coflow laminar methane–air diffusion flame at pressures between 5 and 40 atmospheres. *Combustion and Flame*. 2006;146(3):456-71.
100. Bento DS, Thomson KA, Gülder ÖL. Soot formation and temperature field structure in laminar propane–air diffusion flames at elevated pressures. *Combustion and Flame*. 2006;145(4):765-78.
101. Thomson KA, Gülder ÖL, Weckman EJ, Fraser RA, Smallwood GJ, Snelling DR. Soot concentration and temperature measurements in co-annular, nonpremixed CH<sub>4</sub>/air laminar flames at pressures up to 4 MPa. *Combustion and Flame*. 2005;140(3):222-32.
102. McCrain LL, Roberts WL. Measurements of the soot volume field in laminar diffusion flames at elevated pressures. *Combustion and Flame*. 2005;140(1-2):60-9.
103. Gulder OL, Thomson KA, Weckman EJ, Fraser RA, Smallwood GJ, Snelling DR. Influence of Pressure on Soot Formation in Laminar Diffusion Flames of Methane-Air up to 40 bar. 2005.
104. Lee W, Na YD. Soot Study in Laminar Diffusion Flames at Elevated Pressure Using Two-Color Pyrometry and Abel Inversion. *JSME International Journal Series B*. 2000;43(4):550-5.
105. Bae M-w, Kim K-s. A study on soot formation in premixed constant-volume propane combustion. *KSME Journal*. 1994;8(2):175-82.
106. Bönig M, Feldermann C, Jander H, Lüers B, Rudolph G, Wagner HG. Twenty-Third Symposium (International) on Combustion Soot formation in premixed C<sub>2</sub>H<sub>4</sub> flat flames at elevated pressure. *Symposium (International) on Combustion*. 1991;23(1):1581-7.
107. Flower WL. An investigation of soot formation in axisymmetric turbulent diffusion flames at elevated pressure. *Symposium (International) on Combustion*. 1989;22(1):425-35.
108. Böhm H, Hesse D, Jander H, Lüers B, Pietscher J, Wagner HGG, et al. The influence of pressure and temperature on soot formation in premixed flames. *Symposium (International) on Combustion*. 1989;22(1):403-11.
109. Mätzing H, Wagner HG. Measurements about the influence of pressure on carbon formation in premixed laminar C<sub>2</sub>H<sub>4</sub>-air flames. *Symposium (International) on Combustion*. 1988;21(1):1047-55.
110. Flower WL, Bowman CT. Twentieth Symposium (International) on Combustion Measurements of the structure of sooting laminar diffusion flames at elevated pressures. *Symposium (International) on Combustion*. 1985;20(1):1035-44.
111. Harris SJ, Weiner AM, editors. A picture of soot particle inception. *Symposium (International) on Combustion*; 1989: Elsevier.
112. Frenklach M, Wang H, editors. Detailed modeling of soot particle nucleation and growth. *Symposium (International) on Combustion*; 1991: Elsevier.
113. Wersborg BL, Howard JB, Williams GC, editors. Physical mechanisms in carbon formation in flames. *Symposium (International) on Combustion*; 1973: Elsevier.
114. Colket MB, Hall RJ. Successes and uncertainties in modeling soot formation in laminar, premixed flames. *Soot formation in combustion*: Springer; 1994. p. 442-70.
115. Harris SJ, Weiner AM. Chemical kinetics of soot particle growth. *Annual Review of Physical Chemistry*. 1985;36(1):31-52.
116. Harris SJ, Weiner AM. Surface growth of soot particles in premixed ethylene/air flames. *Combustion Science and Technology*. 1983;31(3-4):155-67.
117. Bejaoui S, Lemaire R, Therssen E. Analysis of laser-induced fluorescence spectra obtained in spray flames of diesel and rapeseed methyl ester using the multiple-excitation wavelength laser-induced incandescence technique with IR, UV, and visible excitations. *Combustion Science and Technology*. 2015;187(6):906-24.

118. Du D, Axelbaum R, Law C. Soot formation in strained diffusion flames with gaseous additives. *Combustion and flame*. 1995;102(1-2):11-20.
119. Haynes B, Jander H, Mätzing H, Wagner HG, editors. The influence of gaseous additives on the formation of soot in premixed flames. *Symposium (International) on Combustion*; 1982: Elsevier.
120. Tang Q, Mei J, You X. Effects of CO<sub>2</sub> addition on the evolution of particle size distribution functions in premixed ethylene flame. *Combustion and Flame*. 2016;165:424-32.
121. Liu F, Guo H, Smallwood GJ, Gülder ÖL. The chemical effects of carbon dioxide as an additive in an ethylene diffusion flame: implications for soot and NO<sub>x</sub> formation. *Combustion and Flame*. 2001;125(1-2):778-87.
122. Karataş AE, Gülder ÖL. Effects of carbon dioxide and nitrogen addition on soot processes in laminar diffusion flames of ethylene-air at high pressures. *Fuel*. 2017;200:76-80.
123. Chen L, Zhou J, Zheng X, Wu J, Wu X, Gao X, et al. Effects of Carbon Dioxide Addition on the Soot Particle Sizes in an Ethylene/Air Flame. *Aerosol and Air Quality Research*. 2017;17(10):2522-32.
124. Mancarella S, Sully A, Derudi M, Rota R, Granata S, Faravelli T, et al., editors. Chemical and thermal effects of CO<sub>2</sub> addition in fuel-rich premixed ethylene flames. *Proceedings of the 8th International Conference on Chemical and Process Engineering*; 2007.
125. Zhang Y, Wang L, Liu P, Guan B, Ni H, Huang Z, et al. Experimental and kinetic study of the effects of CO<sub>2</sub> and H<sub>2</sub>O addition on PAH formation in laminar premixed C<sub>2</sub>H<sub>4</sub>/O<sub>2</sub>/Ar flames. *Combustion and Flame*. 2018;192:439-51.
126. El Bakali A, Mercier X, Wartel M, Acevedo F, Burns I, Gasnot L, et al. Modeling of PAHs in low pressure sooting premixed methane flame. *Energy*. 2012;43(1):73-84.
127. Appel J, Bockhorn H, Frenklach M. Kinetic modeling of soot formation with detailed chemistry and physics: laminar premixed flames of C<sub>2</sub> hydrocarbons. *Combustion and Flame*. 2000;121(1-2):122-36.
128. Elvati P, Violi A. Thermodynamics of poly-aromatic hydrocarbon clustering and the effects of substituted aliphatic chains. *Proceedings of the Combustion Institute*. 2013;34(1):1837-43.
129. Wang Y, Raj A, Chung SH. Soot modeling of counterflow diffusion flames of ethylene-based binary mixture fuels. *Combustion and Flame*. 2015;162(3):586-96.
130. Raj A, Sander M, Janardhanan V, Kraft M. A study on the coagulation of polycyclic aromatic hydrocarbon clusters to determine their collision efficiency. *Combustion and Flame*. 2010;157(3):523-34.
131. Migliorini F, De Iuliis S, Cignoli F, Zizak G. How “flat” is the rich premixed flame produced by your McKenna burner? *Combustion and Flame*. 2008;153(3):384-93.
132. Li H, Zhou Z, Niu Y, Yao J, Zhou D, Wang J. Effect of Pressure and Type of Fuel on Laminar Diffusion Flame Height at Subatmospheric Pressures. *Chemistry and Technology of Fuels and Oils*. 2015;51(4):389-96.
133. Köhler M, Geigle KP, Meier W, Crosland BM, Thomson KA, Smallwood GJ. Sooting turbulent jet flame: characterization and quantitative soot measurements. *Applied Physics B*. 2011;104(2):409-25.
134. Charalampopoulos T, Felske J. Refractive indices of soot particles deduced from in-situ laser light scattering measurements. *Combustion and flame*. 1987;68(3):283-94.
135. Kohse-Höinghaus K, Jeffries JB. *Applied combustion diagnostics*. 2002.
136. Liu P, He Z, Hou G-L, Guan B, Lin H, Huang Z. The Diagnostics of Laser-Induced Fluorescence (LIF) Spectra of PAHs in Flame with TD-DFT: Special Focus on Five-Membered Ring. *The Journal of Physical Chemistry A*. 2015;119(52):13009-17.
137. Shaddix CR. Correcting thermocouple measurements for radiation loss: a critical review. Sandia National Labs., Livermore, CA (US); 1999.

138. Bird RB, Stewart WE, Lightfoot EN. Transport phenomena: John Wiley & Sons; 2007.
139. Goulay F, Schrader P, López-Yglesias X, Michelsen H. A data set for validation of models of laser-induced incandescence from soot: temporal profiles of LII signal and particle temperature. *Applied Physics B: Lasers & Optics*. 2013;112(3):287–306.
140. Dalzell W, Sarofim A. Optical constants of soot and their application to heat-flux calculations. *Journal of Heat Transfer*. 1969;91(1):100-4.
141. Abid A, Camacho J, Sheen D, Wang H. Quantitative measurement of soot particle size distribution in premixed flames – The burner-stabilized stagnation flame approach. *Combustion and Flame*. 2009;156:1862-70.
142. Beyler C. Flammability limits of premixed and diffusion flames. *SFPE handbook of fire protection engineering*: Springer; 2016. p. 529-53.
143. Bockhorn H. Soot formation in combustion: mechanisms and models: Springer Science & Business Media; 2013.
144. Appel J, Bockhorn H, Frenklach M. Kinetic modeling of soot formation with detailed chemistry and physics: laminar premixed flames of C<sub>2</sub> hydrocarbons. *Combustion and Flame*. 2000;121(1):122-36.
145. Zhao B, Yang Z, Li Z, Johnston MV, Wang H. Particle size distribution function of incipient soot in laminar premixed ethylene flames: effect of flame temperature. *Proceedings of the Combustion Institute*. 2005;30(1):1441-8.
146. Gomez A, Littman M, Glassman I. Comparative study of soot formation on the centerline of axisymmetric laminar diffusion flames: fuel and temperature effects. *Combustion and Flame*. 1987;70(2):225-41.
147. Saito K, Gordon A, Williams F, Stickle W. A study of the early history of soot formation in various hydrocarbon diffusion flames. *Combustion Science and Technology*. 1991;80(1-3):103-19.
148. McEnally CS, Pfefferle LD, editors. Flow time effects on hydrocarbon growth and soot formation in coflowing methane/air non-premixed flames. *Symposium (International) on Combustion*; 1998: Elsevier.
149. McEnally CS, Pfefferle LD. Comparison of non-fuel hydrocarbon concentrations measured in coflowing nonpremixed flames fueled with small hydrocarbons. *Combustion and flame*. 1999;117(1):362-72.
150. Tsurikov M, Geigle KP, Krüger V, Schneider-Kühnle Y, Stricker W, Lückerrath R, et al. Laser-based investigation of soot formation in laminar premixed flames at atmospheric and elevated pressures. *Combustion science and technology*. 2005;177(10):1835-62.
151. Baumgärtner L, Hesse D, Jander H, Wagner HG. Rate of soot growth in atmospheric premixed laminar flames. *Symposium (International) on Combustion*. 1985;20(1):959-67.
152. Dasch CJ. The decay of soot surface growth reactivity and its importance in total soot formation. *Combustion and Flame*. 1985;61(3):219-25.
153. Friedman CL, Zhang Y, Selin NE. Climate change and emissions impacts on atmospheric PAH transport to the Arctic. *Environmental science & technology*. 2013;48(1):429-37.
154. Miller JA, Pilling MJ, Troe J. Unravelling combustion mechanisms through a quantitative understanding of elementary reactions. *Proceedings of the Combustion Institute*. 2005;30(1):43-88.
155. Richter H, Howard JB. Formation of polycyclic aromatic hydrocarbons and their growth to soot—a review of chemical reaction pathways. *Progress in Energy and Combustion science*. 2000;26(4-6):565-608.
156. Liu F, He X, Ma X, Zhang Q, Thomson M, Guo H, et al. An experimental and numerical study of the effects of dimethyl ether addition to fuel on polycyclic aromatic hydrocarbon and

soot formation in laminar coflow ethylene/air diffusion flames. *Combustion and Flame*. 2011;158(3):547-63.

157. Yoon S, Lee S, Chung S. Effect of mixing methane, ethane, propane, and propene on the synergistic effect of PAH and soot formation in ethylene-base counterflow diffusion flames. *Proceedings of the Combustion Institute*. 2005;30(1):1417-24.

158. Frenklach M. Reaction mechanism of soot formation in flames. *Physical chemistry chemical Physics*. 2002;4(11):2028-37.

159. Wang H, Frenklach M. Calculations of rate coefficients for the chemically activated reactions of acetylene with vinylic and aromatic radicals. *The Journal of Physical Chemistry*. 1994;98(44):11465-89.

160. Dandajeh HA, Talibi M, Ladommatos N, Hellier P. Influence of Combustion Characteristics and Fuel Composition on Exhaust PAHs in a Compression Ignition Engine. *Energies*. 2019;12(13):2575.

161. Frenklach M, Clary DW, Gardiner WC, Stein SE. Effect of fuel structure on pathways to soot. *Symposium (International) on Combustion*. 1988;21(1):1067-76.

162. Teini PD, Karwat DMA, Atreya A. The effect of CO<sub>2</sub>/H<sub>2</sub>O on the formation of soot particles in the homogeneous environment of a rapid compression facility. *Combustion and Flame*. 2012;159(3):1090-9.

163. Wang Y, Chung SH. Formation of Soot in Counterflow Diffusion Flames with Carbon Dioxide Dilution. *Combustion Science and Technology*. 2016;188(4-5):805-17.

164. F. Xu HM, M. Chaos, and R.H. Chen. Effects of Dilution on Soot Formation in Laminar C<sub>2</sub>H<sub>4</sub> Diffusion Flame  
<http://www.icders.org/ICDERS2005/PapersICDERS2005/ICDERS2005-67.pdf>. [

165. Angrill O, Geitlinger H, Streibel T, Suntz R, Bockhorn H. Influence of exhaust gas recirculation on soot formation in diffusion flames. *Proceedings of the Combustion Institute*. 2000;28(2):2643-9.

166. Liu F, Guo H, Smallwood G, L Gülder Ö. The chemical effects of carbon dioxide as an additive in an ethylene diffusion flame: Implications for soot and NO<sub>x</sub> formation2001. 778-87 p.

167. Gu M, Chu H, Liu F. Effects of simultaneous hydrogen enrichment and carbon dioxide dilution of fuel on soot formation in an axisymmetric coflow laminar ethylene/air diffusion flame. *Combustion and Flame*. 2016;166:216-28.

## **Appendix A**

### **Mass flow controller calibration sheet**

To calibrate the tube and ball flowmeter, thermal mass flow controller (MFCs) from Bronkhorst High-Tech are used to precisely determine the separate flow of ethylene and air. Both mass flow controller (Model F-201CV-5K0-AAD-22-V) are connected and controlled via reader unit (Model E-5714-AAA). Calibration sheets for these MFCs are shown in Figure A.1 and Figure A.2.

**CALIBRATION CERTIFICATE**

**FLUID NO. 1 OF 1**  
 CERTIFICATE NO. BHT179/1855091

Calibration by comparison  
 Calibration date: 15 Jun 2015

We hereby certify that the instrument mentioned below has been calibrated in accordance with the stated values and conditions. The calibration standards used are traceable to national standards of the Dutch Metrology Institute VSL.

**Calibrated instrument**

Type Flow controller (D)  
 Serial number M15205655A  
 Model number F-201CV-5K0-AAD-22-V  
 Rated accuracy\*  $\pm(0.5\%Rd + 0.1\%FS)$

**Calibration standard**

Type Piston Prover  
 Serial number 80204  
 Certificate no. BCC001/1804351  
 Uncertainty  $\pm 0.3\% Rd$

**Customer conditions**

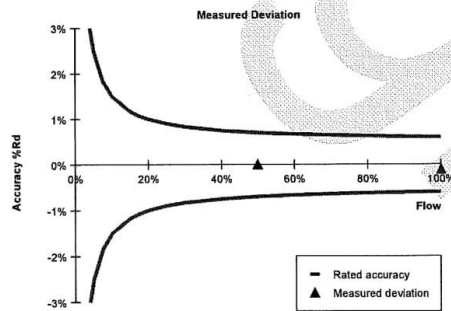
Fluid **C2H4**  
 Flow **4.000 In/min**  
 Pressure **760.0 torr (g)**  
 Temperature **20.0 °C**

**Calibration conditions**

Fluid **AIR**  
 Flow **6.467 In/min (equivalent flow)**  
 Pressure **5.0 bar (a)**  
 Temperature **23.5 °C**  
 Atm. pressure **1018.6 hPa (a)**

**Calibration and conversion results**

Output signal	Customer flow** C2H4	Equivalent flow** AIR	Reference flow AIR	Measured deviation*	Measurement uncertainty*
100.07%	4.003 In/min	6.471 In/min	6.478 In/min	-0.11 % Rd	0.4 % Rd
49.98%	1.999 In/min	3.246 In/min	3.246 In/min	0.00 % Rd	0.4 % Rd
0.00%	0.000 In/min	0.000 In/min	0.000 In/min	-	-



**Notes**

Flow unit In/min is defined at conditions 0.00 °C, 1013.25 hPa (a).  
 \* Rated accuracy, measured deviation and measurement uncertainty are specified under calibration conditions in digital mode.  
 \*\* The customer flow at customer conditions is converted to equivalent flow at calibration conditions using Bronkhorst High-Tech FLUIDAT® software.  
 Measurement uncertainties are based upon 95% (k=2) confidence limits. Although the item calibrated meets the specifications and performance at the time of calibration, due to any number of factors, this does not imply continuing conformance to the specifications.

Calibrator C.L.

QC A.F.K.  
 Date 17 Jun 2015  
 Signed .....

**Figure A.1: Calibration sheets for C<sub>2</sub>H<sub>4</sub> mass flow controller.**





**Bronkhorst**  
HIGH-TECH

**CALIBRATION CERTIFICATE**

**FLUID NO. 1 OF 1**

CERTIFICATE NO. BHTG19/1856276

Calibration by comparison  
Calibration date: 16 Jun 2015

We hereby certify that the instrument mentioned below has been calibrated in accordance with the stated values and conditions. The calibration standards used are traceable to national standards of the Dutch Metrology Institute VSL.

**Calibrated instrument**

Type Flow controller (D)  
Serial number M15205655B  
Model number F-201CV-10K-AAD-22-V  
Rated accuracy\*  $\pm(0.5\%Rd + 0.1\%FS)$

**Calibration standard**

Type Piston Prover  
Serial number M4200265A  
Certificate no. BCC001/1841917  
Uncertainty  $\pm 0.3\% Rd$

**Customer conditions**

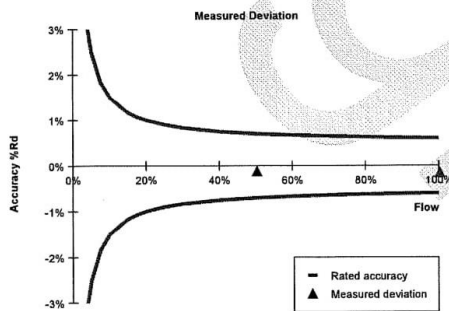
Fluid **AiR**  
Flow **10.00 In/min**  
Pressure **760.0 torr (g)**  
Temperature **20.0 °C**

**Calibration conditions**

Fluid **AiR**  
Flow **9.972 In/min (equivalent flow)**  
Pressure **5.0 bar (a)**  
Temperature **22.3 °C**  
Atm. pressure **1023.8 hPa (a)**

**Calibration and conversion results**

Output signal	Customer flow** AiR	Equivalent flow** AiR	Reference flow AiR	Measured deviation*	Measurement uncertainty*
100.28%	10.03 In/min	10.00 In/min	10.02 In/min	-0.15 % Rd	0.4 % Rd
50.35%	5.035 In/min	5.019 In/min	5.025 In/min	-0.12 % Rd	0.4 % Rd
0.00%	0.000 In/min	0.000 In/min	0.000 In/min	-	-



**Notes**

Flow unit In/min is defined at conditions 0.00 °C, 1013.25 hPa (a).

\* Rated accuracy, measured deviation and measurement uncertainty are specified under calibration conditions in digital mode.

\*\* The customer flow at customer conditions is converted to equivalent flow at calibration conditions using Bronkhorst High-Tech FLUIDAT® software.

Measurement uncertainties are based upon 95% (k=2) confidence limits. Although the item calibrated meets the specifications and performance at the time of calibration, due to any number of factors, this does not imply continuing conformance to the specifications.

Calibrator M.Se.

QC A.F.K.

Date 17 Jun 2015

Signed .....

**Figure A.2:** Calibration sheets for Air mass flow controller.

## **Appendix B**

### **Gas temperature after correction**

Gas temperature are corrected to compensate for heat and losses by radiation heat loses (see chapter 3, section 3.2.4.1 Thermocouple (gas phase)). The final temperatures results are shown on Table B.1 to Table B.5.

- Premixed Ethylene-Air at  $\Phi$  2.1.

Table B.1: Temperature after radiation correction for 48 kPa, 46 kPa and 40 kPa at  $\Phi$  2.1

HAB (mm)	Measured Temperature (K)	Corrected Temperature (K)	Measured Temperature (K)	Corrected Temperature (K)	Measured Temperature (K)	Corrected Temperature (K)
	48 kPa		46 kPa		40 kPa	
1	776	781.60	773	777.30	755	759.23
2	964	974.26	954	962.18	913	920.27
3	1180	1189.96	1174	1189.46	1160	1175.22
4	1333	1345.56	1268	1287.74	1254	1273.66
5	1373	1386.72	1363	1388.69	1353	1377.56
6	1434	1450.02	1399	1427.47	1435	1466.99
7	1453	1469.97	1464	1497.36	1476	1511.59
8	1464	1481.59	1470	1504.38	1474	1509.90
9	1433	1449.78	1443	1475.94	1465	1483.24
10	1434	1451.14	1440	1473.33	1450	1485.42
11	1383	1398.77	1392	1422.56	1406	1438.56
12	1375	1390.87	1373	1402.77	1393	1425.32
13	1370	1386.14	1372	1402.55	1383	1400.05
14	1354	1370.06	1369	1400.18	1384	1417.43
15	1352	1368.59	1358	1389.42	1371	1404.48
16	1333	1349.55	1344	1375.52	1354	1387.37
17	1331	1348.27	1339	1371.53	1353	1371.68
18	1314	1331.56	1309	1340.78	1330	1364.63
19	1302	1320.26	1305	1338.37	1322	1357.92
20	1293	1312.43	1295	1329.98	1309	1346.39

Table B.2: Temperature after radiation correction for 38 kPa, 35 kPa,32 kPa and 27 kPa at  $\Phi$  2.1

HAB (mm)	Measured Temperature (K)	Corrected Temperature (K)	Measured Temperature (K)	Corrected Temperature (K)	Measured Temperature (K)	Corrected Temperature (K)	Measured Temperature (K)	Corrected Temperature (K)
	38 kPa		35 kPa		32 kPa		27 kPa	
1	733	736.92	728	731.97	709	712.73	706	709.94
2	902	909.13	885	891.78	863	869.26	856	863.05
3	1148	1163.00	1133	1147.48	1120	1134.37	1112	1128.17
4	1244	1263.54	1234	1253.20	1210	1228.55	1208	1228.87
5	1355	1381.60	1343	1367.13	1323	1348.59	1321	1348.24
6	1436	1468.68	1434	1466.91	1423	1456.15	1433	1469.26
7	1480	1516.56	1473	1509.41	1473	1510.55	1475	1515.30
8	1473	1509.47	1474	1511.00	1478	1516.49	1482	1523.46
9	1474	1511.06	1473	1510.50	1485	1524.70	1489	1531.88
10	1452	1488.44	1453	1489.52	1448	1485.28	1451	1491.10
11	1414	1447.77	1425	1460.03	1442	1479.53	1449	1489.77
12	1393	1425.94	1403	1437.07	1420	1456.58	1416	1454.66
13	1395	1428.97	1403	1437.99	1415	1452.06	1413	1452.37
14	1392	1426.75	1402	1437.91	1414	1452.09	1413	1430.87
15	1383	1418.16	1389	1424.97	1403	1441.33	1410	1428.43
16	1365	1399.90	1376	1412.20	1393	1431.85	1403	1445.39
17	1363	1399.25	1372	1409.35	1383	1422.65	1393	1435.66
18	1334	1369.41	1344	1380.70	1362	1401.48	1372	1415.07
19	1332	1369.43	1339	1377.40	1353	1391.51	1362	1406.38
20	1315	1353.48	1324	1363.68	1343	1385.93	1348	1393.98

- Premixed Ethylene-Air at  $\Phi$  2.3.

Table B.3: Temperature after radiation correction for 48 kPa, 46 kPa and 40 kPa at  $\Phi$  2.3

HAB (mm)	Measured Temperature (K)	Corrected Temperature (K)	Measured Temperature (K)	Corrected Temperature (K)	Measured Temperature (K)	Corrected Temperature (K)
	48 (kPa)		46 (kPa)		40 (kPa)	
1	843	856.04	841	854.35	833	846.42
2	952	970.76	953	972.19	963	983.89
3	1057	1074.51	1063	1090.35	1073	1102.15
4	1153	1175.55	1158	1194.32	1163	1201.01
5	1253	1282.86	1265	1314.69	1282	1333.42
6	1269	1300.52	1271	1322.08	1274	1327.16
7	1275	1307.64	1278	1330.51	1295	1351.63
8	1283	1316.72	1292	1346.61	1302	1360.26
9	1288	1322.65	1284	1338.63	1295	1329.91
10	1302	1338.40	1308	1366.94	1315	1376.89
11	1313	1351.12	1318	1379.47	1324	1388.33
12	1333	1373.78	1335	1400.26	1343	1411.55
13	1329	1370.42	1334	1400.43	1349	1391.97
14	1348	1392.40	1352	1422.90	1358	1432.08
15	1344	1389.35	1349	1421.12	1363	1439.88
16	1339	1385.45	1344	1417.30	1359	1437.22
17	1334	1381.72	1344	1419.57	1354	1403.51
18	1323	1371.70	1335	1411.62	1342	1422.14
19	1318	1368.84	1324	1401.82	1339	1421.85
20	1295	1346.30	1304	1381.86	1313	1394.59

Table B.4: Temperature after radiation correction for 38 kPa, 35 kPa, 32 kPa and 27 kPa at  $\Phi$  2.3

HAB (mm)	Measured Temperature (K)	Corrected Temperature (K)	Measured Temperature (K)	Corrected Temperature (K)	Measured Temperature (K)	Corrected Temperature (K)	Measured Temperature (K)	Corrected Temperature (K)
	38 (kPa)		35 (kPa)		32 (kPa)		27 (kPa)	
1	773	783.68	772	782.92	753	763.41	733	743.03
2	973	995.10	982	1005.26	995	1020.21	1000	1027.03
3	1081	1111.19	1089	1120.40	1093	1125.63	1113	1149.61
4	1173	1212.52	1184	1225.37	1193	1236.51	1203	1250.27
5	1288	1342.94	1293	1349.42	1294	1352.04	1292	1352.88
6	1282	1336.75	1284	1339.83	1289	1346.95	1303	1366.36
7	1294	1350.96	1301	1359.87	1304	1364.78	1313	1378.56
8	1305	1364.24	1313	1374.35	1314	1377.00	1323	1390.91
9	1300	1359.18	1308	1369.35	1315	1378.94	1325	1394.06
10	1318	1380.85	1321	1385.21	1322	1387.99	1327	1397.33
11	1334	1400.41	1335	1402.55	1350	1421.82	1361	1438.58
12	1350	1420.38	1353	1424.89	1355	1428.91	1363	1442.19
13	1356	1428.72	1364	1439.13	1375	1454.00	1380	1464.06
14	1365	1441.01	1369	1446.70	1372	1452.12	1373	1418.05
15	1370	1448.79	1374	1454.59	1383	1467.12	1387	1434.93
16	1364	1443.68	1372	1454.36	1380	1465.71	1383	1473.47
17	1359	1440.09	1369	1453.13	1373	1459.85	1384	1477.28
18	1354	1436.94	1359	1444.10	1364	1451.82	1367	1459.60
19	1341	1424.82	1344	1429.35	1354	1443.29	1358	1451.98
20	1318	1401.08	1323	1407.98	1332	1420.57	1333	1425.54

- Premixed Ethylene-Air with different gas additive at  $\Phi$  2.1.

Table B.5: Temperature after radiation correction with different gas additive to flame.

HAB (mm)	Measured Temperature (K)	Corrected Temperature (K)	Measured Temperature (K)	Corrected Temperature (K)	Measured Temperature (K)	Corrected Temperature (K)	Measured Temperature (K)	Corrected Temperature (K)
	C <sub>2</sub> H <sub>4</sub> +Air		C <sub>2</sub> H <sub>4</sub> +Air+N <sub>2</sub>		C <sub>2</sub> H <sub>4</sub> +Air+CO <sub>2</sub>		C <sub>2</sub> H <sub>4</sub> +Air+Ar	
1	-	-	-	-	-	-	-	-
2	1122	1134.43	324	324.07	363	363.16	308	308.05
3	1345	1364.98	625	626.36	660	661.66	319	319.09
4	1450	1463.45	1110	1115.58	1121	1126.77	374	374.31
5	1445	1458.52	1203	1210.27	1349	1359.32	442	442.69
6	1441	1454.68	1394	1405.53	1394	1405.56	783	788.09
7	1435	1448.70	1414	1426.30	1408	1420.16	1109	1125.20
8	1429	1442.72	1413	1425.52	1405	1417.34	1174	1193.51
9	1419	1432.67	1402	1414.51	1394	1406.21	1343	1373.58
10	1404	1417.52	1391	1403.46	1374	1386.09	1353	1385.01
11	1384	1397.26	1370	1382.25	1363	1375.10	1345	1377.16
12	1368	1381.13	1343	1354.86	1325	1336.36	1330	1361.98
13	1341	1353.73	1315	1326.49	1313	1324.42	1290	1319.77
14	1273	1284.23	1240	1249.90	1220	1229.44	1270	1299.67
15	1213	1223.10	1170	1178.63	1194	1203.16	1144	1165.97
16	1156	1165.02	1140	1148.31	1105	1112.47	1104	1124.41
17	1104	1112.19	1085	1092.48	1075	1082.22	1054	1072.39
18	1055	1062.51	1035	1041.82	1005	1011.26	1004	1020.52
19	998	1004.72	975	981.02	956	961.59	955	969.91
20	930	935.81	904	909.13	893	897.90	883	895.26

## Appendix C

### Reaction time

#### 1) Flame C<sub>2</sub>H<sub>4</sub>-air at $\Phi$ 2.1 with total flow rate 5 Lmin<sup>-1</sup>:

Table C. 1: Reaction time calculation at 48 kPa

HAB (mm)	$V_{\text{flame}}$ (mm/s)	dt (ms)	Reaction time (ms)
0	65	0	0
1	109	9.17	9.17
2	139	7.19	16.37
3	218	4.59	20.96
4	295	3.39	24.35
5	296	3.38	27.72
6	280	3.57	31.30
7	269	3.72	35.01
8	261	3.83	38.84
9	252	3.97	42.81
10	242	4.13	46.94
11	230	4.35	51.29
12	218	4.59	55.88
13	205	4.88	60.76
14	192	5.21	65.97
15	177	5.65	71.62
16	162	6.17	77.79
17	146	6.85	84.64
18	129	7.75	92.39
19	111	9.01	101.40
20	92	10.87	112.27



Table C. 2: Reaction time calculation at 46 kPa

<b>HAB (mm)</b>	<b><math>V^{flame}</math> (mm/s)</b>	<b>dt (ms)</b>	<b>Reaction time (ms)</b>
0	72	0	0
1	194	5.15	5.15
2	231	4.33	9.48
3	278	3.60	13.08
4	282	3.55	16.63
5	268	3.73	20.36
6	258	3.88	24.23
7	251	3.98	28.22
8	243	4.12	32.33
9	233	4.29	36.63
10	223	4.48	41.11
11	212	4.72	45.83
12	201	4.98	50.80
13	188	5.32	56.12
14	176	5.68	61.80
15	162	6.17	67.98
16	148	6.76	74.73
17	133	7.52	82.25
18	117	8.55	90.80
19	101	9.90	100.70
20	84	11.90	112.60

Table C. 3: Reaction time calculation at 40 kPa

<b>HAB (mm)</b>	<b><math>V_{\text{flame}}</math> (mm/s)</b>	<b>dt (ms)</b>	<b>Reaction time (ms)</b>
0	73	0	0
1	189	5.29	5.29
2	243	4.12	9.41
3	291	3.44	12.84
4	296	3.38	16.22
5	281	3.56	19.78
6	271	3.69	23.47
7	262	3.82	27.29
8	254	3.94	31.22
9	246	4.07	35.29
10	231	4.33	39.62
11	222	4.50	44.12
12	210	4.76	48.88
13	197	5.08	53.96
14	184	5.43	59.39
15	170	5.88	65.28
16	155	6.45	71.73
17	139	7.19	78.92
18	123	8.13	87.05
19	106	9.43	96.49
20	88	11.36	107.85

Table C. 4: Reaction time calculation at 38 kPa

<b>HAB (mm)</b>	<b><math>V^{flame}</math> (mm/s)</b>	<b>dt (ms)</b>	<b>Reaction time (ms)</b>
0	74	0	0
1	191	5.24	5.24
2	247	4.05	9.28
3	297	3.37	12.65
4	302	3.31	15.96
5	287	3.48	19.45
6	277	3.61	23.06
7	269	3.72	26.77
8	261	3.83	30.61
9	251	3.98	34.59
10	234	4.27	38.86
11	228	4.39	43.25
12	215	4.65	47.90
13	202	4.95	52.85
14	188	5.32	58.17
15	174	5.75	63.92
16	159	6.29	70.21
17	143	6.99	77.20
18	127	7.87	85.07
19	109	9.17	94.25
20	91	10.99	105.24

Table C. 5: Reaction time calculation at 35 kPa

<b>HAB (mm)</b>	<b><math>V_{\text{flame}}</math> (mm/s)</b>	<b>dt (ms)</b>	<b>Reaction time (ms)</b>
0	76	0	0
1	189	5.29	5.29
2	257	3.89	9.18
3	313	3.19	12.38
4	318	3.14	15.52
5	302	3.31	18.83
6	291	3.44	22.27
7	282	3.55	25.82
8	273	3.66	29.48
9	263	3.80	33.28
10	252	3.97	37.25
11	239	4.18	41.43
12	226	4.42	45.86
13	212	4.72	50.57
14	198	5.05	55.63
15	183	5.46	61.09
16	167	5.99	67.08
17	151	6.62	73.70
18	133	7.52	81.22
19	115	8.70	89.91
20	96	10.42	100.33

Table C. 6: Reaction time calculation at 32 kPa

<b>HAB (mm)</b>	<b><math>V^{flame}</math> (mm/s)</b>	<b>dt (ms)</b>	<b>Reaction time (ms)</b>
0	70	0	0
1	191	5.24	5.24
2	275	3.64	8.87
3	315	3.17	12.05
4	320	3.13	15.17
5	304	3.29	18.46
6	292	3.42	21.89
7	284	3.52	25.41
8	275	3.64	29.04
9	265	3.77	32.82
10	253	3.95	36.77
11	241	4.15	40.92
12	227	4.41	45.32
13	214	4.67	50.00
14	199	5.03	55.02
15	184	5.43	60.46
16	168	5.95	66.41
17	151	6.62	73.03
18	134	7.46	80.49
19	116	8.62	89.12
20	96	10.42	99.53

Table C. 7: Reaction time calculation at 27 kPa

<b>HAB (mm)</b>	<b><math>V_{\text{flame}}</math> (mm/s)</b>	<b>dt (ms)</b>	<b>Reaction time (ms)</b>
0	77	0	0
1	195	5.13	5.13
2	233	4.29	9.42
3	270	3.70	13.12
4	287	3.48	16.61
5	311	3.22	19.82
6	299	3.34	23.17
7	291	3.44	26.60
8	282	3.55	30.15
9	270	3.70	33.85
10	259	3.86	37.72
11	246	4.07	41.78
12	233	4.29	46.07
13	219	4.57	50.64
14	204	4.90	55.54
15	188	5.32	60.86
16	172	5.81	66.67
17	155	6.45	73.12
18	137	7.30	80.42
19	119	8.40	88.83
20	99	10.10	98.93

2) Flame C<sub>2</sub>H<sub>4</sub>-air at  $\Phi$  2.3 with total flow rate 5 Lmin<sup>-1</sup>:

Table C. 8: Reaction time calculation at 48 kPa

HAB (mm)	$V_{\text{flame}}$ (mm/s)	dt (ms)	Reaction time (ms)
0	71	0	0
1	221	4.52	4.52
2	257	3.89	8.42
3	266	3.76	12.18
4	270	3.70	15.88
5	257	3.89	19.77
6	247	4.05	23.82
7	240	4.17	27.99
8	232	4.31	32.30
9	223	4.48	36.78
10	214	4.67	41.45
11	203	4.93	46.38
12	192	5.21	51.59
13	180	5.56	57.14
14	168	5.95	63.10
15	155	6.45	69.55
16	141	7.09	76.64
17	127	7.87	84.51
18	112	8.93	93.44
19	96	10.42	103.86
20	80	12.50	116.36

Table C. 9: Reaction time calculation at 46 kPa

<b>HAB (mm)</b>	<b><math>V_{\text{flame}}</math> (mm/s)</b>	<b>dt (ms)</b>	<b>Reaction time (ms)</b>
0	71	0	0
1	213	4.69	4.69
2	256	3.91	8.60
3	268	3.73	12.33
4	272	3.68	16.01
5	258	3.88	19.88
6	249	4.02	23.90
7	242	4.13	28.03
8	234	4.27	32.31
9	225	4.44	36.75
10	215	4.65	41.40
11	204	4.90	46.30
12	193	5.18	51.49
13	181	5.52	57.01
14	169	5.92	62.93
15	156	6.41	69.34
16	142	7.04	76.38
17	128	7.81	84.19
18	113	8.85	93.04
19	97	10.31	103.35
20	80.4	12.44	115.79



Table C. 10: Reaction time calculation at 40 kPa

<b>HAB (mm)</b>	<b><math>V^{flame}</math> (mm/s)</b>	<b>dt (ms)</b>	<b>Reaction time (ms)</b>
0	72	0	0
1	215	4.65	4.65
2	250	4.00	8.65
3	276	3.62	12.27
4	281	3.56	15.83
5	266	3.76	19.59
6	256	3.91	23.50
7	249	4.02	27.51
8	241	4.15	31.66
9	232	4.31	35.97
10	221	4.52	40.50
11	210	4.76	45.26
12	199	5.03	50.29
13	187	5.35	55.63
14	174	5.75	61.38
15	160	6.25	67.63
16	146	6.85	74.48
17	132	7.58	82.06
18	116	8.62	90.68
19	100	10.00	100.68
20	83	12.05	112.73

Table C. 11: Reaction time calculation at 38 kPa

<b>HAB (mm)</b>	<b><math>V^{flame}</math> (mm/s)</b>	<b>dt (ms)</b>	<b>Reaction time (ms)</b>
0	74	0	0
1	213	4.69	4.69
2	251	3.98	8.68
3	287	3.48	12.16
4	292	3.42	15.59
5	277	3.61	19.20
6	267	3.75	22.94
7	260	3.85	26.79
8	251	3.98	30.77
9	242	4.13	34.91
10	231	4.33	39.23
11	220	4.55	43.78
12	207	4.83	48.61
13	195	5.13	53.74
14	181	5.52	59.26
15	167	5.99	65.25
16	153	6.54	71.79
17	138	7.25	79.03
18	122	8.20	87.23
19	105	9.52	96.76
20	87	11.49	108.25

Table C. 12: Reaction time calculation at 35 kPa

<b>HAB (mm)</b>	<b><math>V^{flame}</math> (mm/s)</b>	<b>dt (ms)</b>	<b>Reaction time (ms)</b>
0	73	0	0
1	211	4.74	4.74
2	254	3.94	8.68
3	296	3.38	12.05
4	301	3.32	15.38
5	286	3.50	18.87
6	275	3.64	22.51
7	267	3.75	26.26
8	258	3.88	30.13
9	248	4.03	34.16
10	238	4.20	38.37
11	226	4.42	42.79
12	213	4.69	47.48
13	201	4.98	52.46
14	187	5.35	57.81
15	172	5.81	63.62
16	157	6.37	69.99
17	142	7.04	77.03
18	125	8.00	85.03
19	108	9.26	94.29
20	90	11.11	105.40

Table C. 13: Reaction time calculation at 32 kPa

<b>HAB (mm)</b>	<b><math>V^{flame}</math> (mm/s)</b>	<b>dt (ms)</b>	<b>Reaction time (ms)</b>
0	74	0	0
1	203	4.93	4.93
2	246	4.07	8.99
3	296	3.38	12.37
4	302	3.31	15.68
5	286	3.50	19.18
6	276	3.62	22.80
7	268	3.73	26.53
8	259	3.86	30.39
9	249	4.02	34.41
10	238	4.20	38.61
11	226	4.42	43.04
12	214	4.67	47.71
13	201	4.98	52.68
14	187	5.35	58.03
15	173	5.78	63.81
16	158	6.33	70.14
17	142	7.04	77.18
18	126	7.94	85.12
19	108	9.26	94.38
20	90.3	11.07	105.45

Table C. 14: Reaction time calculation at 27 kPa

<b>HAB (mm)</b>	<b><math>v_{\text{flame}}</math> (mm/s)</b>	<b>dt (ms)</b>	<b>Reaction time (ms)</b>
0	74	0	0
1	204	4.90	4.90
2	249	4.02	8.92
3	300	3.33	12.25
4	305	3.28	15.53
5	290	3.45	18.98
6	279	3.58	22.56
7	271	3.69	26.25
8	262	3.82	30.07
9	252	3.97	34.04
10	241	4.15	38.19
11	229	4.37	42.55
12	217	4.61	47.16
13	203	4.93	52.09
14	190	5.26	57.35
15	175	5.71	63.07
16	160	6.25	69.32
17	144	6.94	76.26
18	127	7.87	84.13
19	110	9.09	93.23
20	91.4	10.94	104.17

3) Flame C<sub>2</sub>H<sub>4</sub>-air with addition of specific gas with total flow rate 7 Lmin<sup>-1</sup> :

Table C. 15: Reaction time calculation from flame C<sub>2</sub>H<sub>4</sub>-air at pressure 40 kPa

<b>HAB (mm)</b>	<b>V<sub>flame</sub> (mm/s)</b>	<b>dt (ms)</b>	<b>Reaction time (ms)</b>
0	100	0	0
1	211	4.74	4.74
2	311	3.22	7.95
3	423	2.36	10.32
4	429	2.33	12.65
5	414	2.42	15.07
6	396	2.53	17.59
7	384	2.60	20.19
8	371	2.70	22.89
9	357	2.80	25.69
10	341	2.93	28.62
11	324	3.09	31.71
12	306	3.27	34.98
13	287	3.48	38.46
14	268	3.73	42.19
15	247	4.05	46.24
16	226	4.42	50.67
17	204	4.90	55.57
18	181	5.52	61.09
19	157	6.37	67.46
20	132	7.58	75.04

Table C. 16: Reaction time calculation from flame C<sub>2</sub>H<sub>4</sub>-air with addition of N<sub>2</sub> at pressure 40 kPa

<b>HAB (mm)</b>	<b>V<sup>flame</sup> (mm/s)</b>	<b>dt (ms)</b>	<b>Reaction time (ms)</b>
0	110	0	0
1	317	3.15	3.15
2	413	2.42	5.58
3	485	2.06	7.64
4	484	2.07	9.70
5	469	2.13	11.84
6	453	2.21	14.04
7	436	2.29	16.34
8	418	2.39	18.73
9	399	2.51	21.24
10	379	2.64	23.87
11	359	2.79	26.66
12	338	2.96	29.62
13	316	3.16	32.78
14	293	3.41	36.20
15	270	3.70	39.90
16	246	4.07	43.96
17	221	4.52	48.49
18	196	5.10	53.59
19	170	5.88	59.47
20	143	6.99	66.47

Table C. 17: Reaction time calculation from flame C<sub>2</sub>H<sub>4</sub>-air with addition of CO<sub>2</sub> at pressure 40 kPa

<b>HAB (mm)</b>	<b>V<sup>flame</sup> (mm/s)</b>	<b>dt (ms)</b>	<b>Reaction time (ms)</b>
0	120	0	0
1	321	3.12	3.12
2	418	2.39	5.51
3	476	2.10	7.61
4	481	2.08	9.69
5	468	2.14	11.82
6	451	2.22	14.04
7	435	2.30	16.34
8	416	2.40	18.74
9	401	2.49	21.24
10	376	2.66	23.90
11	357	2.80	26.70
12	340	2.94	29.64
13	317	3.15	32.79
14	295	3.39	36.18
15	272	3.68	39.86
16	251	3.98	43.84
17	224	4.46	48.31
18	193	5.18	53.49
19	172	5.81	59.30
20	145	6.90	66.20



Table C. 18: Reaction time calculation from flame C<sub>2</sub>H<sub>4</sub>-air with addition of Ar at pressure 40 kPa

<b>HAB (mm)</b>	<b>V<sub>flame</sub> (mm/s)</b>	<b>dt (ms)</b>	<b>Reaction time (ms)</b>
0	110	0	0
1	311	3.22	3.22
2	364	2.75	5.96
3	416	2.40	8.37
4	438	2.28	10.65
5	454	2.20	12.85
6	455	2.20	15.05
7	438	2.28	17.33
8	420	2.38	19.71
9	401	2.49	22.21
10	381	2.62	24.83
11	361	2.77	27.60
12	339	2.95	30.55
13	317	3.15	33.71
14	294	3.40	37.11
15	271	3.69	40.80
16	247	4.05	44.85
17	222	4.50	49.35
18	197	5.08	54.43
19	171	5.85	60.28
20	144	6.94	67.22

## Appendix D

In this project, we used six flames conditions. The following tables present a summarised result of each flame condition.

### 4) Flame C<sub>2</sub>H<sub>4</sub>-air at $\Phi$ 2.1 with total flow rate 5 Lmin<sup>-1</sup>:

Table D. 1: Summarised result from flame at pressure 48 kPa

<b>HAB</b> <b>(mm)</b>	<b>Reaction time</b> <b>(ms)</b>	<b>T<sub>g</sub></b> <b>(K)</b>	<b>T<sub>s</sub></b> <b>(K)</b>	<b>f<sub>v</sub></b> <b>(ppm)</b>	<b>CH*</b> <b>(a.u.)</b>	<b>C<sub>2</sub>*</b> <b>(a.u.)</b>
1	9.17	781.60	--	--	0.02639	0.01017
2	16.37	974.26	--	--	0.03214	0.01399
3	20.96	1189.96	--	--	0.16386	0.01807
4	24.35	1345.56	--	--	1	0.1874
5	27.72	1386.72	--	--	0.81683	1
6	31.30	1450.02	--	7.97E-04	0.45585	0.48963
6.5	--	--	--	7.50E-04	--	--
7	35.01	1469.97	--	7.83E-04	0.24843	0.22641
8	38.84	1481.59	--	8.18E-04	0.08462	0.01017
9	42.81	1449.78	--	9.65E-04	0.0393	--
10	46.94	1451.14	--	0.00119	0.03304	--
11	51.29	1398.77	1508.5	0.00145	0.00649	--
12	55.88	1390.87	1468.1	0.00189	--	--
13	60.76	1386.14	1418	0.00265	--	--
14	65.97	1370.06	1385.5	0.004	--	--
15	71.62	1368.59	1385.5	0.00584	--	--
16	77.79	1349.55	1352.9	0.00731	--	--
17	84.64	1348.27	1329	0.00962	--	--
18	92.39	1331.56	1288.9	0.0117	--	--
19	101.40	1320.26	1273.1	0.01455	--	--
20	112.27	1312.43	1264.4	0.01819	--	--
21	--	--	--	0.02007	--	--
22	--	--	--	0.02499	--	--

Table D. 2: Summarised result from flame at pressure 46 kPa

<b>HAB</b>	<b>Reaction time</b>	<b>T<sub>g</sub></b>	<b>T<sub>s</sub></b>	<b>f<sub>v</sub></b>	<b>CH*</b>	<b>C<sub>2</sub>*</b>
<b>(mm)</b>	<b>(ms)</b>	<b>(K)</b>	<b>(K)</b>	<b>(ppm)</b>	<b>(a.u.)</b>	<b>(a.u.)</b>
1	5.15	777.30	--	--	0.00171	0.0024
2	9.48	962.18	--	--	0.02093	0.0024
3	13.08	1189.46	--	--	0.15105	0.0024
4	16.63	1287.74	--	--	1	0.71931
5	20.36	1388.69	--	--	0.92328	1
6	24.23	1427.47	--	7.36E-04	0.4773	0.38166
6.5	--	--	--	7.39E-04	--	--
7	28.22	1497.36	1518.7	8.14E-04	0.18375	0.01428
8	32.33	1504.38	1469.5	8.36E-04	0.07636	0.0059
9	36.63	1475.94	1443.9	9.46E-04	0.00548	--
10	41.11	1473.33	1412.7	0.00114	0.00936	--
11	45.83	1422.56	1386.8	0.00143	--	--
12	50.80	1402.77	1359.9	0.00234	--	--
13	56.12	1402.55	1340.4	0.00275	--	--
14	61.80	1400.18	1304.9	0.00411	--	--
15	67.98	1389.42	1295.1	0.00549	--	--
16	74.73	1375.52	1272.9	0.00746	--	--
17	82.25	1371.53	1280.2	0.00937	--	--
18	90.80	1340.78	--	0.01248	--	--
19	100.70	1338.37	--	0.0164	--	--
20	112.60	1329.98	--	0.01861	--	--
21	--	--	--	0.02041	--	--
22	--	--	--	0.0255	--	--

Table D. 3: Summarised result from flame at pressure 40 kPa

<b>HAB</b>	<b>Reaction time</b>	<b>T<sub>g</sub></b>	<b>T<sub>s</sub></b>	<b>CH*</b>	<b>C<sub>2</sub>*</b>	<b>f<sub>v</sub></b>	<b>(2-3 R) PAH LIF</b>	<b>(3-4 R) PAH LIF</b>
<b>(mm)</b>	<b>(ms)</b>	<b>(K)</b>	<b>(K)</b>	<b>(a.u.)</b>	<b>(a.u.)</b>	<b>(ppm)</b>	<b>(a.u.)</b>	<b>(a.u.)</b>
1	5.29	759.23	--	1.71E-02	7.05E-04	0	--	--
2	9.41	920.27	--	1.81E-02	8.89E-04	0	--	--
3	12.84	1175.22	--	1.06E-01	0.00531	--	328770	--
4	16.22	1273.66		8.00E-01	0.51267	--	810659.6	188844.1
5	19.78	1377.56	--	1.00E+00	1	--	2.18E+06	620011.7
6	23.47	1466.99	--	5.12E-01	0.43996	5.28E-04	1.91E+06	2.08E+06
6.5	--	--	--	--	--	5.32E-04	--	--
7	27.29	1511.59	1530.5	0.24346	0.16984	4.97E-04	1.76E+06	1.90E+06
8	31.22	1509.90	1479.3	0.11889	0.01274	7.46E-04	1.43E+06	1.74E+06
9	35.29	1483.24	1447.6	0.04005	7.05E-04	8.47E-04	1.27E+06	1.48E+06
10	39.62	1485.42	1417.1	0.02548	--	0.00107	1.13E+06	1.38E+06
11	44.12	1438.56	1389.5	0.01332	--	0.00127	986053.8	1.21E+06
12	48.88	1425.32	1361.7	--	--	0.00214	947507	1.13E+06
13	53.96	1400.05	1352.9	--	--	0.00241	818825.1	1.06E+06
14	59.39	1417.43	1297.7	--	--	0.00388	732949.4	1.01E+06
15	65.28	1404.48	1269.5	--	--	0.0051	751542.6	924525.5
16	71.73	1387.37	1259.5	--	--	0.00674	659896.8	993696.1
17	78.92	1371.68	--	--	--	0.00915	617212.1	965928.6
18	87.05	1364.63	--	--	--	0.01161	563303.3	1.04E+06
19	96.49	1357.92	--	--	--	0.01353	563307	1.19E+06
20	107.85	1346.39	--	--	--	0.01706	--	--
21	--	--	--	--	--	0.01948	--	--
22	--	--	--	--	--	0.02261	--	--

Table D. 4: Summarised result from flame at pressure 38 kPa

<b>HAB</b>	<b>Reaction time</b>	<b>T<sub>g</sub></b>	<b>T<sub>s</sub></b>	<b>f<sub>v</sub></b>	<b>CH*</b>	<b>C<sub>2</sub>*</b>
<b>(mm)</b>	<b>(ms)</b>	<b>(K)</b>	<b>(K)</b>	<b>(ppm)</b>	<b>(a.u.)</b>	<b>(a.u.)</b>
1	5.24	736.92	--	--	0.01954	1.51E-04
2	9.28	909.13	--	--	0.01974	4.98E-04
3	12.65	1163.00	--	--	0.08725	0.0019
4	15.96	1263.54	--	--	0.65502	0.29325
5	19.45	1381.60	--	--	1	1
6	23.06	1468.68	--	3.86E-04	0.62867	0.62895
6.5	--	--	--	4.19E-04	--	--
7	26.77	1516.56	1543.7	3.98E-04	0.28705	0.24879
8	30.61	1509.47	1481.8	5.91E-04	0.10617	0.01405
9	34.59	1511.06	1440.9	7.96E-04	0.04778	--
10	38.86	1488.44	1423	9.09E-04	0.02015	--
11	43.25	1447.77	1387.6	0.0011	0.01419	--
12	47.90	1425.94	1360.2	0.0018	--	--
13	52.85	1428.97	1327.4	0.0021	--	--
14	58.17	1426.75	1299	0.00339	--	--
15	63.92	1418.16	1276.6	0.00414	--	--
16	70.21	1399.90	1259.8	0.00583	--	--
17	77.20	1399.25	--	0.00814	--	--
18	85.07	1369.41	--	0.00997	--	--
19	94.25	1369.43	--	0.01203	--	--
20	105.24	1353.48	--	0.01438	--	--
21	--	--	--	0.01703	--	--
22	--	--	--	0.0192	--	--

Table D. 5: Summarised result from flame at pressure 35 kPa

<b>HAB</b>	<b>Reaction time</b>	<b>T<sub>g</sub></b>	<b>T<sub>s</sub></b>	<b>f<sub>v</sub></b>	<b>CH*</b>	<b>C<sub>2</sub>*</b>
<b>(mm)</b>	<b>(ms)</b>	<b>(K)</b>	<b>(K)</b>	<b>(ppm)</b>	<b>(a.u.)</b>	<b>(a.u.)</b>
1	5.29	731.97	--	--	0.01218	0.00595
2	9.18	891.78	--	--	0.01236	0.00595
3	12.38	1147.48	--	--	0.06766	8.84E-03
4	15.52	1253.20	--	--	0.42277	0.15237
5	18.83	1367.13	--	--	1	1
6	22.27	1466.91	--	2.80E-04	0.7078	0.77951
6.5	--	--	--	3.07E-04	--	--
7	25.82	1509.41	1578.5	2.83E-04	0.31535	0.31883
8	29.48	1511.00	1508.2	2.85E-04	0.12353	0.13781
9	33.28	1510.50	1459.8	3.76E-04	0.05329	0.00595
10	37.25	1489.52	1429.8	7.91E-04	0.02828	--
11	41.43	1460.03	1403.8	8.99E-04	0.02107	--
12	45.86	1437.07	1380.6	0.00142	0.01346	--
13	50.57	1437.99	1349.2	0.00172	0.01198	--
14	55.63	1437.91	1329.4	0.00281	--	--
15	61.09	1424.97	1310.1	0.0035	--	--
16	67.08	1412.20	1325.3	0.00452	--	--
17	73.70	1409.35	--	0.00606	--	--
18	81.22	1380.70	--	0.00784	--	--
19	89.91	1377.40	--	0.00938	--	--
20	100.33	1363.68	--	0.01092	--	--
21	--	--	--	0.01219	--	--
22	--	--	--	0.01457	--	--

Table D. 6: Summarised result from flame at pressure 32 kPa

<b>HAB</b>	<b>Reaction time</b>	<b>T<sub>g</sub></b>	<b>T<sub>s</sub></b>	<b>f<sub>v</sub></b>	<b>CH*</b>	<b>C<sub>2</sub>*</b>
<b>(mm)</b>	<b>(ms)</b>	<b>(K)</b>	<b>(K)</b>	<b>(ppm)</b>	<b>(a.u.)</b>	<b>(a.u.)</b>
1	5.24	712.73	--	--	0.01296	0.00453
2	8.87	869.26	--	--	0.01411	0.00453
3	12.05	1134.37	--	--	0.05061	4.47E-03
4	15.17	1228.55	--	--	0.30342	0.09703
5	18.46	1348.59	--	--	1	0.71145
6	21.89	1456.15	--	2.25E-04	0.96854	1
6.5	--	--	--	2.23E-04	--	--
7	25.41	1510.55	--	2.11E-04	0.41791	0.50238
8	29.04	1516.49	1573	2.75E-04	0.1781	0.16278
9	32.82	1524.70	1502.8	2.99E-04	0.08497	0.01434
10	36.77	1485.28	1460.9	5.81E-04	0.04783	0.00528
11	40.92	1479.53	1427.4	6.82E-04	0.04021	--
12	45.32	1456.58	1405.7	0.00108	0.03193	--
13	50.00	1452.06	1375.3	0.00127	0.01073	--
14	55.02	1452.09	1358	0.0017	0.008	--
15	60.46	1441.33	1357.6	0.00255	0.00174	--
16	66.41	1431.85	--	0.00325	--	--
17	73.03	1422.65	--	0.00425	--	--
18	80.49	1401.48	--	0.00527	--	--
19	89.12	1391.51	--	0.00631	--	--
20	99.53	1385.93	--	0.00725	--	--
21	--	--	--	0.00805	--	--
22	--	--	--	0.00974	--	--

Table D. 7: Summarised result from flame at pressure 27 kPa

<b>HAB</b>	<b>Reaction time</b>	<b>T<sub>g</sub></b>	<b>T<sub>s</sub></b>	<b>CH*</b>	<b>C<sub>2</sub>*</b>	<b>f<sub>v</sub></b>	<b>(2-3 R) PAH LIF</b>	<b>(3-4 R) PAH LIF</b>
<b>(mm)</b>	<b>(ms)</b>	<b>(K)</b>	<b>(K)</b>	<b>(a.u.)</b>	<b>(a.u.)</b>	<b>(ppm)</b>	<b>(a.u.)</b>	<b>(a.u.)</b>
1	5.13	709.94	--	0.01028	0.00797	--	--	--
2	9.42	863.05	--	1.28E-02	4.33E-03	--	--	--
3	13.12	1128.17	--	1.41E-02	3.40E-03	--	94851.59	--
4	16.61	1228.87	--	8.22E-02	0.01288	--	138693.8	81394.81
5	19.82	1348.24	--	5.00E-01	0.18945	--	3.28E+05	1.75E+05
6	23.17	1469.26	--	1	0.92456	--	5.37E+05	5.19E+05
6.5	--	--	--	--	--	--	--	--
7	26.60	1515.30	--	0.71222	1.00E+00	1.90E-04	6.11E+05	1.01E+06
8	30.15	1523.46	--	0.36507	3.86E-01	2.36E-04	4.78E+05	1.20E+06
9	33.85	1531.88	1629.1	0.16503	1.35E-01	2.34E-04	479250.2	9.56E+05
10	37.72	1491.10	1534.5	0.08175	4.18E-02	3.52E-04	458208.5	9.14E+05
11	41.78	1489.77	1510.4	0.03232	1.18E-02	3.31E-04	426514.6	8.84E+05
12	46.07	1454.66	1475.6	0.02083	8.78E-03	4.95E-04	346844.7	7.90E+05
13	50.64	1452.37	1453.4	0.01746	2.15E-03	5.55E-04	327539.8	633246.3
14	55.54	1430.87	1453.5	0.01136	--	8.88E-04	306348.3	618111.7
15	60.86	1428.43	--	0.01087	--	9.43E-04	337109.5	570148.2
16	66.67	1445.39	--	0.00581	--	0.00134	315298	5.93E+05
17	73.12	1435.66	--	0.00193	--	0.0016	315298	5.50E+05
18	80.42	1415.07	--	--	--	0.00193	318904.5	513909
19	88.83	1406.38	--	--	--	0.00211	247260.6	448266.5
20	98.93	1393.98	--	--	--	0.00236	--	--
21	--	--	--	--	--	0.00249	--	--
22	--	--	--	--	--	0.00291	--	--



5) Flame C<sub>2</sub>H<sub>4</sub>-air at  $\Phi$  2.3 with total flow rate 5 Lmin<sup>-1</sup>:

Table D. 8: Summarised result from flame at pressure 48 kPa

<b>HAB</b>	<b>Reaction time</b>	<b>T<sub>g</sub></b>	<b>T<sub>s</sub></b>	<b>f<sub>v</sub></b>	<b>CH*</b>	<b>C<sub>2</sub>*</b>
<b>(mm)</b>	<b>(ms)</b>	<b>(K)</b>	<b>(K)</b>	<b>(ppm)</b>	<b>(a.u.)</b>	<b>(a.u.)</b>
1	4.52	856.04	--	--	0.01579	--
2	8.42	970.76	--	--	0.01586	--
3	12.18	1074.51	--	--	0.04119	--
4	15.88	1175.55	--	--	5.96E-01	--
5	19.77	1282.86	--	1.15E-04	1.00E+00	--
6	23.82	1300.52	--	1.03E-04	6.39E-01	3.658133
6.5	--	--	--	1.38E-04	--	--
7	27.99	1307.64	--	2.05E-04	0.385	3.726919
8	32.30	1316.72	--	3.86E-04	0.11465	3.809172
9	36.78	1322.65	--	8.70E-04	0.0184	3.926451
10	41.45	1338.40	1423.4	0.0014	0.01312	4.048117
11	46.38	1351.12	1380	0.00229	--	4.220783
12	51.59	1373.78	1360.1	0.00572	--	4.414568
13	57.14	1370.42	1340	0.00637	--	4.760563
14	63.10	1392.40	1331.9	0.00916	--	5.108971
15	69.55	1389.35	1354.6	0.01421	--	5.6669
16	76.64	1385.45	1367.2	0.01939	--	6.398767
17	84.51	1381.72	1333.6	0.02399	--	7.365567
18	93.44	1371.70	1342	0.03145	--	8.704522
19	103.86	1368.84	--	0.03791	--	10.48034
20	116.36	1346.30	--	0.04592	--	13.11282
21	--	--	--	0.05099	--	--
22	--	--	--	0.05165	--	--

Table D. 9: Summarised result from flame at pressure 46 kPa

<b>HAB</b>	<b>Reaction time</b>	<b>T<sub>g</sub></b>	<b>T<sub>s</sub></b>	<b>f<sub>v</sub></b>	<b>CH*</b>	<b>C<sub>2</sub>*</b>
<b>(mm)</b>	<b>(ms)</b>	<b>(K)</b>	<b>(K)</b>	<b>(ppm)</b>	<b>(a.u.)</b>	<b>(a.u.)</b>
1	4.69	854.35	--	--	0.01008	0.05981
2	8.60	972.19	--	--	0.00551	0.0153
3	12.33	1090.35	--	--	0.03016	0.04844
4	16.01	1194.32	--	--	0.36888	5.11E-01
5	19.88	1314.69	--	1.06E-04	1	1.00E+00
6	23.90	1322.08	--	1.12E-04	0.72535	0.74577
6.5	--	--	--	1.47E-04	--	--
7	28.03	1330.51	--	1.82E-04	0.30206	0.11948
8	32.31	1346.61	--	3.93E-04	0.15386	0.08361
9	36.75	1338.63	--	8.57E-04	0.06083	--
10	41.40	1366.94	--	0.00146	0.02556	--
11	46.30	1379.47	1419.9	0.0024	--	--
12	51.49	1400.26	1368.1	0.00576	--	--
13	57.01	1400.43	1367.6	0.00709	--	--
14	62.93	1422.90	1380.6	0.00975	--	--
15	69.34	1421.12	1376.2	0.01396	--	--
16	76.38	1417.30	1363.2	0.01858	--	--
17	84.19	1419.57	1350.2	0.0232	--	--
18	93.04	1411.62	1340.5	0.02939	--	--
19	103.35	1401.82	1355.4	0.0368	--	--
20	115.79	1381.86	1384	0.04422	--	--
21	--	--	--	0.04767	--	--
22	--	--	--	0.0511	--	--

Table D. 10: Summarised result from flame at pressure 40 kPa

<b>HAB</b>	<b>Reaction time</b>	<b>T<sub>g</sub></b>	<b>T<sub>s</sub></b>	<b>CH*</b>	<b>C<sub>2</sub>*</b>	<b>f<sub>v</sub></b>	<b>(2-3 R) PAH LIF</b>	<b>(3-4 R) PAH LIF</b>
<b>(mm)</b>	<b>(ms)</b>	<b>(K)</b>	<b>(K)</b>	<b>(a.u.)</b>	<b>(a.u.)</b>	<b>(ppm)</b>	<b>(a.u.)</b>	<b>(a.u.)</b>
1	4.65	846.42	--	0.01012	0.07559	--	--	--
2	8.65	983.89	--	0.00803	0.0795	--	--	--
3	12.27	1102.15	--	0.04376	0.04541	--	349079.2	--
4	15.83	1201.01	--	0.20808	4.68E-02	--	4.45E+05	168383.2
5	19.59	1333.42	--	1	5.44E-01	--	8.30E+05	266184.1
6	23.50	1327.16	--	0.95404	1.00E+00	1.05E-04	1.10E+06	788289.7
6.5	--	--	--	--	--	1.32E-04	--	--
7	27.51	1351.63	--	0.30183	0.05879	1.56E-04	1.05E+06	1.19E+06
8	31.66	1360.26	--	0.16917	0.07508	3.39E-04	859940.2	1.14E+06
9	35.97	1329.91	--	0.06354	--	7.62E-04	809430.8	1.02E+06
10	40.50	1376.89	1447.8	0.00803	--	0.00138	682355.6	990045.6
11	45.26	1388.33	1410.1	--	--	0.00235	508866.4	926666.4
12	50.29	1411.55	1384.3	--	--	0.00573	507711.3	771078
13	55.63	1391.97	1368.9	--	--	0.00759	475043.8	759543.5
14	61.38	1432.08	1367.6	--	--	0.00996	455201.5	838015.5
15	67.63	1439.88	1354.3	--	--	0.01262	403456.4	810424
16	74.48	1437.22	1356	--	--	0.01816	333738	923668.9
17	82.06	1403.51	1301.5	--	--	0.02123	438798.8	922503.5
18	90.68	1422.14	--	--	--	0.02903	333583.8	--
19	100.68	1421.85	--	--	--	0.03469	--	--
20	112.73	1394.59	--	--	--	0.04205	--	--
21	--	--	--	--	--	0.04729	--	--
22	--	--	--	--	--	0.04782	--	--

Table D. 11: Summarised result from flame at pressure 38 kPa

<b>HAB</b>	<b>Reaction time</b>	<b>T<sub>g</sub></b>	<b>T<sub>s</sub></b>	<b>f<sub>v</sub></b>	<b>CH*</b>	<b>C<sub>2</sub>*</b>
<b>(mm)</b>	<b>(ms)</b>	<b>(K)</b>	<b>(K)</b>	<b>(ppm)</b>	<b>(a.u.)</b>	<b>(a.u.)</b>
1	4.69	783.68	--	--	0.01768	0.00984
2	8.68	995.10	--	--	0.01665	0.00984
3	12.16	1111.19	--	--	0.03846	0.00984
4	15.59	1212.52	--	--	0.20141	0.02265
5	19.20	1342.94	--	--	9.21E-01	2.53E-01
6	22.94	1336.75	--	1.10E-04	1.00E+00	1.00E+00
6.5	--	--	--	1.25E-04	--	--
7	26.79	1350.96	--	1.48E-04	0.6326	5.51E-01
8	30.77	1364.24	--	2.99E-04	0.22504	0.014
9	34.91	1359.18	--	6.98E-04	0.13459	--
10	39.23	1380.85	--	0.00128	0.09118	--
11	43.78	1400.41	--	0.00217	0.0114	--
12	48.61	1420.38	1438.2	0.00522	--	--
13	53.74	1428.72	1410.4	0.00717	--	--
14	59.26	1441.01	1419.6	0.0094	--	--
15	65.25	1448.79	1384.9	0.01231	--	--
16	71.79	1443.68	1382.4	0.01653	--	--
17	79.03	1440.09	1363.1	0.02119	--	--
18	87.23	1436.94	1346.7	0.02563	--	--
19	96.76	1424.82	1367	0.03258	--	--
20	108.25	1401.08	1349.7	0.04031	--	--
21	--	--	--	0.04225	--	--
22	--	--	--	0.04645	--	--

Table D. 12: Summarised result from flame at pressure 35 kPa

<b>HAB</b>	<b>Reaction time</b>	<b>T<sub>g</sub></b>	<b>T<sub>s</sub></b>	<b>f<sub>v</sub></b>	<b>CH*</b>	<b>C<sub>2</sub>*</b>
<b>(mm)</b>	<b>(ms)</b>	<b>(K)</b>	<b>(K)</b>	<b>(ppm)</b>	<b>(a.u.)</b>	<b>(a.u.)</b>
1	4.74	782.92	--	--	0.03212	0.00953
2	8.68	1005.26	--	--	0.04209	0.00953
3	12.05	1120.40	--	--	0.04495	0.00953
4	15.38	1225.37	--	--	0.13667	0.00953
5	18.87	1349.42	--	--	0.62316	0.14516
6	22.51	1339.83	--	1.09E-04	1.00E+00	1
6.5	--	--	--	1.28E-04	--	--
7	26.26	1359.87	--	1.45E-04	7.55E-01	0.72209
8	30.13	1374.35	--	2.53E-04	3.30E-01	0.0977
9	34.16	1369.35	1.41E+03	5.76E-04	1.80E-01	0.00953
10	38.37	1385.21	1369.2	0.00108	9.48E-02	--
11	42.79	1402.55	1332.7	0.00186	0.02953	--
12	47.48	1424.89	1402.3	0.00421	--	--
13	52.46	1439.13	1384.2	0.00629	--	--
14	57.81	1446.70	1371.5	0.00799	--	--
15	63.62	1454.59	1354.6	0.01093	--	--
16	69.99	1454.36	1366.4	0.0157	--	--
17	77.03	1453.13	1397.3	0.01785	--	--
18	85.03	1444.10	--	0.02557	--	--
19	94.29	1429.35	--	0.02925	--	--
20	105.40	1407.98	--	0.03517	--	--
21	--	--	--	0.03994	--	--
22	--	--	--	0.03859	--	--

Table D. 13: Summarised result from flame at pressure 32 kPa

<b>HAB</b>	<b>Reaction time</b>	<b>T<sub>g</sub></b>	<b>T<sub>s</sub></b>	<b>f<sub>v</sub></b>	<b>CH*</b>	<b>C<sub>2</sub>*</b>
<b>(mm)</b>	<b>(ms)</b>	<b>(K)</b>	<b>(K)</b>	<b>(ppm)</b>	<b>(a.u.)</b>	<b>(a.u.)</b>
1	4.93	763.41	--	--	0.0162	0.00291
2	8.99	1020.21	--	--	0.01792	0.00291
3	12.37	1125.63	--	--	0.02021	0.00291
4	15.68	1236.51	--	--	0.06711	0.00291
5	19.18	1352.04	--	--	0.2144	0.05393
6	22.80	1346.95	--	--	0.86817	0.60195
6.5	--	--	--	--	--	--
7	26.53	1364.78	--	--	1	1
8	30.39	1377.00	--	2.06E-04	0.55484	0.61538
9	34.41	1378.94	--	4.64E-04	0.22239	0.06441
10	38.61	1387.99	1394.7	8.31E-04	0.09616	0.02516
11	43.04	1421.82	1443	1.55E-03	0.07718	--
12	47.71	1428.91	1412.9	3.17E-03	0.0676	--
13	52.68	1454.00	1381.3	5.04E-03	0.01837	--
14	58.03	1452.12	1374.1	0.00633	--	--
15	63.81	1467.12	1350.6	0.00969	--	--
16	70.14	1465.71	1349.7	0.01233	--	--
17	77.18	1459.85	1377.6	0.01668	--	--
18	85.12	1451.82	--	0.01934	--	--
19	94.38	1443.29	--	0.02487	--	--
20	105.45	1420.57	--	0.02636	--	--
21	--	--	--	0.03021	--	--
22	--	--	--	0.02841	--	--

Table D. 14: Summarised result from flame at pressure 27 kPa

<b>HAB</b>	<b>Reaction</b>	<b>T<sub>g</sub></b>	<b>T<sub>s</sub></b>	<b>CH*</b>	<b>C<sub>2</sub>*</b>	<b>f<sub>v</sub></b>	<b>(2-3 R)</b>	<b>(3-4 R)</b>
<b>(mm)</b>	<b>time</b>	<b>(K)</b>	<b>(K)</b>	<b>(a.u.)</b>	<b>(a.u.)</b>	<b>(ppm)</b>	<b>PAH LIF</b>	<b>PAH LIF</b>
	<b>(ms)</b>						<b>(a.u.)</b>	<b>(a.u.)</b>
1	4.90	743.03	--	0.00347	0.00741	--	--	--
2	8.92	1027.03	--	0.00379	0.00741	--	78073.97	72273.1
3	12.25	1149.61	--	0.00527	0.00741	--	69055.98	69104.55
4	15.53	1250.27	--	0.01062	0.00741	--	64245.11	53947.95
5	18.98	1352.88	--	0.02954	0.00109	--	135071.3	138810.6
6	22.56	1366.36	--	0.08045	0.00686	--	177746.8	226713.4
6.5	--	--	--	--	--	--	--	--
7	26.25	1378.56	--	0.37974	0.17706	--	183251.3	313707.3
8	30.07	1390.91	--	0.92079	0.87775	--	194874	354639.8
9	34.04	1394.06	--	1	1	--	251620.5	428584.7
10	38.19	1397.33	--	0.72697	0.64238	3.86E-04	273837.9	465999.8
11	42.55	1438.58	1.62E+03	0.39492	0.34422	7.13E-04	195197.1	354505.1
12	47.16	1442.19	1.60E+03	0.19383	0.06567	0.00104	249018.6	413794.4
13	52.09	1464.06	1.54E+03	0.10271	--	0.00157	200508.6	385259.3
14	57.35	1418.05	1.52E+03	0.03724	--	0.00267	237832.3	425074.3
15	63.07	1434.93	1.52E+03	0.01642	--	0.00401	201737.5	395283.8
16	69.32	1473.47	1.60E+03	0.01396	--	0.00493	225874.2	452645.6
17	76.26	1477.28	--	0.00994	--	0.00652	216148.5	519617.4
18	84.13	1459.60	--	--	--	0.00739	--	--
19	93.23	1451.98	--	--	--	0.00933	--	--
20	104.17	1425.54	--	--	--	0.0101	--	--
21	--	--	--	--	--	0.01161	--	--
22	--	--	--	--	--	0.01066	--	--

**6) Flame C<sub>2</sub>H<sub>4</sub>-air with addition of specific gas with total flow rate 7 Lmin<sup>-1</sup> :**

Table D. 15: Summarised result from flame C<sub>2</sub>H<sub>4</sub>-air at pressure 40 kPa

<b>HAB</b>	<b>Reaction time</b>	<b>T<sub>g</sub></b>	<b>CH*</b>	<b>C<sub>2</sub>*</b>	<b>f<sub>v</sub></b>	<b>(2-3 R) PAH LIF</b>	<b>(3-4 R) PAH LIF</b>
<b>(mm)</b>	<b>(ms)</b>	<b>(K)</b>	<b>(a.u.)</b>	<b>(a.u.)</b>	<b>(ppm)</b>	<b>(a.u.)</b>	<b>(a.u.)</b>
1	4.74	--	0.00833	0.00418	--	--	--
2	7.95	1134.43	0.22889	0.00577	--	244783	234616.6
3	10.32	1364.98	1	0.04814	--	625946.4	835173.8
4	12.65	1463.45	0.91495	0.75427	--	1.12E+06	1.80E+06
5	15.07	1458.52	0.34327	1.00E+00	2.74E-04	1.11E+06	1.88E+06
6	17.59	1454.68	0.08815	3.53E-01	2.11E-04	1.02E+06	1.72E+06
7	20.19	1448.70	0.00448	3.73E-02	2.18E-04	932238.1	1.57E+06
8	22.89	1442.72	--	--	3.13E-04	801999	1.47E+06
9	25.69	1432.67	--	--	6.04E-04	877233.9	1.45E+06
10	28.62	1417.52	--	--	0.00101	847782.7	1.44E+06
11	31.71	1397.26	--	--	0.00181	738813.7	1.32E+06
12	34.98	1381.13	--	--	0.00307	777141.3	1.36E+06
13	38.46	1353.73	--	--	0.00515	718988.8	1.36E+06
14	42.19	1284.23	--	--	0.00853	701188.2	1.27E+06
15	46.24	1223.10	--	--	0.01169	660207.9	1.24E+06
16	50.67	1165.02	--	--	0.01611	669531.6	1.25E+06
17	55.57	1112.19	--	--	0.01914	603929.8	1.19E+06
18	61.09	1062.51	--	--	0.02652	--	--
19	67.46	1004.72	--	--	0.02818	--	--
20	75.04	935.81	--	--	--	--	--



Table D. 16: Summarised result from flame C<sub>2</sub>H<sub>4</sub>-air with addition of N<sub>2</sub> at pressure 40 kPa

<b>HAB</b>	<b>Reaction time</b>	<b>T<sub>g</sub></b>	<b>CH*</b>	<b>C<sub>2</sub>*</b>	<b>f<sub>v</sub></b>	<b>(2-3 R) PAH LIF</b>	<b>(3-4 R) PAH LIF</b>
<b>(mm)</b>	<b>(ms)</b>	<b>(K)</b>	<b>(a.u.)</b>	<b>(a.u.)</b>	<b>(ppm)</b>	<b>(a.u.)</b>	<b>(a.u.)</b>
1	3.15	--	--	--	--	294413.8	163772.8
2	5.58	324.07	--	--	--	164031.7	163875.8
3	7.64	626.36	--	--	--	276933.1	78817.44
4	9.70	1115.58	--	--	--	283830.1	162083.5
5	11.84	1210.27	7.31E-03	1.05E-03	--	576933.5	203439.9
6	14.04	1405.53	4.48E-02	8.51E-03	--	1.16E+06	735840.4
7	16.34	1426.30	0.32984	1.76E-01	--	1.77E+06	1.87E+06
8	18.73	1425.52	1	1.00E+00	--	1.79E+06	2.75E+06
9	21.24	1414.51	0.58172	7.76E-01	--	1.70E+06	2.83E+06
10	23.87	1403.46	0.20608	2.31E-01	9.81E-05	1.64E+06	2.73E+06
11	26.66	1382.25	5.87E-02	4.63E-02	1.77E-04	1.39E+06	2.55E+06
12	29.62	1354.86	3.77E-01	3.67E-01	2.76E-04	1.29E+06	2.28E+06
13	32.78	1326.49	1.67E-01	1.69E-01	5.42E-04	1.37E+06	2.15E+06
14	36.20	1249.90	4.89E-02	8.06E-03	8.88E-04	1.25E+06	2.35E+06
15	39.90	1178.63	6.03E-03	--	0.00126	1.18E+06	2.11E+06
16	43.96	1148.31	--	--	0.00174	1.05E+06	2.10E+06
17	48.49	1092.48	--	--	0.00224	--	--
18	53.59	1041.82	--	--	0.00265	--	--
19	59.47	981.02	--	--	0.00321	--	--
20	66.47	909.13	--	--	--	--	--

Table D. 17: Summarised result from flame C<sub>2</sub>H<sub>4</sub>-air with addition of CO<sub>2</sub> at pressure 40 kPa

<b>HAB</b>	<b>Reaction time</b>	<b>T<sub>g</sub></b>	<b>CH*</b>	<b>C<sub>2</sub>*</b>	<b>f<sub>v</sub></b>	<b>(2-3 R) PAH LIF</b>	<b>(3-4 R) PAH LIF</b>
<b>(mm)</b>	<b>(ms)</b>	<b>(K)</b>	<b>(a.u.)</b>	<b>(a.u.)</b>	<b>(ppm)</b>	<b>(a.u.)</b>	<b>(a.u.)</b>
1	3.12	--	--	--	--	203458	--
2	5.51	363.16	--	--	--	138556.5	193055.8
3	7.61	661.66	--	--	--	185489.4	135081.7
4	9.69	1126.77	--	--	--	226619.8	180543.2
5	11.82	1359.32	7.73E-03	6.79E-03	--	4.17E+05	289478.2
6	14.04	1405.56	4.67E-02	3.61E-03	--	651352.2	699718.2
7	16.34	1420.16	3.16E-01	0.18115	--	730672.9	1.15E+06
8	18.74	1417.34	1.00E+00	1	--	673451.3	1.30E+06
9	21.24	1406.21	6.43E-01	0.8412	--	710630.7	1.31E+06
10	23.90	1386.09	0.17429	0.1801	8.09E-05	659163.7	1.29E+06
11	26.70	1375.10	0.06551	3.35E-02	1.34E-04	689284	1.28E+06
12	29.64	1336.36	0.38059	3.57E-01	2.27E-04	611983	1.28E+06
13	32.79	1324.42	0.15386	1.31E-01	3.64E-04	626924.7	1.22E+06
14	36.18	1229.44	0.03376	-3.34E-03	5.36E-04	606302.2	1.21E+06
15	39.86	1203.16	0.0071	-4.19E-02	8.38E-04	--	1.25E+06
16	43.84	1112.47	-0.0037	-6.61E-02	9.39E-04	--	--
17	48.31	1082.22	-0.02275	-1.45E-01	1.18E-03	--	--
18	53.49	1011.26	--	--	0.00132	--	--
19	59.30	961.59	--	--	0.00148	--	--
20	66.20	897.90	--	--	--	--	--

Table D. 18: Summarised result from flame C<sub>2</sub>H<sub>4</sub>-air with addition of Ar at pressure 40 kPa

<b>HAB</b>	<b>Reaction time</b>	<b>T<sub>g</sub></b>	<b>CH*</b>	<b>C<sub>2</sub>*</b>	<b>f<sub>v</sub></b>	<b>(2-3 R) PAH LIF</b>	<b>(3-4 R) PAH LIF</b>
<b>(mm)</b>	<b>(ms)</b>	<b>(K)</b>	<b>(a.u.)</b>	<b>(a.u.)</b>	<b>(ppm)</b>	<b>(a.u.)</b>	<b>(a.u.)</b>
1	3.22	--	--	--	--	--	--
2	5.96	308.05	--	--	--	21971.21	5186.413
3	8.37	319.09	--	--	--	80248.37	76339.36
4	10.65	374.31	--	--	--	7.06E+04	76908.13
5	12.85	442.69	--	--	--	8.18E+04	8.35E+04
6	15.05	788.09	6.88E-03	4.09E-03	--	7.04E+04	72594.76
7	17.33	1125.20	1.99E-02	8.96E-03	--	8.27E+04	81448.48
8	19.71	1193.51	1.44E-01	4.13E-02	--	1.30E+05	135476.6
9	22.21	1373.58	7.79E-01	5.49E-01	--	1.55E+05	174216
10	24.83	1385.01	1.00E+00	1	--	1.93E+05	273955.8
11	27.60	1377.16	0.50742	0.61451	4.56E-05	1.94E+05	284251.7
12	30.55	1361.98	0.14742	0.14379	4.66E-05	1.83E+05	298037.8
13	33.71	1319.77	0.14425	0.06868	9.00E-05	1.63E+05	255328.9
14	37.11	1299.67	0.23383	0.10331	1.14E-04	1.63E+05	266254.1
15	40.80	1165.97	0.24089	0.11463	1.54E-04	1.72E+05	260649.6
16	44.85	1124.41	0.13653	0.07011	2.10E-04	1.52E+05	259432.7
17	49.35	1072.39	0.05885	0.02345	2.34E-04	1.48E+05	270411.7
18	54.43	1020.52	0.01185	0.00271	2.96E-04	--	--
19	60.28	969.91	--	--	3.06E-04	--	--
20	67.22	895.26	--	--	--	--	--

- **Result summary**

Table D. 19: Soot surface growth rate constant  $k_{SG}$

Flames	Total flow rate (l/min)	$\Phi$	Pressure (kPa)	$k_{SG}$ ( $s^{-1}$ )
				Linear fitting
C <sub>2</sub> H <sub>4</sub> -air	5	2.1	48	
			46	
			40	
			38	
			35	
			32	
			27	20
C <sub>2</sub> H <sub>4</sub> -air	5	2.3	48	
			46	
			40	
			38	
			35	12.11
			32	25.13
	27	32		
C <sub>2</sub> H <sub>4</sub> -air	7			8.3
C <sub>2</sub> H <sub>4</sub> -air:N <sub>2</sub>	7.6			15.35
C <sub>2</sub> H <sub>4</sub> -air:CO <sub>2</sub>	7.6	2.1	40	35
C <sub>2</sub> H <sub>4</sub> -air:Ar	7.6			60.30

Table D. 20: The Spatially phenomenological removing rate constant of PAHs

Flames	Total flow rate (l/min)	$\Phi$	Pressure (kPa)	Spatially phenomenological removing rate constant (s <sup>-1</sup> )	
				( $k_{phen}^{2-3R}$ )	( $k_{phen}^{3-4R}$ )
C <sub>2</sub> H <sub>4</sub> -air	5	2.1	40	24.61	21.64
			27	15.29	18.26
C <sub>2</sub> H <sub>4</sub> -air	5	2.3	40	23.33	16.9
			27	--	--
C <sub>2</sub> H <sub>4</sub> -air	7	2.1	40	14.1	10.3
C <sub>2</sub> H <sub>4</sub> -air:N <sub>2</sub>	7.6		40	20.58	14.53
C <sub>2</sub> H <sub>4</sub> -air:CO <sub>2</sub>	7.6		40	7.874	4.709
C <sub>2</sub> H <sub>4</sub> -air:Ar	7.6		40	11.2	3.978

## **Publications**

### **Published**

- Algoraini, S., Sun, Z., & Alwahabi, Z. T. (2015). Laser-Induced Incandescence of Laminar Premixed C<sub>2</sub>H<sub>4</sub>-Air flames at Well-Controlled Pressure. In Proceedings of the 7th Australian Conference on Laser Diagnostics in Fluid Mechanics and Combustion (pp. 65-68). Melbourne.
- Algoraini, S., Zhiwei, S., & Alwahabi, Z. T. (2017). Application of spatially resolved emission spectroscopy to study low-pressure premixed ethylene/air sooting flames. In 11th Asia-Pacific Conference on Combustion, ASPACC 2017 Vol. 2017-December.

### **To be submitted**

- Algoraini, S., Zhiwei, S., & Alwahabi, Z. T. (2019). Characterisations of ethylene/air laminar premixed sooting flames at low pressure.